Scuola di Dottorato di Ricerca in Scienze
Tecnologie e Misure Spaziali (STMS)
dell'Università di Padova
-
XXIV Ciclo
Indirizzo: Misure Meccaniche per l'Ingegneria e lo Spazio

PhD Thesis

Advanced Fluid Dynamic Codes for Propellant Behavior, Injection and Combustion Simulation in Hybrid Rockets

Supervisor: Ch.mo Daniele Pavarin
Co-supervisor: Dr. Marco Manente

PhD Student: Marta Lazzarin

January, 2012

To My Family and My Friends

Contents

Abstract

This work focuses on two main topics: the study of a sponge Propellant Management Device (PMD) and of hybrid rockets internal fluid dynamics. The aim is to implement and use CFD codes describing some vital aspects for hybrid rockets, such as propellant dynamics and internal ballistics.

In fluid dynamics, PMD behavior cannot be simulated with standard tools, because a very specific physics needs to be represented concerning capillarity, contact angle, sloshing, bubble point and multiphase fluid dynamics: it is necessary to develop a tool on purpose.

The CFD software developed is 3D, can work in transient conditions and is based on OpenFOAM. It can handle bubble point, sloshing, interface transport between two fluid phases and the pressure drop due to a screen in the fluid domain.

CFD codes have been tested to analyze their capabilities in terms of simulating rockets fluid dynamics. Test beds and experiments have been used to retrieve the data used for codes validation.

The objective of these studies for internal fluid dynamics characterization is to prove that CFD is a powerful design tool, able to reduce the costs connected with experiments and manufacturing. Pressure, characteristic velocity and efficiency are compared between CFD and experiments, to prove that the software can predict the most performing configurations.

Sommario

Questo lavoro si concentra su due temi principali: lo studio di un PMD di tipo sponge e della fluidodinamica interna dei razzi ibridi. L'obiettivo è implementare e utilizzare codici CFD che descrivono alcuni aspetti vitali per i razzi ibridi, come ad esempio la dinamica del propellente e la balistica interna.

Il comportamento fluidodinamico di un PMD non può essere simulato con strumenti standard, perché devono essere rappresentati molti complessi aspetti della fisica, come la capillarità, l'angolo di contatto, lo sloshing, il bubble point e la fluidodinamica multifase: è necessario quindi sviluppare uno strumento ad hoc.

Il software CFD implementato è 3D, lavora in condizioni transitorie e si basa su OpenFOAM. Esso gestisce il bubble point, lo sloshing, il trasporto dell'interfaccia tra due fasi fluide e la perdita di carico dovuta ad una griglia di tipo screen all'interno del dominio fluido.

Codici CFD sono stati testati per analizzarne le capacità in termini di simulazione fluidodinamica di razzi ibridi. Banchi di prova ed esperimenti sono stati utilizzati per ottenere i dati per la validazione dei codici.

L'obiettivo di questi studi per la caratterizzazione della fluidodinamica interna è dimostrare che il CFD è uno strumento di progettazione potente, in grado di ridurre i costi connessi ad esperimenti e produzione dei componenti. Pressione, velocità ed efficienza vengono comparate tra CFD ed esperimenti, per dimostrare che il software è in grado di prevedere le configurazioni geometriche più performanti.

Acronyms

ESA European Space Agency

FEM Finite Element Method

FE Finite Element

SSC Swedish Space Corporation

DLR Deutschen Zentrums für Luft

SPONGE Sounding rocket Propellant OrieNtation micro Gravity Experiment

CFD Computational Fluid Dynamics

CFC Carbon Fiber Carbon

CISAS Centro Interdipartimentale di Studi e Attività Spaziali

PMD Propellant Management Device

SNSB Swedish National Space Board

SPARTAN SPAce exploration Research for Throttable Adavanced eNgine

JPC Joint Propulsion Conference

PLC Programmable Logic Controller

MHD Magneto Hydro Dynamics

VOF Volume Of Fluid

LISA Linearised Instability Sheet Atomisation

RNG Re-Normalisation Group

SST Shear Stress Transport

REXUS Rocket-borne Experiments for University Students

NIST National Institute of Standards and Technology

GAMG Generalised Geometric-Algebraic Multi-Grid

RAM	Random-Access Memory
FFT	Fast Fourier Transform
AB	Acquisition Board
CB	Control Board
OS	Operative System
CCD	Charge-Coupled Device
RTD	Resistance Temperature Detectors

Introduction

In this section, a description is given of the author's personal contribution to the whole thesis. The original aspects of the topics presented are underlined and discussed.

Aim of the Work

The aim of this thesis is to implement and use CFD codes and solvers describing some vital aspects of hybrid rockets, such as propellant dynamics inside tanks containing PMD devices and internal ballistics.
A 3D Computational Fluid Dynamics (CFD) tool has been implemented to simulate PMDs, and other commercial codes have been tested to analyze their capabilities in terms of simulating rockets fluid dynamics. Test beds and experiments have been used to retrieve the data for codes validation.
In particular:

1. Chapter 1 refers to codes implementation and description;
2. Chapter 2 describes the test beds used to get the data needed for codes validation;
3. Chapter 3 contains the validation results.

It follows a brief description of the two main parts in which the work can be divided.

PMD Study

Hybrid rockets often use a propellant pressurization system ensuring a higher combustion chamber pressure and therefore the desired performance. This system is generally composed of a certain number of tanks, containing liquid propellant.
PMDs are used to control liquid behavior inside tanks, especially in micro-gravity conditions. They allow liquid propellant flow without gas ingestion and are static metal structures using surface tension and capillary phenomena. They are often made of titanium, which allows their use in corrosive propellants. With no moving nor deforming parts, they are inherently reliable. They can be used in water, thermal and cryogenic systems and in any liquid system for space applications, which makes the field of their possible applications even wider.
In fluid dynamics, the behavior of these devices cannot be simulated with standard tools, because a very specific physics needs to be reproduced concerning capillarity, contact angle, sloshing, bubble point and multiphase fluid dynamics, so it is necessary to develop a tool on purpose. The CFD software developed is 3D, can work in transient conditions and is based on

OpenFOAM. It can handle bubble point phenomena, sloshing in various gravity conditions, interface transport between two fluid phases and the pressure drop due to the presence of a screen in the fluid domain.
An experiment has been designed and manufactured in order to validate the results of the CFD code implemented; it was called SPONGE and was created in the framework of the Rocket-borne Experiments for University Students (REXUS) program, a hands-on experience started by Lazzarin in 2009.
REXUS9, where SPONGE was installed, was launched in February 2011 from Esrange Space Center in northern Sweden. The data acquired during the flight has been transmitted to the ground station and recorded for successive analysis and for the sponge behavior assessment. The aim was to validate the code comparing the frames deriving from the CFD simulations to the images saved during the real experiment.

Internal Ballistics Study
The other part of this thesis describes the CFD study performed on hybrid rockets internal ballistics.
In this case, the aim was first of all to verify the capabilities of commercial CFDs in reproducing the fluid dynamics of hybrid rockets and to assess their performance in terms of modeling the real physics. The objective was to prove that CFD can be used as a powerful design tool, able to reduce the costs connected with experiments and manufacturing.

Different test cases have been created to validate these simulations reproducing the hybrid rocket geometries analyzed during the experimental tests. Parameters such as pressure, characteristic velocity and efficiency are compared between CFD and experiments, to verify that the software can predict the most performing configurations.
These studies are fundamental in the framework of the SPAce exploration Research for Throttable Adavanced eNgine (SPARTAN) European research program, aiming at developing a throttable propulsion technology, which is needed for any planetary soft and precision landing. It relies on the hybrid engine technology, exploiting its capability of being throttled and its performance.
This program is supported by an advanced coding, and this is the reason why CFD becomes so important.

Approach

Since the work is quite wide, it has been divided into two topics analyzed separately. In each chapter, the PMD-related study is analyzed separately from the hybrid rocket ballistics analysis. The way chapters are organized reflects the study through time: numerical codes have been implemented, then some test facilities have been created and used to retrieve experimental data for the validations. Finally, CFD results have been compared to the measurements acquired during the tests.

The work has been organized into three main chapters. The first refers to the physics beyond each problem (PMD behavior description and internal ballistics modeling), the second describes the related test facilities and experimental set up, the third is about codes validation. Conclusions help resuming the most important aspects of the work done.

Author's Personal Contribution and Work Originality

Concerning the software developed for PMD analysis, a preliminary study has been necessary, about capillarity and bubble point phenomena and about the general physical behavior of different PMD types. This study has been conducted by Lazzarin together with F.Barato and as a consequence it has been possible to formulate the basic equations implemented for the bubble point model and for the pressure drop across a typical perforated surface of a PMD. In particular, Lazzarin designed the sponge used for the experiment, and Barato found the equations for the bubble point description.

The 3D PMD code implementation has been conducted by Lazzarin and D.Rondini. Lazzarin implemented the boundary condition for the contact angle of perforated plates and the bubble point equation and tested these new applications. Rondini created the basic C++ class switching between a wall and a cyclic behavior, which is necessary to simulate correctly the bubble point condition.

This work is absolutely original, in that it simulates bubble point phenomena without reproducing each of the perforated plate channels in which the fluid can flow. The basic idea is to model an average behavior, to reduce the computational time required for a simulation to be completed.

Regarding the studies done in the framework of the SPARTAN program, Lazzarin has started the CFD analyses more than one year ago to acquire experience of hybrid rockets internal fluid dynamics in general, simulating the hybrid rocket geometries tested by Matthias Grosse in 2009 and comparing the results obtained to those deriving from experiments.
The work containing these preliminary analyses, where the oxidizer was injected as a gas phase, is a conference paper published in 2010 and presented at the JPC in Nashville[9]. In order to complete that paper, Lazzarin collaborated with N.Bellomo and F.Barato; more specifically, N.Bellomo organized the test matrix, Barato ran some simulations already prepared, and Lazzarin tested meshes created with different tools and ran the majority of the simulations finding the most appropriate solver parameters.

The CFD study on hybrid rockets and liquid injection was presented in 2011 at the JPC in San Diego by Lazzarin[20]. Even in this case there was a cooperation with other colleagues (M.Faenza, F.Barato and N.Bellomo) who ran some already prepared simulations; the difference with respect to the previous work, consists in using a liquid oxidizer to simulate injection (an evaporation model is introduced). Lazzarin found the most appropriate set up, analyzed the problems related to the meshing technique adopted, applied various models to simulate different injector types and compared CFD results with experiments.

Lazzarin was not directly involved in building CISAS test bench in summer 2011 nor into

Grosse's test facility design in 2009, but she performed all the CFD simulations presented not only in Lazzarin[20], but also those in Bettella[7].
She was informed about experimental results of the Italian facility by the rest of the CISAS propulsion group, who was in charge of the tests and measurements. On the other hand, to obtain Grosse's facility results, she collaborated with him and cooperation is still going on for other research topics.

Introduzione

In questa sezione viene fornita una descrizione del contributo personale dell'autore al lavoro svolto. Inoltre, vengono sottolineati gli aspetti originali degli argomenti presentati.

Obiettivi del Lavoro

Lo scopo di questa tesi è di implementare e utilizzare codici e solutori CFD in grado di descrivere alcuni aspetti di vitale importanza per i razzi ibridi, come la dinamica del propellente all'interno dei serbatoi provvisti di PMD e la fluidodinamica interna al motore.
Si è implementato uno strumento CFD 3D per simulare i PMD e altri codici commerciali sono stati testati per analizzarne la capacità di simulare la fluidodinamica interna dei razzi.
Banchi di prova ed esperimenti sono stati utilizzati per raccogliere dati per la validazione del software.
In particolare:

1. Il capitolo 1 tratta l'implementazione dei codici e la fisica di base;
2. Il capitolo 2 descrive i banchi di prova utilizzati per ottenere i dati per la validazione;
3. Il capitolo 3 contiene i risultati della validazione.

Segue una breve descrizione delle due parti principali in cui si è organizzato il lavoro.

Studio dei PMD

I razzi ibridi spesso utilizzano un sistema di pressurizzazione del propellente in grado di garantire una più alta pressione in camera di combustione e di conseguenza le prestazioni desiderate. Questo sistema è generalmente composto da un certo numero di serbatoi contenenti propellente liquido.
I PMD sono utilizzati per controllare il comportamento del liquido nei serbatoi, soprattutto in condizioni di microgravità. Essi consentono il deflusso del liquido senza ingestione di gas, sono strutture metalliche statiche, che usano la tensione superficiale e fenomeni capillari e spesso sono realizzati in titanio, che ne permette l'utilizzo in propellenti corrosivi. Senza parti in movimento né deformanti, sono molto affidabili e possono essere utilizzati in acqua, sistemi termici e criogenici, il che rende il campo delle loro possibili applicazioni ancora più vasto.
In fluidodinamica, il comportamento di questi dispositivi non può essere simulato con strumenti standard, perché va rappresentata una fisica molto specifica riguardante sia la capillarità che l'angolo di contatto, fenomeni di sloshing, il bubble point e la fluidodinamica multifase,

per cui è necessario sviluppare un tool adeguato.
Il software CFD implementato è in grado di lavorare in condizioni transitorie e si basa su OpenFOAM. Esso gestisce lo sloshing in varie condizioni di gravità, il trasporto di interfaccia tra due fasi fluide e la perdita di carico dovuta alla presenza di una lastra sottile perforata (screen) nel dominio fluido.
Un esperimento è stato progettato e realizzato al fine di validare i risultati del software creato; si tratta di SPONGE, facente parte del programma REXUS, a cui Lazzarin ha partecipato nel 2009-2011.
REXUS è il sounding rocket a bordo del quale è stato installato e lanciato l'esperimento, nel febbraio 2011 dal Centro Spaziale Esrange, nel nord della Svezia.

I dati acquisiti durante il volo sono stati trasmessi alla stazione di terra e registrati per analisi successive e per valutare il comportamento del PMD. L'obiettivo era validare il codice confrontando i fotogrammi derivanti dalle simulazioni CFD con le immagini salvate durante l'esperimento vero e proprio.

Studio della Balistica Interna
L'altra parte di questa tesi descrive lo studio CFD della balistica interna dei razzi ibridi.
In questo caso, lo scopo è prima di tutto verificare le capacità dei CFD commerciali nel riprodurre la fluidodinamica dei razzi ibridi e valutarne le prestazioni in termini di modellazione della fisica. L'obiettivo è dimostrare che il CFD può essere uno strumento di progettazione in grado di ridurre i costi connessi ad esperimenti e produzione di componenti.
Diversi test case sono stati creati per validare alcune simulazioni riproducenti le geometrie dei razzi ibridi testate durante le prove sperimentali. Parametri quali pressione, velocità ed efficienza vengono confrontati tra CFD ed esperimenti, per verificare che il software sia in grado di prevedere le configurazioni geometriche più performanti.
Questi studi sono fondamentali nell'ambito del progetto SPARTAN, un programma di ricerca europeo volto a sviluppare una tecnologia di propulsione throttable, necessaria per qualsiasi atterraggio di precisione in missioni planetarie. Esso si basa sulla tecnologia del motore ibrido e sfrutta le sue prestazioni e la sua capacità di essere regolato in spinta.

Approccio

Dal momento che il lavoro è piuttosto ampio, esso è stato suddiviso in due parti distinte. In ogni capitolo, lo studio del PMD viene analizzato separatamente dall'analisi balistica del razzo ibrido. L'organizzazione della tesi riflette la cronologia dello studio nel tempo: alcuni codici numerici sono stati implementati, poi si sono realizzati dei banchi di test in modo da ottenere i dati sperimentali per le validazioni. Infine, i risultati del CFD sono stati confrontati con le misure acquisite durante le prove.

Il lavoro è stato organizzato in tre capitoli principali. Il primo si riferisce alla fisica caratterizzante gli specifici argomenti trattati (la descrizione del comportamento del PMD e la modellazione della balistica interna), il secondo descrive i banchi di prova e il set up sperimentale, il terzo è relativo alla validazione dei codici.

E' presente una sezione conclusiva, che riprende gli aspetti più importanti del lavoro svolto.

Contributo Personale dell'Autore e Originalità del Lavoro

Per quanto riguarda il software sviluppato per l'analisi dei PMD, è stato necessario uno studio preliminare sulla capillarità e i fenomeni di bubble point e sul comportamento fisico generale di diversi tipi di PMD. Questo studio è stato condotto da Lazzarin insieme a F.Barato, per poter formulare le equazioni del modello di bubble point e della caduta di pressione attraverso una superficie forata tipica dei PMD. In particolare, Lazzarin ha progettato la sponge utilizzata per l'esperimento e Barato ha ricavato le equazioni per la descrizione del bubble point.

L'implementazione del codice 3D è stata condotta da Lazzarin e D.Rondini. Lazzarin ha scritto la condizione al contorno per l'angolo di contatto su piastre forate, implementato l'equazione di bubble point e testato queste nuove applicazioni. Rondini ha creato la classe C++ di base per simulare una parete che si comporta come un muro in certe condizioni e come una patch ciclica in altre, e che è necessaria per riprodurre la condizione di bubble point.
Questo lavoro è assolutamente originale, in quanto simula fenomeni di bubble point senza riprodurre tutti i canali della piastra forata in cui il fluido può scorrere. L'intento di base è modellare un comportamento medio, per ridurre il tempo di calcolo necessario per completare una simulazione.

Per quanto riguarda gli studi legati al programma SPARTAN, l'autore ha iniziato le analisi CFD più di un anno fa per acquisire esperienza della fluidodinamica interna dei razzi ibridi, simulando varie geometrie del razzo testato da M.Grosse nel 2009 e confrontando i risultati ottenuti con quelli derivanti dagli esperimenti. Il lavoro che contiene queste analisi preliminari in cui l'ossidante è stato iniettato in fase gassosa è un articolo pubblicato alla conferenza JPC di Nashville nel 2010[9]. Al fine di completare tale documento, l'autore ha collaborato con N.Bellomo e F.Barato; più specificamente, Bellomo ha organizzato la test matrix, Barato ha eseguito alcune simulazioni già preparate e Lazzarin ha testato varie mesh create con strumenti diversi e realizzato la maggior parte delle simulazioni, in modo da trovare le impostazioni più appropriate per il solutore.

Lo studio CFD sui razzi ibridi con iniezione liquida è stato invece presentato da Lazzarin nel 2011 al JPC di San Diego[20]. Anche in questo caso c'è stata una collaborazione con altri colleghi (M.Faenza, F.Barato e N.Bellomo), i quali hanno dato supporto per alcune simulazioni. La differenza rispetto al lavoro precedente consiste nell'utilizzo di un ossidante liquido per simulare l'iniezione (un modello di evaporazione è quindi stato introdotto). Lazzarin ha trovato il sistema più appropriato per impostare le simulazioni, ha analizzato i problemi legati alla tecnica di meshatura adottata, ha applicato vari modelli per descrivere diversi tipi di iniettori e confrontato i risultati del CFD con quelli sperimentali.

Lazzarin non è stata direttamente coinvolta nella costruzione del banco di prova del CISAS nell'estate del 2011, né in quella del banco di test di Grosse, ma ha realizzato tutte le simulazioni CFD presentate non solo in[20], ma anche in[7].

I risultati sperimentali del banco di test del CISAS le sono stati comunicati dai componenti del gruppo di propulsione responsabili delle prove e delle misure. Per ottenere invece i risultati dei test di Grosse, Lazzarin ha collaborato con lui e la cooperazione è ancora in corso per altri temi di ricerca.

Chapter 1

Numerical Codes for Critical Elements of Space Propulsion Systems

This chapter describes two advanced CFD applications prepared to simulate propellant dynamics in space systems and to analyze the combustion and performance of hybrid rockets.

The first section illustrates the physics implemented in a numerical code for PMD description. PMDs are passive metal structures helping propellant management in micro-gravity conditions. These devices are widely used in space missions to ensure gas-free propellant delivery towards the outlet and to control rocket motor performance without any power consumption. PMDs can be divided into communication and control devices. Communication PMDs guarantee a flow path from the propellant location to the outlet and can provide demand in any direction; control devices retain some or all the propellant inside the tank for repetitious maneuvers, refilling between maneuvers or for once in a lifetime maneuvers (such as spin recovery or station change). With the exception of troughs (Fig.1.1), all PMD components use surface tension to control or deliver liquid.

Surface tension is a force created by the asymmetry of the molecules at the liquid surface. It is quite small in comparison to gravity on Earth, but is often the dominant force in space environment and dictates liquid motion and fluid equilibrium in tanks and reservoirs. The code developed for PMDs is a 3D CFD transient solver, which starts from OpenFOAM (a basic description of the OpenFOAM library is given in the following sections). This numerical code can handle bubble point, liquid cross flow through the perforated plates of a PMD structure, and any physical situation interesting for a PMD.

The second section is related to the use of CFD for hybrid rockets fluid dynamics simulation. In hybrid rockets, the gaseous or liquid oxidizer mixes with the fuel coming from the solid grain combustion and they react forming combustion products. Chemistry and turbulence need to be accurately simulated to reproduce the diffusive flames typical of hybrid rockets, and the fluid dynamics inside the combustion chamber highly depends on oxidizer injection. Particles breakup process needs to be reproduced when simulating liquid injection and an evaporation model has to be introduced.

In this chapter, the physical basis of the models is described and the mathematical formu-

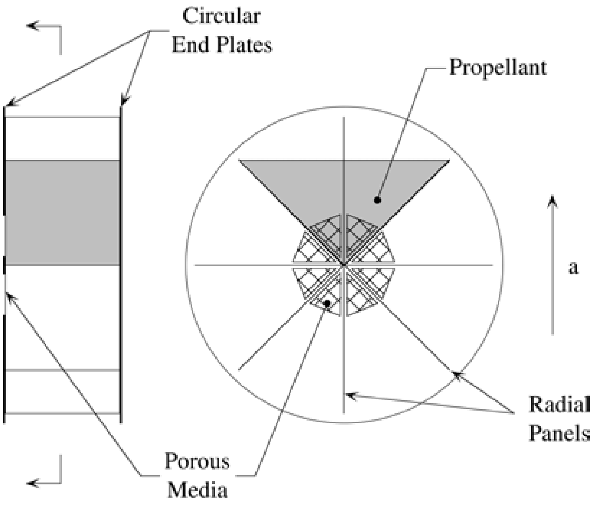

Figure 1.1: Example of a trough PMD. Picture from the website http://www.pmdtechnology.com/.

lation of the different phenomena is illustrated. A description of the appropriate boundary conditions to be applied is given as well, and the required meshing technique is described. The differences between test cases referring to the same geometry and having the same boundary conditions, but characterized by different injection types (liquid or gaseous) are discussed. The results of this study have been published and presented at the 46^{th}[9] and 47^{th} Joint Propulsion Conference (JPC)[20], the most important international propulsion conference. These studies validate commercial CFD tools simulating highly specific space applications, such as hybrid rockets. The objective is to prove that CFD is reliable for design purposes and can predict the most performing geometries in terms of pre and post-combustion chamber shape, and position and geometry of the devices enhancing the species mixing.

1.1 Propellant Management Devices

An Introduction to OpenFOAM

The software developed for PMD analysis is based on the OpenFOAM library. OpenFOAM is an open source CFD software, extremely powerful and flexible. It is developed by OpenCFD Limited, but also by many research centers and universities all around the world, which started it to compete with the best commercial packages. OpenFOAM provides a large set of solvers, mesh conversion and editing tools, making it possible to simulate, among the others[1]:

- Single and multi-phase systems;
- Laminar and turbulent flows (with several turbulence models);
- Incompressible and compressible fluids (and shock waves propagation);
- Combustion;

---

[1] see http://www.openfoam.com/features/ for a complete list)

- Heat transfer mechanisms;
- Molecular dynamics;
- Magneto-hydrodynamics (MHD).

OpenFOAM is structured to be essentially a library implementing a partial differential equation solver based on the finite volume method. It implements a complete set of C++ classes to work easily with vector and tensor arithmetics, and to manipulate vector fields. Its robust structure based on object-oriented programming, the full class documentation available online[2] and the programmer manual, make OpenFOAM the ideal tool for someone who wants to develop specific CFD applications or modify the existing ones.

1.1.1 Physical Model

This code has been created to simulate propellant control devices whose behavior is based on capillary forces.

Communication PMDs can provide unlimited demand in any direction and, therefore, are the most flexible of PMDs. Unfortunately, if the acceleration level precludes vanes (which are open devices, see Fig.1.2), galleries are required. Galleries are the heaviest, the most expensive, and more importantly, the least reliable of PMD components, but also the most capable.

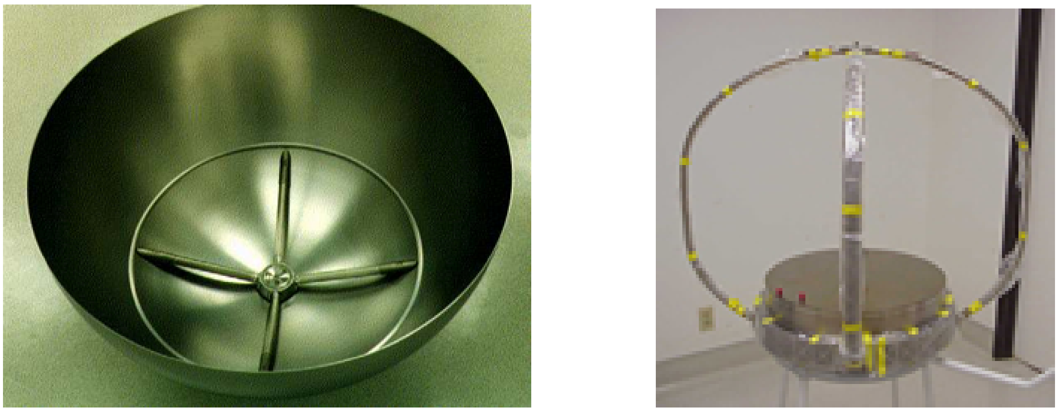

Figure 1.2: Example of two communication PMDs: vanes (left) and galleries (right). Pictures taken from the website http://www.pmdtechnology.com/.

Sponges, Traps and Troughs are control devices and an example of a sponge is shown in Fig.1.3.

The code has been conceived to analyze gas ingestion and/or liquid flow dynamics through the perforated devices constituting PMDs. It treats not only traditional capillary phenomena, but also those cases where mass flow rate has to be taken into account together with capillary effects. This is done without considering the fluid flow through each of the channels characterizing the plate.

---

[2] http://foam.sourceforge.net/doc/Doxygen/html/

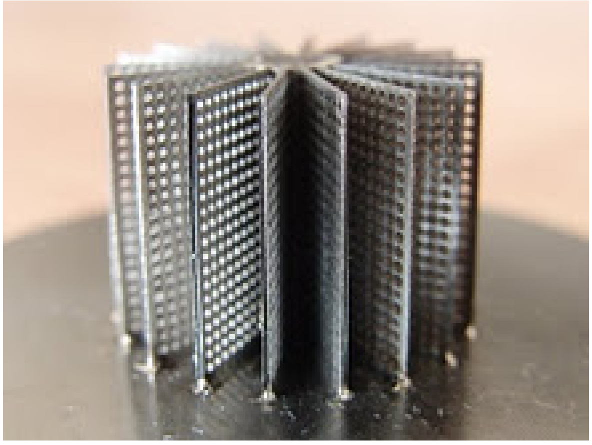

Figure 1.3: Example of a sponge control PMD.

The physics to be simulated concerns two-phase flows, where no phase change occurs, but gas can be trapped into some perforated devices. Another assumption made before the realization of the numerical code is to neglect the liquid mass trapped inside the plate or screen. Thus, no wicking has been considered. This choice is due to the fact that the liquid mass inside the device is usually small because of the reduced plate thickness. Moreover, the simulation is transient, so that the error due to this assumption is usually negligible.

In the following, the physics of the problem into consideration is presented, but before going into more detail, some basic concepts about implementation shall be considered.
A sponge can be simulated through a set of two coupled boundary patches, which let the fluid pass from one side to the other according to some conditions for emulating the sponge behavior.
This model does not simulate the exact behavior of the sponge, which would require an extremely fine mesh, not affordable with current calculation capabilities.
The most important aspects of the flow to be simulated are: energy losses generating a pressure drop across a screen, capillary phenomena involving the contact angle and bubble point.

PMDs are often made of perforated plates (Fig.1.4), which are used to block gas bubbles on one side and let the liquid pass according to the bubble point physics, but also to allow propellant cross flow.

Hereafter the main aspects of PMD physics are described in more detail, in particular the following sections refer to how to implement:

1. The flow through the sponge perforated plate (screen);

2. The pressure drop due to the flow acceleration within the screen channels (which equations and experimentally determined parameters and coefficients have been used);

3. The contact angle at the interface between liquid, solid and gas for a screen-type surface;

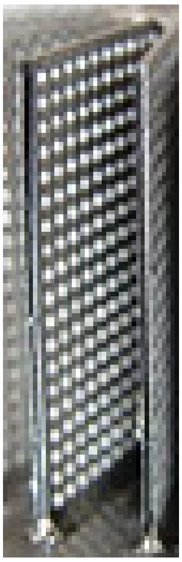

Figure 1.4: Screen panel of a sponge PMD.

4. Bubble point phenomena related to gas and liquid flow through the screen channels.

1.1.1.1 No Slip Condition and Normal Flow

The diameter of the plate or screen holes is very small, thus the liquid flow inside the device can only be parallel to the hole axis. Moreover, the ratio l/d of the holes is generally bigger than 1 for a plate, which allows to consider that the fluid crosses the plate in a direction perpendicular to the plate itself.

For these reasons, the velocity component parallel to the plate is considered to be zero:

$$\vec{U_p} \times \vec{n} = 0 \tag{1.1.1}$$

where $\vec{U_p}$ is the velocity on the patch, and $\vec{n}$ is the face normal on the patch.

1.1.1.2 Cross Flow Pressure Drop

The fluid flow through narrow holes causes an energy dissipation, which results in a pressure drop calculated according to the following formula[8]:

$$\Delta P_{loss} = K_1 \frac{\mu B_s}{D_{BP}} V_P + K_2 \frac{\rho B_S}{D_{BP}} |V_P| V_P \tag{1.1.2}$$

where:

$$\rho = \alpha \rho_L + (1 - \alpha) \rho_G \tag{1.1.3}$$

$$\mu = \alpha \mu_L + (1 - \alpha) \mu_G \tag{1.1.4}$$

The constants K_1, K_2, D_{BP}, B_S are defined by the characteristics of the plate and of the bubble point, which are known parameters.

Their meaning is presented here:

Δp Pressure fall induced by energy losses through the sponge $[Pa]$;

K_1 Experimental coefficient [*non-dimensional*];

K_2 Experimental coefficient $[s^{-1}]$;

d_{BP} Bubble point diameter $[m]$;

U Local Fluid speed $[\frac{m}{s}]$;

l_p Sponge plate thickness $[m]$;

μ_L Liquid dynamic viscosity $[Pa \cdot s]$;

ρ_L Liquid density $[\frac{kg}{m^3}]$.

μ_G Gas dynamic viscosity $[Pa \cdot s]$;

ρ_G Gas density $[\frac{kg}{m^3}]$.

1.1.1.3 Contact Angle and Capillarity

As the sponge appears globally as a wall, it will be affected by capillarity, even though it allows partial flow. The contact angle calculation is done through this equation[21]:

$$\begin{cases} \theta = \arccos(1 - \phi_S + cos(\theta_0) \cdot \phi_S) & if \quad 0 \leq \theta_0 \leq 90^\circ \\ \theta = \arccos(cos(\theta_0) \cdot \phi_S) & if \quad 90^\circ < \theta_0 \leq 180^\circ \end{cases} \tag{1.1.5}$$

where θ_0 is the contact angle calculated for the basic case of a plate wet by a liquid drop (depending on the type of fluid and solid material) and ϕ_S depends on the void fraction of the screen.

In the specific case of the physics simulated, the plate surface on which the contact angle can be seen is not a wall, but a surface allowing gas mass transfer only if the bubble point is exceeded and which always allows liquid flow.
The presence of three phases (solid, liquid and gas) causes a different interface with respect to the one observed when only gas and liquid are present. Moreover, the wetting of a surface is greatly influenced by the holes.

Since the fluid dynamics inside the single holes is not represented, it is worth considering a scale length larger than the characteristic hole size to model the menisci and the related capillary effect, so that it is possible to apply the same equations generally used for composite (instead of perforated) surfaces[21].
According to this approach, the meniscus is treated as that at an ordinary wall, except for

the contact angle value.

The unit vector normal to the interface between the phases is imposed as[2]:

$$\bar{n} = n_w cos\theta + n_t sin\theta \tag{1.1.6}$$

which is the same calculated for an ordinary wall boundary. w and t refer to the parallel and perpendicular directions to the wall respectively. θ is the contact angle in case one side of the plate is wet and the plate is perforated.

Another parameter has to be defined here: ϕ_S, the ratio between the solid area and the total frontal area of the plate.
If the plate is in contact on the one side with the fluid and the latter wets the solid (this is true if θ_0 is lower than 90 °), there is a spontaneous impregnation of the holes. In this case, the most appropriate contact angle model is[21]:

$$cos\theta = (1 - \phi_S) + \phi_S cos\theta_0 \tag{1.1.7}$$

where θ is the same used in Eq.1.1.6, and θ_0 is the contact angle of the basic case.

If instead, the liquid does not fill the holes, then the most suitable equation is[21]:

$$cos\theta = \phi_S cos\theta_0 \tag{1.1.8}$$

1.1.1.4 Bubble Point Treatment

The perforated plates can withstand a certain pressure difference from the gas to the liquid side. The maximum possible pressure differential is called *bubble point.*
If the pressure difference is below this value, then no gas flow occurs, otherwise the gas can cross the plate. The liquid can instead always cross the plate.

As the normal flow condition, this simulates the macroscopic effect of a microscopic phenomenon. While the liquid can always flow through the holes in the sponge, the gas/vapor flow is limited by the bubble point. This is because the gas tends to form bubbles on the exit side of the sponge.
The bubble formation requires a certain amount of energy to be completed, because an interface has to be created, and this depends on the surface tension and many other parameters. The net effect is that, if the two sponge sides are respectively filled with liquid and gas, the gas needs to have a higher pressure compared to the liquid, to flow into it.
The minimum pressure difference letting the gas flow towards the liquid is called the bubble point.

What has just been said can be resumed from a mathematical point of view:

$$\begin{cases} U_p \neq 0 \quad if \quad \Delta p \dfrac{\Delta\alpha}{|\Delta\alpha|} \geq 0 \\ U_p = 0 \quad if \quad -BP < \Delta p \dfrac{\Delta\alpha}{|\Delta\alpha|} < 0 \\ U_p \neq 0 \quad if \quad \Delta p \dfrac{\Delta\alpha}{|\Delta\alpha|} \leq -BP \end{cases} \tag{1.1.9}$$

where the quantity $\Delta p \dfrac{\Delta\alpha}{|\Delta\alpha|}$ is calculated to ensure that the direction of the pressure difference is always set from gas to liquid and not viceversa. α is the relative volume fraction of the two phases, or phase fraction, BP is the bubble point pressure and Δp is the actual pressure difference between gas and liquid. U_p is the flow velocity across the plate.
This equation has been derived from the physics of the phenomenon under study and the only condition of Eq.1.1.9 in which the plate behaves like a wall is the first one; in the other two there are both capillarity and fluid flow.

In conclusion, the new physics implemented in this numerical code allows to simulate a surface which is both affected by capillarity and cross flow. Moreover, the pressure loss inside the plate or screen is modeled and the effects of air pockets and of the liquid wetting the plate are also taken into account by means of the contact angle evaluation.

1.2 Hybrid Rockets

A hybrid rocket uses propellants in two different physical states: the fuel is solid and the oxidizer either is gas or liquid. They have some advantages over both liquid and solid rockets: simplicity, safety, and cost, and they can be shut down easily like liquid rockets.

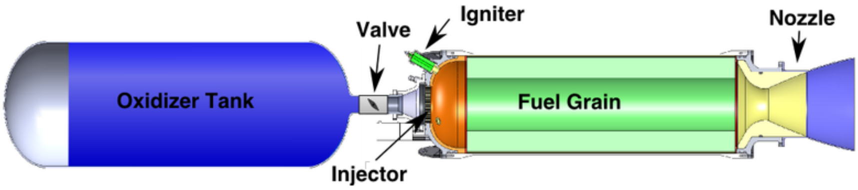

Figure 1.5: Schematics of a hybrid rocket system for an overview.

Hybrid systems are slightly more complex than solids, but they offer other advantages, due to their higher handling security.

Fig.1.6 shows the structure of the flame developing in the combustion chamber and one of the mechanisms characterizing hybrids: droplets entrainment.

Combustion heat melts a layer of fuel from the exposed surface. Actually, the polymerized hydrocarbon molecules are too long and entangled to be completely solid at low temperatures: they never really froze, instead, they are supercooled liquids with high viscosity. Once heated above a critical transition temperature, they flow like a liquid.
As the surface is heated further, the remaining liquid vaporizes to gas. If the fuel is plastic,

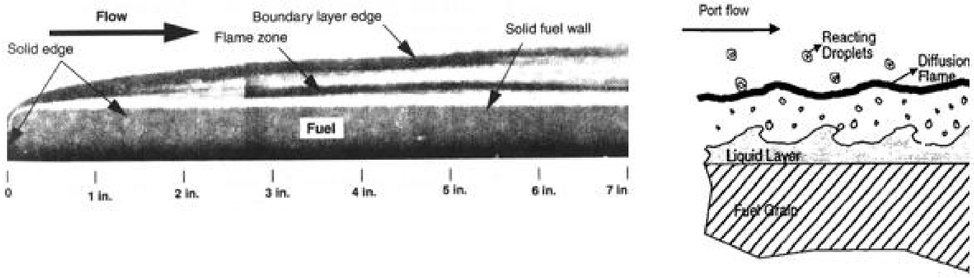

Figure 1.6: Flame development and droplets entrainment.

it may char or slough off tiny chunks before melting, before depolymerizing: the carbon-to-carbon bonds holding the backbone of the polymers together absorb heat and break apart; the fuel turns into a mixture of several gases and simpler hydrocarbons.
A melt layer appears to rest on the surface of the fuel, though this liquid layer is constantly replenished from underneath, and removed from above. It tends to be extremely thin and if its viscosity is low (not a melted polymer) it breaks up into a series of ripples and roll waves due to the gas flow above.
These droplets pass through the flame zone where they heat-up, vaporize, and burn with the oxidizer. This effect, not yet well understood, is the first transport mechanism that gets the fuel and oxidizer mixed, and occurs at moderate temperatures.
With further heating, the remaining fuel in the melt layer (the cracked hydrocarbons for polymers) vaporizes to gas and gets carried off into the main flow. This is the second transport mechanism that gets the fuel and oxidizer mixed, occurring at high temperatures.
Once transported into the port flow, the vaporized fuel burns in a narrow zone within the boundary layer (flame sheet), which is at a depth (between the fuel-grain and the oxidizer flow) close enough to stoichiometric to support combustion. Where burning occurs, it is stoichiometric.
Between the solid grain and the flame zone, there is mainly unburnt fuel, whereas in the flow core there is a mix of combusted gases and unburnt oxidizer.

In this section, the numerical models applied to study gaseous and liquid injection are treated.
For example, the method used to simulate liquid droplets primary and secondary breakup as well as their vaporization and combustion are discussed. Details about combustion and liquid evaporation model are given, and the technique applied to mesh the rocket geometries studied is described.

The analysis of hybrid rockets internal fluid dynamics has been started using commercial codes, because they are highly reliable and already tested for many different applications. Moreover, they are optimized in terms of the computational time required to complete a simulation, which makes them the most appropriate tool to start a feasibility study. In fact, the objective is to prove that it is possible to use CFD to distinguish the most promising rocket motor designs in terms of performance and efficiency.

Figure 1.7: Liquid injection and jet breakup, from the tests conducted in summer 2011 by CISAS propulsion group.

1.2.1 CFD Numerical Models and Mesh

1.2.1.1 Gas Phase Injection

The first simulations run to reproduce the hybrid rocket fluid dynamics, have been characterized by the injection of gaseous N_2O. No injector model has been used, but the N_2O mass flow rate was simply maintained constant through the surface corresponding to the oxidizer inlet.

Only in a second simulation phase, other test cases have been prepared, which were closer to the real experimental conditions and therefore accounted for the injection of a liquid phase. A specific injector model was used, and an appropriate evaporation model was added to the previous simpler system of equations.

1.2.1.2 Liquid Phase Injection

Liquid N_2O has been injected into the fluid domain as a lagrangian phase, represented by a certain number of particles. The particles number is generally chosen in order for the droplets to be statistically representative of the liquid phase. In the test cases analyzed, two injector types needed to be simulated, corresponding to those used during two different experiments:

- A swirl atomizer, for the tests conducted by Grosse in 2009 [18];
- A shower head injector, for those conducted in 2011 by the Centro Interdipartimentale di Studi e Attività Spaziali (CISAS) hybrid rocket team [7]. In this case, two different injection plates were used for the lab-scale and the increased-scale tests. Concerning the lab-scale, the injection plate is characterized by 7 channels having a diameter of 1 mm each; 6 of them are disposed on a circle (radius 7.5 mm) and the other one is at the center of the plate. For the increased-scale rocket, the plate has 47 channels with a 1

mm diameter, disposed on concentric circles of increasing radius. The external circle of 10 channels, with a diameter of 4.5 mm, is just used for the injection plate assembly.

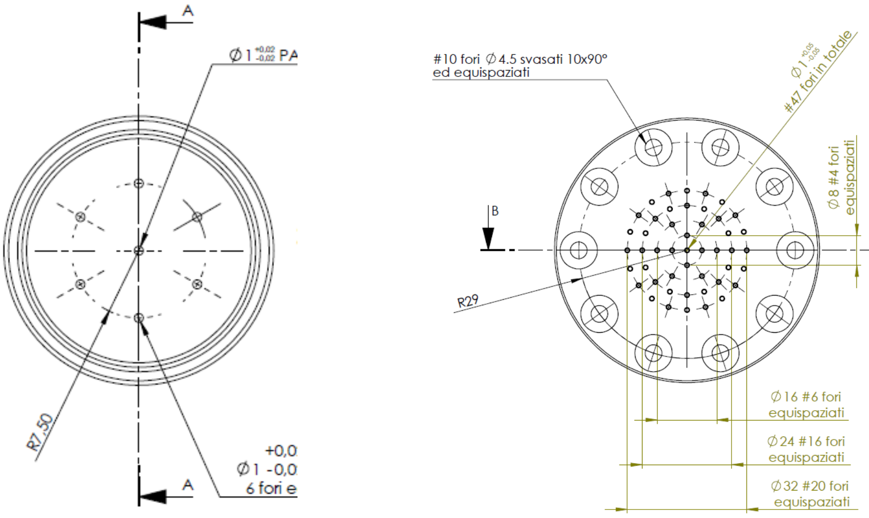

Figure 1.8: Shower head injection plates of the lab-scale (left) and the increased-scale rockets-CISAS tests.

In both cases, particles enter the fluid domain from a circular region on a plane located at the oxidizer inlet section of the rocket, in the axial direction.

Since the injector used by Grosse was a swirl atomizer, for the related test cases it has been possible to apply the Linearised Instability Sheet Atomisation (LISA) model[3]. In fact, it allows to determine the initial velocity of the droplets leaving the injector and their diameter before secondary breakup. This numerical model simulates liquid injection, including primary breakup in pressure-swirl atomizers. With pressure swirl injectors, liquid undergoes a rotational motion and the resulting centrifugal forces cause a thin liquid film to form along the walls of the injector channel, surrounding an air core at the center. Outside the injector nozzle, the liquid tangential motion is transformed into a radial component, and a liquid sheet appears. This sheet is subjected to aerodynamic instabilities that cause it to breakup into ligaments, which are liquid structures larger than droplets. The pressure-swirl atomizer model, refers to the geometry in Fig.1.9.

The initial velocity magnitude of the liquid particles leaving the injector, has been calculated using [4]:

$$U = C_D \sqrt{\frac{2\Delta p}{\rho_l}} \tag{1.2.1}$$

where Δp is the pressure drop calculated using the pressure values before and after the injector and ρ_l is liquid density. The discharge coefficient C_D is modeled through the following equation [26]:

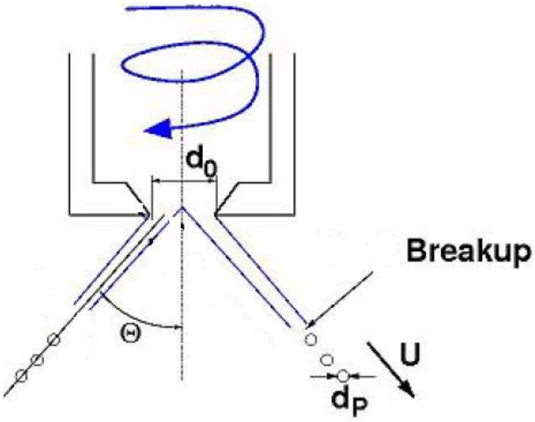

Figure 1.9: Model determining particles initial size and velocity, for a pressure-swirl atomizer.

$$C_D = max\left(0.7, \frac{4\dot{m}}{\pi l_0^2 \rho_l cos\theta}\sqrt{\frac{\rho_l}{2\Delta p}}\right) \tag{1.2.2}$$

where $\dot{m}$ is the effective mass flow rate through the injector, d_0 is the injector nozzle diameter, and θ_0 is the spray cone angle.
Finally, the most probable liquid droplets diameter after the primary breakup process, is evaluated from the following relation [26]:

$$d_{P0} = 1.88 d_l \left(1 + 3Oh\right) \tag{1.2.3}$$

where d_l is the ligament diameter, Oh the Ohnesorge number and d_{P0} is the initial particle diameter after primary breakup.

For the CFD test cases referring to the experiments conducted with a shower head injector, a different approach has been applied to model injection. In particular, the Blob numerical method[3] has been applied to the lab-scale rocket motor, whereas the full cone option has been applied to simulate liquid injection in the increased-scale rocket.
The Blob method estimates particles velocity from the mass flow rate (Eq.1.2.4), whereas their initial diameter is evaluated assuming that a detailed description of the atomization and breakup processes within the primary breakup zone of the spray is not required, and thus the initial droplets diameter is considered to be equal to the injector nozzle diameter (Eq.1.2.5). Spherical droplets with uniform size are injected and then subjected to a secondary breakup induced by aerodynamics.
The equations used by this model are presented below [23]:

$$U = \frac{\dot{m}}{A_{inj}\rho_l} \tag{1.2.4}$$

where $\dot{m}$ is the mass flow rate through the injector, A_{inj} is the injector nozzle section and ρ_l is the liquid density.
And:

$$d_{P0} = d_0 \tag{1.2.5}$$

where d_{P0} is the initial diameter of the particle injected and d_0 is the injector nozzle diameter.

In order to properly simulate the injection plate, it has been decided to inject particles from every single channel, specifying the injection location by means of the appropriate coordinates. However, when the channels number becomes high, it is desirable to avoid creating as many injection points as the real channels, and to use other methods to represent injection plates.

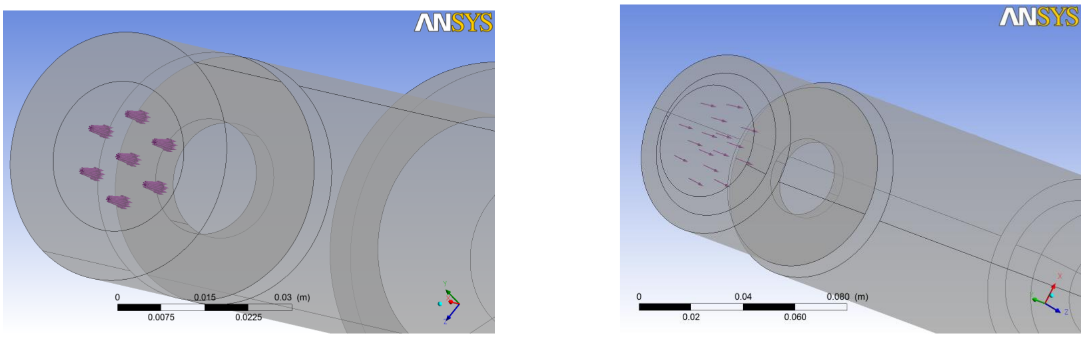

Figure 1.10: Injector plate model for the lab-scale CISAS rocket motor (left) and the increased-scale rocket (right).

To avoid the problem of representing a high number of channels in the CFD, the full cone option has been applied to the 47-hole injection plate used for the increased-scale rocket. To use this option, it is necessary to specify some other parameters with respect to those required by the Blob model, such as particles initial diameter and velocity. In this case and in all the cases where a high number of channels needs to be simulated, the injection plate can be represented by a surface having a diameter equal to the total diameter of the injection plate and this is an acceptable approximation, because the channels location and disposition allows a uniform injection over the whole injection area.

The experiments with the increased-scale motor have been performed in a self-pressurized blow-down mode.
Even if the injector L/d is low, in this case it is not possible to calculate the velocity of the injected liquid considering full liquid injection: in fact this would produce an unacceptable underestimation of the liquid velocity, because in a two-phase mixture with a low vapor density, an acceleration of the liquid flow occurs.
Unfortunately, it is very difficult to predict liquid velocity when two-phase nitrous oxide flow is concerned. Modeling two-phase flow inside the injector is out of the scope of this paper, for this reason it has been decided to calculate velocity from the total mass flux using a simple rough estimation for density. The latter has been defined as the average between the densities calculated respectively for an isotherm and an isentropic expansion to chamber pressure. In conclusion, the equation used to determine particles initial velocity is analogous to Eq.1.2.4:

$$U = \frac{\dot{m}_{TOT}}{NA_{ing}\tilde{\rho}_l} \tag{1.2.6}$$

where $\dot{m}_{TOT}$ is the total injection plate mass flow rate, N is the number of channels in the plate, A_{inj} is the area of the single channel at the exit section and $\tilde{\rho}_l$ is the liquid density calculated with the approximation described.

Particles initial diameter has been set equal to the value calculated adopting the Blob method.

N_2O Properties for the Liquid Evaporation Model

In order to inject liquid oxidizer into the fluid domain, it has been necessary to create new material tables. Liquid N_2O is not present in fact, among the materials available in the library of the used software. Moreover, for the liquid evaporation model to be activated, it has been necessary to introduce not only the characteristics of the liquid N_2O, but also the Antoine equation coefficients, in order to simulate the equilibrium between the vapor and liquid phase. The Antoine equation relates vapor pressure and temperature for pure substances. The parameters required for liquid N_2O simulations are summarized in the following tables:

Physical Parameter	Value	Units
Molar Mass	44.0129	[kg/kmol]
Density	907.83	[kg/m3]
Specific Heat Capacity	2.2695, at constant pressure	[J/gK]
Reference State (p,T)	273, 31.101	[K], [bar]
Reference Specific Enthalpy	165250	[J/kg]
Reference Specific Entropy	0.713768	[J/kgK]
Dynamic Viscosity	9e-5	[Pa s]
Latent Heat of Vaporization	2.5e5	[J/kg]
Surface Tension	0.005	[N/m]

Table 1.1: Physical quantities used for liquid N_2O.

The coefficients used for the Antoine equation are presented in Tab. 1.2 :

Physical Parameter	Value	Units
Reference Constant A	9.67086	—
Enthalpy Coefficient B	1429.91	[K]
Temperature Offset C	-44	[K]
Pressure Scale	1	[bar]

Table 1.2: Physical quantities of liquid N_2O.

To obtain these physical quantities, an isentropic process has been assumed between the reservoir and the injector, and this justifies the temperature assigned to the liquid at the inlet, which is the saturation temperature corresponding to combustion chamber pressure. The data

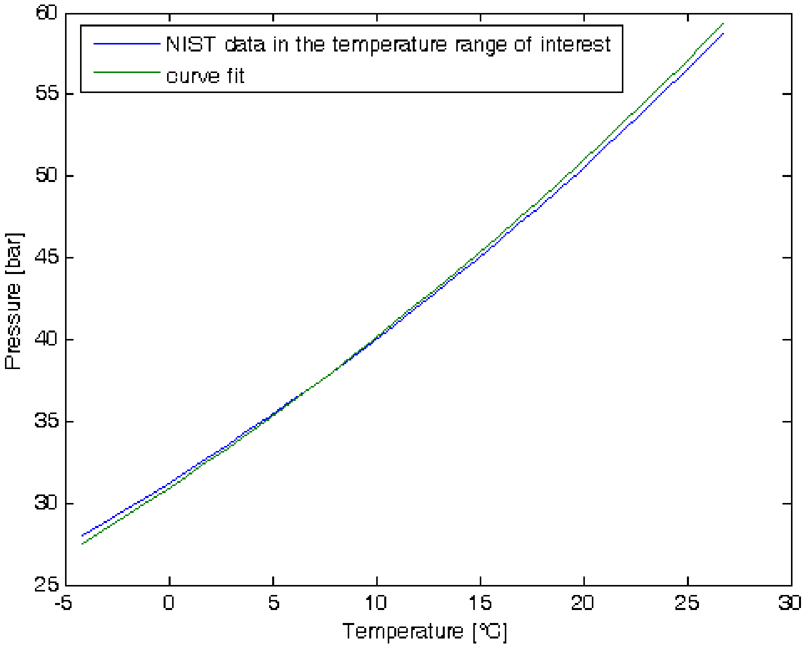

Figure 1.11: Comparison between the NIST saturation data and the Antoine curve used in the CFD simulations.

used in Tab.1.2 refer to a 31 bar pressure, but they have been corrected for each simulation according to the average combustion chamber pressure.

In general, the Antoine equation cannot be considered as representative of the entire saturated vapor-pressure curve from the triple point to the critical point and multiple parameter sets for a single component are frequently used. Antoine equation can be written as follows:

$$p_{vap} = p_{scale} e^{\left(A - \dfrac{B}{pT + C}\right)} \tag{1.2.7}$$

where p_{vap} is the vapor pressure and T is the temperature of interest. A, B and C are the coefficients that need to be determined.

In this study, the best coefficients to describe the N_2O vapor-pressure curve, have been found trying to fit the experimental data available from the National Institute of Standards and Technology (NIST) website [3], and considering the specific temperature range of interest. Picture 1.11 shows the NIST data within a specific temperature range; the obtained Antoine curve (in green) has been superimposed to the experimental data.

Fig.1.12 shows the percentage error between the empirical data coming from the NIST website and the Antoine curve used for the CFD study.

---

[3] http://webbook.nist.gov/chemistry/fluid/

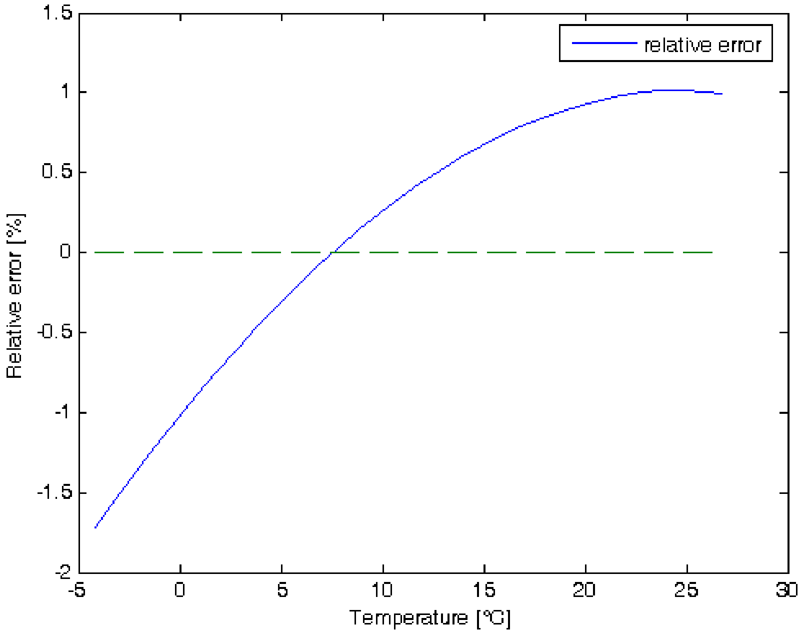

Figure 1.12: Percentage error between the empirical NIST data and the Antoine curve created to fit the data.

As can be seen from Fig.1.12, in the temperature range of interest for this study, the percentage error between the empirical data and the Antoine curve created is always lower than 2%. Therefore the A, B and C coefficients found have been considered as suitable for the purpose of this work.

1.2.1.3 Secondary Breakup Model for Liquid Particles

In general, different mechanisms can cooperate to cause the breakup of a liquid jet into droplets: turbulence within the liquid phase, the external aerodynamic forces acting on the liquid after it leaves the injector nozzle, the implosion of eventual cavitation bubbles.
The contribution of these different phenomena varies depending on some parameters, such as the relative velocity between liquid and gas, liquid and gas densities, liquid viscosity and surface tension. Consequently, it is possible to recognize many breakup regimes, according to the value assumed by two non-dimensional groups: the Weber and Ohnesorge numbers.

In the specific case of these CFD simulations, liquid N_2O enters the fluid domain with a characteristic diameter corresponding to the primary breakup process. After that, and before undergoing the evaporation and finally the combustion processes, the liquid phase is subjected to the secondary breakup. The analytical model used to represent this physical phenomenon, is the Schmehl model [22].
In this model, the deformation and breakup times for the droplet are based on experimental findings. It can be proved that, the time required to deform a particle from a spherical to a disk shape is [15],[19]:

$$t = 1.6t^* \tag{1.2.8}$$

where t^* is a characteristic time given by [15],[19]:

$$t^* = \frac{d_{P0}}{V_{rel}}\sqrt{\frac{\rho_l}{\rho_g}} \tag{1.2.9}$$

where d_{P0} is the initial particle diameter, V_{rel} is the relative velocity between the gas phase and the liquid phase, ρ_l and ρ_g are the liquid and gas densities respectively.

The second breakup phase, which mainly consists in a further particle distortion and in its final breakup, is characterized by the tbr time. tbr can be estimated as a fraction of the t^* time, using different correlations depending on the We number[3].
The droplet size after secondary breakup is computed as a function of We, Oh and the initial particle diameter d_{P0}, using a specific correlation, which depends on the breakup mode followed. In general, the velocity of the particle after secondary breakup is computed as the sum of the parent particle velocity (i.e. velocity of the particle from which it is formed) and an additional velocity component, given by [15],[19]:

$$V_{new} = \frac{5d_{P0}}{2(t_{br} - t)} \tag{1.2.10}$$

This new velocity component is assumed to belong to a plane orthogonal to the direction of the parent droplet velocity, whereas its circumferential orientation is chosen randomly by the CFD software, because it is not otherwise specified. In conclusion, the resulting total velocity vector for a droplet generated by the secondary breakup mechanism, can be computed as [15],[19]:

$$\mathbf{U} = \mathbf{U}_{parent} + \mathbf{V}_{new} \tag{1.2.11}$$

1.2.1.4 Particle Evaporation and Chemistry for Liquid Injection Cases

Liquid N_2O particles enter the fluid domain from the pre-combustion chamber and are surrounded by hot gases and combustion products. In this environment, they are subjected to some heat and mass exchange processes during their evaporation. The evaporation point is determined by means of the Antoine equation (vapor pressure equation describing the relationship between vapor pressure and temperature for pure components) which is given by:

$$p_{vap} = p_{scale} e^{\left(A - \dfrac{B}{pT + C}\right)} \tag{1.2.12}$$

According to this model, the particle starts evaporating when the vapor pressure is greater than the ambient gas pressure. When the particle is above the evaporation point, the mass transfer starts to be accounted for, and it is determined by:

$$\frac{dm_P}{dt} = \frac{Q_c}{L_v} \tag{1.2.13}$$

where L_v is the latent heat of evaporation of the particle component and Q_c is the convective heat transfer.

The influence of the chemical reaction used in the CFD is particularly related to the number of chemical species used: the higher the species number, the closer to reality the simulation. However, in this work, a trade off has been searched between the necessity to represent the real reaction, and the importance of keeping the computational time affordable. It has been decided to use the following reaction:

$$25C_2H_4 + H_2 + 151N_2O - > \tag{1.2.14}$$

$$- > 27CO + 23CO_2 + 5H_2 + 2H + 2O + 40H_2O + 6NO + 148N_2 + 10O_2 + 10OH$$

Using a greater amount of species would require more Random-Access Memory (RAM) and can become considerably more expensive; on the other hand, it has been observed that if a too low number of chemical products is used for the combustion reaction, the flame temperature can become higher than the flame adiabatic temperature, which results in an unphysical situation. This formulation of the chemical reaction is used to model a one-phase combustion process, where all the reactants are in a gaseous state.

In order to model combustion, the eddy dissipation was selected as the most suitable combustion model. Several authors in the past used the finite rate chemistry model to simulate the combustion process inside hybrid rocket motors [5],[6],[13]. In this model, the Arrhenius chemistry equations are used with the local averaged values, therefore the real turbulence-chemistry interaction is not taken into account. In fact, it is not possible to calculate the average reaction rate directly from the mean values of concentration and temperature and, if this is done, large errors could occur [11].

The eddy dissipation is a semi-empirical model, developed according to the hypothesis of fast chemistry (large Damkohler number). In this case, the reaction rate is controlled by the turbulent mixing of fuel and oxidizer[1].
This model has been widely and successfully applied to the prediction of turbulent non-premixed flames, such as those of hybrid rockets. Reaction rate is proportional to the reactants molar fraction and to the rate of dissipation of the eddies, which is the turbulent eddy frequency (i.e. the inverse of the large eddy mixing time scale k/ϵ).
The reaction rate is:

$$R = A\frac{\epsilon}{k}\left(min\left(\frac{[reactant_r]}{V_r'}\right)\right) \tag{1.2.15}$$

where A is an empirical constant (equal to 4), [reactant] is the molar concentration of the r-th reactant, and $V_r^{'}$ is the stoichiometric coefficient of the r-th reactant.

A one-step equation has been used for simplicity and because the use of a complex multi-step reaction mechanism with the eddy dissipation model produces incorrect results. This occurs because the eddy dissipation is a *mixed is burnt* model and is not suited to take into account complex kinetics. If the interest is focused on the global performance and behavior of hybrid motors during normal operating conditions, this is not a drawback (this is not true for example during ignition or far from equilibrium conditions).

As a confirmation of this aspect, a simulation was carried out and briefly discussed in a previous analysis [9], with the combined finite rate/eddy dissipation model.
The reaction rates have first of all been computed for each model separately, and then the lowest has been used. A global model for hydrocarbon oxidation was chosen. Simulation results showed that, in this case, the limiting rate was the eddy dissipation one. Another advantage of the eddy dissipation model over the finite rate chemistry model, is that it is much more robust, because Arrhenius equations are steep. Moreover, the complex chemical kinetics, which are time consuming and often unknown, can be safely neglected.

The eddy dissipation model has been applied only to the gaseous mixture forming inside the combustion chamber, whereas the liquid phase has to evaporate and become part of the gas mixture, before undergoing combustion.

1.2.1.5 Chemistry Model for Gas Injection Cases

The gaseous N_2O enters the fluid domain from the pre-combustion chamber, being injected by the whole inlet patch. It starts being heated by the surrounding hot gases inside the combustion chamber, due to the initialization of the fluid domain. Choosing as an initial condition a temperature around 1000 K (as well as a sufficiently high pressure) and a non-zero mass fraction for the combustion products, allows an easier and faster start of the combustion process. This is true also for the liquid injection case, where particles are helped in reaching an equilibrium in their evaporation process, thanks to this domain initialization.

The influence of the chemical reaction is the same presented and discussed for the liquid injection case. It has been decided to use the reaction presented in Eq.1.2.1.4 for the gaseous case as well.
The eddy dissipation was selected as the most suitable combustion model, it is a semi-empirical model developed according to the hypothesis of fast chemistry, where reaction rate is controlled by the turbulent mixing of fuel and oxidizer. For the gaseous simulations, a one-step equation has been used, for the same reason explained in the liquid injection case.

1.2.1.6 Turbulence Model

Many different turbulence models have been tested for the hybrid rocket numerical simulation.
The models used are the k-ϵ, k-ϵ Re-Normalisation Group (RNG), the k-ω and k-ω Shear Stress Transport (SST). They have been applied using the lab-scale no-diaphragm geometry of the rocket tested by Grosse and creating different simulations starting from that configuration.

The results obtained are fully described in chapter 3, where the software validation against experiments is exposed.

In general, results can vary in terms of the average combustion chamber temperature or the other interesting physical parameters, but it is difficult to say which model is better than the other, especially due to the complex physics that needs to be represented. There are in fact different numerical errors sources, which are very difficult to determine and quantify without a very complete analysis about uncertainty in CFD.

It is, in other words, impossible to conclude with this very simple initial analysis what are the differences among these turbulence models, because the final differences found in the CFD results can depend on many other parameters, or errors can compensate.
A more detailed and specific analysis should be performed to assess which turbulence model is the more suitable.

1.2.1.7 Required Meshing Technique

The meshes created to simulate the gas injection cases have a number of cells varying from 1.2 to 1.6 million; the related simulations have been carried out with dual or quad core machines in the steady state solver mode.
In particular, the dual core machine is an Intel Core 2 Duo CPU P8700, with a 4 GB RAM memory and 2.53 GHz clock frequency. The quad core is an AMD Phoenom IIx4-955, with 3.2 GHz RAM memory 4 GB DDR3.
With this hardware, the average calculation time is roughly 1.67 iteration/minute for the quad core machine. The average calculation time on the dual core is instead 0.53 iteration/minute.

To assess convergence within a single simulation, the following criteria have been applied:

- RMS residuals below 10^{-4};
- At least 700 iterations;
- Negligible variation of the results from one iteration to the following one (less than 5%).

The basic test case is the hybrid rocket with no diaphragm. It has been used for global mesh convergence evaluation, to find the minimum number of cells necessary to generate an appropriate mesh. The procedure followed to find mesh convergence consists in creating meshes with an increasing number of elements. When results do not change from a number of elements to the other, convergence has been reached.
Three different meshes have been prepared with the hybrid CFX standard mesh method (in particular tetrahedron patch dependent) creating hexahedrons and tetrahedrons.
The first mesh has a number of elements of about six hundred thousand, the second has 1 million elements, and the third has roughly 1.2 million.
The difference in many physical properties is calculated to ensure that convergence is reached: Ma (mach number), U (velocity), P (pressure), T (temperature). The differences between the results of the meshes with 1 and 1.2 million of finite volumes are respectively:

1. 0.58% for maximum pressure;
2. 0.15% for maximum temperature;
3. 0.48% for Mach number;
4. 0.09% for velocity.

Therefore, 1.2 million elements have been considered as sufficient to obtain a reliable and stable result and for this reason all the meshes created for the gas injection tests, have a number of elements approximately equal to 1.5 million. The elements have a side size of 1 mm, with a minimum on the grain surface of 0.75 mm.
It is worth noting that the necessary mesh quality depends on the particular problem into consideration as well. In fact, if the aim is not only to predict the global motor performance (like efficiency, I_{sp} and chamber pressure), but also to obtain an accurate view of the internal flow field, it is necessary to refine the mesh next to the combustion chamber walls. This is due to the high local gradients of the physical quantities present in these areas. When a mesh refinement next to the chamber walls and to the sections variations is performed (in particular at the diaphragm location), it is possible to find a more accurate description of the flow field. In the specific case of the meshing technique applied, the global variables are converged, but the mesh refinement should be improved to have a detailed fluid dynamic description.

The meshes created for the liquid injection test cases have all a number of cells varying from 1.2 to 1.6 million, and the simulations have been carried out with dual or quad core machines using the steady state solver. With respect to the meshes created for the simulation of the gas phase injection, the cell size in the areas close to the liquid injection region had to be set to a higher value. This is due to the strong recirculation of the flow, which can be seen in the liquid injection test cases (Fig.1.13).

In fact, this recirculation causes an instability of the flow, which cannot be reproduced in a steady state simulation and that generally requires a bigger cell size, in order to filter this effect out from the steady state solution.

The characteristics of the machines used for this numerical study are resumed in Tab.1.3.

Machine type	**RAM**	**Clock freq.**	**Core n.**	**Average calc. time [it/min]**
DELL XPS L501 X	4 [GB]	1.73 [GHz]	4 (I7 CPU)	2.5(gas)-2.1(liquid)
DELL	8 [GB]	3.30 [GHz]	4 (I5-2500 CPU)	2.2 (liquid)
DELL VOSTRO	4 [GB]	2.53 [GHz]	2 (P8600 CPU)	0.8 (liquid)

Table 1.3: Description of the machine characteristics.

The results of the test cases presented have all been compared to the corresponding experiments. Since the initial solution used to run the liquid injection cases is the steady state solution of the same geometry with N_2O injected as a gas, also the differences between the numerical results obtained for the same motor configuration and using different phases injected, have been investigated.

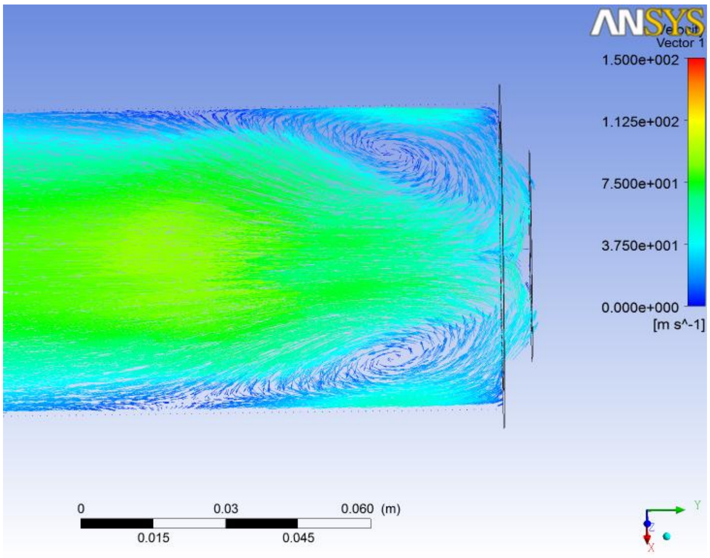

Figure 1.13: Flow recirculation close to the injection plane and extending inside the pre-chamber for one of the liquid injection test cases analyzed.

In order to select the appropriate number of mesh elements, the same analysis described for gaseous cases has been applied.

As already seen for the gas injection case, if the aim is to obtain an accurate solution of the internal flow field, it is necessary to refine the mesh at the combustion chamber walls. In this case, the filtering effect of the mesh is less strong on the results obtained from the CFD, and this accounts often for the recirculation effects in the flow field solution.

If such a mesh refinement is needed, the solution cannot converge using the steady state mode, because results will continue oscillating between a minimum and a maximum. The only option is, in this case, to switch to a transient solver, which requires a greater computational time and occupies far more RAM.

In conclusion, the mesh has been created following a trade off between the necessity to have the best possible refinement for good results and the need for the simulation to be run with a steady state solver to be computationally affordable.

1.2.2 Appropriate Boundary Conditions

The boundary conditions associated to the fluid domain surfaces are particularly important because they have to be the closest possible to reality. Therefore, first of all the phenomena under observation have to be very clear; then the initial and boundary conditions of the physical problem to be represented through CFD can be imposed. Due to the recent development and spreading in the use of CFD tools to analyze fluid dynamic problems for many different applications, there is a wide variety of boundary conditions available in a commercial CFD software.

In this section, the most appropriate ones for hybrid rockets internal fluid dynamics are described.

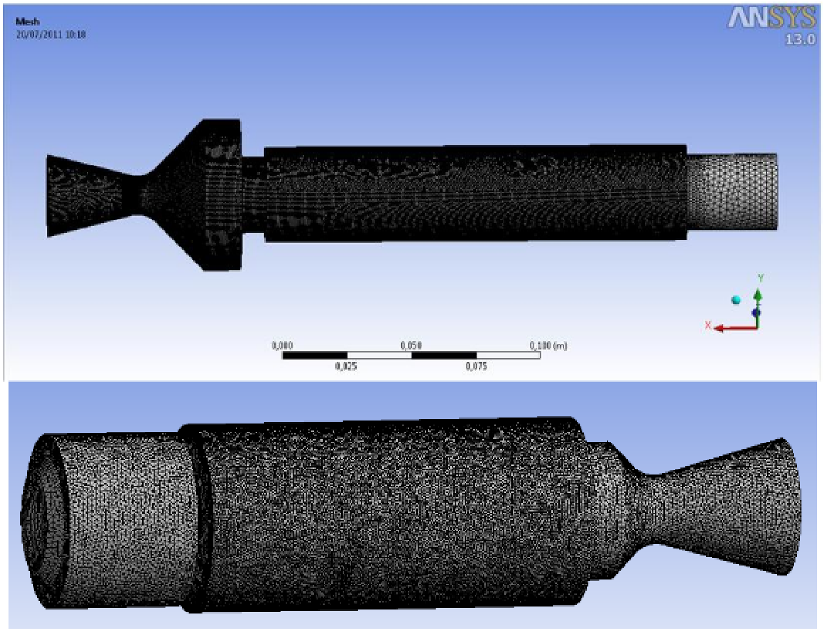

Figure 1.14: Examples of the meshes created for the hybrid rocket motor configurations.

The boundary conditions applied to the different surfaces in the various test cases analyzed are the same as presented by Lazzarin [20]. In particular, for the liquid injection simulations, the inlet boundary type used for the oxidizer has been changed compared to that used for gas injection simulations, in order to allow the simulation of the liquid particles injected into the fluid domain. In fact, liquid is simulated as a lagrangian phase and gas is treated as an eulerian phase, as is generally done to represent a continuous fluid.

All the boundary conditions applied are summarized in the list below:

- Liquid Injector: it is modeled using a *particle injection region* where a mass flow has been defined for liquid N_2O together with the other required quantities (initial particles diameter, distribution, velocity and temperature). Depending on the specific injector geometry, it is possible to create more than one injection region;
- Fuel grain: it is modeled applying a *wall+source* condition, where wax enters the simulation domain with a fixed mass flow. The wall has a fixed temperature (725 K), no slip conditions are applied;
- Outlet: nozzle exit modeled using a traditional *outlet* condition, pressure of 0 atm defined, the reference pressure used for the whole simulation is 1 atm;
- Adiabatic wall: this is applied to all the remaining boundaries (e.g. nozzle walls, splash ring, end protection), no slip conditions.

When gaseous injection is simulated, the only difference is how the oxidizer is treated, because it is modeled as an eulerian phase. Therefore, the way it enters the domain is not characterized by a traditional injector model, but at the inlet surface a mass flow rate is specified, together with the mass fraction of the chemical species entering the fluid domain. The gas is injected in a direction orthogonal to the boundary patch itself and it comes from the whole boundary, not from a section of it.

A further step is to create an appropriate user-defined function, to implement and simulate the correlation between wall heat flux and regression rate. This way it is not necessary to apply the average fuel mass flow rate calculated from experiments, but it is possible to calculate a time varying mass flow rate, automatically updated by the CFD during the simulation, as a function of the convection heat due to the combustion process.
This also allows to account for local regression rate variations along the fuel grain.

Chapter 2

Design of Instruments for Numerical Codes Validation

This chapter is divided into two main sections:

- The first describes into detail the system created to validate the numerical code implemented for PMDs;
- The second illustrates the test facilities testing the rocket configurations simulated with the CFD.

2.1 Design of an Experiment to Validate the CFD Code about PMD

Sounding rocket Propellant OrieNtation micro Gravity Experiment (SPONGE) experiment aims at validating the numerical code developed at CISAS and at determining sponge retention capabilities.
Sponges are open control devices consisting of perforated metal panels in close proximity, generally located over the tank outlet. The panels form tapered gaps in which propellant clings. The taper forces the bubbles inside the sponge to go outboard, and it ensures that the propellant surface moves from outboard to inboard as it is consumed. A porous element located near the center tube is required to access the propellant within the sponge.

The REXUS program allows European Universities to carry out scientific and technological experiments on research rockets. Each year, two rockets are launched, carrying experiments designed and built by research teams. For SPONGE experiment, a team of 6 engineers was created from University of Padova: Marta Lazzarin (program manager), Francesco Barato (scientific expert), Nicolas Bellomo and Federico Moretto (design and structure engineers), Devis Paulon (electronic engineer) and Davide Rondini (software engineer).
SPONGE has been launched on board the REXUS9 sounding rocket, from Esrange in Kiruna (Sweden), in February 2011, thanks to the REXUS program, funded by European Space Agency (ESA), Deutschen Zentrums für Luft (DLR) and Swedish Space Corporation (SSC).

REXUS is an unguided, spin-stabilized rocket, powered by an Improved Orion Motor with 290 kg of solid propellant. It can take 40 kg of student experiment modules to an altitude of approximately 100 km. The vehicle has a length of 5.6 m and a body diameter of 35.6 cm. SPONGE has been switched on when REXUS was reaching its maximum height during the flight parable; during the micro gravity phase, the capillary forces were predominant compared to the hydrostatic ones and this has allowed to test the PMD installed and to verify the numerical code capabilities.

2.1.1 SPONGE Experiment Objectives

This experiment concerns liquid dynamics control in sloshing tanks. To apply controlled accelerations to the sponge device positioned inside the tank and immersed in a liquid, the experiment is provided with a horizontal-plate centrifuge. The idea is to monitor the behavior of the two fluid phases (gas and liquid) controlling the accelerations, and to measure the sponge directional retention capability, which depends on the acceleration applied. During the experiment, the dripping and positioning of the liquid-gas free surface are observed.
In conclusion, SPONGE objectives are:

1. To validate the code under development for the sponge PMD simulation;
2. To study the behavior of a specific PMD under low-g operations in terms of bubble point, different accelerations and design of the perforated plates;
3. To apply the fluid dynamic similitude theory.

2.1.2 SPONGE Experiment Overview

SPONGE main requirements are resumed:

1. The experiment diameter shall be smaller than 348 mm;
2. The experiment maximum height shall be lower than 220 mm;
3. The electronic components shall resist a minimum operative temperature as low as -30 °C;
4. The experiment shall survive launch accelerations (around 20g);
5. Any momentum transfer to the rocket, due to SPONGE rotating plates, shall be avoided;
6. Power consumption shall be lower than 28 W;
7. Signal allowing experiment and sensors activation shall be correctly received by the module;
8. Data shall be recorded on board and transmitted to the ground station;
9. Motors shall be locked during the ascent phase, before activation, to avoid experiment rotation;

10. The experiment shall provide the rotating plate and sponge with different rotational velocities, causing different accelerations on the liquid;
11. The experiment shall measure accelerations along the three axes in order to monitor the acceleration level on the sponge;
12. The experiment shall contain a sensor to measure the rotational velocity;
13. Temperature shall be measured inside the SPONGE module to monitor liquid properties;
14. The experiment shall take pictures of the liquid behavior inside the tank during the micro gravity phase of the flight with two video cameras having an appropriate frame rate.

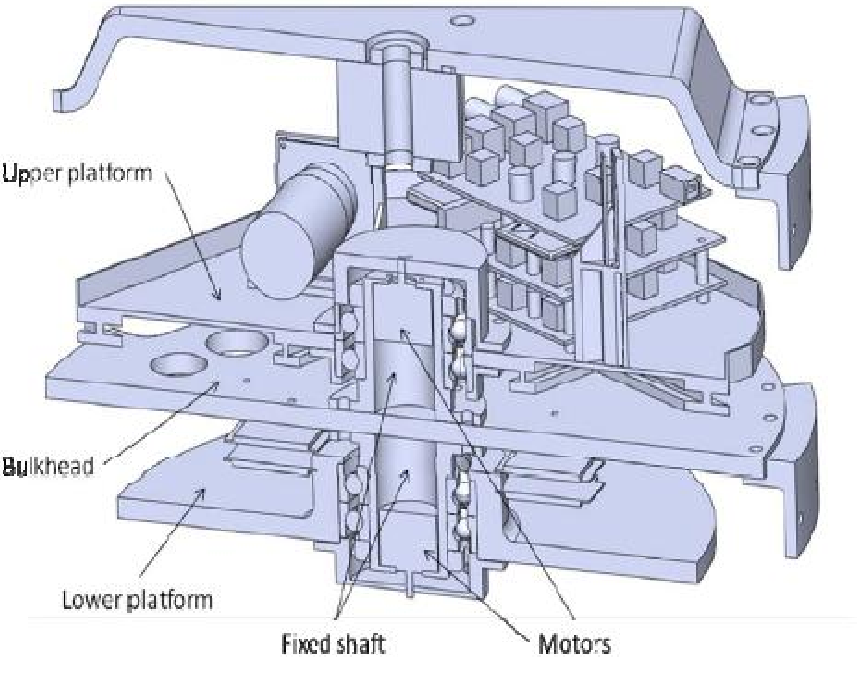

Figure 2.1: Overview of the experiment helping the identification of the different parts composing the module.

The sponge test article is composed of a bundle of titanium perforated panels attached to a cylindrical filter inserted in the middle of the sample. The wetting liquid is a silicon oil called Polydimethylsoxane, or PDMS. This liquid is nontoxic and has a solidification point around $-120\,^{\circ}\mathrm{C}$, thus it has no problems in case of cold storage.
By placing the panels in close proximity to one another (see Fig.2.2 and 2.3), liquid resides within the gaps and large amounts of propellant can be controlled even during thruster accelerations.
This structure is installed within a transparent cylinder and has its bottom part welded on

a titanium supporting plate. The tank is made of polycarbonate (rotation is applied by the underlying motor) and its axis is not coincident with the plate rotation axis: by maintaining a certain distance between the test sample and the rotation axis, it is possible to predefine the exact rotation velocity of the motor associated to the investigated acceleration.
Within the container, a certain amount of liquid is inserted and initially positioned upon the tank titanium base, under the effect of the ground/boost acceleration. When micro gravity is engaged, the liquid reaches its low-g stable position. After that, a sequence of different rotations is applied by the motor to the plate on which the experiment is accommodated, and the retention behavior is expected to begin.

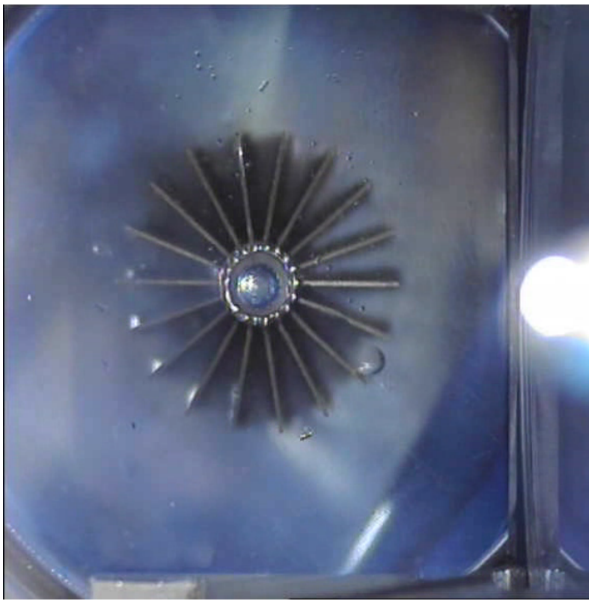

Figure 2.2: Sponge PMD installed in the experiment module. Liquid is attached to the tank wall, due to the rocket spin.

Two cameras monitor the experiment: they are positioned on the side and above the container and fixed on the rotating plate, in order to be in the same rotating reference frame.
At a certain rotation velocity, the liquid reaches its critical condition, after which it is expected to escape from the sample. The rotational velocity corresponding to this condition is measured and registered as the maximum sponge retention capability. A further increase in the rotational velocity, can cause the start of a supercritical condition and the sample depletion.
The rotation velocity corresponding to the maximum retention capability is measured. It is then possible to calculate the relative lateral acceleration of the test sample and, knowing its geometrical characteristics, the Bond number (for fluid dynamics similitude simulations) can be determined as well.

A three-axis accelerometer is inserted into the experiment module, in order to measure the acceleration directly affecting the platform housing the experiment. The data for diagnostics

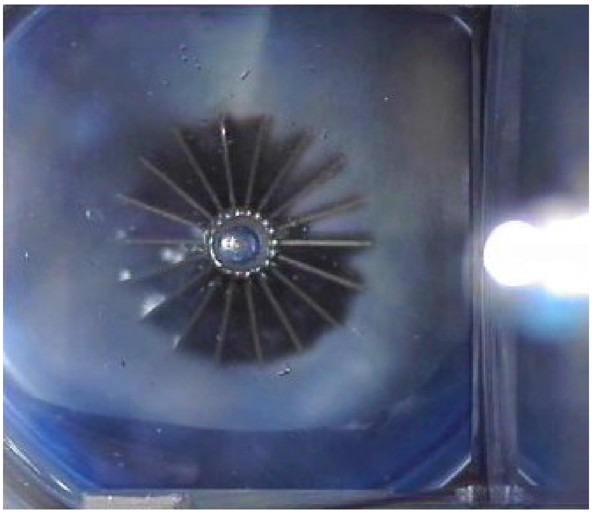

Figure 2.3: In this case, a certain amount of liquid is retained within the panels by capillarity.

is recorder continuously, during all the micro gravity phase.
In particular, the vision system is composed of two cameras and a led lighting system. It collects the data used to monitor the PMD behavior. The temperature sensor measures eventual temperature variations within the liquid to account for any possible surface tension change.

Figure 2.4: SPONGE prepared for functional tests before the flight, in Kiruna.

Motors are off before the lift off and until the micro gravity condition. When micro gravity is reached, they are switched on and the experiment starts. The rest of the sensors are on since the countdown.
The electric motors rotations are controlled by two separated feedback loops and data for the

diagnostics is recorded. At the end of the micro gravity phase, the experiment is terminated and remains off until landing.

2.1.3 SPONGE Experiment Design

2.1.3.1 PMD Design

Sponge design starts assuming a specific acceleration to be assigned to the liquid PDMS within the tank.
The choice of the appropriate acceleration is determined by both REXUS acceleration profile during the micro gravity phase and considerations connected to the sponge manufacturing process.
In particular, considering the possible disturbing accelerations during the flight estimated by ESA to be around 1e-2 m/s^2, it has been necessary to apply accelerations higher than that, for the experiment. On the other hand, the maximum possible acceleration to be applied is limited by the fact that a higher acceleration means a smaller sponge, to retain the same liquid quantity.
Therefore, in order to have a sponge big enough to be manufactured without any problems, but at the same time small enough to be able to apply considerably higher accelerations than 1e-2 m/s^2 during the experiment, the following values have been chosen:

1. 0.5 m/s^2 (sub-critical);
2. 1 m/s^2 (critical);
3. 1.5 m/s^2 (super-critical).

After having selected the accelerations to be imposed to test the sponge PMD retention, the design procedure can be started.

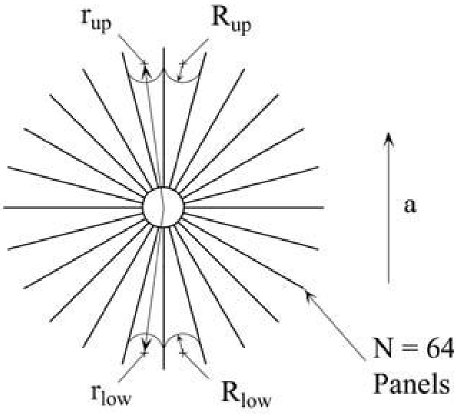

Figure 2.5: Main parameters used for the equations describing the sponge physics.

The liquid propellant in Fig.2.5 stays within the sponge only if the upper radius R_{up} is sufficiently lower than R_{low}, to overcome the hydrostatic forces. If the pressure difference due to surface tension in the liquid does not balance the hydrostatics, the sponge leaks or drips. Laplace equation[14] defines the pressure difference across the gas-liquid interface due to surface tension:

$$\Delta P_{laplace} = P_{gas} - P_{liquid} = \sigma \left(\frac{1}{R_1} + \frac{1}{R_2} \right) \tag{2.1.1}$$

where R_1 and R_2 are the principal radii of curvature of the surface at the interface and σ is the surface tension.
According to Eq.2.1.1, it is possible to calculate the pressure difference within the liquid retained by the sponge, from the lower to the upper side[12]:

$$\Delta P = P_{low} - P_{up} = \left[P_{gas} - \frac{\sigma}{R_{low}} \right] - \left[P_{gas} - \frac{\sigma}{R_{up}} \right] \tag{2.1.2}$$

This approach to the problem is one-dimensional, but the errors associated with it are accepted to simplify the description of the design process.
Assuming negligible flow losses, only hydrostatic pressure difference opposes surface tension pressure difference, resulting in[12]:

$$\sigma \left(\frac{1}{R_{up}} - \frac{1}{R_{low}} \right) = \rho a (z_{up} - z_{low}) \tag{2.1.3}$$

where $(z_{up} - z_{low})$ is the total height of the propellant within the sponge in the acceleration direction indicated in Fig.2.5, a is the acceleration and ρ represents liquid density.

Assuming that R_{up} and R_{low} are equal to one half the sponge panel gap and looking at Fig.2.5, it can be written:

$$(z_{up} - z_{low}) = \frac{(R_{up} + R_{low})}{sin \frac{\pi}{N}} \tag{2.1.4}$$

where N is the panels number.
The resulting equation becomes[12]:

$$\sigma \left(\frac{1}{R_{up}} - \frac{1}{R_{low}} \right) = \rho a \frac{(R_{up} + R_{low})}{sin \frac{\pi}{N}} \tag{2.1.5}$$

Sizing the Sponge

The chosen accelerations to be imposed during the experiment are: 0.5 m/s^2, 1 m/s^2, 1.5 m/s^2. At this point, according to Eq.2.1.5, the dimensions of the sponge for which the critical acceleration value is 1 m/s^2 are calculated.
The critical acceleration is that particular value provoking liquid isolation inside the sponge, because of the impossibility for the device to reject the liquid through the tapered gaps.

Eq.2.1.3 can be written to apply to any point of the liquid surface within the sponge[12]:

$$\sigma \frac{1}{R} - \rho a z = \sigma \frac{1}{R_0} - \rho a z_0 \tag{2.1.6}$$

where R is the generic fillet radius, z is a generic coordinate with respect to the sponge center, whereas R_0 and z_0 are respectively the fillet radius and the coordinate with respect to the sponge center of a specific liquid surface.

Given a particular sponge, the relationship between z and R can be substituted into Eq.2.1.6 to solve the surface in each gap. The radius R cannot indicate a position outside the sponge, thus a possible relationship between R and z can be as follows[12]:

1. If $r < r_{sponge}$:

$$R = rsin\frac{\phi}{N} - t/2 \tag{2.1.7}$$

   where t is the sponge thickness and r is the distance from the sponge center.

$$z = rcos\phi \tag{2.1.8}$$

   where ϕ is the angle from the thrust vector.

2. If $r > r_{sponge}$:

$$R = r_{sponge} \tag{2.1.9}$$

$$z = r_{sponge}cos\phi \tag{2.1.10}$$

Eq.2.1.3 can be rewritten, neglecting the sponge panel thickness, as:

$$\sigma\left(\frac{1}{r_{up}} - \frac{1}{r_{low}}\right)\frac{1}{sin\frac{\pi}{N}} = \rho a(r_{up} - r_{low})cos\phi \tag{2.1.11}$$

where the symbols have already been described for the previous equations.

Eq.2.1.11 allows to calculate r_{up} if r_{low} is fixed. It has been solved for different r_{low} and r_{up} values and for various accelerations. The resulting plot is in Fig.2.7, where the horizontal line represents the chosen r_{low}.
This particular r_{low} of 11 mm has been selected because it corresponds to the maximum possible r_{up}, after which no stable liquid surface exists.
The curves represent different acceleration levels that could be imposed to the PMD: each of them determines a different condition for liquid stability and consequently, a different liquid surface within the sponge (the values of r_{up} obtained are different).

As previously discussed, the experiment critical acceleration is 1 m/s^2 (due to the rocket external residual acceleration during the micro gravity phase), which means that the curve in Fig.2.7 to be considered for sponge design, is the one indicated by the arrow.
The other curves from left to right are obtained for decreasing acceleration levels. The plot confirms that, in order to retain a certain liquid quantity, the sponge radius has to decrease

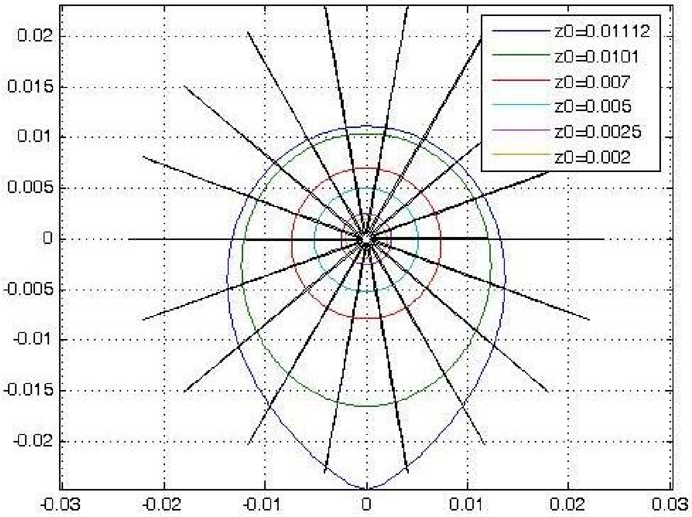

Figure 2.6: Example showing different possible equilibrium liquid surfaces. Each z_0 corresponds to the position of a specific liquid surface with respect to the sponge center. The surfaces have been found using Eq.2.1.6.

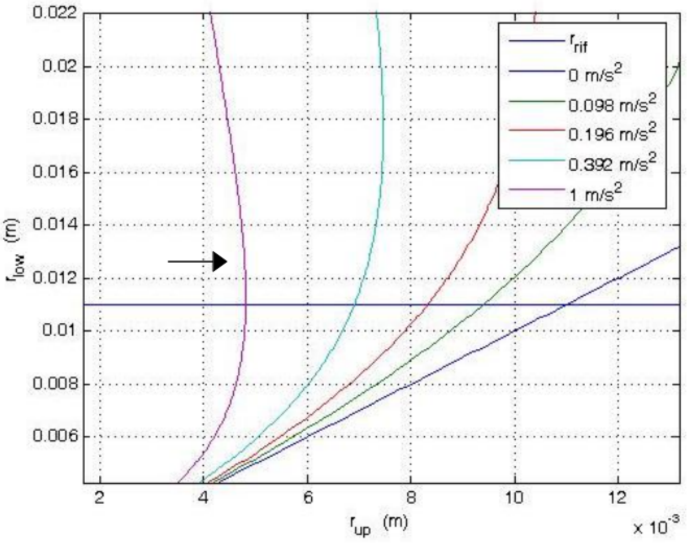

Figure 2.7: For a critical acceleration of 1 m/s^2 and a fixed r_{low} of 11 mm for liquid stability, the resulting r_{up} is 4.5145 mm.

when acceleration increases.

In conclusion, for the specific case considered for this experiment, if r_{up} exceeds the critical value of 4.5145 mm given by the intersection of the 1 m/s^2 acceleration curve with the horizontal curve representing the r_{low} radius of 11 mm, the sponge drips and no stable surface exists.

These conditions have been applied to the liquid:

1. 0.5 m/s^2 acceleration (sub-critical);
2. 1 m/s^2 acceleration (critical);
3. 1.5 m/s^2 acceleration (super-critical).

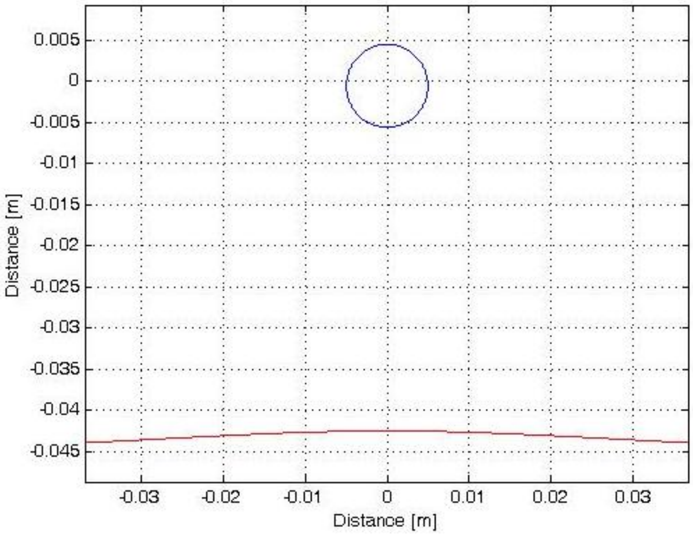

Figure 2.8: Liquid surface for z_0=0.0045145 m and a = 0.5 m/s^2.

Fig.2.8 and 2.9 refer to an initial liquid surface having a distance of 4.5145 mm from the center of the sponge, according to what has been described for the critical acceleration of 1 m/s^2.

The plot in Fig.2.8 represents the solution of Eq.2.1.6, giving the radial position of the liquid within the sponge, when an acceleration of 0.5 m/s^2 is applied.
This acceleration is sub-critical for a radius of 11 mm and an internal filter of radius 3 mm. The closed elliptical surface represents the liquid retained by the sponge, whereas the other solution does not apply in this case. The condition described is not critical for the liquid, and this is proved by the fact that the two solutions are well separated.

Fig.2.9 represents again the solution of Eq.2.1.6, but when an acceleration of 1.5 m/s^2 is applied. In this case, the liquid surface is subjected to a super-critical acceleration and no

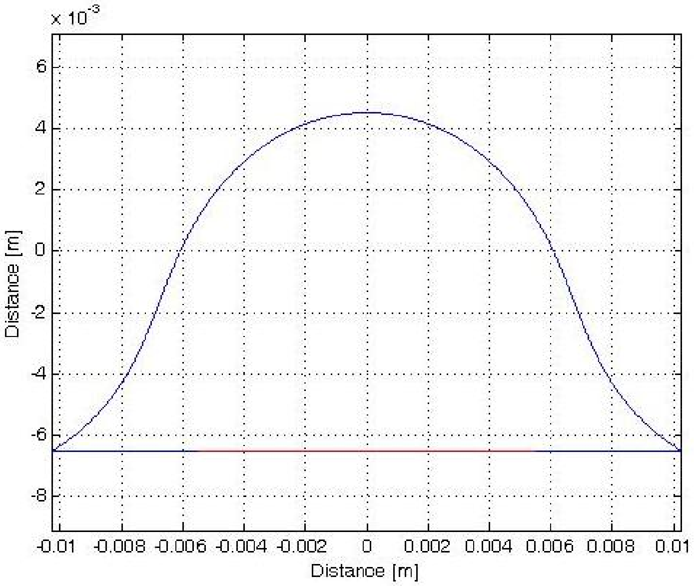

Figure 2.9: Liquid profile at z_0=0.0045145 m and a = 1.5 m/s^2.

closed surface exists, which means that the gas is not able to be ejected by the tapers of the sponge and some liquid gets isolated.
The liquid surface breaks after a 1 m/s^2 acceleration has been reached. It is also important to note that the critical condition sets only if the initial liquid quantity within the sponge (and therefore z_0) is sufficient.

In Fig.2.10, the liquid surface at the critical acceleration of 1 m/s^2 is shown. In this case, the two possible solutions of Eq.2.1.6 intersect in one point, which is the evidence that the critical condition has been reached.

Fig.2.11 is another picture showing the liquid surface for a fixed acceleration value, at different z_0 corresponding to different initial liquid quantities.

In conclusion, the dimensions of the sponge installed in the experiment and having 1 m/s^2 as the critical acceleration are:

1. 11 mm radius;
2. 3 mm, radius of the internal cylindrical filter;
3. 16 mm is the height of the device;
4. 0.5 mm is the thickness of its panels (or less, depending on the manufacturing process limitations).

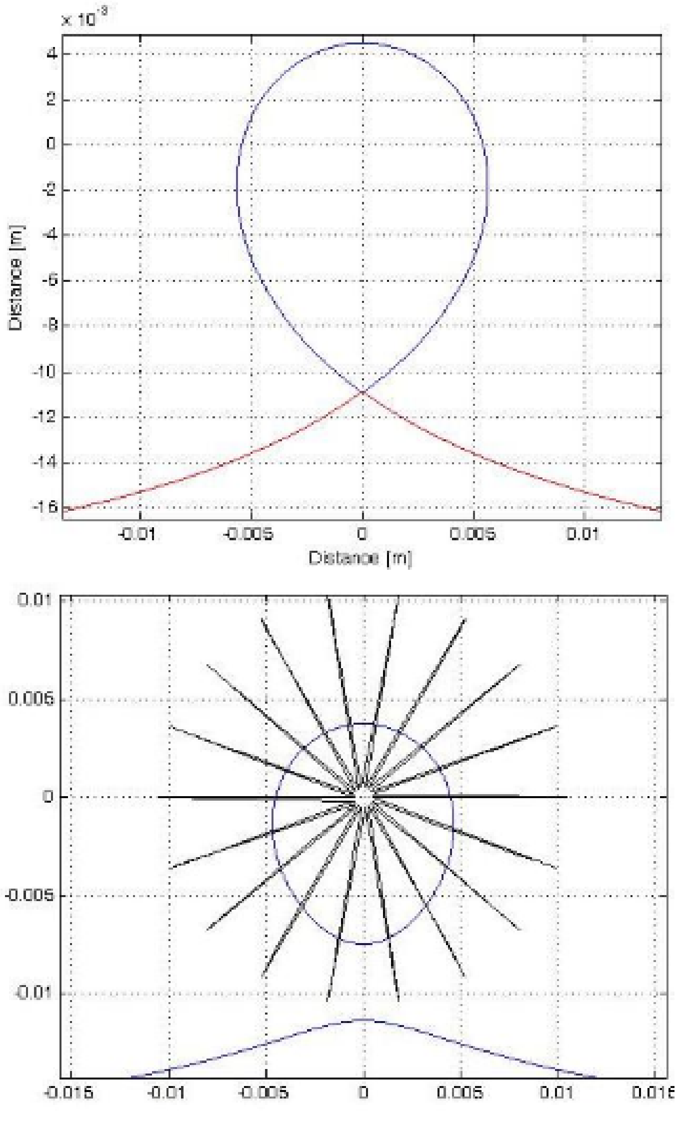

Figure 2.10: Liquid profile at z_0=0.0045145 m and an acceleration of 1 m/s^2. There are two different possible solutions for Eq.2.1.11. In the case presented, only the one internal to the sponge is acceptable.

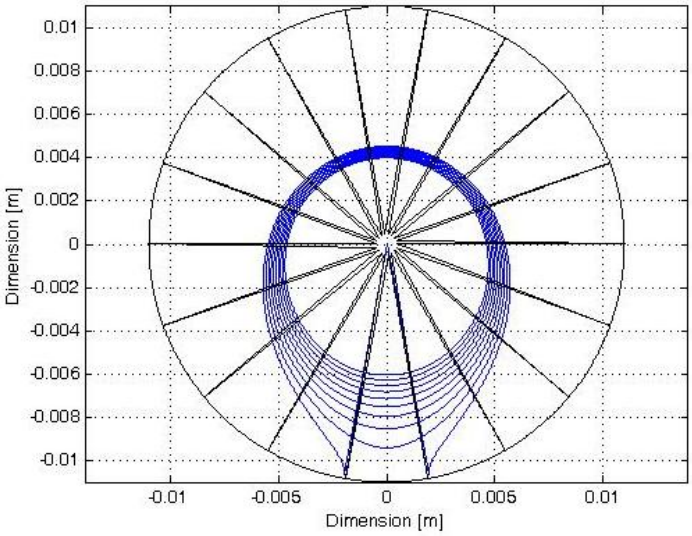

Figure 2.11: Liquid surfaces for different initial levels z_0 and a fixed acceleration.

Sizing the Tank

After having decided which accelerations to apply and having concluded the sponge design, tank dimensions have to be defined. These are chosen after a trade off process, because leaking phenomena between the liquid and tank walls have to be avoided, but tank dimensions are limited by the structure of the experiment inside the module as well.

The main requirements in this case are to:

- Avoid leaking between the liquid and tank walls. This can easily happen especially when micro gravity is engaged;
- Avoid excessive dimensions, due to the reduced space available on the experiment platform;
- Make the manufacturing process possible, using appropriate dimensions for the tank;
- Use an appropriate sealing technique, in order for the liquid not to exit.

The tank dimensions are:

1. Height: 25 mm;
2. Diameter: 50 mm;
3. Cylindrical shape: to keep the manufacturing process as simple as possible.

The following results refer to the preliminary analysis of the sponge behavior, calculated by means of a two dimensional, laminar, two-phase OpenFOAM simulation. The solver used is already present in OpenFOAM and has been used as the basis for the PMD custom code development. This solver is used to analyze sloshing tanks and capillarity conditions and has already been tested and validated for vanes.

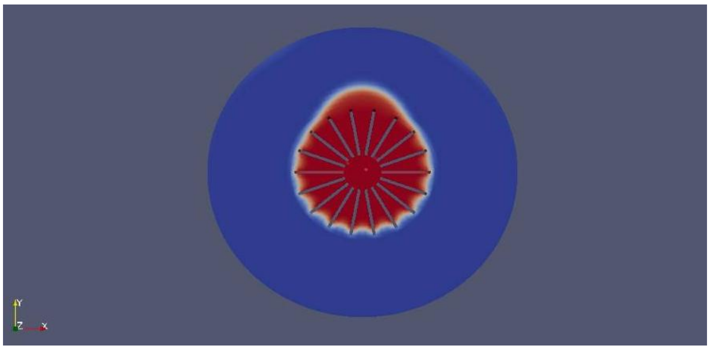

Figure 2.12: 2D solution of the liquid dynamics within the sponge with an acceleration of 0.5 m/s^2.

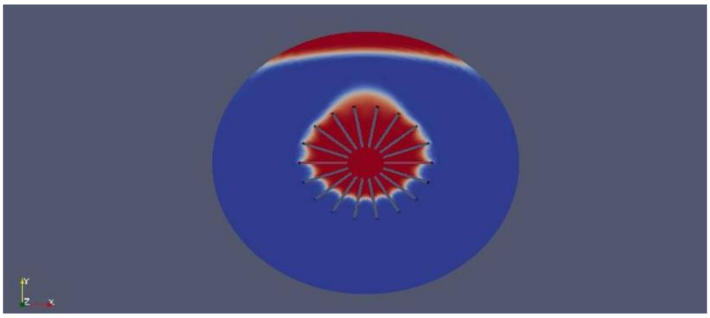

Figure 2.13: 2D solution of the liquid dynamics within the sponge with an acceleration of 1 m/s^2.

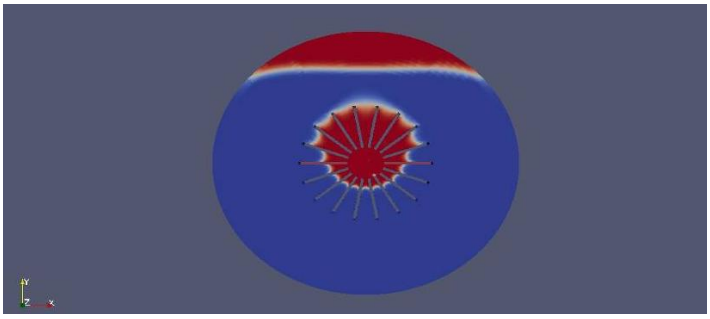

Figure 2.14: 2D solution of the liquid dynamics within the sponge with an acceleration of 1.5 m/s^2.

Another important factor is the tank fill level. In fact, even in a tank where a liquid path exists, it is possible to reduce its incidence by using a smaller quantity of liquid. For this reason, some simulations have been conducted considering a container of fixed size and subjected to defined accelerations, but with different fill levels. The results of these 3D numerical tests are presented below and refer to a tank having the dimensions listed above.

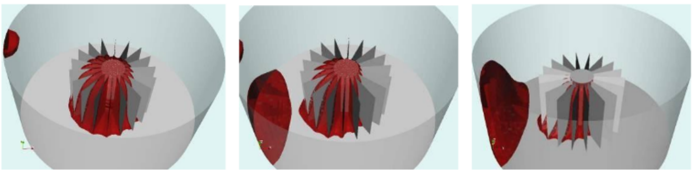

Figure 2.15: 3D solution of the liquid dynamics within the sponge with acceleration levels of: 0.5/1/1.5 m/s^2. The liquid fill level is the 10% of sponge height.

Figure 2.16: 3D solution of the liquid dynamics within the sponge with acceleration levels of: 0.5/1/1.5 m/s^2. The liquid fill level is the 15% of sponge height.

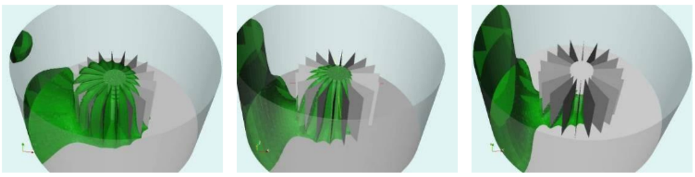

Figure 2.17: 3D solution of the liquid dynamics within the sponge with acceleration levels of: 0.5/1/1.5 m/s^2. The liquid fill level is the 20% of sponge height.

During the experiment, two views of the liquid inside the tank are recorded. The first from above and the second sideways. Due to space and optical constraints, the first image is taken indirectly with the aid of a mirror placed above the tank. The mirror is oriented at 45 ° with respect to the vertical axis, in order to reflect the image at 90 ° toward the camera. This way, both the cameras can be fixed on the rotating platform and have a sufficient distance from the tank to avoid focusing problems.
The images dimensions are approximately 48 mm x 36 mm, while the sensor dimensions are 4.8 mm x 3.6 mm (1/3”), so that an optical magnification equal to 0.1 is required. The working distance is 160 mm, the focal length is 16 mm and the focal ratio is around 8. These values have been selected to achieve a depth of field equal to the sponge height (16 mm). A fixed-focal-length lens has been chosen, because it is more compact and reliable than other types.

Particular attention has been dedicated to the polycarbonate tank design. Proper O-rings have been chosen, to grant a perfectly sealed lock.
Another material option was plexiglass, because it suffers less from time degradation from an optical point of view, but it has been discarded due to its fragile mechanical behavior.

The tank internal diameter is 50 mm. Upon the tank, a mirror is placed to reflect the up-view of the PMD and of the liquid inside it, which are then captured by one of the two cameras (Fig2.18).
The mirror is a 4-6 Wave First Surface Mirror produced by Edmund Optics. Its dimensions are 38 mm x 51 mm and it is mounted with its larger dimension in a vertical position.
The field of view of interest is reflected to the corresponding camera.
The nuts locking the whole tank structure are glued, to avoid unlocking during the ascent, due to vibrations.

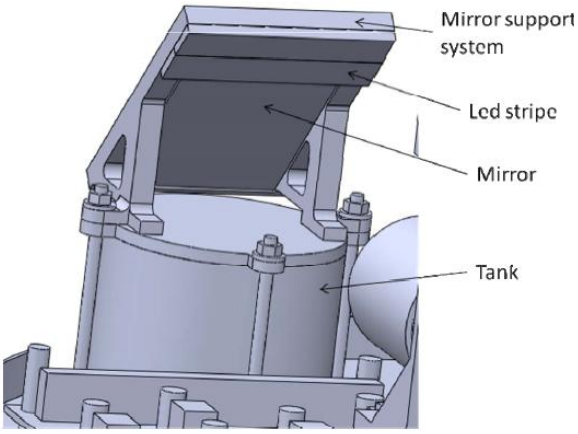

Figure 2.18: SPONGE tank configuration and installation.

In the structural preliminary design, two loads have been applied:

1. Internal pressure: 5 bar (FS = 5);

2. Inertial force of the structure acting on the top: 1 kg @ 20g (instead of 0.135 kg, FS = 5).

With a 40 MPa yield stress coming from the material characteristics and a 1 mm thickness, the resulting stress safety factor is 2.7. Anyway, the final thickness is 5 mm, due to construction constraints (the O-ring sealing could not fit in such a tank), so that the safety factor has become 12.5.
O-rings are considered to be a sufficient means to ensure a complete sealing capacity in all the foreseen experiment conditions (ground and flight operations).

Fig.2.19 shows the manufactured and designed sponge device.

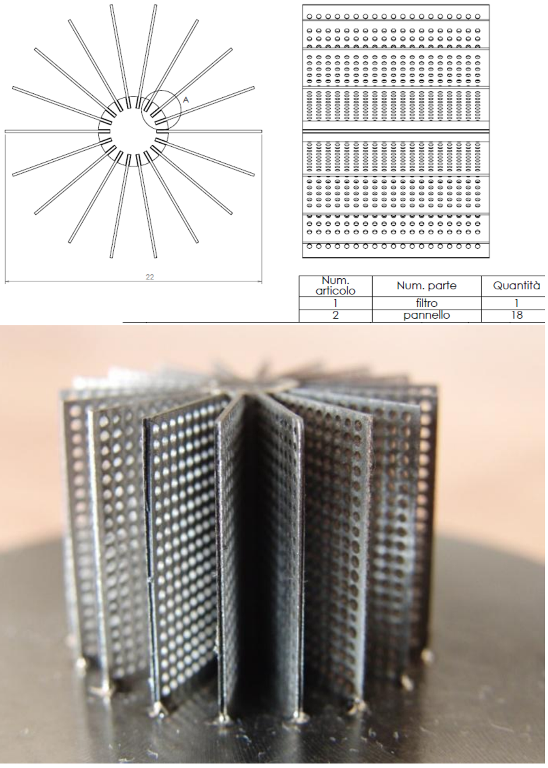

Num. articolo	Num. parte	Quantità
1	filtro	1
2	pannello	18

Figure 2.19: Designed and manufactured sponge PMD.

2.1.3.2 SPONGE Structure Mechanical Design

The main requirements followed to design SPONGE structure are:

- The structure shall have a natural frequency sufficiently higher than the launcher;
- The structure shall withstand the loads during the various mission phases;

- The structure shall be compatible with the constraints on the size of the whole experiment module;
- The structure shall allow all the operations foreseen for the scientific goal of the experiment.

The experiment works in vacuum and two venting ports are present on the module walls. From the mechanical point of view, the platform accommodating the experiment rotates to give the desired acceleration to the PMD and a counter rotating disk provides a momentum-balancing effect, which otherwise would be transferred to the other experiments and to the rest of the rocket.
Each rotating platform is guided by a dedicated electric motor; this configuration simplifies the system and the experiment as much as possible. It is possible to separately test and control the performance of the two motors. This independence also allows to calibrate separately the motors on ground, during the tests.
It is sufficient to impose a single specific velocity to the counter rotating platform to reduce as much as possible the momentum transfer to the rocket. This provides a further simplification, because it is possible to calibrate the velocity of the counter rotating plate without applying any active control in connection with the other rotating platform.

The maximum disturbance that SPONGE can transmit to the rocket is $5°/s$, which corresponds to $1/6$ of the residual rocket rotational speed of $30°/s$ after the de-spin.
The rotational disturbance created is calculated using this simple conservation equation, where L is the angular momentum of the entire system:

$$\frac{dL}{dt} = M = 0 \tag{2.1.12}$$

M is the torque transferred to the system. From the above equation and the definition: $L = I\omega$, it results:

$$I_{rp}\omega_{rp} + I_{cp}\omega_{cp} + I_p\omega_p = \Delta L = 0 \tag{2.1.13}$$

where rp = rotating platform, cp = counter rotating platform and p = REXUS payload.
In ideal conditions:

$$I_{rp}\omega_{rp} + I_{cp}\omega_{cp} = \Delta L_{exp} = 0 \tag{2.1.14}$$

which means that no momentum is transferred and consequently the residual momentum of the experiment ΔL_{exp} is zero.

Considering the maximum residual velocity of $5°/s$ which can be transferred to the rocket, it is possible to calculate SPONGE residual momentum, due to imperfect balancing of the two rotating plates.
Assuming that the rocket can be approximated with the service module for safety reasons (m = 60 kg, R = 0.18 m), its inertia is given by: $I_p \simeq \frac{1}{2}mR^2$, $I_p \simeq 1kgm^2$.
The maximum disturbing rotational velocity for the rocket is therefore $\omega_p = 5°/s = 0.087rad/s$.

Using these parameters, the resulting maximum residual angular momentum for the experiment is:

$$\Delta L_{exp} = -I_p \omega_p = 0.087 kgm^2/s \tag{2.1.15}$$

During the test conducted on the plates mock-up, it has been possible to record a video and estimate the rotational velocity transmitted to the rocket and due to the fact that ΔL_{exp} was not perfectly zero.
The ω_p estimated was lower than $1°/s$ and this slow rotation was visible only after the motors activation, but disappeared soon after it. For this reason, the requirement about momentum was considered to be satisfied.

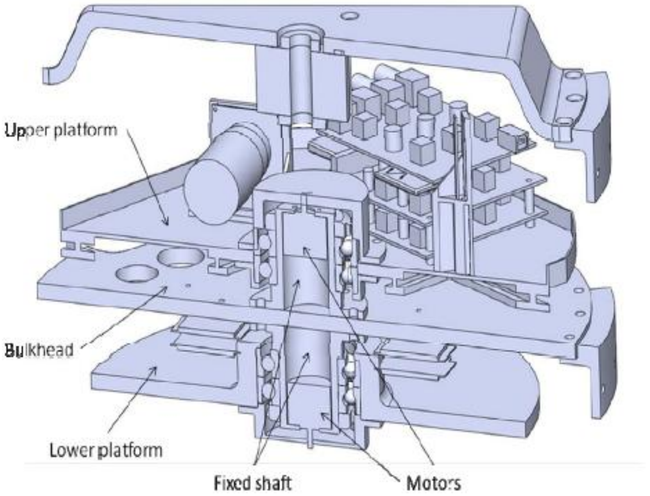

Figure 2.20: Section of the SPONGE experiment.

From the mechanical point of view, the experiment (shown in Fig.2.20) needs three mechanisms to achieve the scientific goals:

1. Two rotating plates: the upper plate is used for the experiment installation (PMD tank, diagnostics and conditioning); whereas the bottom platform counter-rotates with respect to the first one. The two platforms are singularly controlled by two dedicated motors, to keep a simple electronic control.
2. The platform locking/release device (Fig.2.21): used during launch phase to keep the rotating platforms in the same locked position as during rocket balancing.

From equation 2.1.14, it is possible to determine the angular velocity of the two plates knowing their physical parameters, such as inertia (which can be easily determined both in the design phase and after their manufacturing).
Then, the zero-momentum condition is achieved using the electronic control of the two motors.

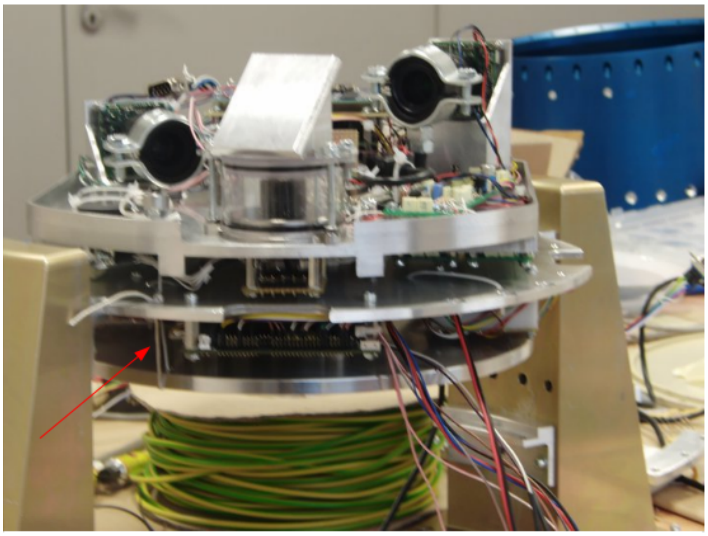

Figure 2.21: The wire used to lock the platforms during ascent is indicated by the red arrow. It is cut by a pyro device before the experiment start.

Rotating Plates

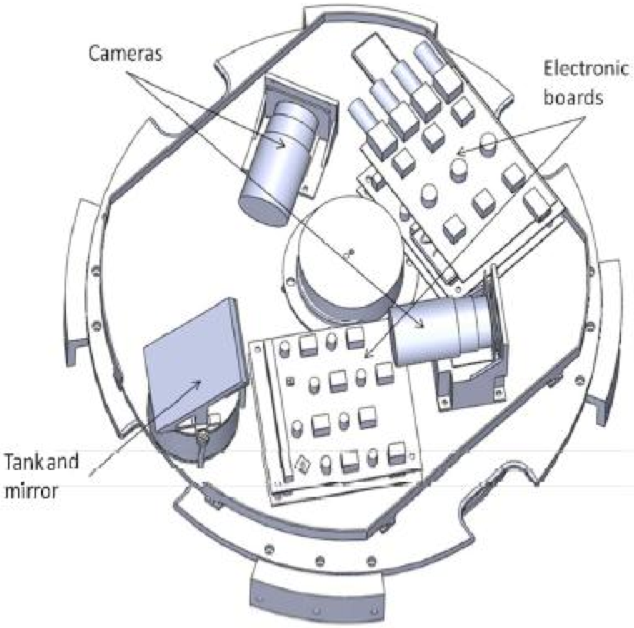

Figure 2.22: Rotating plate components location.

The upper rotating platform is the main part of the experiment and it can be seen in Fig.2.22. It is mounted onto a fixed base by means of dedicated bearings, and it holds various devices:

- The SPONGE tank, with the PMD. It is connected to the platform using three M3 threaded rods and nuts, keeping the tank closed and fixed to the structure. The same rods are used to fix a mirror on the upper side of the tank as well, to allow the diagnostics of the liquid behavior with a camera. The mirror is mounted on a specific seat using glue: this is a typical way of mounting mirrors for space applications;
- The electronic boards for experiment diagnostics (Acquisition Board (AB)). All electronic devices are mounted with M3 threaded screws.

Figure 2.23: Manufactured rotating plate housing the experiment.

All the rotating mechanical connections are obtained by using deep groove, single row ball bearings in double back to back configuration, able to bear both axial and radial loads and granting a high stiffness level.

It is not possible to mount the rotating platforms directly to the motor shaft, because the motors are small (the selected ones are provided by Faulhaber, series 2619-024SR), due to the reduced experiment dimensions. This also means that they cannot be subjected to heavy loads.

Since the total static load in the worst possible flight condition has been estimated as 2.2 kN, the chosen bearings can be subjected to a maximum axial load of 5.1 kN and to a maximum static load of 10.2 kN, resulting in a total safety factor of 4.6.
These bearings are Barden 107HE and lubrication is performed with Castrol Braycote 601 EF grease, used in space applications.

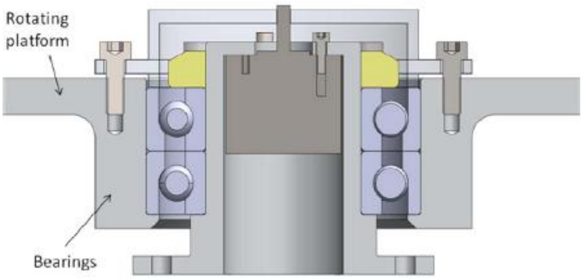

Figure 2.24: Bearings detail.

Every plate can rotate by means of a dedicated electrical motor. The existing requirements for the rotational velocity allow to use the same motor type for both the platforms: the difference is only connected to the power supply, which is controlled by the electronics.
Each motor is connected to the fixed base and to the rotating platform (only rotational connection, axial and radial loads are sustained by bearings).
The motor is linked to the fixed shaft with three M2 screws. This has been verified as sufficient to withstand the axial acceleration obtained by the FEM analysis (100g).

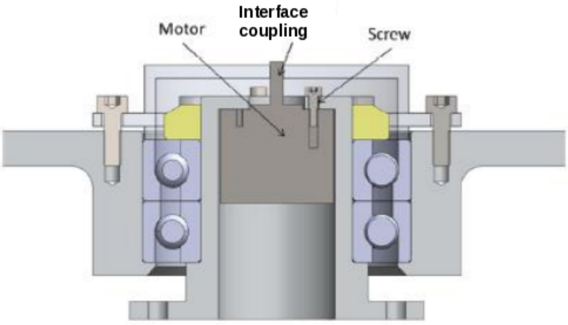

Figure 2.25: Motor installation and connection to the rotating platforms.

Locking Device Solutions

It is required to lock the platforms during launch, to prevent them from rotating. In case of rotation, two problems could arise:

1. Possible gearhead breaking;
2. Unbalanced rocket inertia and errors on trajectory.

The chosen mechanism is a wire cutter, a device used to cut cables. It is fixed to the bulkhead: after the cut, no springs are needed as winders, because the free wire can cause no danger in terms of mission failure. The advantages of this solution are:

1. Reliable and already tested;
2. No gears.

The disadvantages are:

1. Explosive device;
2. One shot only device;
3. High cost compared to other solutions.

The main risks are:

1. Rod not correctly retracting;
2. Device not cutting the rod.

Fig.2.26 presents the way cutters lock the whole structure during the launch phase. The specific device selected in order to block the platforms is made by Cypres. The cutter is activated by means of an impressed current.

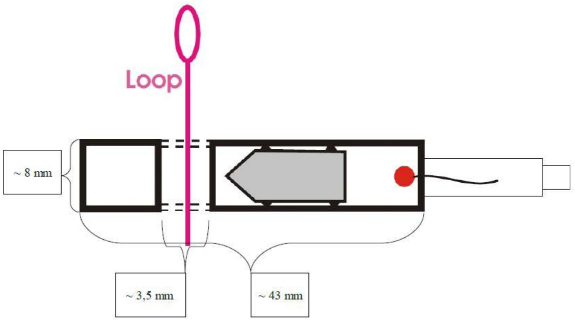

Figure 2.26: Cypres wire cutter device dimensions and cutting procedure.

The wire is by CYPRES as well, with a diameter of 1.8 mm and a break tension of 200 kg. It is the same loop used in fast deployment of safety parachutes.

2.1.3.3 Electronics Design

The main requirements for the electronics system are:

- To consume less than 28 W;
- To allow all the storage operations required for the data collection;

- To transmit the data to the ground station;
- To communicate with REXUS service module for experiment activation and signals transmission.

Two different boards are foreseen to cope with system requirements. The first is fixed on the rotating platform and used for sensors acquisition/recording and image compression; this board is called AB.
The other board is needed to control the electric motors and to impose the correct acceleration profile to the liquid inside the tank; it allows the transmission of the diagnostics to the RS-422 as well, in order to down-link the data. It is fixed to the bulkhead, which is in turn connected to the REXUS external case. This board is also called Control Board (CB).
These two boards are connected by the slip-ring, because a wireless system for data transmission could have caused important disturbances affecting the signals. This connection is also used to communicate the start signal to the upper board on the rotating platform.
The experiment start signal is transferred through the slip-ring, by means of the RS-422 serial port.

The choice of two different boards is due to the necessity to reduce the wires passing through the slip-ring. Images are recorded inside a flash disk, but they are not down-linked, for reasons connected to both the power consumed and the experiment complexity.
In conclusion, the slip-ring is used to bring the power supply to the board fixed on the SPONGE rotating platform and to send the data to the rocket service module for down-link. Moreover, some sensors need to be accommodated next to the tank containing the liquid, but there is no need to place the CB on that platform, because in this case the rotating platform can be heavier. Instead, if the CB is on the fixed bulkhead directly attached to the REXUS module, the whole structure has a center of gravity nearer to the fixed bulkhead and therefore it can be more stable.

The AB is connected to a two-channel frame grabber for the two cameras. The images are recorded on a flash disk, but this has a limited velocity in writing, so that it is necessary to compress the images in jpg format, reducing the total amount of data to be transferred. The schemes of the electronics are presented below, starting from a general one presenting the signals and data transmitted or communicated.

Power and Electrical Connections

Due to the rotational configuration of the experiment, a slip-ring has been chosen as the appropriate system to guarantee the electrical connection between the fixed structure and the moving parts.
The structure housing the slip-ring is an aluminum bar, it is aligned with the rotational axis of the platform and is connected to REXUS case by means of dedicated brackets.

Wires from the REXUS service module are fixed to the internal wall of the experiment module and to the slip-ring holder, then they are connected to the slip-ring. Rotating connec-

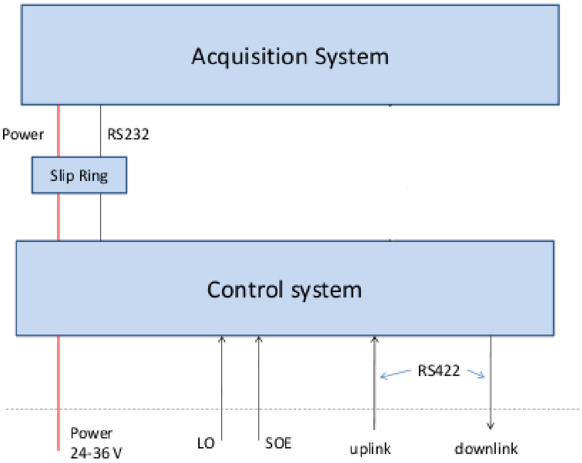

Figure 2.27: Scheme representing the global structure of the electronics subsystem and the communication between the two boards through the slip-ring.

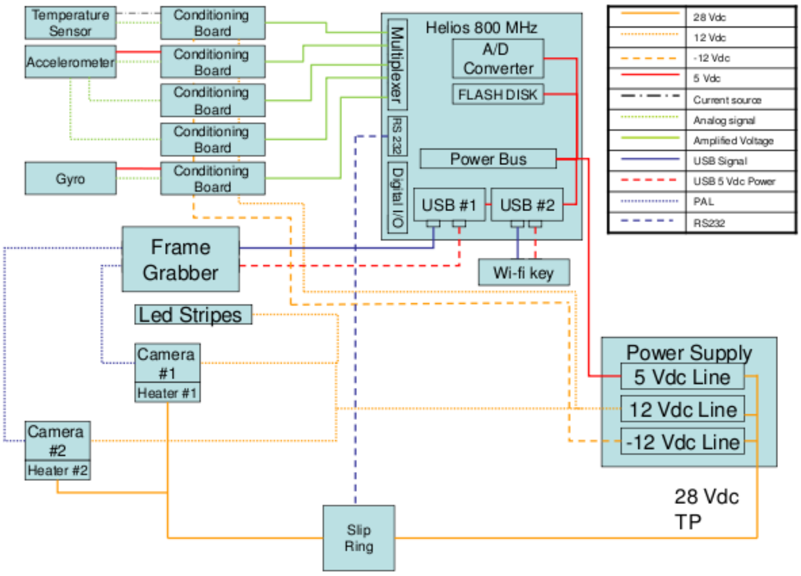

Figure 2.28: Board for sensors control and LED activation.

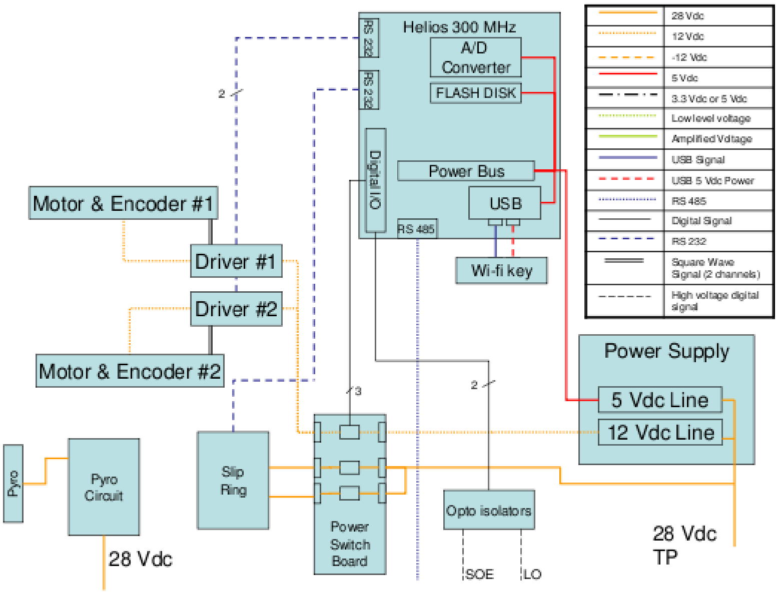

Figure 2.29: Scheme of the motors control board on the fixed bulkhead.

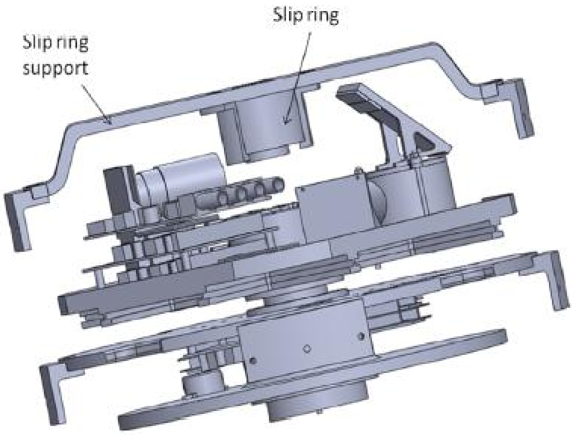

Figure 2.30: Slip ring and supporting system.

tions depart from the slip-ring shaft and reach the electronic board on the rotating platform.

To avoid stresses on the wires, a mechanical connection for the slip-ring has been designed. Two parts have been distinguished: a fixed one (with respect to the external module of the rocket) and a rotating one. The latter rotates with the rotating platform, and the slip-ring is used to connect the bulkhead electronic devices with the rotating plate.

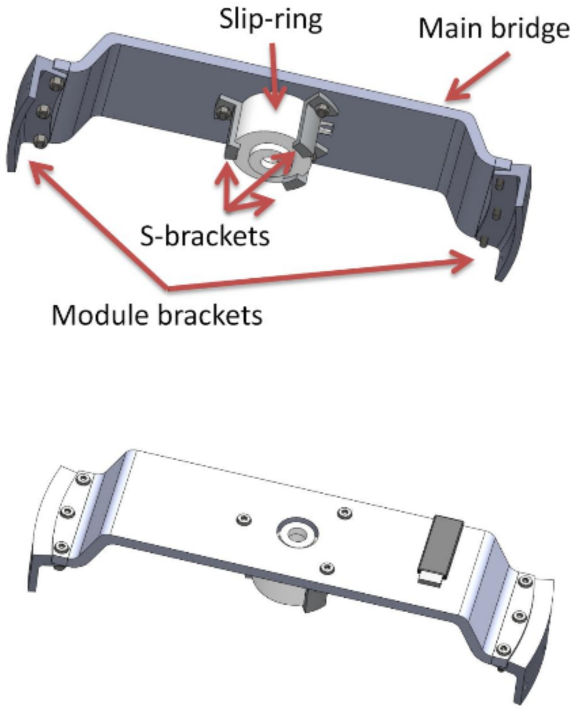

Figure 2.31: Fixed slip-ring holder.

The fixed slip-ring holder is composed of three parts:

- A main bridge;
- Two module brackets, to connect the bridge to the external module;
- Three S-brackets, to sustain the non-rotating part of the slip-ring and fix it to the main bridge.

The rotating part of the slip-ring is fixed to the rotating platform through a cylindrical support mounted on it.
An M2 setscrew fixes the holder to the slip-ring. The final design of the slip-ring holder has been simplified compared to the initial one, due to the necessity to reduce the manufacturing costs.

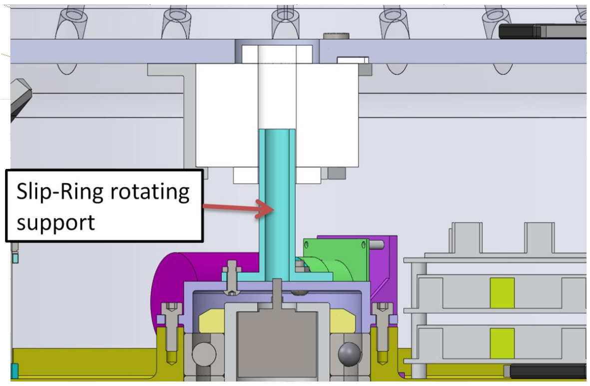

Figure 2.32: Detail of the experiment structure.

2.1.3.4 Thermal Design

For the thermal verification of the whole experiment module, three different basic cases have been considered:

1. Worst hot case;
2. Worst cold case;
3. Experiment duration phase.

Worst Hot Case

The worst hot case is represented by the ascent phase. In fact, during the ascent, the thermal environment of the outer structure of a front-end positioned parallel module on an Improved Orion motor can reach 110 °C at 50 s after lift-off.
A one-thermal-node model has been used to simulate the experiment temperature profile during the ascent phase. Radiation and convection heat transfer have been taken into account between the skin and the experiment.
The results highlight that all the experiment components do not reach their maximum storage temperature. The components accommodated do not reach their maximum operative temperature, apart from the cameras, in case of a high initial temperature. The maximum temperature in the pre-launch phase is 24 °C, whereas during the countdown, the temperature is not likely to rise more than 10 °C. Consequently, the maximum operative temperature of the cameras (40 °C) cannot be reached. Peak temperatures above 200 °C are reached during the re-entry, but none of the components exceeds its temperature range.

To achieve more reliable data concerning the thermal control results, other more accurate studies have been conducted. A transient FE analysis has been performed to determine the maximum temperatures reached by each component during the ascent phase.

The temperature profile represented in Fig.2.35 has been applied as a boundary condition to the supporting brackets of the bulkhead. The same temperature has been applied as the shroud for radiative heat transfer.
Between screwed surfaces, only the thermal contact conductance through the contact area

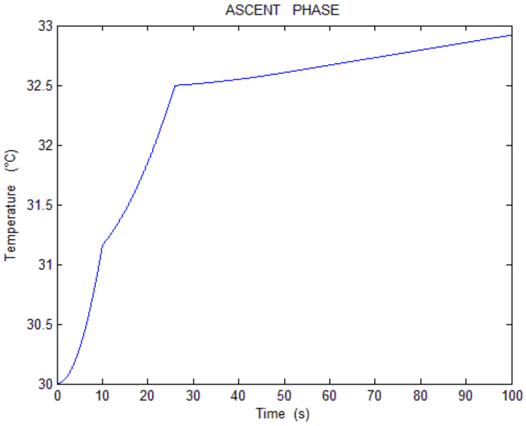

Figure 2.33: Estimated temperature profile in the REXUS experiment module during ascent.

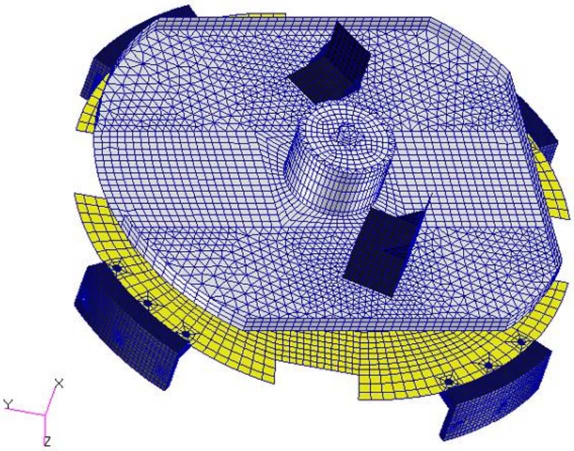

Figure 2.34: Finite elements model for thermal analysis.

under screw pressure has been considered.
Electronic equipment power dissipation has been taken into account.

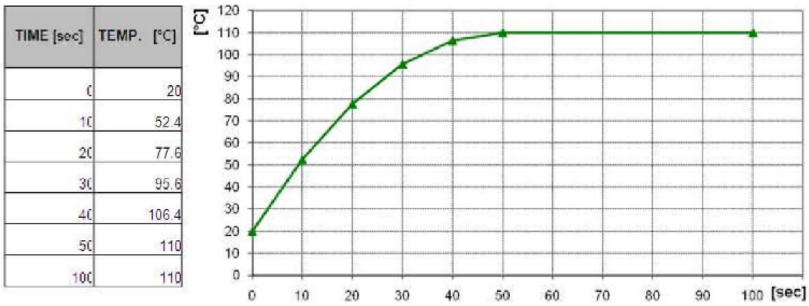

TIME [sec]	TEMP. [°C]
0	20
10	52.4
20	77.6
30	95.6
40	106.4
50	110
100	110

Figure 2.35: Estimated temperature profile applied to the supporting brackets.

The maximum temperatures reachable by SPONGE components during the ascent phase are resumed in Fig.2.36.

These results highlight again that all the experiment components do not reach their maximum operative temperature during ascent. Peak temperatures above 200 °C are reached during the re-entry, but none of the components exceeds its temperature range when the experiment is working.

Worst Cold Case in Storage

The worst cold case is usually given by winter temperatures on ground in Kiruna (−30 °C), where the rocket is out in the cold for prolonged periods of time. Therefore, all the components are selected to have a minimum storage temperature of at least −30 °C.

Worst Cold Case in Operation

Another specific event has been considered: the experiment can be switched on after a period of storage at a temperature of approximately −30 °C. In this case, it is necessary to be sure that the electronics and the system components can resist such a temperature, even at the beginning of the operative phase. For this reason, the components selected have a very wide temperature range, with a sufficiently low minimum temperature.
Problems during the operative phase could involve only the two cameras, consequently a solution involving heaters has been evaluated. A FE analysis has been performed to estimate the time required to heat up the cameras from −30 °C to 0 °C with a power of 10 W. An experiment has been prepared as well, to verify the heating time of the cameras, and in this case cameras were heated up more quickly compared to the simulations prediction. Moreover, the cold test showed that cameras can cope with a −25 °C temperature without any damage, thus it has been decided not to use any heaters for the flying experiment.
Some samples of the simulation results are presented below, to show the difference with respect to the test.

By analyzing the difference between the results of the simulations and of the experimental tests, it can be concluded that numerical simulations are not completely reliable, due to

COMPONENTS		MAX INTERFACE TEMPERATURE [°C]
ROTATING PLATFORM		
1	Power Supply Board 1	26
	Helios 800 MHz Board 1	
	Flash Disk SSD	
	Frame Grabber	
	Sensors Power Supply	
	Sensors Converters	
2	Power Supply Board 2	27
	Helios 800 MHz Board 2	
3	ZigBee USB	26
4	LED -TANK	25
5	Camera 1	30
6	Camera 2	28

FIXED PLATFORM		
7	Helios 300 MHz Board	38
8	ZigBee USB	50
9	Motor Driver #1	30
10	Motor Driver #2	30
11	Motor #1	22
12	Motor #2	22
13	Power Supply Board	38

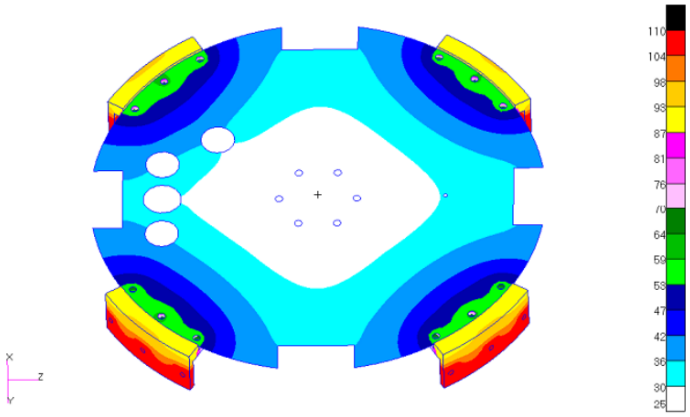

Figure 2.36: Maximum temperature map on the bulkhead [°C] during ascent.

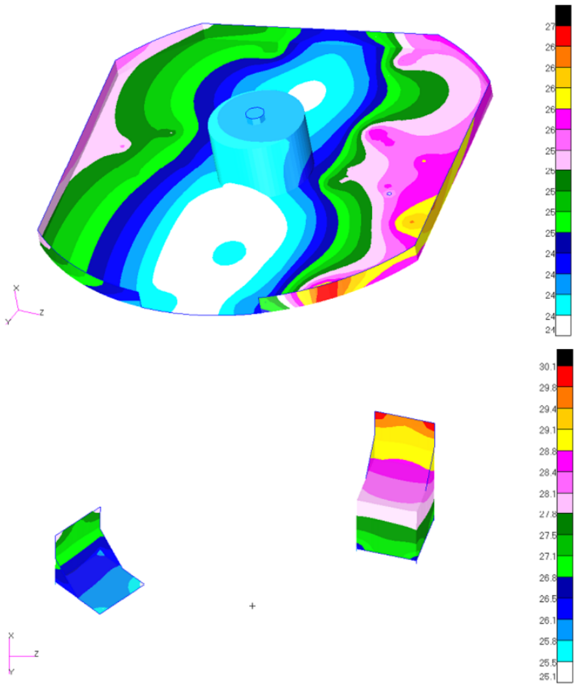

Figure 2.37: Maximum temperature map on rotating plate [°C] and on the camera supports during ascent.

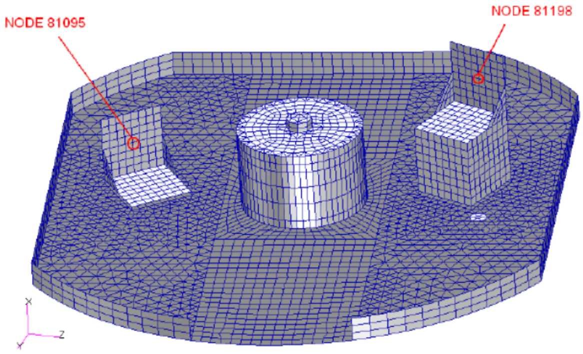

Figure 2.38: Monitored nodes corresponding to the cameras supporting elements.

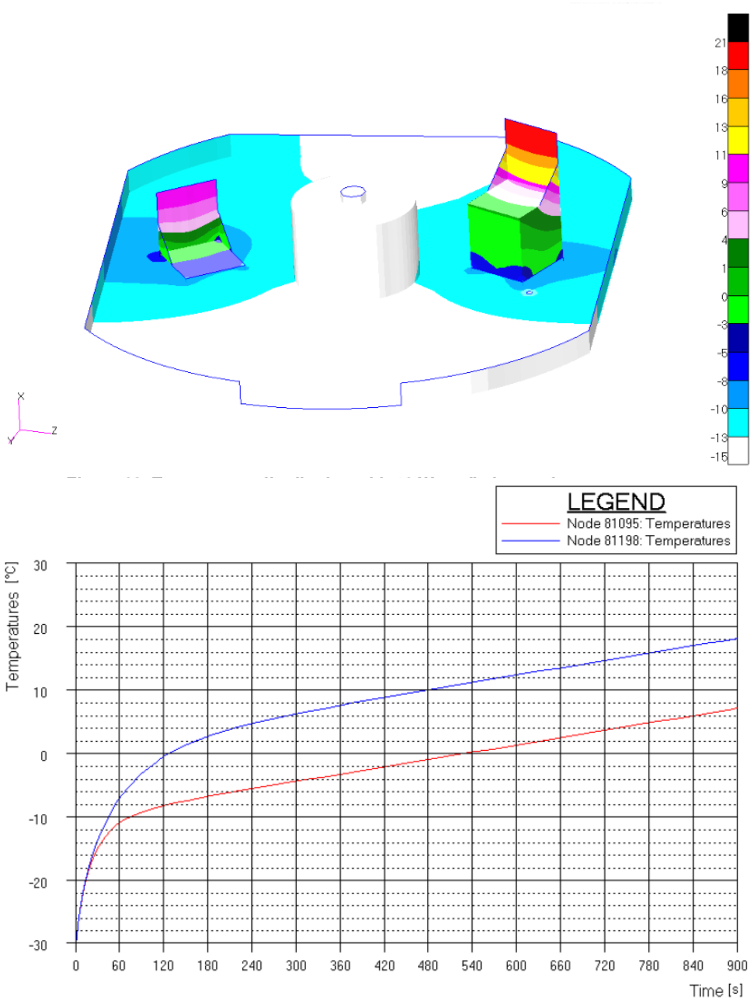

Figure 2.39: Temperature distribution and profiles with 10 W applied to each camera.

the approximations and uncertainties within the model. Particularly, it is difficult to predict convection losses and thermal contact resistances. For these reasons it becomes necessary to perform some experimental tests, in order to measure the effective time required to heat the cameras. For the experiment performed, a sample has been put in a freezer and the temperature has been monitored with some Resistance Temperature Detectors (RTD)s. As already said, the test results proved that it is not necessary to account for the use of any heaters.
The following table compares the maximum temperature that the electronic components mounted on the rotating platform can reach and the corresponding maximum temperature expected according to the FE analysis.

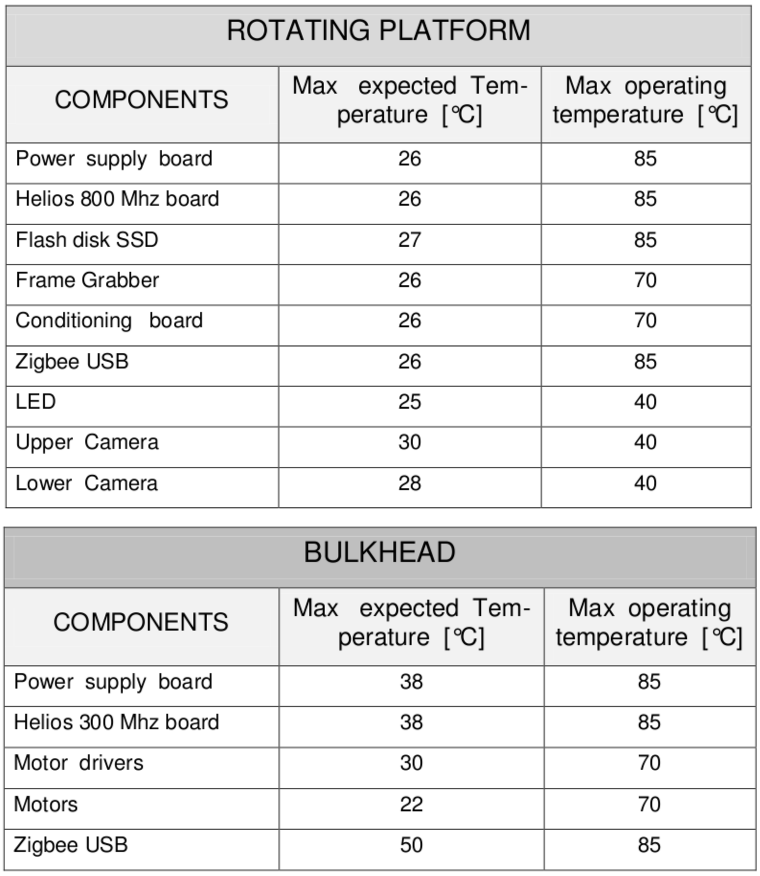

ROTATING PLATFORM

COMPONENTS	Max expected Temperature [℃]	Max operating temperature [℃]
Power supply board	26	85
Helios 800 Mhz board	26	85
Flash disk SSD	27	85
Frame Grabber	26	70
Conditioning board	26	70
Zigbee USB	26	85
LED	25	40
Upper Camera	30	40
Lower Camera	28	40

BULKHEAD

COMPONENTS	Max expected Temperature [℃]	Max operating temperature [℃]
Power supply board	38	85
Helios 300 Mhz board	38	85
Motor drivers	30	70
Motors	22	70
Zigbee USB	50	85

Figure 2.40: Table resuming the expected temperatures versus the operative temperatures for both the components on the rotating plate and those on the bulkhead.

Experiment Duration Phase

SPONGE is switched on for about 100 s with a maximum power dissipated lower than 28 W. The formula calculating the heating due to the internal dissipation is the following:

$$\Delta T = P\frac{dt}{mC} \tag{2.1.16}$$

It has been applied not only to estimate the total heating inside the module, but also the local heating of the single components. The radiative heat transfer has been evaluated with this equation:

$$Q = \sigma \epsilon A_{skin} \frac{(T_{skin}^4 - T_{in}^4)}{1 - \epsilon} \tag{2.1.17}$$

which has a certain safety margin and where ϵ is the material emissivity, T_{in} represents the high temperature source and T_{skin} the low temperature of the rocket case surface. A_{skin} is the surface subjected to heat exchange.
In conclusion, the temperature variation during the experiment phase sets around ±5 °C.

2.1.3.5 Software Design

Software requirements are listed here:

- The software shall allow signals transmission to the boards, from REXUS service module;
- It shall allow data recording and down-link;
- It shall allow the imposition of the selected velocity profile to the upper platform;
- It shall implement an appropriate protocol for data transmission.

The section below presents some schemes, created to explain the logic order of the electronic boards tasks. The overall software structure looks as follows:

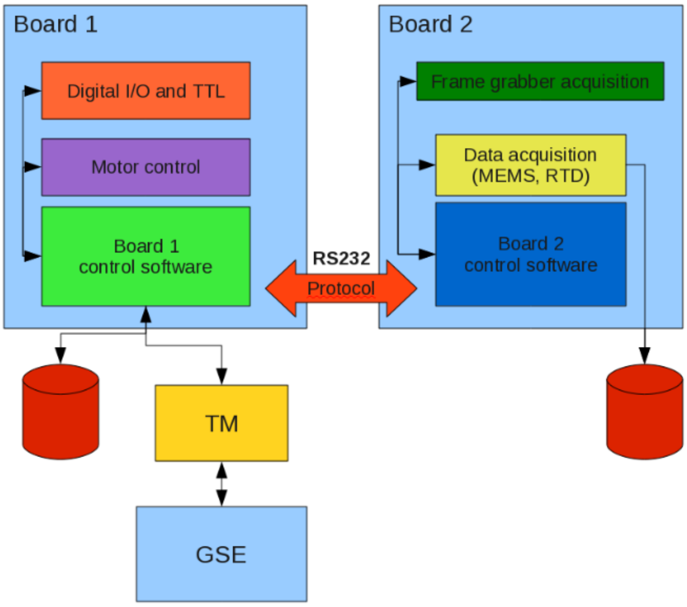

Figure 2.41: SPONGE software architecture.

Software Development Plan

This section resumes what has been decided about SPONGE experiment software.

- Motor Control Helios Board:
    1. Controls the two drivers through serial ports (one for each driver);
    2. Through another serial port communicates with the ground station;
    3. Through the slip-ring communicates with the other Helios;
    4. Controls digital I/O channels for locking device, solid state device and LO-SOE signals.
- Data Acquisition Helios Board:
    1. Controls and acquires the frame grabber;
    2. Controls the sensors acquisition channels;
    3. Through the slip-ring communicates with the other Helios.

Software for the Acquisition Board

The Helios board used on the experiment rotating platform is already supplied with the software for the acquisition of the various sensors. Since this software is embedded, it is sufficient to configure it for the specific sensors used.
A flow chart of the various tasks of this board is presented in Fig.2.42.

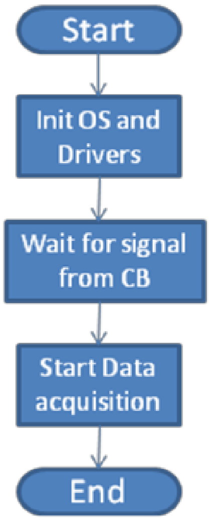

Figure 2.42: Flow chart of the tasks of the board controlling and acquiring the sensors.

This diagram refers to the micro gravity phase, when the experiment is activated. In fact, the sensors which are not specifically quoted in the flow chart in Fig.2.42, are switched on

since the countdown, to verify that the whole system is working correctly.
Moreover, also the two CPUs and the drivers are on during the ascent and since the countdown. The objective is to avoid switching off the whole system at the lift off to switch it on once again when the SOE is transmitted, thus reducing the complexity as much as possible.
During the data acquisition, the AB communicates with the CB through the slip-ring. The latter is responsible for the data transmission to the RS-422 serial port, which allows the down-link.

Software for the Control and Down-link Board

The flow chart presented in Fig.2.43 refers to the various tasks of the CB and to their logic order. First of all, the board waits for the SOE to be given by REXUS Service Module. When this signal is received, it sends a message to the AB via slip-ring connection. The SOE passes through the slip-ring by means of an RS-422 serial port.

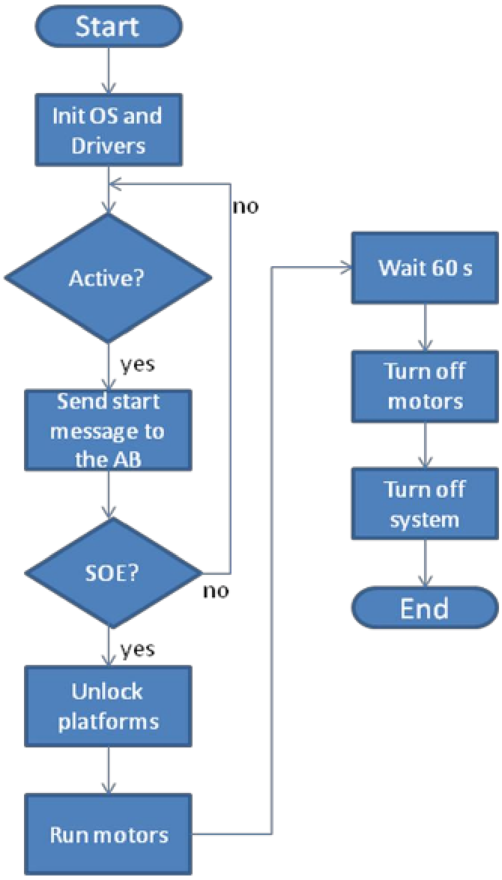

Figure 2.43: Flow chart of the board controlling the motors.

When the tests are finished and the module has been launched, the board unlocks the two platforms and starts the motors, which are controlled by drivers and perform a four-velocity profile. The experiment runs for about 100 s and after this time it is switched off by a timer. At that time, the sensors and the other board for acquisition are switched off as well.

Software for the Ground Station

The software used for the ground station data acquisition is a custom developed C software with a user interface. The data acquired is composed of the three acceleration components, the absolute velocity measured by the gyro and the RTD output. These data are then saved in a file for the following analyses.

REXUS rocket gives an RS232 serial cable. An RS232-USB interface (NI USB-232 1-Port RS232 Interface for USB) is plugged to a laptop with the ground station software for data acquisition. During the experiment, the data received is saved and a check is performed with checksum, in post-processing.

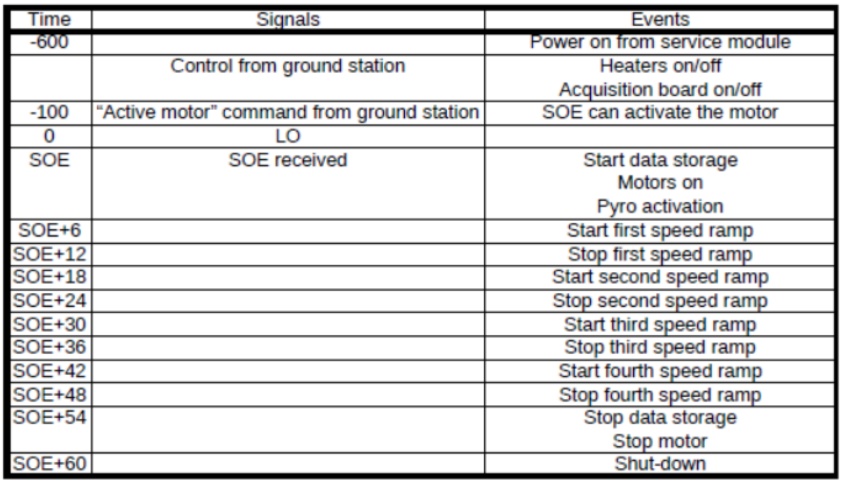

Time	Signals	Events
-600		Power on from service module
	Control from ground station	Heaters on/off Acquisition board on/off
-100	"Active motor" command from ground station	SOE can activate the motor
0	LO	
SOE	SOE received	Start data storage Motors on Pyro activation
SOE+6		Start first speed ramp
SOE+12		Stop first speed ramp
SOE+18		Start second speed ramp
SOE+24		Stop second speed ramp
SOE+30		Start third speed ramp
SOE+36		Stop third speed ramp
SOE+42		Start fourth speed ramp
SOE+48		Stop fourth speed ramp
SOE+54		Stop data storage Stop motor
SOE+60		Shut-down

SOE=120s

Figure 2.44: SPONGE commands and related time line.

2.1.4 SPONGE Testing

Tab.2.2 resumes the tests performed for the SPONGE experiment assessment.

Various types of tests have been done: vacuum tests for the single components and the whole system, vibration tests of SPONGE structure, vision system verification, sensors tests. The electronic system has been tested as well, together with the software developed for the Helios boards and for the ground station.

The last tests on the experiment module have been conducted in Kiruna, during the launch campaign, after having the rocket assembled. They were meant to verify the power and elec-

Test	**Description**
Test 1 type	Thermal vacuum
Test facility	CISAS lab
Test item	whole experiment
Test level/procedure	system level
Test duration	3 times flight duration
Test result	positive
Test 2 type	Vision system validation
Test facility	CISAS lab
Test item	PMD tank, leds, cameras
Test level/procedure	verify no light reflection
Test duration	as necessary
Test result	positive
Test 3 type	Sinusoidal sweep vibration
Test facility	TAS-I facility
Test item	whole experiment
Test level/procedure	verify resonance
Test duration	20 s/axis
Test result	positive
Test 4 type	Random vibration
Test facility	TAS-I facility
Test item	whole experiment
Test level/procedure	6.0 g_{RMS}
Test duration	20 s/axis
Test result	positive
Test 5 type	Electronics test
Test facility	CISAS lab
Test item	electronic boards and related components
Test level/procedure	current and voltage control
Test duration	as necessary
Test result	positive
Test 6 type	Vacuum test single components
Test facility	CISAS lab
Test item	electronic boards
Test level/procedure	RTD to verify the temperatures reached
Test duration	1 minute
Test result	positive

Table 2.1: Tests performed on SPONGE.

Test	**Description**
Test 7 type	Locking device release
Test facility	CISAS lab
Test item	locking device
Test level/procedure	device functionality assessment
Test duration	as required to complete procedure
Test result	positive
Test 8 type	Locking device functionality
Test facility	CISAS lab
Test item	locking device
Test level/procedure	device release-rotational tests
Test duration	as for test #7
Test result	positive
Test 9 type	Momentum transfer
Test facility	CISAS lab
Test item	rotating/counter-rotating arm verification
Test level/procedure	described in a dedicated section
Test duration	time necessary to observe the behavior
Test result	positive
Test 10 type	Slip-ring electrical connections
Test facility	CISAS lab
Test item	slip-ring
Test level/procedure	slip-ring tested with loads accommodated
Test duration	at least as the micro gravity phase
Test result	positive
Test 11 type	Protocol and data transmission
Test facility	CISAS lab
Test item	AB-CB communication and CB-ground station
Test level/procedure	Activate sensors, transmit and control data
Test duration	as required by procedure
Test result	positive
Test 12 type	Linux kernel implementation and installation of firmware+drivers
Test facility	CISAS lab
Test item	Operative System (OS) verification and possibility to activate frame-grabber
Test level/procedure	Activate the processor and hardware
Test duration	as required by procedure
Test result	positive

Table 2.2: Tests performed on SPONGE (II).

tronic connections between REXUS service module and the various experiments mounted on board.
They were also performed to verify the correct reception of the activation signals by the experiments.

With the software development procedure adopted, the two related complete tests (#11 and #12) can be easily and independently subdivided into a series of sub-tests, in order to monitor the progress of the single sub-tasks. This way, it is easier to find eventual failures and to fix them.

2.1.4.1 Mock-Ups Built for SPONGE Tests

This section illustrates the two mock-ups created to prove that:

1. The disturbance caused by the rotating experiment is lower than the maximum value allowed, corresponding to 1/6 of the residual rotational velocity after de-spin;
2. The tank does not leak because the sealing method adopted is properly conceived.

These preliminary tests have been required by ESA before starting to manufacture the flight experiment module, to investigate two possible causes of failure for SPONGE and prove that no critical condition exists in terms of leaking nor angular momentum transfer.

The methodology followed for the experiment manufacturing is the same normally used for a proto-flight model. In fact, at the beginning it had been planned to build two SPONGE models: the qualification model and the flight one; but unfortunately this has been impossible due to some budget restrictions. Consequently, it has been decided to build only a proto-flight model and some other mock-ups allowing the necessary preliminary verifications.
The protoflight has been tested to vibrations at TÜV Italia and to vacuum conditions. It has been used for the software tests as well.

Tank Mock-Up

The main objective of the tests conducted on the tank mock-up is to assess the container resistance to the pressure level to which it shall be subjected during the flight.

Moreover, liquid PDMS has been inserted into it, in order to verify the absence of leaking, and therefore the O-ring performance in terms of sealing.

The first test performed with the tank consists in rotating it and waiting to see if leaking problems arise. This is to assure the functionality of the O-rings in various positions that can be assumed by the experiment during launch operations and flight. The tank is then pressurized, to see if it resists the loads without any problems and also to ensure the absence of leaking problems in this condition.

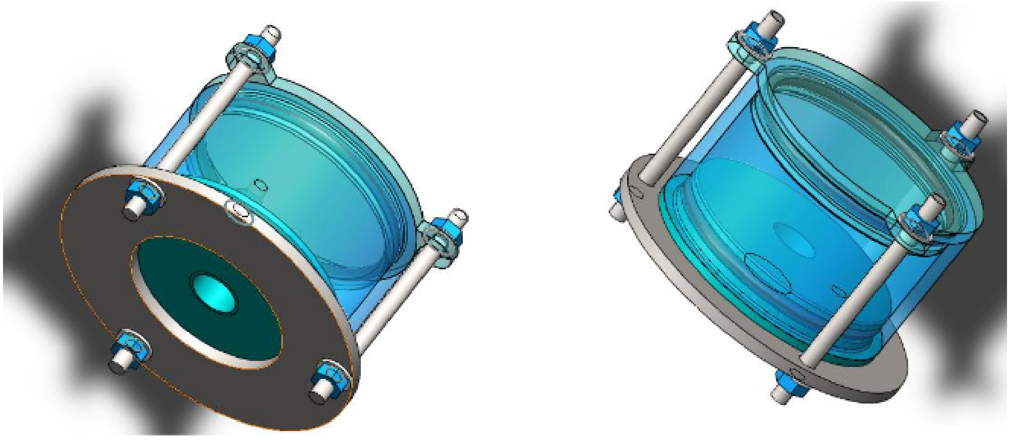

Figure 2.45: SPONGE reservoir mock-up.

SPONGE Rotating Plates Mock-Up

The objectives of the tests conducted on the SPONGE rotating and counter-rotating plates are to verify:

1. The momentum transmission due to the experiment and the bearings;
2. The correct implementation of the control software;
3. The communication of the data from one platform to the other by means of the slip-ring;
4. The appropriate collocation of the accelerometers;
5. The functionality of all the electronics mounted;
6. The solution for the locking system, which foresees the use of a wire cutter.

Fig.2.48 shows the mock-up designed for the tests.

The momentum transmission from the experiment to the structure needs to be verified. Two platforms represent those in the real experiment, whereas the third represents REXUS sounding rocket.

The two experiment plates are smaller than the real ones, but they have the same inertia. To have lower costs, the material used for this mock-up is different from the Al7075 used for the flying experiment.

After the first tests verifying a lower disturbance with respect to the maximum value allowed of $5\,°/s$ (see section 2.1.3.2 for the disturbance estimation), the same mock-up has been used to test the communications between the other electronic devices.

This way, the behavior of the plate with the devices in their final positions has been assessed as well. Moreover, the communication between the electronic devices on different platforms has been controlled and tested and the cables locations optimized.

Another aim of these tests has been to check the functionality of the locking device. In this

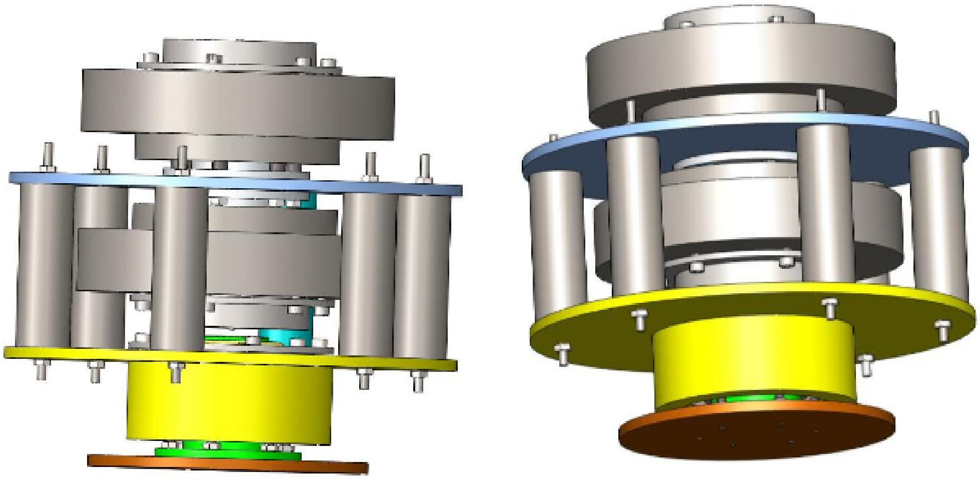

Figure 2.46: Plates mock-up.

case, the pyro has been substituted with a resistor, which is meant to cut the nylon wire. After the preliminary tests and the requirements verification, the real pyro locking device has been tested.

2.1.4.2 Test of the Optics and Cameras

The main aim of these tests is to verify the correct focus of the cameras, considering the operative working distance. The quality of the image acquired through mirror reflection has to be assessed and also led light has to be verified.

Another aspect to be verified with the optical functional tests is the quality of the image in terms of eventual reflections or deformations due to the tank shape. By means of these tests, the correct choice of the camera lenses is verified as well.

The adapter for camera lenses needs to be installed and it has to focus on an object of the same dimensions of the sponge and from the same distance, as within the experiment module. Then, the mirror has to be used in the same relative position with respect to the cameras, as in the real experiment, to verify the quality of the image acquired.

2.1.4.3 Test of the Platform for the Temperature Ranges Assessment

The temperatures reached by the electronic components during the pre-launch phase and the eventual temperature differences between the different components need a verification.

These experimental tests are extremely important to measure the time required to heat up the cameras with the available power. An experiment sample has been put in a freezer and the temperature has been monitored with some RTDs.

The camera connected to the frame grabber has been introduced into the fridge at −24.5 °C as well, in order to verify and simulate a worst cold case as expected in Kiruna. The objective was to verify that the time required to heat up the cameras was comparable to the value estimated through the FE analysis.

The camera has been tested with heaters on, and it heated up in approximately 1 minute, which is the 10% of the time predicted by the simulations. This means that the power consumption is even less than previously estimated, which is another positive result.

2.1.4.4 Power Supply - Slip-Ring Test

The power supply system has been verified connecting the slip-ring to the power supply boards, which were in turn connected to the Helios board. Finally, the frame grabber has been connected to the Helios as well, through an appropriate USB port. Everything worked properly.

2.1.4.5 Vibration Tests

SPONGE vibration tests have been performed in Scarmagno in November 2011 on the protoflight model, at TÜV Italia.
The experiment has been tested to assess that its first natural frequency was sufficiently higher than the launcher frequency. In order to do this, it has been vibrated along the three axes, following a specific procedure and at defined acceleration levels.

The requirements for vibration tests are:

- Verify that the first natural frequency of the system is higher than the launcher frequency applying a sinusoidal sweep;
- Assess the system resistance to 6 grms randomly applied.

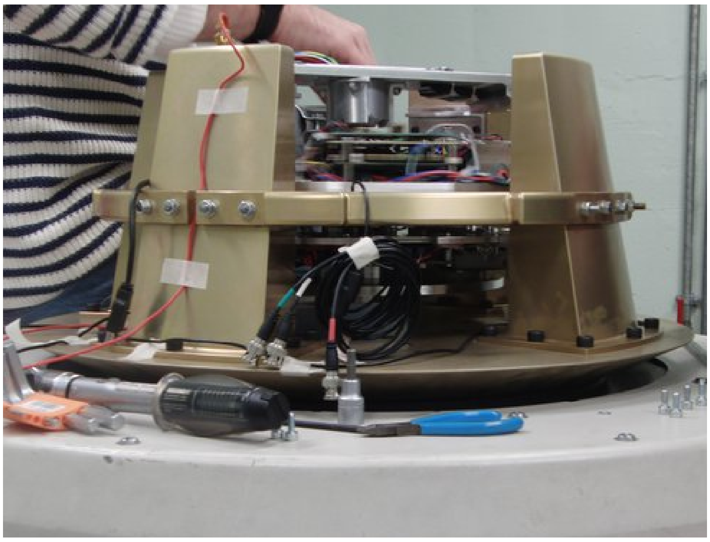

Figure 2.47: Vibration tests at TÜV Italia in 2010.

The random acceleration levels applied to the protoflight model have been:

1. The so-called *low low* level, where 1.49 grms have been applied;
2. The *notched low level*, where 1.98 grms have been applied to the structure;
3. The *first intermediate level*, applying an acceleration of 2.8 grms;
4. The *second intermediate level*, applying an acceleration of 3.97 grms;
5. The *full level*, applying an acceleration of 5.6 grms;

For the low, intermediate and full levels, a notched profile has been created to avoid structural damages due to a coupling with the fixture natural frequencies.
The evaluation of the correct profiles to be imposed to avoid any possible fracture risk, has been done by the mechanical vibrations experts of the company funding these tests.

Before starting the experiment random vibration along a specific axis, a sinusoidal sweep has been performed to determine the natural frequencies of the structure. Then, the random acceleration levels listed have been applied and at the end, another verification of the structure frequency was performed, to assess model integrity.
The same procedure has been applied for each of the axes identified.

The results of the tests showed that SPONGE can survive the flight vibrational environment without being damaged. After having concluded the vibration test along each of the axes, a complete functional test was performed to ensure that the electronics and mechanics were still working properly.
No problems were found and all the experiment functionalities were preserved.

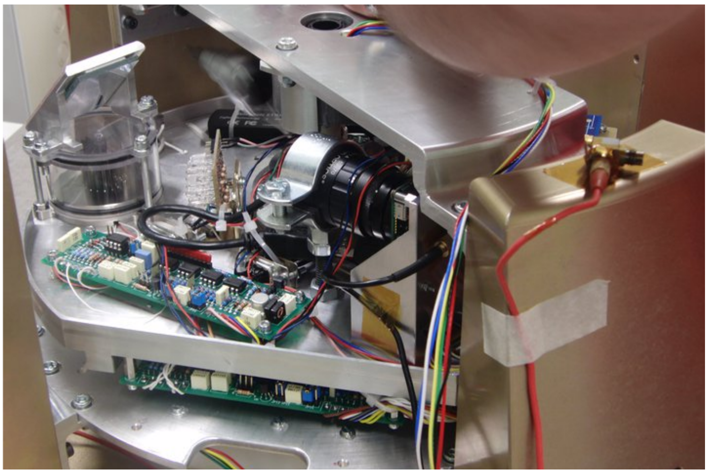

Figure 2.48: Vibration tests at TÜV Italia in 2010 (II).

2.1.5 SPONGE Camera Calibration

In this section, the camera used and mounted on board SPONGE is described and its calibration is discussed. A dedicated software has been applied for calibration, to determine the intrinsic and extrinsic parameters. A SPONGE section is shown in Fig.2.49. The camera represented is just one of the two that have been used for liquid analysis during REXUS9 flight.

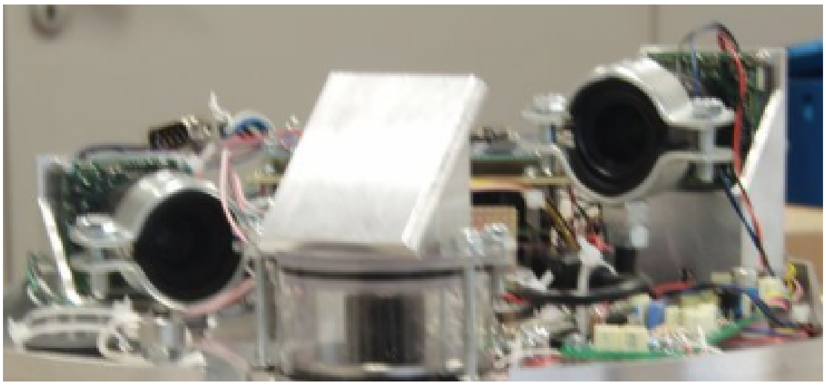

Figure 2.49: Cameras constituting SPONGE vision system.

Perspective Geometry and Projection Space

A 2D image point is denoted by $m = [x; y]^T$. A 3D point is identified by $M = [X^C; Y^C; Z^C]^T$ in the camera reference frame. The pinhole camera model is often used for 3D reconstruction. Each camera captures a 2D image of the 3D world. This conversion from 3D to 2D is referred to as a *perspective projection* and is described by the pinhole camera model. It is common to model this projection operation by rays emanating from the camera and passing through its focal point; each ray corresponds to a single point in the image.

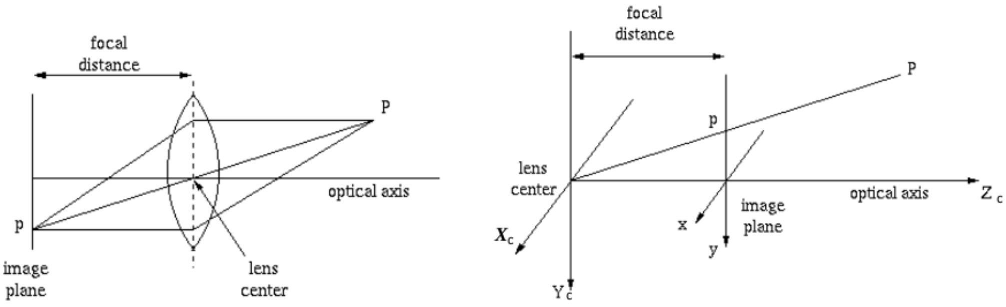

Figure 2.50: Pinhole camera model; on the left, the image plane is after the optical center (lenses center); on the right it is before the optical center.

Perspective geometry gives the following relations, where the signs depend on the image plane position with respect to the optical center:

$$x = \pm f \frac{X^C}{Z^C} \tag{2.1.18}$$

$$y = \pm f \frac{Y^C}{Z^C} \tag{2.1.19}$$

f is the focal length.

These equations can be linearized using projective spaces.

$$\forall x \in R^n \Rightarrow \begin{bmatrix} x \\ 1 \end{bmatrix} \in P^n \tag{2.1.20}$$

$$\forall \begin{bmatrix} x \\ \gamma \end{bmatrix} \in P^n, \gamma \neq 0 \Rightarrow \frac{x}{\gamma} \in R^n \tag{2.1.21}$$

Two points of the projective space P^n are equivalent if they differ less than a specific scale factor; coordinates are called homogeneous.

$$\begin{bmatrix} x \\ y \\ z \end{bmatrix} \in P^2, \Longleftrightarrow \begin{bmatrix} x \\ y \\ z \end{bmatrix} \in R^3 \tag{2.1.22}$$

$$\gamma \begin{bmatrix} x \\ y \\ z \end{bmatrix} \approx \begin{bmatrix} x/z \\ y/z \\ 1 \end{bmatrix} \in P^2 \tag{2.1.23}$$

$\sim$ denotes the augmented vector by adding 1 as the last element: $\tilde{m} = [x; y; 1]^T$ and $[X^C; Y^C; Z^C; 1]^T$. The relationship between a 3D point M and its image projection m is given by:

$$\gamma \tilde{m} = [P]^C \tilde{M} \tag{2.1.24}$$

where γ is an arbitrary scale factor and [P] is the projection matrix.

$$P = \begin{bmatrix} f & 0 & 0 & 0 \\ 0 & f & 0 & 0 \\ 0 & 0 & 1 & 0 \\ 0 & 0 & 0 & 1 \end{bmatrix} \approx \begin{bmatrix} x/z \\ y/z \\ 1 \end{bmatrix} \in P^2 \tag{2.1.25}$$

It is possible to apply a rotation and a translation relating the world to the camera coordinate system, using the extrinsic parameters resulting from calibration. The roto-translation matrix multiplies $\tilde{M}^w$ in the world frame to obtain $\tilde{M}^C$ in the camera frame.

2.1.5.1 Description of the Calibration Parameters

Camera parameters can be divided into two categories: intrinsic and extrinsic.

The extrinsic parameters consist in the spatial relative position between the object frame i and the camera reference frame C. This is described by a rotation matrix $[R]_i^C$ and a translation vector T_i^C. Fig.2.51 shows the reference frame $(O, X, Y, Z)^i$. It also shows the i^{th}

calibration grid (attached to the i^{th} image), and the camera reference frame attached to that grid.

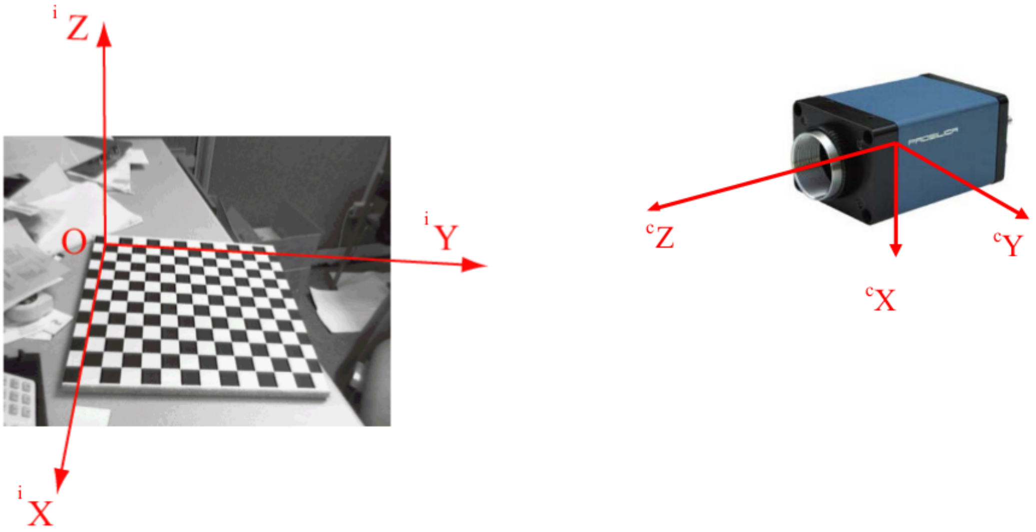

Figure 2.51: Reference frame $(O, X, Y, Z)^i$ attached to the calibration grid and camera reference frame $(X^C; Y^C; Z^C)$ with the origin in the camera optical center and Z^C along its optical axis.

Assuming P is a point space of coordinates $XX^i = [X^i; Y^i; Z^i]$ in the grid reference frame (Fig.2.51) and $XX^C = [X^C; Y^C; Z^C]$ are the coordinates of P in the camera reference frame, XX^i and XX^C are related to each other through the following rigid motion equation:

$$XX^C = [R]_i^C XX^i + T_i^C \tag{2.1.26}$$

In particular, the translation vector consists of the coordinates of the grid pattern origin (O^i) in the camera reference frame, and the third column of the matrix $[R]_i^C$ is the surface normal vector to the grid plane in the camera reference frame. Once a point is expressed in the camera reference frame, it can be projected on the image plane using the intrinsic camera parameters. The 3x1 vectors om^i are the rotation vectors associated to the rotation matrices $[R]_i^C$.

$$\Theta = \sqrt{om(1)^2 + om(2)^2 + om(3)^2} \tag{2.1.27}$$

with: $\alpha = cos(\theta)$, $\beta = sin(\theta)$, $\gamma = 1 - cos(\theta)$.

$$\Omega = \frac{om}{\theta} \tag{2.1.28}$$

$$[\Omega_v] = \begin{bmatrix} 0 & -\Omega(3) & \Omega(2) \\ \Omega(3) & 0 & -\Omega(1) \\ -\Omega(2) & \Omega(1) & 0 \end{bmatrix} \tag{2.1.29}$$

$$[R] = \alpha \begin{bmatrix} 1 & 0 & 0 \\ 0 & 1 & 0 \\ 0 & 0 & 1 \end{bmatrix} + \beta[\Omega_v] + \gamma(\Omega\Omega^T) \tag{2.1.30}$$

A roto-translation matrix can be used as well to operate the coordinates transformation.

$$\begin{bmatrix} XX^C \\ 1 \end{bmatrix} = \begin{bmatrix} [R]_i^C & T_i^C \\ 0 & 1 \end{bmatrix} \begin{bmatrix} XX^i \\ 1 \end{bmatrix} \tag{2.1.31}$$

Intrinsic Parameters

A list of the intrinsic parameters is presented hereafter.

- Focal length f: The focal length in pixels is the distance between the camera optical center and the image plane. The focal length of a lens determines the magnification of distant objects, it is equal to the distance between the image plane and a pinhole. The focal length of an optical system is a measure of how strongly it converges (focuses) or diverges (diffuses) light. A system with a shorter focal length has a greater optical power compared to one with a long focal length.
  The image plane is not usually perfectly orthogonal to the optical axis, so that the focal length effects are different in the x and y direction. The pixels as well could be not perfectly square, and might have a rectangular shape. $f_c(1)$ and $f_c(2)$ are the effective focal lengths in the x and y direction respectively, in pixels.

  $$f_c(1) = fk_x \tag{2.1.32}$$

  $$f_c(2) = fk_y \tag{2.1.33}$$

  k_x and k_y are two coefficients related to pixels dimensions:

  $$k_x = \frac{1}{width_p}[pixel/mm] \tag{2.1.34}$$

  $$k_y = \frac{1}{height_p}[pixel/mm] \tag{2.1.35}$$

- Principal point cc: The principal point coordinates are stored in the 2x1 vector cc, they represent the intersection coordinates of the image plane with the optical axis. Most times they do not coincide with the image center.

- Skew coefficient α_c: It defines the angle between the x and y pixel axes. If the pixels are perfectly square, the skew angle is 90 ° and the skew coefficient is 0.

  $$Skew = 90\,^\circ - atan(\alpha_c)\frac{180\,^\circ}{\pi} \tag{2.1.36}$$

- Distortions: The image distortion coefficients (radial and tangential) are stored in the 5x1 vector k_c.

Definition of the Camera Model

Consider P as a point of coordinate vector $XX^C = [X^C; Y^C; Z^C]$ in the camera reference frame. It can be projected on the image plane according to the intrinsic parameters (f_c, cc, α_c, k_c).
Let x_n be the normalized (pinhole) image projection:

$$x_n = \begin{bmatrix} X_C/Z_C \\ Y_C/Z_C \end{bmatrix} = \begin{bmatrix} x \\ y \end{bmatrix} \tag{2.1.37}$$

Let $r = x^2 + y^2$. After including lens distortion, the new normalized point coordinate x_d is defined as follows:

$$x_d = \begin{bmatrix} x_d(1) \\ x_d(2) \end{bmatrix} = (1 + k_c(1)r^2 + k_c(2)r^4 + k_c(5)r^6)x_n + dx \tag{2.1.38}$$

where dx is the tangential distortion vector:

$$dx = \begin{bmatrix} 2k_c(3)xy + k_c(4)(r^2 + 2x^2) \\ k_c(3)(r + 2y^2) + 2k_c(4)xy \end{bmatrix} \tag{2.1.39}$$

The 5-component vector k_c contains both radial and tangential distortion coefficients (the coefficient of the sixth order radial distortion term is the fifth entry of the vector k_c and can often be neglected).
Tangential distortion is due to imperfect centering of the lens components and other manufacturing defects.

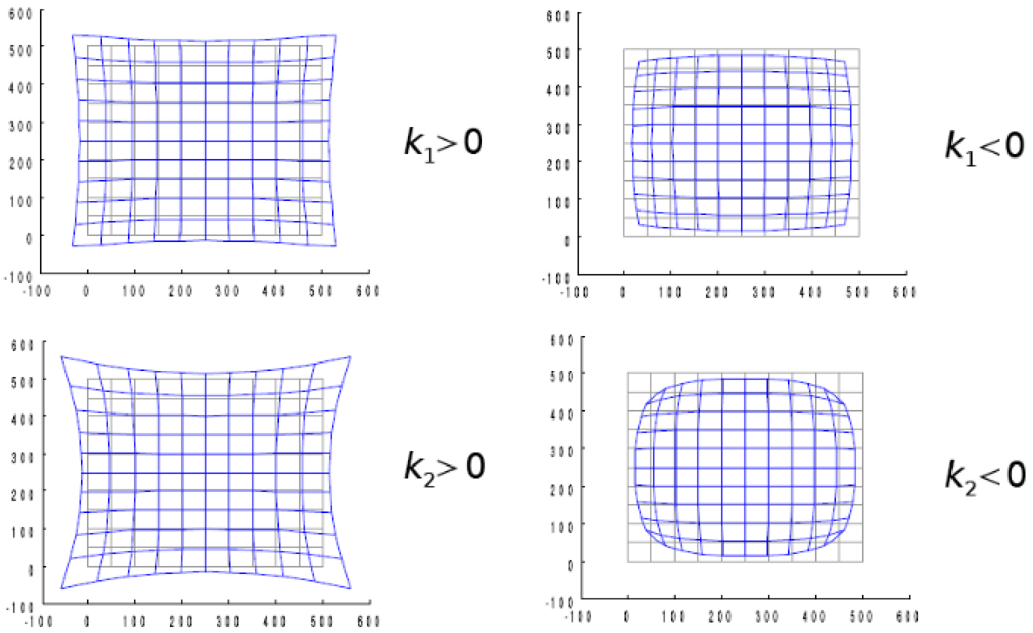

Figure 2.52: Radial distortion coefficients.

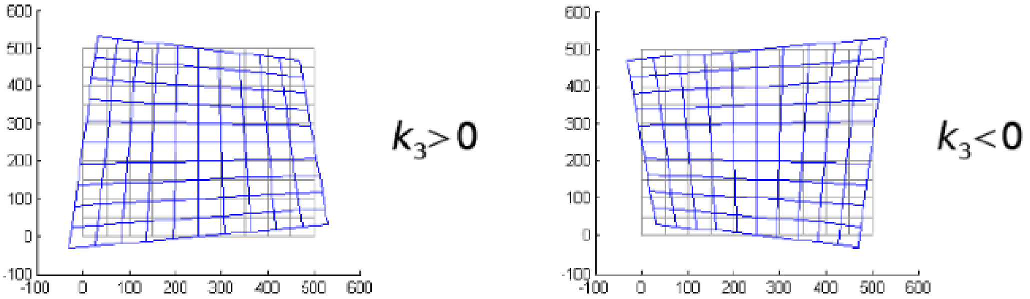

Figure 2.53: Tangential distortion.

Currently manufactured cameras do not always justify this very general optical model. For example, it is now customary to assume rectangular pixels, and thus zero skew ($\alpha_c = 0$). Furthermore, the very generic (6th order radial plus tangential) distortion model is often not considered. The tangential distortion component can often be discarded, because most of the lenses currently manufactured do not have centering imperfections.

Once distortion is applied, the final pixel coordinates $x_{pixel} = [x_p; y_p]$ of the P projection on the image plane are:

$$\begin{cases} x_p = f_c(1)[x_d(1) + \alpha_c x_d(2)] + cc(1) \\ y_p = f_c(2)x_d(2) + cc(2) \end{cases}$$

With matrices:

$$\begin{bmatrix} x_p \\ y_p \\ z_p \end{bmatrix} = \begin{bmatrix} f_c(1) & f_c(1)\alpha_c & cc(1) \\ 0 & f_c(2) & cc(2) \\ 0 & 0 & 1 \end{bmatrix} \begin{bmatrix} x_d(1) \\ x_d(2) \\ 1 \end{bmatrix} \tag{2.1.40}$$

$f_c(1)$ and $f_c(2)$ represent the focal distance in terms of horizontal and vertical pixels. The components of f_c vector are usually very similar. The ratio $f_c(2)/f_c(1)$, called *aspect ratio*, is different from 1 if the pixels in the Charge-Coupled Device (CCD) array are not square. Therefore, the camera model handles non-square pixels. In addition, the coefficient α_c encodes the angle between the x and y sensor axes. Consequently, pixels are even allowed to be non-rectangular.
In addition to computing estimates for the intrinsic parameters f_c, cc, k_c and α_c, the software returns estimates of the uncertainties of those parameters (approximately three times the standard deviations of the estimation errors).

Pixel coordinates are defined such that (0;0) is the center of the upper left pixel of the image, (n_x-1;0) is the center of the upper right corner pixel, (0;n_y-1) is the center of the lower left corner pixel and (n_x-1;n_y-1) is the center of the lower right corner pixel, where n_x and n_y are the width and height of the image.
With all the intrinsic parameters, a specific function computes the direct pixel projection map. It uses as inputs the 3D coordinates of a set of points (in world or camera reference

frame) and the intrinsic camera parameters (f_c, cc, k_c,α_c), and returns the pixel projections of the points on the image plane.

2.1.5.2 Calibration Procedure Followed for SPONGE

To avoid any possible errors and for uncertainty evaluation, it is important to follow a precise procedure when calibrating the system.
The work started with a first calibration on ground, before the flight and continued with another post-flight calibration of the cameras. In fact, during the launch phase, different kinds of vibrations can affect or change the initial optical center position. Depending on the accuracy required, when cameras are subjected to strong vibrations, it might be necessary to re-calibrate the system more frequently. In this experiment, a frequent recalibration has not been possible, due to the lack of an appropriate system performing this task.
It has only been possible to calibrate cameras before launch and after system recovery. During these analyses of the system, no permanent optical center displacement has been observed, but nothing can be said about what happened during the flight.
This means that with the only data collected, it is impossible to verify if some displacements occurred at any time during the flight and of which entity. However, modifications occurring during the ascent phase and completely recovered during the descent are considered unlikely to be happened.

The following list resumes the main points of the calibration procedure before launch and after system recovery. In both cases a chessboard has been used as the calibration pattern. It was printed using a standard HP printer and the dimensions were: 2.5 mm x 2.56 mm.

1. Print the calibration chessboard pattern (black and white squares). The minimum number of squares for each side is 3-4, the maximum number depends on the camera resolution. The printed paper must be as precise as possible; the precision level depends on the kind of paper leaf and on the printer type. The calibration pattern size should be slightly bigger than the object which we want to get information about (150% of the peculiar dimension), so as to occupy most of the camera field of view.

2. Paste the pattern on a tile rigid and flat enough. The paper should be pasted homogeneously, to avoid any bubbles or glue lumps.

3. The exact knowledge of the squares dimensions is extremely important for the calibration process. Printers are not perfect and the paper pasting could deform the pattern. For this reason, it is necessary to know the squares dimensions with the highest possible accuracy. It is recommended to measure the total length of the chessboard along x and y directions at least in three different locations.

$$L_{x,average} = \frac{\sum \frac{L_{tot,x}}{n_x}}{N} \tag{2.1.41}$$

$$L_{y,average} = \frac{\sum \frac{L_{tot,y}}{n_y}}{N} \tag{2.1.42}$$

where N is the number of positions, n_x and n_y are the numbers of squares along x and y direction.

4. Put the calibration chessboard in front of the SPONGE camera, in whatever position outside the tank. Turn on the camera and control that all the calibration corners are captured. If something is out of sight, the tile position or orientation has to be changed. The distance from the camera should be comparable with the distance of the object in the previous check.

5. Repeat the previous point, but placing the chessboard inside the tank, to collect images from which to extract the deformations induced by the tank.

6. Repeat the last two points changing the pattern orientation and position until 20 to 30 images are stored. Three pictures are sufficient for a calibration, but a greater number reduces errors and uncertainty.

The other steps connected to the calibration procedure concern the software, both in terms of numerical elaboration and image analysis.
A specific procedure will be described in a dedicated section, concerning the determinations of the optical deformations induced by the reservoir curved surface.

2.1.5.3 Uncertainty Analysis

The uncertainty of a measurement is stated by giving a range of values which are likely to enclose the true value. The acceptable uncertainty level depends on the measurement purpose. Since the parameters estimated by calibration completely characterize a vision system, it is important to obtain the values affected by errors to maintain the measurements within the imposed limits. For this reason, in addition to the choice of the calibration algorithms, the accuracy of the pattern features is important as well.

For the SPONGE experiment, the aim of the measurement is to prove that an appropriately designed vision system can be used to retrieve information about the liquid level and surfaces during operation.
To evaluate the global uncertainty is not easy, and it is necessary to start searching the uncertainty sources during the measurement procedure. There could be systematic errors or errors due to the repeatability and reproducibility of the measurement method.

The uncertainty sources found are listed below.
Vision system model errors:

- The mathematical distortion model is fourth order accurate and considers only radial and tangential distortion.

- Pixels shape and dimensions are slightly different compared to each other.
- Camera model is based on the pinhole camera theory, without any light refraction.
- Image plane (CCD surface) is supposed to be ideally flat.
- Digital images have intrinsic resolution errors.
- Surface is particularly rough or unclean.
- Errors in the calibration procedure.
- The tile on which the calibration pattern is pasted is not perfectly flat. Paper pasting could worse this ideal condition as well.
- The printer cannot produce a perfect chessboard.
- Mathematical optimization gets values inside a tolerance range.

Other error sources:

- Temperature could influence the camera, even if it has been tested in all the operative temperature range and it proved to work as expected.
- In some object views, reflective or transparent surfaces could affect the images depending on the light source.
- Correlation coefficients have been neglected during the uncertainty analysis.
- Vibration of the workbench or camera due to clicking during the on-ground calibration.
- Strong vibrations temporarily causing a displacement of the optical center location, in a way which has been impossible to quantify. Between two successive frames of the liquid profile during the launch phase, it is possible that the optical center had changed its location.

Some of these errors can be neglected because they are orders of magnitude smaller than others. These uncertainty sources have been analyzed with the assumption of *non-correlation* and they have been used to estimate the uncertainties, starting from an hypothetical probability distribution.

Camera Calibration Uncertainty

Camera calibration gives as a result, the intrinsic and extrinsic parameters of the system, which are affected by uncertainty. The errors on the intrinsic parameters become systematic for the 3D points extractions. In fact, each image point is managed using the same intrinsic parameters.
After having the calibration done, camera parameters are known, and it is possible to calculate the projection of the calibration points on the calibration image.

$$[E_{ij}]_{point} = ||m_{ij} - \hat{m}([KK], k_c, [R]_i^C, T_i^C, M_j)|| \tag{2.1.43}$$

i^{th} image=1,.,.,...n and j^{th} point=1,.,.,...N

where m is the reprojected point on the image plane and $\hat{m}$ is the effective reprojected point, as a function of the calibration parameters, the initial 3D point M and the rotation matrix and translation vector between the camera and world reference frames.

Matrix $[E]_{point}$ has dimensions 2xNn, where N is the number of points of the calibration pattern used and n is the number of calibration images. The first row contains all the errors along the x coordinate, whereas the second row contains the errors along the y coordinate. These errors are due to most of the uncertainty sources listed above, so that it is reasonable to suppose that the total error on the reprojected points is random.
Assuming a Gaussian error distribution, the corresponding standard deviation σ_p is calculated on all the $[E]_{point}$ matrix elements, and it represents the maximum distance between the reprojected point and the real image point, with a confidence level of 68%. With this assumption, σ_p can be assumed as the common error for all the calibration corners.

Each point in an image is a function of a homogeneous 3D point and of all the calibration parameters:

$$\hat{m_{ij}} = f(f_c, cc, \alpha_c, k_c, [R]_i^C, T_i^C, M_j) \tag{2.1.44}$$

All the derivatives calculated with respect to the various input parameters can be expressed analytically. From the analytical formulation point of view, it is possible to evaluate the numerical values of the derivatives corresponding to each of the points analyzed; the total number of points is Nn.
The calculation should be executed for all the points of a single image.

$$[Int]_i = \begin{bmatrix} \frac{\partial m}{\partial f_c} \\ \frac{\partial m}{\partial cc} \\ \frac{\partial m}{\partial \alpha_c} \\ \frac{\partial m}{\partial k_c} \end{bmatrix} \tag{2.1.45}$$

where dimensions are: 10xN.

$$[Ext]_i = \begin{bmatrix} \frac{\partial m}{\partial om} \\ \frac{\partial m}{\partial T} \end{bmatrix} \tag{2.1.46}$$

where dimensions are: 6xN and om is the rotation vector associated to the rotation matrix.

The two matrices are calculated for each calibration image, then they can be grouped altogether as follows:

$$[J_{param}] = \begin{bmatrix} [Int]_1 & [Ext]_1 & 0 & 0 & ... & 0 \\ ... & 0 & ... & 0 & ... & ... \\ [Int]_i & ... & 0 & [Ext]_i & 0 & ... \\ ... & ... & ... & 0 & ... & 0 \\ [Int]_n & 0 & 0 & ... & 0 & [Ext]_n \end{bmatrix} \tag{2.1.47}$$

From the theoretical expression of uncertainty propagation from one set of variables onto another and using the hypothesis of uncorrelation for the intrinsic parameters errors:

$$\begin{aligned} [\sigma^2]_{point} &= [J_{param}][\sigma^2_{param}][J_{param}]^T \\ [\sigma^2]_{param} &= [J_{param}]^{-1}[\sigma^2_{point}]([J_{param}]^T)^{-1} \end{aligned} \tag{2.1.48}$$

which can also be written as:

$$[E]_{param} = \sqrt{diag([JJ]^{-1})}\sigma_p \tag{2.1.49}$$

where: $[JJ_{param}] = [J_{param}]^T[J_{param}]$.

$$[JJ_{param}] = \begin{bmatrix} \sum[Int]_i[Int]_i^T & [Int]_1[Ext]_1^T & [Int]_2[Ext]_2^T & ... & ... & [Int]_n[Ext]_n^T \\ [Ext]_1[Int]^T & [Ext]_1[Ext]_1^T & 0 & 0 & 0 & 0 \\ [Ext]_2[Int]_2^T & 0 & [Ext]_2[Ext]_2^T & 0 & 0 & 0 \\ ... & 0 & 0 & ... & 0 & 0 \\ ... & 0 & 0 & 0 & ... & 0 \\ [Ext]_n[Int]_n^T & 0 & 0 & 0 & 0 & [Ext]_n[Ext]_n^T \end{bmatrix} \tag{2.1.50}$$

The vector $[E]_{param}$ contains all the uncertainties connected with camera calibration parameters; they are the standard deviations of the Gaussian distribution assumed for the different parameters.

$$\begin{aligned} f_{c_{error}} &= \pm[E]_{param}(1:2) \\ cc_{error} &= \pm[E]_{param}(3:4) \\ alpha_{c_{error}} &= \pm[E]_{param}(5) \\ k_{c_{error}} &= \pm[E]_{param}(6:10) \end{aligned} \tag{2.1.51}$$

The remaining vector elements refer to the extrinsic parameters of each single calibration image. The best possible efficiency in the numerical elaboration is reached using matrices in sparse form, because several zeros are present in $[J]_{param}$.

Skew Angle Uncertainty

The relation between the intrinsic parameter $alpha_c$ and the skew angle (between the x and y pixel axes) is:

$$skew = 90^\circ - atan(\alpha_c)\frac{180^\circ}{\pi} \tag{2.1.52}$$

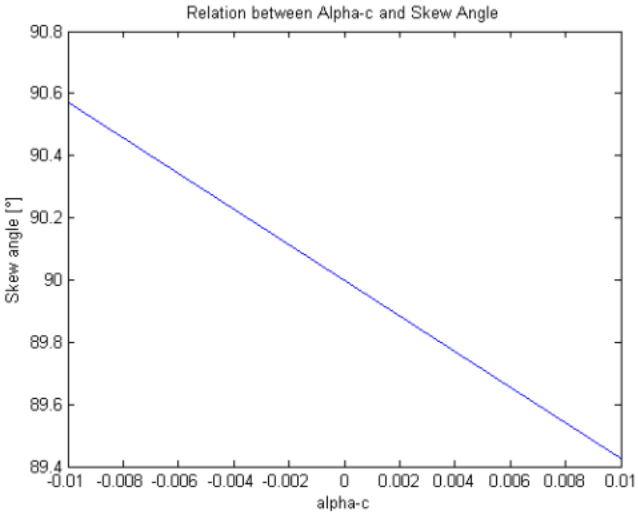

Figure 2.54: Relationship between the intrinsic parameters α_c and the skew angle.

The skew angle value decreases almost linearly with increasing α_c, therefore the easiest way to determine the skew angle uncertainty is to evaluate the angle in correspondence of the error range extremes.

Uncertainty Sensitivity to Computer Simulations

The aim of this section is to evaluate the influence of some input parameters errors on the calibration output errors.

Concerning the sensitivity with respect to model inaccuracy, the 2D model pattern should be printed using a high-quality printer. It is possible to find some inaccuracies in the 2D model pattern if it is printed with a normal printer, or if the pattern is not glued on a flat surface.
Regarding the random noise in the model calibration grid points, an experiment has been conducted on five real images. To simulate model inaccuracy, a Gaussian noise with zero average has been added to the corners of each square in the model.
The standard deviation of the added noise varies from 1% to 15% of the side of each square. For each noise level, 100 tests have been conducted, and average errors (deviations from the results obtained without the Gaussian noise) have been calculated (see Fig.2.55).

Errors increase with the noise added to the model points. The pixel scale factors $f_c(1)$ and $f_c(2)$ remain very stable: the error is lower than 0.02%. Principal point coordinates are quite stable: the errors are about 20 pixels for the noise level corresponding to 15%. The estimated radial distortion coefficient $k_c(1)$ becomes less useful, and the second term $k_c(2)$ is even lower than $k_c(1)$.

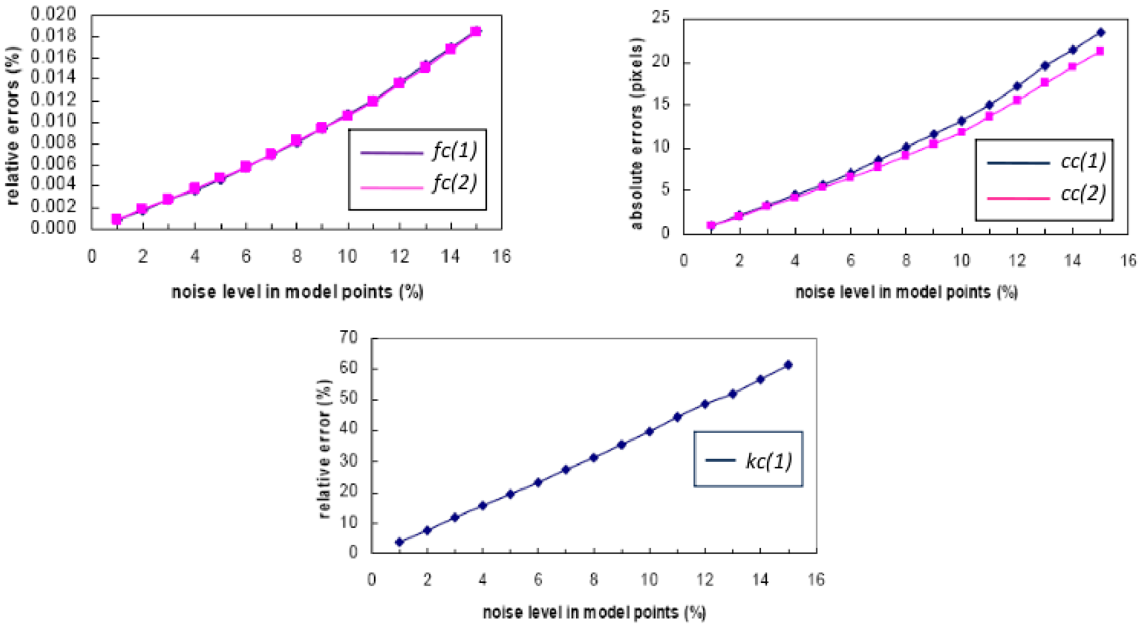

Figure 2.55: Camera calibration sensitivity evaluation, using Gaussian noise added to the model points.

Systematic Non-Planarity of the Model Pattern

The non-planarity can be a problem, for example, when a printed pattern is attached to a soft book cover. The model plane needs to be distorted in two systematic ways, to simulate the non-planarity: using a spherical and a cylindrical geometry.

1. With a spherical distortion, the points located away from the pattern center are displaced along the z axis, according to:

   $$z = p\sqrt{x^2 + y^2} \tag{2.1.53}$$

   where p indicates the non-planarity (the model points are coplanar when p = 0). The displacement is symmetric around the center.

2. With a cylindrical distortion, image points are displaced along the z axis according to:

   $$z = p\sqrt{x^2 + y^2} \tag{2.1.54}$$

   Again, p indicates the non-planarity. This simulates the model pattern tendency to bend around the vertical axis .

Four images of the model pattern have been used: the first is parallel to the image plane; the second is rotated of 30 ° around the horizontal axis, compared to the other; the third is rotated of 30 ° around the vertical axis compared to the first and the fourth is rotated of 30 °

around the diagonal axis with respect to the first. Although model points are not coplanar, they have been treated using this assumption, and the calibration technique is described in the following.

A gaussian noise having a standard deviation of 0.5 pixels was added to the image points and 100 independent trials have been performed. The average calibration errors calculated using these test results, are shown in Fig.2.56 for both cylindrical and spherical non-planarity.

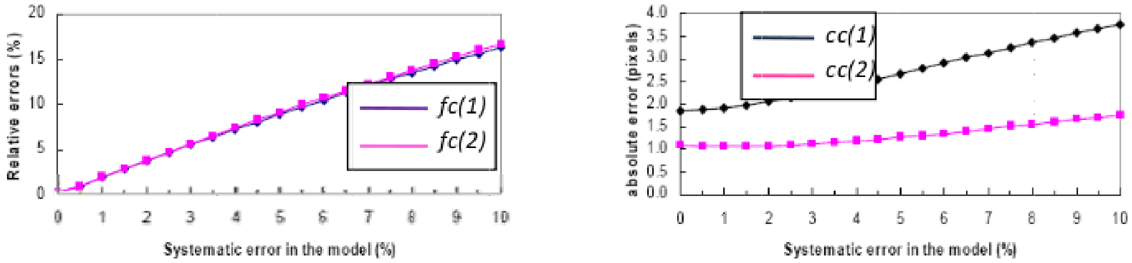

Figure 32 Sensitivity of camera calibration with respect to systematic spherical non-planarity

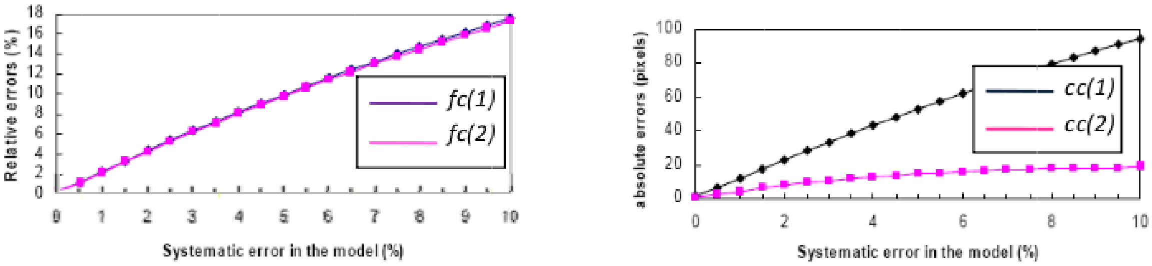

Figure 2.56: Camera calibration sensitivity versus systematic cylindrical non-planarity.

The horizontal axis indicates the non-planarity increase, which is measured as the ratio of the maximum z displacement to the size of the pattern. Therefore, the 10% of non-planarity is equivalent to a maximum displacement of 2.5 cm along z, which does not likely happen in practice.

Several points can be observed:

- The systematic non-planarity of the model has more effect on the calibration accuracy than random errors on positions;
- The aspect ratio $f_c(1)/f_c(2)$ is very stable (0.4% error for 10% non-planarity);
- Systematic cylindrical non-planarity is worse than systematic spherical non-planarity, especially for the principal point coordinates (cc(1); cc(2)). The reason for this is that cylindrical non-planarity is only symmetric with respect to one axis. That is also the reason why cc(1) error is much larger than cc(2) error.

2.1.5.4 SPONGE Calibration Conclusions and Tank Deformations

The recommended calibration procedure is resumed as follows for the chessboard pictures taken from inside the tank, as well as from the outside:

1. Print a pattern and attach it to a planar surface;
2. Take a few images of the model plane under different orientations by moving either the plane or the camera;
3. Detect the feature points in the images;
4. Estimate all the intrinsic and extrinsic parameters using the closed-form solution;
5. Estimate the coefficients of the radial distortion by solving the linear least-squares;
6. Refine all parameters by minimization.

Dimensions of the Squares of the Calibration Pattern

The calibration chessboard dimensions have to be known to perform a metric calibration. The dimensions measured with a decimeter are:

Position	**X length [mm]**	**Uncertainty [mm]**
Top	25.56	±0.56
Middle	25.56	±0.56
Bottom	25.56	±0.56

Table 2.3: X dimension of the calibration pattern.

Position	**Y length [mm]**	**Uncertainty [mm]**
Left	25.00	±0.56
Middle	25.00	±0.56
Right	25.00	±0.56

Table 2.4: Y dimension of the calibration pattern.

The number of squares along x direction is $n_x = 9$ and the squares in the y direction are $n_y = 6$; the measurement uncertainty is due to the instrument resolution ($i_{res} = 0.5$ mm) and to both reading and alignment error ($i_{read} = 0.25$ mm).

$$i = \sqrt{i_{res}^2 + i_{read}^2} = \sqrt{0.5^2 + 0.25^2} = 0.56mm(95\%) \tag{2.1.55}$$

The dimension of a single square is (same formula for X and Y directions):

$$L_x \frac{L_{totX}}{n_x} \tag{2.1.56}$$

Position	**X length [mm]**	**Uncertainty [mm]**
Top	2.56	±0.06 (95%)
Middle	2.56	±0.06 (95%)
Bottom	2.56	±0.06 (95%)

Table 2.5: X size of the calibration pattern squares.

Position	**Y length [mm]**	**Uncertainty [mm]**
Left	2.5	±0.09 (95 %)
Middle	2.5	±0.09 (95 %)
Right	2.5	±0.09 (95 %)

Table 2.6: Y size of the calibration pattern squares.

$$i_{L_x} = \sqrt{\left(\frac{1}{n_x}\right)^2 i^2_{L_{totX}}} = \frac{i_{L_{totX}}}{n_x}$$

In order to reduce the uncertainty, three measurements performed in three different positions of the pattern have been used, to get an average value for both L_x and L_y. This has been done using the Student probability distribution.

$$\bar{L}_x = \frac{\sum_{i=1}^{N} L_{x,i}}{N} = 23.00mm \tag{2.1.57}$$

$$\bar{L}_y = \frac{\sum_{i=1}^{N} L_{y,i}}{N} = 15.00mm \tag{2.1.58}$$

In this case the Student parameter is: $t_{st}(95\%)_{n=2} = 4.303$

$$\bar{i}_{L_x} = \frac{t_{st}\sigma_x}{\sqrt{3}} = 0mm \tag{2.1.59}$$

$$\bar{i}_{L_y} = \frac{t_{st}\sigma_y}{\sqrt{3}} = 0mm$$

The average uncertainty cannot be lower than the uncertainty due to instrument resolution. If this happens, the global uncertainty is set equal to the resolution uncertainty. The small number of measurements recorded causes the impossibility to define a distribution with sufficient accuracy; for this reason, instead of assuming a probability distribution, the Kline-McClintock formula calculating the average uncertainty has been applied.

$$\bar{i}_{L_x} = \sqrt{\left(\frac{i_{L_x,top}}{3}\right)^2 + \left(\frac{i_{L_x,middle}}{3}\right)^2 + \left(\frac{i_{L_x,bottom}}{3}\right)^2} = 0.29mm(95\%) \tag{2.1.60}$$

$$\bar{i}_{L_y} = \sqrt{\left(\frac{i_{L_y,left}}{3}\right) + \left(\frac{i_{L_y,middle}}{3}\right) + \left(\frac{i_{L_y,right}}{3}\right)} = 0.29mm(95\%) \tag{2.1.61}$$

Taking the maximum uncertainty between the values found, the dimensions of the pattern used for camera calibration are:

1. $L_x = 2.56 \pm 0.29$ mm (95%)
2. $L_y = 2.5 \pm 0.29$ mm (95%)

Determination of the Distortions Caused by the Curved Surface of the Tank

The set up used to collect the images required for this analysis does not change with respect to that exploited for the intrinsic parameters determination; it is still possible to refer to section 2.1.5.2 for the complete procedure description.
The calibration pattern based on a black-white chessboard has 9 squares along x and 6 squares along y direction. The calibration grid is composed by 9x6 points. The dimensions of each square are:

1. $L_x = 2.56 \pm 0.29$ mm (95%)
2. $L_y = 2.5 \pm 0.29$ mm (95%)

As already pointed out, two different types of images have been collected:

1. Pictures taken from outside the cylindrical tank, to have as the output the intrinsic parameters due to the optical characteristics of the camera;
2. Pictures from inside the cylindrical tank, in order to obtain the intrinsic parameters due to both the optical characteristics of the camera and the deformation caused by the tank shape or superficial defects.

The assumption is that a specific point of given coordinates in the projection space is deformed according to this formula:

$$x_{def} = \left[KK_{camera}\right] x \tag{2.1.62}$$

x_{def} is the deformed point and x is the real one. $[KK_{camera}]$ is the deformation matrix containing the intrinsic parameters given by the calibration of the pictures taken outside of the tank, therefore only referring to the optics. For the pictures taken from the inside, it is possible to define a similar formulation:

$$x_{def} = \left[KK_{camera}\right] \left[KK_{tank}\right] x \tag{2.1.63}$$

where $[KK_{tank}]$ is the deformation matrix due to the tank shape and superficial defects. It is assumed that a generic real point of the chessboard pattern is first of all deformed due to the tank shape, and then due to the imperfect camera. The total deformation matrix is called $[KK_{total}]$ and contains both the effects of the tank and of the camera model:

$$\left[KK_{total}\right] = \left[KK_{camera}\right] \left[KK_{tank}\right] \tag{2.1.64}$$

From Eq.2.1.63 and 2.1.64 it is possible to obtain the following formulation for the deformation matrix due to the tank alone:

$$\left[KK_{tank}\right] = \left[KK_{camera}^{-1}\right]\left[KK_{total}\right] \tag{2.1.65}$$

The valid images used to find the intrinsic parameters of the camera, without considering the tank effect, are 17 (Fig.2.57). These pictures have been selected because edges can be clearly identified and they have been judged of sufficient quality. They have been taken with different inclinations, but the calibration pattern was always within the sponge tank area and the distance from the camera was therefore not varied from one image to the other.

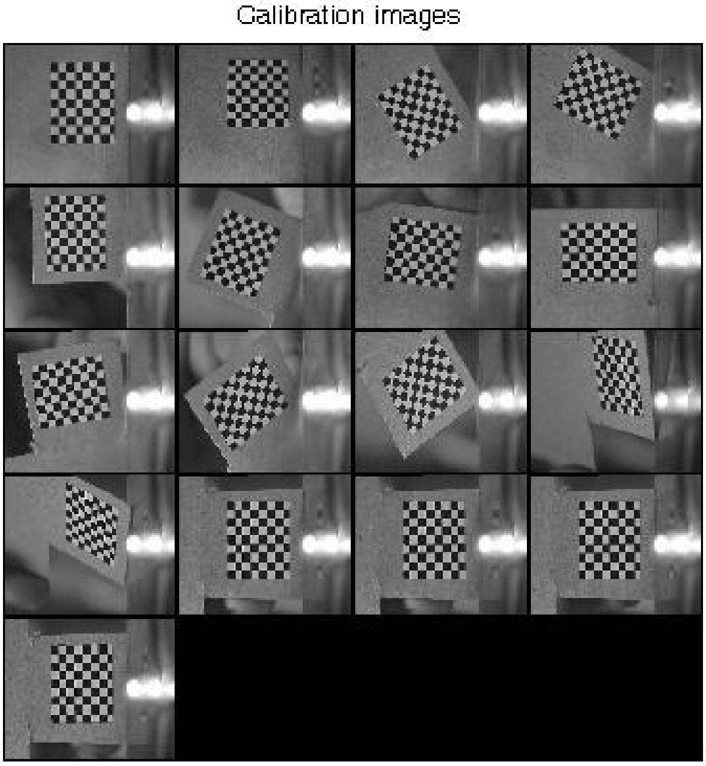

Figure 2.57: Pictures used for the camera calibration after a preliminary selection.

The orientation and the position of the calibration pattern over the 17 valid images acquired can be inspected by watching at Fig.2.57.

These pictures have been created after camera calibration and are related to the extrinsic parameters of the pattern in each image.

Camera calibration starts with an initialization phase where:

- Both f_c components are estimated to be equal;
- The principal point position is initialized at the center of the image;

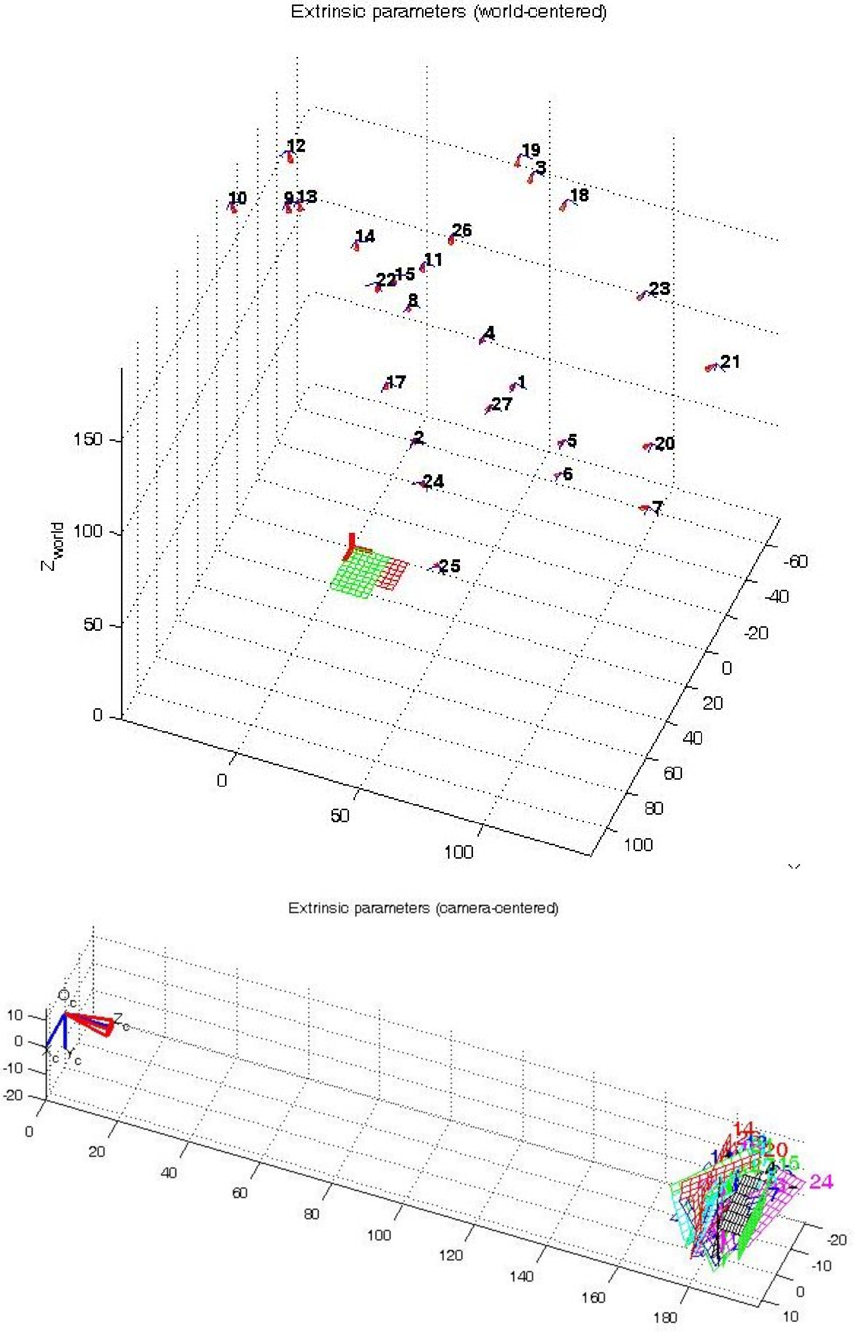

Figure 2.58: Camera extrinsic parameters in the world reference system and camera reference frame.

- Skew is not optimized (α_c=0);
- Distortion is not yet estimated (k_c=0).

The calibration parameters after initialization result in Tab.2.7.

Intrinsic Parameters	**Values**
Focal Length	$f_c(1)$=2674.62361, $f_c(2)$=2674.62361 [pix]
Principal Point	cc(1)=351.50000, cc(2)=287.50000 [pix]
Skew	coeff=0.00000, pix.angle = 90°
Distortion	$k_c(1) = k_c(2) = k_c(3) = k_c(4) = 0$

Table 2.7: Initial camera parameters.

The calibration procedure in some gradient descent iterations gives the optimized results. Distortions are not fully estimated, because the sixth order distortion has not been estimated in this analysis ($k_c(5)$=0).

Intrinsic Parameters	**Values**
Focal Length	$f_c(1)$=2537.78722±42.18608, $f_c(2)$=2683.31566±43.98216 [pix]
Principal Point	cc(1)=279.50313±43.29119, cc(2)=265.53902±50.64043 [pix]
Skew	coeff=0.00000, pix.angle = 90°
Distortion (I)	$k_c(1)$=-0.24264±0.26837, $k_c(2)$=-10.21496±25.34587
Distortion (II)	$k_c(3)$=-0.00415±0.00277, $k_c(4)$=-0.00660±0.00329, $k_c(5)$=0.0±0.0
Pixel error	Pixel error: x=0.26792, y=0.36866

Table 2.8: Camera parameters after calibration.

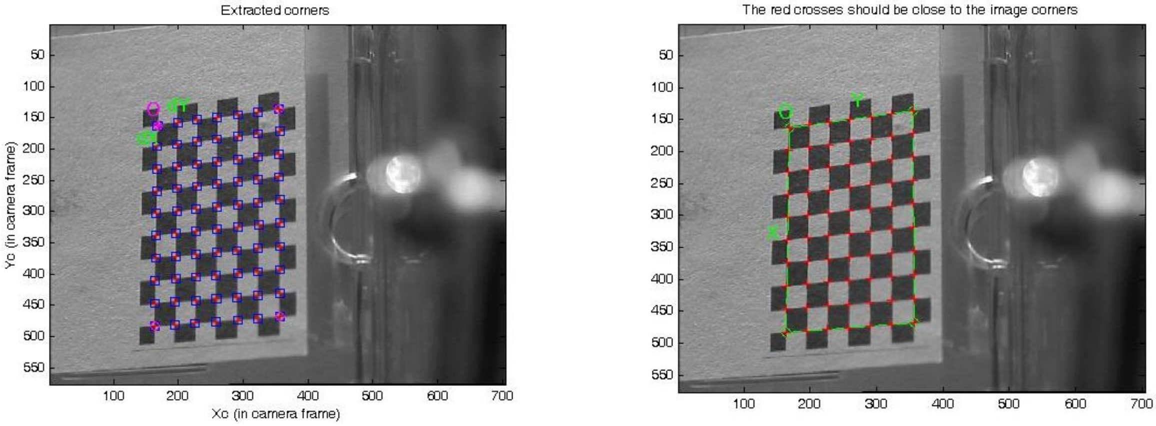

Figure 2.59: SPONGE camera corners extraction.

The image corners have been extracted from all the images automatically. Using the reprojected grid as the initial guess for the corners location, the reprojected grid points are very

close to the actual image corners.
The numerical errors are approximately three times the standard deviations of the corresponding parameter, resulting in a confidence level of 99.7%.

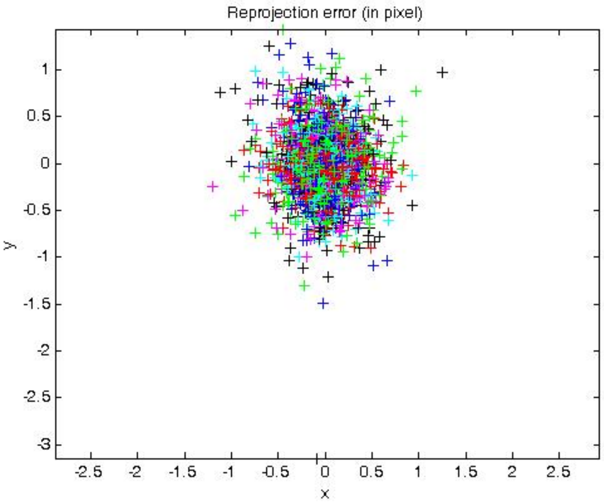

Figure 2.60: SPONGE camera error as a function of the pixels.

The camera calibration aim is to search the camera parameters minimizing the reprojection error of all points.
By looking at Fig.2.60, it can be observed that the maximum camera reprojection error is about 1.5 pixels, but most of the points have even lower errors.
In particular, after the calibration optimization, it is possible to have a lower reprojection error.

In order to better understand which is the appropriate distortion model, it is useful to visualize the distortion effects on the pixel image, and the importance of the radial versus tangential distortion component. Three images are produced to illustrate pixel distortions.

In particular, Fig.2.61 and 2.62 contain the results obtained in terms of radial and tangential distortions.
On the tangential distortion plot, the maximum induced displacement is larger than 20 pixels.
Finally, the radial distortion plot shows a maximum displacement of about 10 pixels.
The circle indicates the principal point location.

Fig.2.62 shows the impact of the complete distortion model (radial and tangential) on each pixel of the image. Each arrow represents the effective displacement of a pixel induced by the camera lens distortion. Points at the corners of the image are displaced by 15 pixels.

Concerning the pictures taken from inside the tank, they have allowed to obtain the intrinsic parameters and distortions due to the combined camera and tank effects. The pictures

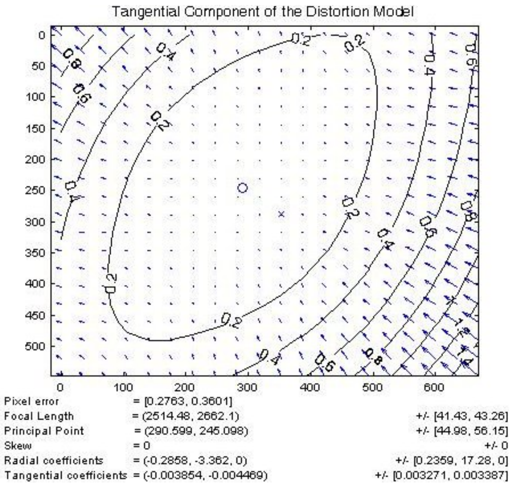

```
Pixel error             = [0.2763, 0.3601]
Focal Length            = (2514.48, 2662.1)                +/- [41.43, 43.26]
Principal Point         = (290.599, 245.098)               +/- [44.98, 56.15]
Skew                    = 0                                          +/- 0
Radial coefficients     = (-0.2858, -3.362, 0)            +/- [0.2359, 17.28, 0]
Tangential coefficients = (-0.003854, -0.004469)     +/- [0.003271, 0.003387]
```

```
Pixel error             = [0.2763, 0.3601]
Focal Length            = (2514.48, 2662.1)                +/- [41.43, 43.26]
Principal Point         = (290.599, 245.098)               +/- [44.98, 56.15]
Skew                    = 0                                          +/- 0
Radial coefficients     = (-0.2858, -3.362, 0)            +/- [0.2359, 17.28, 0]
Tangential coefficients = (-0.003854, -0.004469)     +/- [0.003271, 0.003387]
```

Figure 2.61: Tangential and radial distortions are showed respectively on the left and on the right.

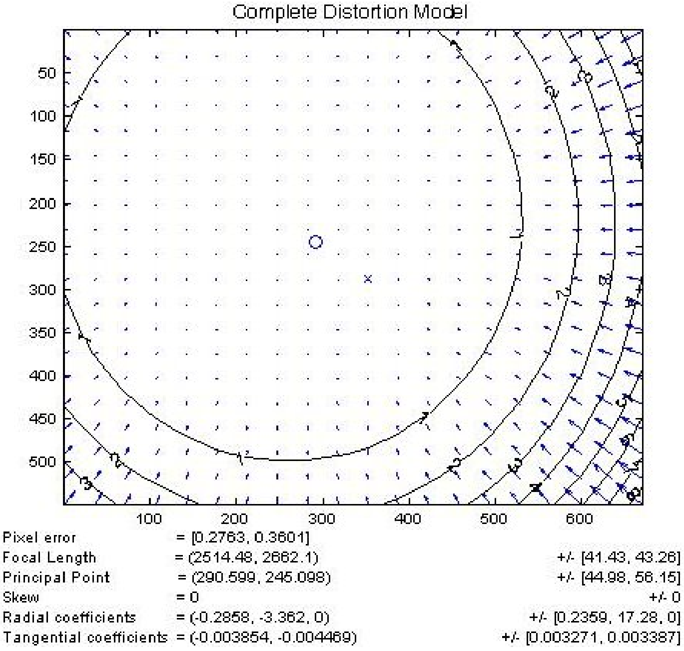

```
Pixel error             = [0.2763, 0.3601]
Focal Length            = (2514.48, 2662.1)                +/- [41.43, 43.26]
Principal Point         = (290.599, 245.098)               +/- [44.98, 56.15]
Skew                    = 0                                          +/- 0
Radial coefficients     = (-0.2858, -3.362, 0)            +/- [0.2359, 17.28, 0]
Tangential coefficients = (-0.003854, -0.004469)     +/- [0.003271, 0.003387]
```

Figure 2.62: Complete distortion model.

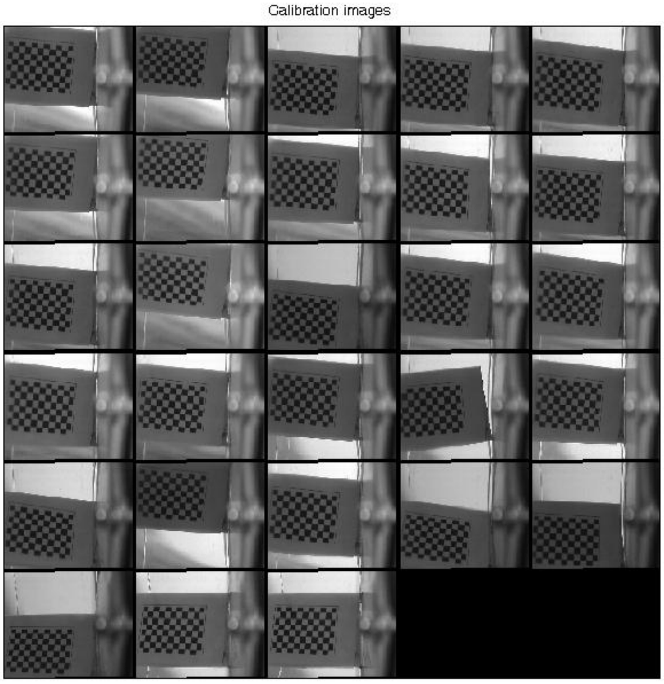

Figure 2.63: Pictures taken from inside SPONGE tank.

used have been 28 in this case and they can be seen in Fig.2.63.

In this case, the parameters obtained after corners extraction for the distortions are those in Tab.2.9.

Intrinsic Parameters	**Values**
Focal Length	$f_c(1)$=2582.98633±306.12133, $f_c(2)$=2772.71320±328.29754 [pix]
Principal Point	cc(1)=211.55697±36.71649, cc(2)=195.85998±111.87377 [pix]
Skew	coeff=0.00000, pix.angle = 90°
Distortion (I)	$k_c(1)$=-1.41433±0.73106, $k_c(2)$=56.65309±71.12618
Distortion (II)	$k_c(3)$=0.00044±0.02907, $k_c(4)$=-0.00514±0.00915, $k_c(5)$=0.0±0.0
Pixel error	Pixel error: x=0.37049, y=1.82472

Table 2.9: Camera parameters after calibration.

The error in pixels due to calibration is in Fig.2.64.

When the calibration chessboard is put inside the tank and pictures are taken in this configuration, the resulting distortions are much more important than considering just the

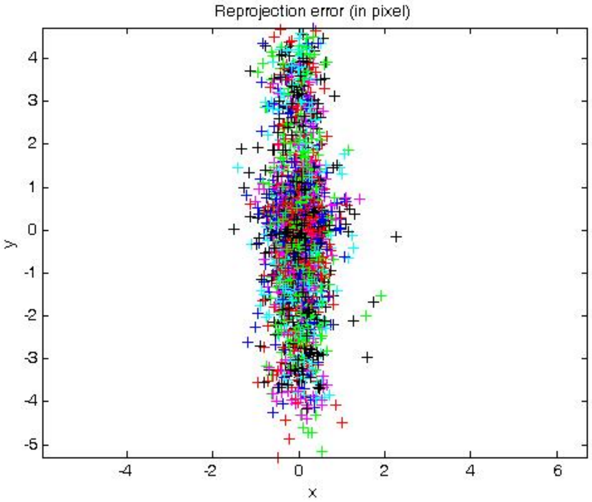

Figure 2.64: Calibration error [pix] for pictures taken from inside the tank.

optical characteristics of the camera.
This is due to the cylindrical shape of the tank, but also to the surface machining of the polycarbonate, which is not perfect and therefore causes the images to be unsharp in some points or corners.

In Fig.2.66, the radial, tangential and complete distortion models are presented for the images, combining the effects of the tank and optics.

The distortion matrix resulting from the analysis of the pictures taken from outside the tank is:

$$[KK_{camera}] = \begin{bmatrix} 2537.8 & 0 & 279.53 \\ 0 & 2683.3 & 265.52 \\ 0 & 0 & 1 \end{bmatrix} = \begin{bmatrix} f_c(1) & \alpha_c f_c(1) & cc(1) \\ 0 & f_c(2) & cc(2) \\ 0 & 0 & 1 \end{bmatrix} \tag{2.1.66}$$

whereas the resulting distortion matrix for the combination of the tank and camera effects is:

$$[KK_{total}] = \begin{bmatrix} 2583 & 0 & 211.56 \\ 0 & 2772.7 & 195.86 \\ 0 & 0 & 1 \end{bmatrix} \tag{2.1.67}$$

Finally, using Eq.2.1.65, it is possible to have the distortion matrix due to the tank alone, as:

$$[KK_{tank}] \begin{bmatrix} 1.0178 & 0 & -23.3026 \\ 0 & 1.0333 & -19.3809 \\ 0 & 0 & 1 \end{bmatrix} \tag{2.1.68}$$

The matrix calculated for the deformation due to the tank shape and manufacturing has the same shape of the other deformation matrices, where the last row is composed by $[0\ \ 0\ \ 1]$. The associated intrinsic parameters are in this case:

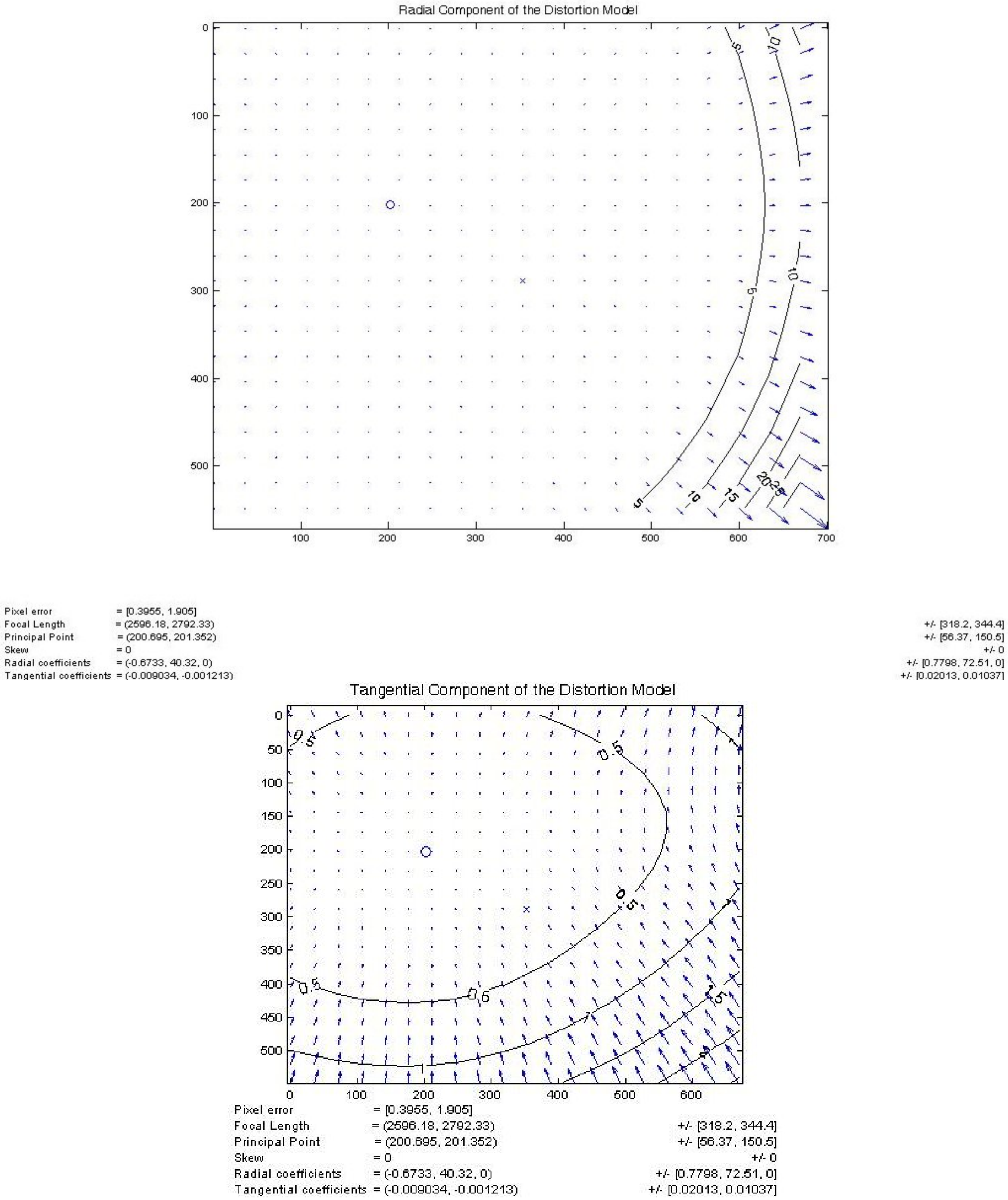

```
Pixel error            = [0.3955, 1.905]
Focal Length           = (2596.18, 2792.33)                         +/- [318.2, 344.4]
Principal Point         = (200.695, 201.352)                         +/- [56.37, 150.5]
Skew                   = 0                                                     +/- 0
Radial coefficients    = (-0.6733, 40.32, 0)                     +/- [0.7798, 72.51, 0]
Tangential coefficients = (-0.009034, -0.001213)                 +/- [0.02013, 0.01037]
```

```
Pixel error            = [0.3955, 1.905]
Focal Length           = (2596.18, 2792.33)                         +/- [318.2, 344.4]
Principal Point         = (200.695, 201.352)                         +/- [56.37, 150.5]
Skew                   = 0                                                     +/- 0
Radial coefficients    = (-0.6733, 40.32, 0)                     +/- [0.7798, 72.51, 0]
Tangential coefficients = (-0.009034, -0.001213)                 +/- [0.02013, 0.01037]
```

Figure 2.65: Distortions for the pictures taken from inside the tank.

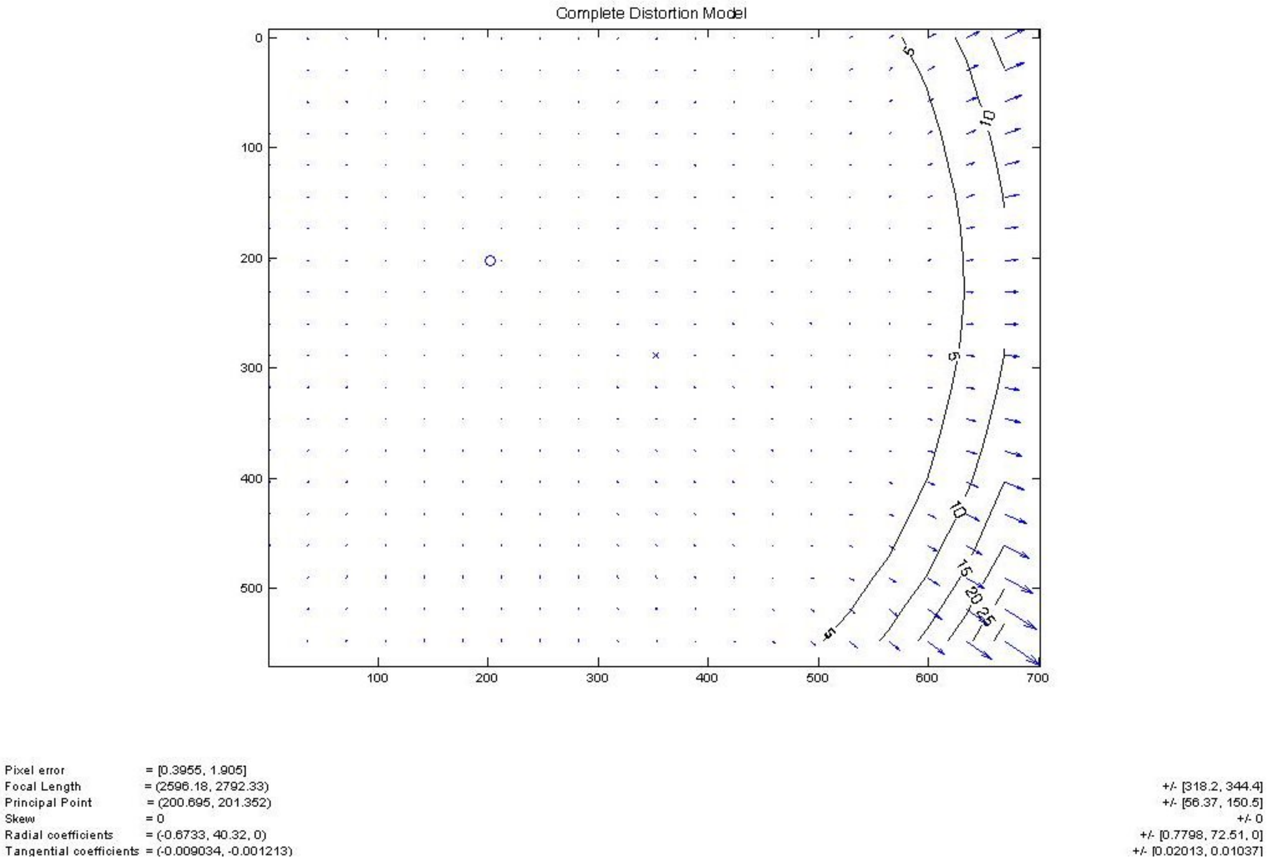

```
Pixel error            = [0.3955, 1.905]
Focal Length           = (2596.18, 2792.33)                +/- [318.2, 344.4]
Principal Point        = (200.695, 201.352)                +/- [56.37, 150.5]
Skew                   = 0                                  +/- 0
Radial coefficients    = (-0.6733, 40.32, 0)              +/- [0.7798, 72.51, 0]
Tangential coefficients = (-0.009034, -0.001213)          +/- [0.02013, 0.01037]
```

Figure 2.66: Complete distortions for the pictures taken from inside the tank.

1. $f_c(1)$=1.0178;
2. $f_c(2)$=1.0333;
3. α_c=0;
4. $cc(1)$=-23.3026;
5. $cc(2)$=-19.3809.

The calculation of the distortion parameters and the application of this method for the determination of the image deformations due to the tank shape have been possible thanks to some assumptions:

- The distance from the calibration pattern to the camera does not vary for the different pictures;
- The relationship from the point real coordinates to the distorted coordinates is linear.

This study could be further investigated by performing a calibration of the stereoscopic system composed of the two cameras, in order to find the characteristics of the liquid surfaces, when the tank is subjected to different acceleration loads.

2.2 Use of Hybrid Rockets Test Facilities to Validate the CFD

2.2.1 German Facility built by Dr.Grosse in 2009

Dr. Matthias Grosse revised the diaphragm concept and applied it for the first time to the hybrid propellant combination paraffin/nitrous oxide. His studies have been published in 2009, after he presented his work at the JPC[18].
Dr. Grosse performed various tests, whose results have been used to retrieve data to be compared with the parameters extracted from the CFD.

Grosse designed and built a hybrid rocket with a thrust up to 1000 N corresponding to a 40 bar pressure combustion chamber. The grain was created in order for a CFC diaphragm to be placed at different positions along the fuel grain. The diaphragm was manufactured in two different versions: with just one hole or four holes.
The average values of specific impulse, thrust coefficient and characteristic velocity, the thrust efficiencies, nozzle diameter and the average regression rates upstream and downstream of the diaphragm were analyzed, to find a dependency on the specific diaphragm type and position. Then, results were compared to a reference case, represented by the motor without the diaphragm. The pressure loss caused by the diaphragm was determined as well.
As a result of the diaphragm insertion, the fuel grain was partitioned into two separated combustion and fuel regression zones.

The scheme of the hybrid rocket motor is shown in Fig.2.67. The diaphragm is placed at the 24% and 33% of the paraffin grain length and it can have a single central opening or a

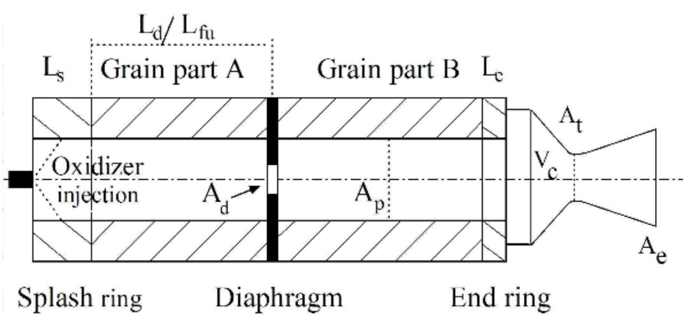

Figure 2.67: Geometry of the hybrid lab-scale rocket tested by Grosse.

four-opening perforation (Fig.2.68).
The oxidizer mass flow has been adjusted during the experiments, selecting different industrial swirl injectors.

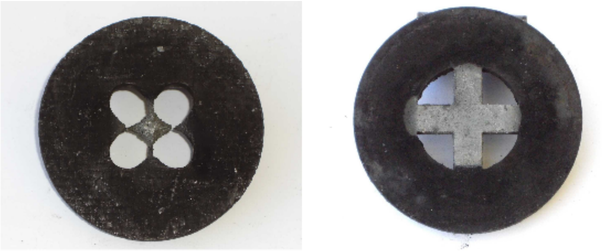

Figure 2.68: CFC 4-hole diaphragms (initial and final version) after firing.

The injector full cone angle was 90 °; the length of the splash and end ring, nozzle geometry and grain length remained constant during all the tests.

In Tab.2.10, the geometrical parameters of the test motor are listed.
For L^* calculation, the volume from the grain end (including the end ring) to the nozzle throat (69 cm^3) has been used.

2.2.1.1 Rocket Configuration and Tests

The motor is composed of a robust aluminum injection head, an aluminum combustion chamber and a non-cooled nozzle section (Fig.2.69). The former consists of a high density graphite nozzle insert and of a nozzle casing made of nickel-based alloys.

High-quality graphite nozzles are normally preserved after the firings and can be reused because the propellant combination delivers relatively moderate thermal and chemical loads. An extra cavity has been manufactured near the injector, to house the igniter, which is a piece of AP/HTPB composite propellant of 10-14 g, normally initiated by a small commercial squib.

Parameter	**Value**
Fuel port r_0	14.6 mm
Splash ring-End ring length	35-10 mm
Fuel grain length L	162 mm
Relative diaph. position	24 %,33 %
Nozzle throat diam.	14.99 mm
Contour radius at nozzle throat	11.2 mm
Diaph. to throat area ratio	1.80
Characteristic length L^*	0.4 m
Inj. H_2O discharge at 3 bar	3,7.5,9 dm^3/min
Nozzle area ratio Ae/At	4.5
Port to throat area ratio Ap/At	3.82
Port to diaph. area ratio Ap/Ad	2.25

Table 2.10: Geometry of the lab-scale motor tested by Dr. Grosse.

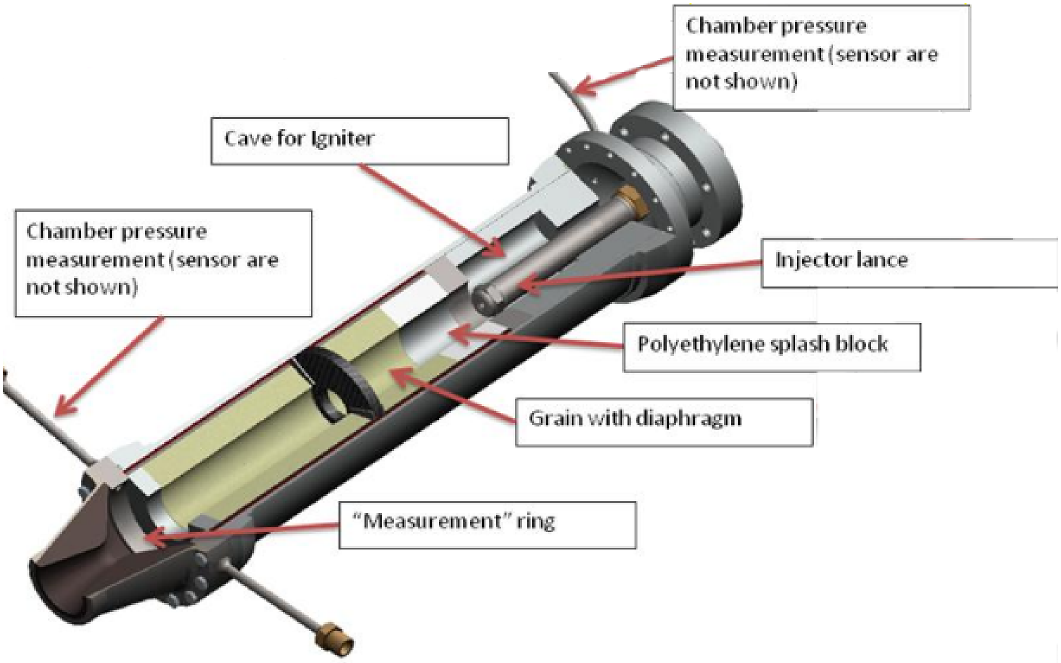

Figure 2.69: Section of the laboratory hybrid motor.

A single Schlick industrial swirl injector was used to atomize and distribute the nitrous oxide. A low regression polyethylene or polyoxymethylene splash ring was added upstream of the grain to straighten the full cone nitrous oxide flow.
Injection pressure was not changed widely during the tests, due to the limitations in pressure regulation and to the need for a sufficient supercharging pressure.
Significant changes in nitrous oxide flow were achieved by means of three different injectors. Their characterization (3, 7.5 and 9) stands for the water discharge value (l/min) at $\Delta p = 3$ bar.

The three grain segments were held in place thanks to special rings (Fig.2.70).

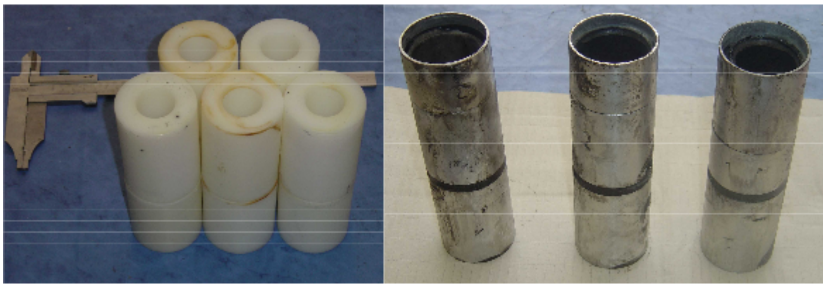

Figure 2.70: Final cast and cut fuel grain segments (left) and cartouches after firings (right).

Segments made of aluminum were only used for low regression rate tests or short-time firings, because they can melt if exposed for a sufficiently long time to the hot flow. For high regression rate tests, where N_2O mass flow was higher, the support rings were made of CFC tubes to protect the chamber walls. A polyethylene end ring was added (Fig.2.67 and 2.69) to support the grain against the nozzle and protect the grain end from regression.

In Fig.2.70, two of the 4-hole perforated diaphragms are shown, on the left the initial uncoated CFC with four circular openings, used for the first two firings with a 4-hole diaphragm. It was unable to withstand the hot gas flow and burnt out. The one on the right (Fig.2.70) was used for all the other tests with the 4-hole perforation. It was coated with silicon carbide and no regression was observed anymore.

Test Bench

The test stand used, shown in Fig.2.71, was equipped with a rocket motor supporting thrust frame, movable thanks to a friction-free linear slide for thrust measurement.

The laboratory motor was fed from a small spherical titanium tank, having a three-liters capacity. The tank could be detached from the test stand to determine the mass of the consumed oxidizer and was equipped with ball valves at the gas and liquid side for filling, pressurization and transportation sealing.
The oxidizer flow was controlled by a pneumatically driven ball valve. This main valve and the igniter were controlled by the same electrical circuit. The delay of the valve opening was conceived to give the igniter the right lead time and avoid the unburnt oxidizer ejection. The

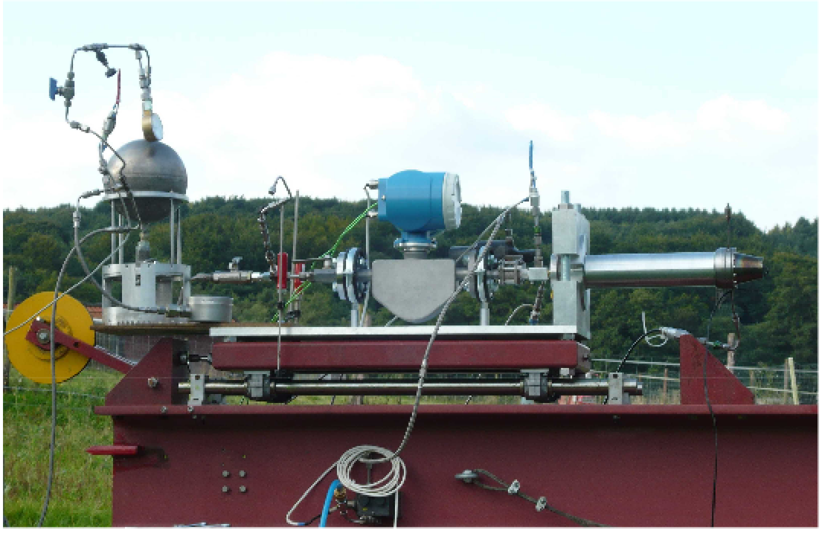

Figure 2.71: Test bench for the lab-scale rocket.

instrumentation scheme of the used test set up is shown in Fig.2.72.

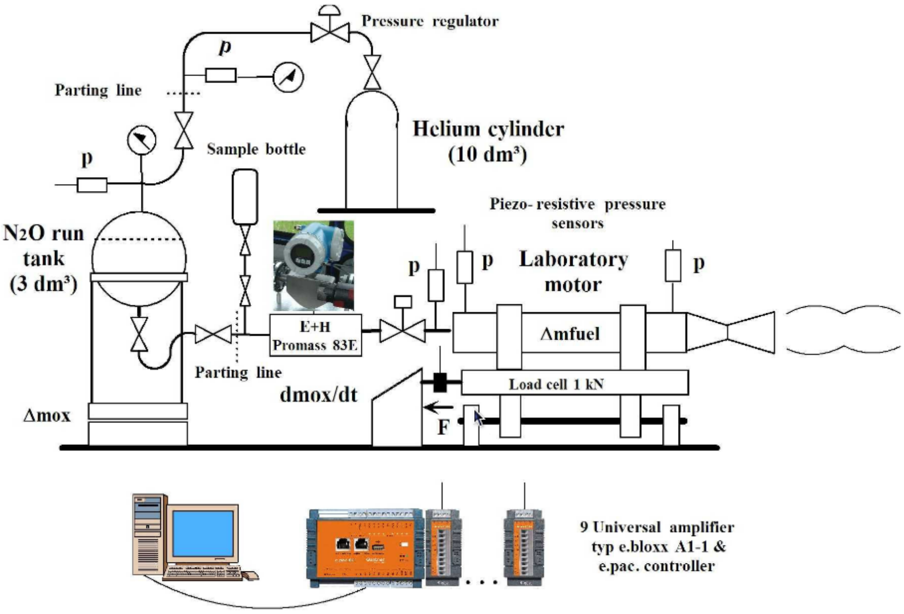

Figure 2.72: Instrumentation scheme of the test set up.

The nitrous oxide flow was measured by the mass flow sensor Promass 83 E, sponsored by Endress and Hauser. The sensor measures the mass flow directly and with a high accuracy (if N_2O cavitation is prevented) without relying on volume flow nor pressure measurements and possible inaccurate nitrous oxide density assumptions. Its measurement principle is based on the Coriolis force acting on a vibrating tube assembly.

Pressure values near the injector and at the nozzle entrance were measured by temperature-compensated piezo-resistive high accuracy pressure sensors. Furthermore, the injection and tank pressures were recorded.
The thrust measurement using the force sensor KMM-5 (Inelta) was used to derive the specific impulse I_{sp} and thrust coefficient C_f. Data was acquired by a modular and economic system by Gantner Instruments.

Tab.2.11 contains the measurements overview. The mass flow sensor was tested for accuracy using water and nitrous oxide cold flow.

Measurement	**Range**	**Estimated accuracy**
P_{cc} near inj.	0-60 bar	$<$ 1%
P_{cc} nozzle inlet.	0-60 bar	$<$ 1%
Inj. P	0-00 bar	$<$ 1%
Tank P	0-100 bar	$<$ 1%
Thrust	0-1000 N	1% 500 N
N_2O mass flow	0-500 g/s	0.7 %
N_2O density	0-2000 kg/m^3	not available
Ox weighting	0-6 kg	0.5 g
He weighting	0-30 kg	2 g

Table 2.11: Measurements Overview.

The thrust-measuring assembly was calibrated by hanging weights in nine steps up to 100 kg on a rope roll (yellow disk in Fig.2.71) to simulate the thrust. Pressure sensors were checked every day and recalibrated if necessary, by means of a high-accuracy reference manometer (0.1% accuracy).

2.2.2 Italian Facility built by CISAS in Summer 2011

The main idea behind the drafting of the test matrix for the experiments conducted in Summer 2011, was to validate the preliminary CFD simulations required for the SPARTAN research program.
These tests allowed the optimization of the diaphragm center-hole diameter of a rocket designed at CISAS, to assess regression rate and combustion efficiency at a greater rocket scale compared to that used by Dr.Grosse.

As the starting point, the better diaphragm position identified with previous works was selected: the mixing device was placed at the 25% of the grain length and with a simple circular hole.
Pre and post-chamber sizes have been minimized, to maximize volumetric efficiency for a future flight configuration.
Experiments have been done at lab scale with three different Ad/At ratios. Ad/At is the ratio between the diaphragm center-hole diameter and the nozzle throat diameter and it is

used to define diaphragms independently from motor scale. The diaphragm giving the best performance was selected for scaling up and tested.
For both lab and increased-scale motors, the reference experiments are without diaphragms and with increased grain length to maintain the same OF ratio of the experiments using a diaphragm. Data about the tests performed is reported in Tab.2.12 and 2.13.

More than one test has been conducted for each configuration, and the results obtained have been averaged, in order to be used for a comparison with CFD analyses. The averaged results calculated for software validation are presented in the tables of the following chapter 3.

Preliminary testing has been done for each configuration with steel diaphragms, whereas the final experiment used CFC diaphragms.
For the lab scale, the following Ad/At ratios have been used: 1.5, 1 and 0.5. For the increased scale, only diaphragms with Ad/At = 1 have been used.

Test	**Ad/At**	**Scale**	**Upstream Grain (ϕxL)[mm]**
6	1.5	Lab	30x30
8	1	Lab	30x30
4	0.5	Lab	30x30
3	No-diaphragm	Lab	—
5	1	Increased	57x58
2	No-diaphragm	Increased	—

Table 2.12: Set up of the lab-scale and increased-scale motors: ϕ is the grain internal initial diameter and L is the length (I).

Test	**Downstream Grain (ϕxL)[mm]**	$\dot{m}_{ox}$ **[g/s]**	**Burn t [s]**
6	30x90	250	3
8	30x90	250	3
4	30x90	250	3
3	30x155	250	3
5	57x172	935	4
2	57x300	935	4

Table 2.13: Set up of the lab-scale and increased-scale motors: ϕ is the grain internal initial diameter and L is the length (II).

2.2.2.1 Lab-scale Rocket

Fig.2.73 shows the combustion chamber of the lab-scale motor with and without the diaphragm. To avoid the pre-chamber effect on the flow fields, a long injector was mounted in the combustion chamber with the diaphragm.

The motor was ignited with a custom KNO_3/SORBITOL propellant charge, at the grain section upstream of the diaphragm.

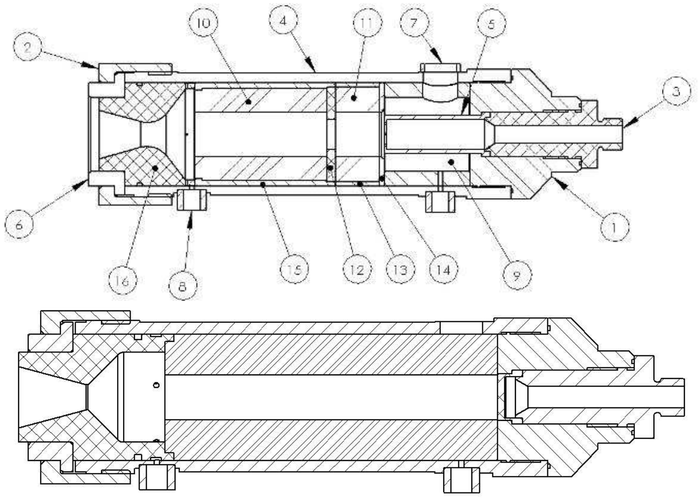

Figure 2.73: Schematic of the lab motor combustion chamber: above the diaphragm case, below the reference configuration. Both operate at the same OF ratio. The Main parts are: 1) motor head, 2) aft-nozzle enclosure, 3) injection interface, 4) combustion chamber external case, 5) injection plate, 6) nozzle enclosure interface, 7-8) pressure sensor interface, 9) pre-combustion chamber, 10) post-diaphragm fuel grain, 11) pre-diaphragm fuel grain, 12) diaphragm, 13) pre-diaphragm grain protection, 14) pre-combustion chamber thermal protection, 15) post-diaphragm grain protection, 16) nozzle.

Pressure was measured in the pre-chamber (only if a diaphragm was used) and in the post-chamber, just before the nozzle inlet; general purpose Kistler sensors were used (model 4260A, full scale 7 MPa, accuracy 0.1%, response time < 1 ms).
The combustion chamber was decoupled from the oxidizer tank and mounted on linear slides for thrust measurement. Thrust time history was measured by means of a 1000 N traction load cell with 0.02 % accuracy.
Regression rate was estimated by differentially weighting the fuel grain.

The motors were controlled by a custom PLC control and data acquisition system. The sampling frequency was 1 kHz for all sensors, except for the thermocouples (10 Hz). This system provides power for the igniters as well.

N_2O oxidizer was fed into the combustion chamber by a pressure-regulated system to achieve a constant oxidizer mass flow rate.
Pressure in the oxidizer tank and in the feed line was measured by GEFRAN TK sensors (0.25% FS accuracy, rise time 1 ms, temperature compensated between -10°C to 85°C), and TPSA sensors (0.1% FS accuracy, rise time $<$ 1 ms, temperature compensated between -40°C to 105°C).

Fuel grains were made with SASOL 0907 paraffin wax with 83°C-94°C freezing point, 14-18 mm^2/s dynamic viscosity at 100°C and approximate chemical composition $C_{50}H_{102}$. Grains were obtained via gravitational casting followed by slow cooling. The port diameter was subsequently machined. Fig.2.76 shows fuel grains after casting and machining.

Diaphragms were made of CFC impregnated with SiC and showed excellent thermal stability, resistance to thermal shock and low erosion due to the oxidizer-rich-flow they have been exposed to. CFC diaphragms are sponsored by Dr.Roland Weiss and Mr.Damian Obruschnik from Schunk GmbH.

Figure 2.74: On the left, paraffin fuel grain after gravitational casting. 1% of carbon black was added. On the right, single grain after machining. CFC diaphragms impregnated with SiC for the Lab Scale Motor, before and after usage.

Lab motor experiments were made in a closed environment: the test bed was mounted inside a container, connected to the environment through a silencing device.
When the motor was fired, the Venturi effect reduced the ambient pressure to the nozzle section. For this reason, the thrust coefficient C_f evaluated experimentally exceeds the theoretical values and the data analysis is focused on combustion efficiency.

The tests of the increased scale motor were instead performed in open-air. C_f values were measured and used for motor performance evaluation without any discrepancy.

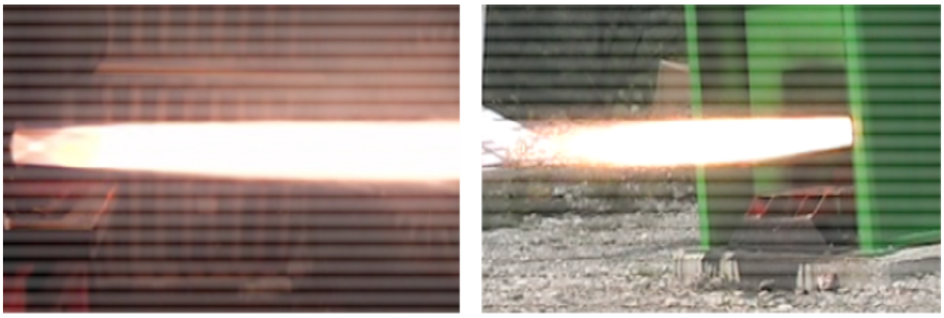

Figure 2.75: Motor burn experiments: (left) lab motor in close environment, (right) increased scale open air testing.

2.2.2.2 Increased-scale Rocket

The increased scale motor generates three times the thrust of the lab scale (2500 N).

The combustion chamber internal configuration is shown in Fig.2.76: the reference configuration without the diaphragm has a longer grain to compensate the loss in regression rate.

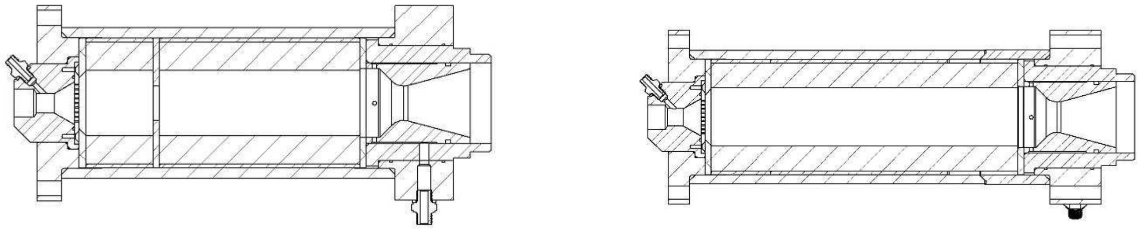

Figure 2.76: On the left, increased-scale with the diaphragm (center-hole diameter equal to nozzle throat diameter), on the right without the diaphragm. The grain of the reference configuration was longer to maintain the same OF ratio of the other geometry.

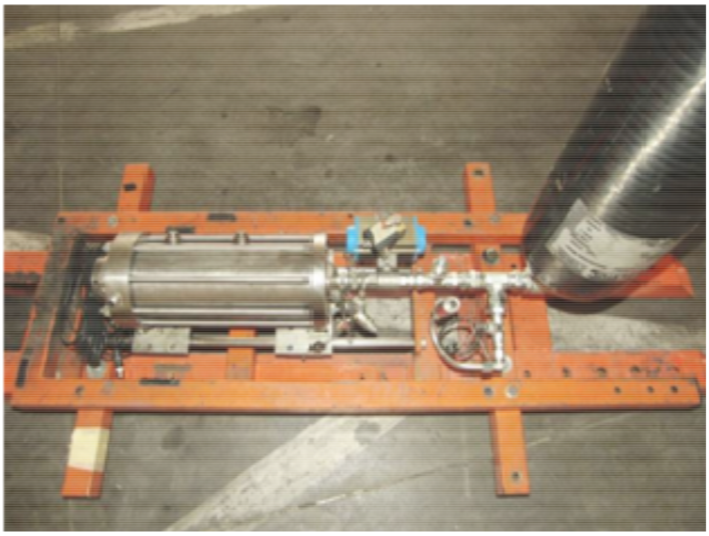

Figure 2.77: Increased-scale motor on the test bench. From the left, the motor parts are visible: combustion chamber, main oxidizer valve, hydraulic circuit with diagnostics and oxidizer bottle.

There is no pre-chamber, whereas the post-chamber is as small as possible, to allow pressure measurement before the nozzle inlet. Pressure was measured only in the post-chamber section by two redundant Kistler pressure probes.
Regression rate was estimated by differentially weighting the fuel grain.

Oxidizer was self-pressurized, in fact pressure regulation was not possible due to the excessive oxidizer mass flow rate.

The burnt oxidizer mass was measured weighting the oxidizer bottle before and after each test.

Figure 2.78: Diaphragms for the increased-scale rocket: CFC-SiC diaphragm before and after testing.

Fig.2.78 shows the diaphragm before and after firing for the increased-scale case.

Chapter 3

Numerical Codes Validation and Related Results

This chapter contains validations results. The whole discussion is organized as follows:

- The first section details the verification of the PMD software;
- The second describes the validation of the hybrid rocket simulations carried out by CFD.

The validations of the rocket simulations have been performed thanks to the experimental data available; the CFD simulations discussed in the following are meant to reproduce the corresponding test conditions.
The experimental results of interest are presented as well, to allow a better comparison with the flow conditions predicted by the software.

On the other hand, the PMD numerical code has not been validated yet, due to the lack of experimental data. The necessary test beds are managed by TAS-I industrial company and tests are foreseen in the near future.
In the meanwhile, simulations have been performed to verify the code numerical stability, the correct coexistence of the new boundary conditions implemented, the possibility to handle the contact angle when capillarity becomes important.
Therefore, concerning the PMD code, it is more appropriate to refer to a verification procedure, rather than a real validation and the results exposed are qualitative rather than quantitative.

3.1 Validation of the CFD Code Reproducing PMD Behavior

Many different test cases have been prepared to verify the spongeFoam code.
The first tests were meant to assess that the new sponge boundary condition worked as a wall if the bubble point value specified was not overcome by the gas phase and as a traditional cyclic in the opposite case.

In order to test this basic boundary condition, different damBreak cases were prepared, with different bubble point values.

Then, those test cases have been modified inserting the spongeCyclicScalarPressureFall boundary condition, accounting for the eventual pressure drop across the PMD screen in case of gas passage.
Other tests have been created with a different geometry, where a gas bubble (air) was immersed in a liquid volume (water). Different accelerations were applied to the system and the bubble was made to move inside the liquid towards the screen panel modeled. According to the bubble point across the PMD and to the accelerations imposed, different results were registered and the gas bubble could pass through the screen or remained attached to it.
Other tests were necessary to verify the possibility to set different contact angles between the sponge plate and the fluid. In this case, various contact angles were applied, with different bubble point values, in both 2D and 3D test cases. This allowed to verify the difference between the fluids behavior in 2D and 3D.

3.1.1 Simulations Run using spongeFoam

A list follows where all the test cases prepared are presented:

1. 2D dam break case with the spongeCyclic boundary condition and the bubble point set to 0 Pa;
2. 2D dam break case with the spongeCyclic boundary condition, the bubble point set to zero and the pressure drop activation across the screen;
3. 2D air bubble dynamics in water, with the spongeCyclic boundary applied, and a 20 Pa bubble point activated;
4. 2D air bubble dynamics in water, with the spongeCyclic boundary applied, and a 200 Pa bubble point activated;
5. 2D air bubble dynamics in water, with the spongeCyclic boundary applied, and a 5000 Pa bubble point activated;
6. 3D air bubble dynamics in water, with spongeCyclic boundary applied and a 10 Pa bubble point activated;
7. 2D air bubble dynamics in water, with spongeCyclic and spongeCyclicScalarPressureFall boundaries applied, with a bubble point of 20 Pa;
8. 2D air bubble dynamics in water, with spongeCyclic and spongeCyclicScalarPressureFall boundaries applied, with a bubble point of 200 Pa;
9. 2D air bubble dynamics in water, with spongeCyclic and spongeCyclicScalarPressureFall boundaries applied, with a bubble point of 5000 Pa;
10. 2D air bubble dynamics in water, with spongeCyclic and spongeDynamicAlphaContactAngle boundaries applied, with a bubble point of 20 Pa and a contact angle of 30 °;

11. 2D air bubble dynamics in water, with spongeCyclic and spongeDynamicAlphaContactAngle boundaries applied, with a bubble point of 200 Pa and a contact angle of 30 °;
12. 2D air bubble dynamics in water, with spongeCyclic and spongeDynamicAlphaContactAngle boundaries applied, with a bubble point of 5000 Pa and a contact angle of 30 °;
13. 3D air bubble dynamics in water, with spongeCyclic and spongeDynamicAlphaContactAngle boundaries applied, with a bubble point of 200 Pa and a contact angle of 60 °;
14. 3D air bubble dynamics in water, with spongeCyclic and spongeDynamicAlphaContactAngle boundaries applied, with a bubble point of 20 Pa and a contact angle of 30 °;
15. 2D air bubble dynamics in water, with spongeCyclic and spongeDynamicAlphaContactAngle boundaries applied, with a bubble point of 5000 Pa and a contact angle of 60 °;
16. 2D air bubble dynamics in water, with spongeCyclic and spongeDynamicAlphaContactAngle boundaries applied, with a bubble point of 200 Pa and a contact angle of 60 °;
17. 2D air bubble dynamics in water, with spongeCyclic and spongeDynamicAlphaContactAngle boundaries applied, with a bubble point of 20 Pa and a contact angle of 60 °;
18. 2D air bubble dynamics in water, with spongeCyclic, spongeDynamicAlphaContactAngle and spongeCyclicScalarPressureFall boundaries applied, with a bubble point of 200 Pa and contact angle of 60 °;
19. 2D air bubble dynamics in water, with spongeCyclic, spongeDynamicAlphaContactAngle and spongeCyclicScalarPressureFall boundaries applied, with a bubble point of 10 Pa and contact angle of 60 °;

3.1.2 Main Aspects to be Tested and Verified

The main code features to be verified before validation (to be performed by means of ad hoc experimental data) are:

- The correct interaction between the new boundary conditions representing PMD fluid dynamics;
- The numerical code stability when simulating a complete test case;
- The code ability to simulate 2D as well as 3D test geometries;
- The possibility to impose different contact angles, and therefore of simulating different fluids. This is a very important aspect, because this ability can have limitations due to the Volume Of Fluid (VOF) simulation technique, which is the basis of the code.

3.1.3 Examples of the Results Obtained

In this section, some results obtained from the simulations (see 3.1.1 for a complete list of the test cases created) are presented. These verification simulations have the aim to recreate different gas bubble behaviors, according to the different conditions simulated.

It has been impossible to perform a rigorous validation of the code, due to the lack of experimental data in this phase of the study. Experiments are foreseen in the future, from which the screen bubble point data and the contact angle can be determined. With this data, it will be possible to create more adherent test cases, from which to extract specific fluid dynamic parameters.

3.1.3.1 Air Bubble in Water, Bubble Point of 5000 Pa

This test case simulates an air bubble immersed in liquid water. The phases are compressible and immiscible, and the interface between them is tracked by a VOF algorithm. In this case, only the sponge boundary condition has been applied, whereas no specific contact angle nor pressure drop have been activated.
The gas bubble has to stick to the screen as if it was a wall, due to the high bubble point value, which does not allow the gas to pass through the channels of the PMD plate.

This simulation was created to verify the possibility to reproduce this behavior for the gas bubble rising into a liquid phase.
Some pictures showing the results are presented hereafter.

From the pictures in Fig.3.1, it is possible to see the bubble rising inside liquid water. Then it sticks to the screen, which behaves like a wall, and bounces staying attached to it, until viscosity damps this oscillation down.

3.1.3.2 Air Bubble in Water, Bubble Point of 10 Pa, Pressure Drop and 60 ° Contact Angle

This test case simulates an air bubble immersed in liquid water, as in the previous case. The phases are still compressible and immiscible. Not only the sponge boundary condition has been applied: the pressure drop through the screen channels has been simulated as well. A contact angle of 60 ° has been accounted for between the fluid phases.
The gas bubble does not stick to the screen as to a wall, due to the low bubble point value, which allows the gas to pass through the channels of the PMD plate.

This simulation was created to verify the compatibility between the three boundary conditions implemented to fully describe the PMD behavior. In particular, the numerical code stability was under investigation.
Some pictures showing the results are presented hereafter.

In the pictures collected in Fig.3.2, the bubble rises inside liquid water. Then it passes through the PMD screen, which shows a behavior similar to that of a filter. The gas flow

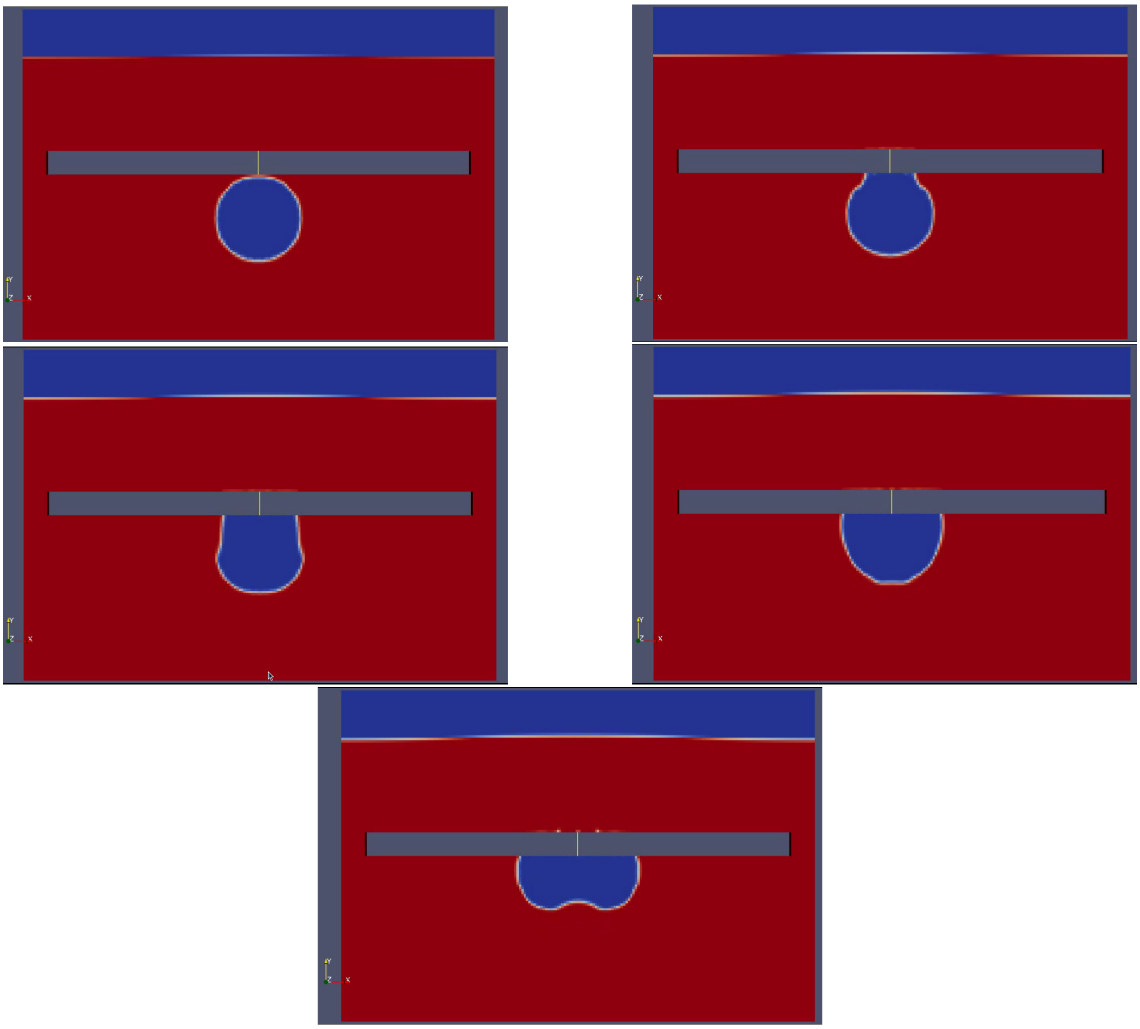

Figure 3.1: Frames taken from the gas bubble dynamics in case of a 5000 Pa bubble point. The order is from left to right and from the top.

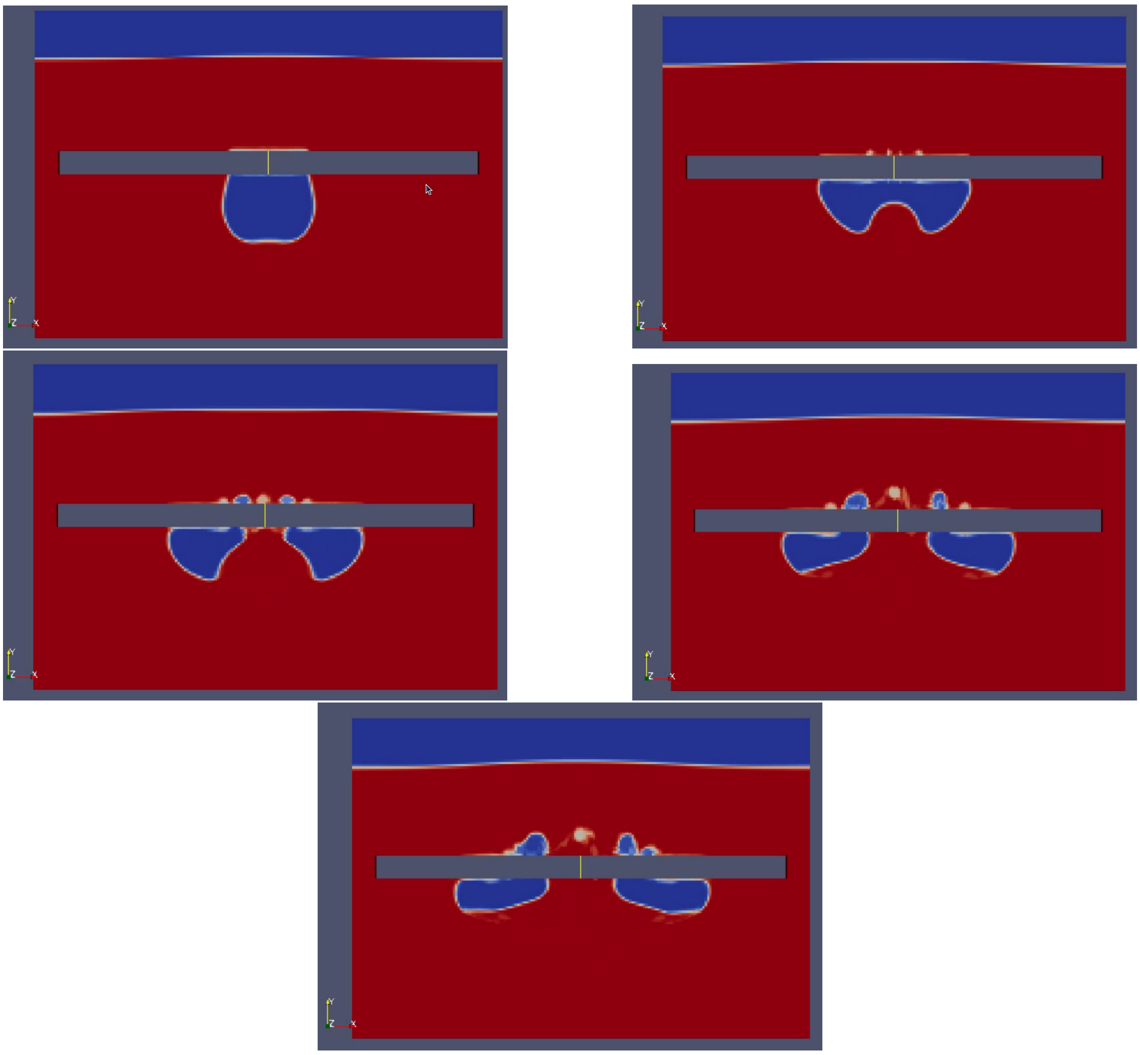

Figure 3.2: Frames taken from the gas bubble dynamics with a 10 Pa bubble point, a contact angle of 60 ° and a pressure drop across the sponge panel proportional to velocity. The order is from left to right and from the top.

through the pores is due to the low bubble point pressure.

3.1.3.3 Air Bubble in Water, Bubble Point of 5000 Pa and Pressure Drop

This test case simulates an air bubble in liquid water. The phases are compressible and immiscible, and a VOF algorithm has been used as in the previous cases. The sponge boundary condition has been applied, no specific contact angle is present, but the pressure drop through the screen is activated.
The gas bubble has to stick to the screen as to a wall, due to the high bubble point value, which does not allow the gas to pass through the channels of the PMD plate. Since there is no gas passage, the result shall be the same as the case where no pressure drop is applied.

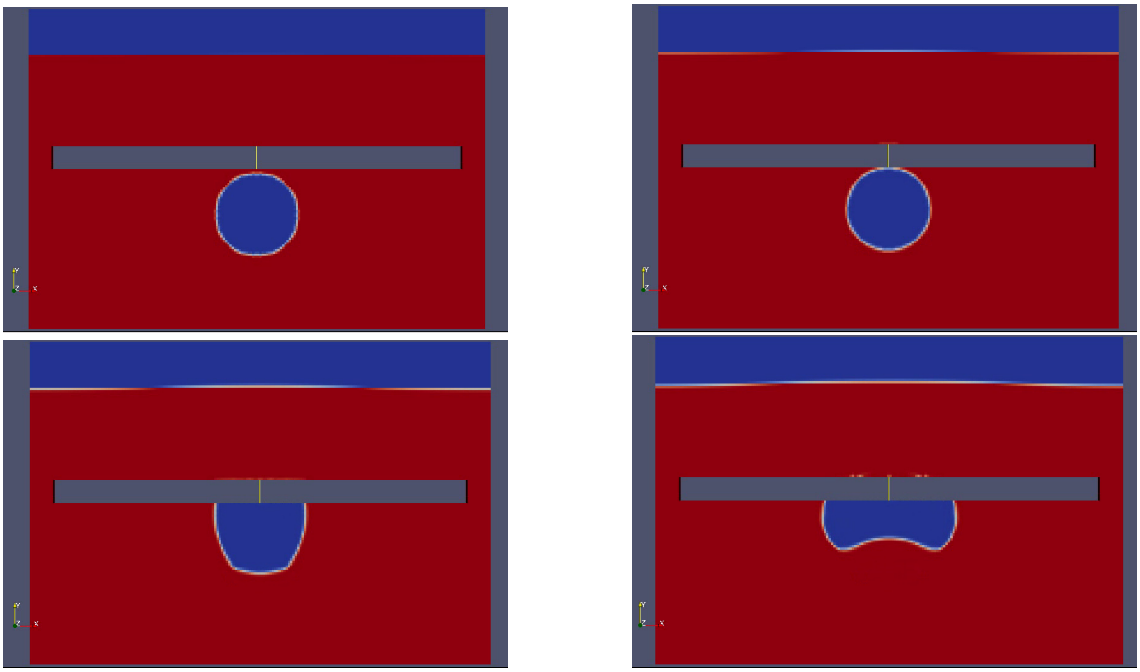

Figure 3.3: Gas bubble dynamics in case of a 5000 Pa bubble point with pressure drop. The order is from left to right and from the top.

From Fig.3.3, it is possible to see the bubble rising inside liquid water. Then it sticks to the screen, which behaves like a wall, and bounces staying attached to it, until viscosity damps this oscillation down. The pressure drop activation does not make any difference in the flow field, because it is calculated only if the gas flows through the screen and this is not the case, due to the high bubble point value.

3.1.3.4 3D Air Bubble in Water, Bubble Point of 20 Pa, 30° Contact Angle

This test case simulates a 3D air bubble immersed in liquid water, capturing all the dynamics connected with a 3D case. Not only the sponge boundary condition has been applied, but a contact angle of 30° has been accounted for between the fluid phases as well.

The gas bubble does not stick to the screen as to a wall, due to the low bubble point value, which allows the gas to pass through the channels of the PMD plate.

This simulation was created to verify the compatibility between the three boundary conditions implemented to fully describe the PMD. In particular, the numerical code stability was under investigation; the interest was in verifying the difference between the 2D and 3D fluid dynamics, with all the related effects.

Some pictures showing the results are presented hereafter.

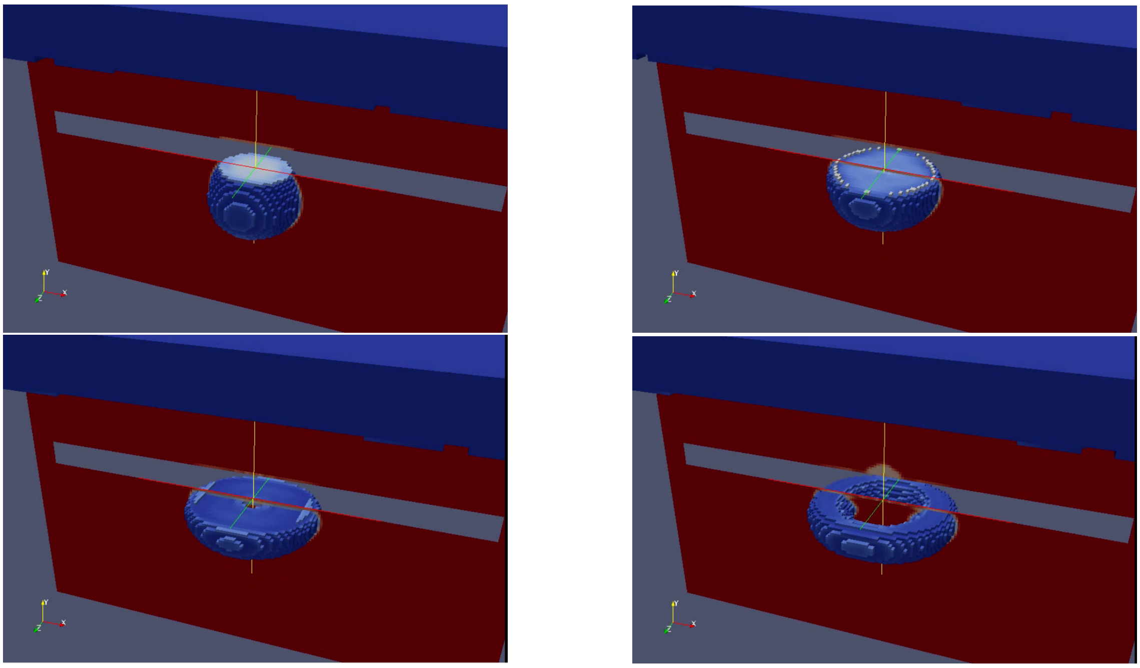

Figure 3.4: 3D gas bubble dynamics, with a 20 Pa bubble point and a contact angle of 30 °. The order is from left to right and from the top.

From the pictures collected in Fig.3.4, it is possible to see the bubble rising inside the liquid water and passing through the PMD screen, which is similar to a filter. The gas flow through the pores is due to the low bubble point pressure.

3.1.3.5 3D Air Bubble in Water, Bubble Point of 200 Pa, 60 ° Contact Angle

This test case simulates a 3D air bubble immersed in liquid water, capturing 3D dynamics. Not only the sponge boundary condition has been applied, but also a contact angle of 60 °. The gas bubble sticks to the screen as to a wall, due to the bubble point value, which does not allow the gas to pass through the PMD plate.

This simulation was created to verify the compatibility between the three boundary conditions implemented to fully describe the PMD behavior. In particular, the numerical code stability was under investigation; the interest was in verifying the difference between the 2D and 3D fluid dynamics, with all the related effects.

Some pictures showing the results are presented hereafter.

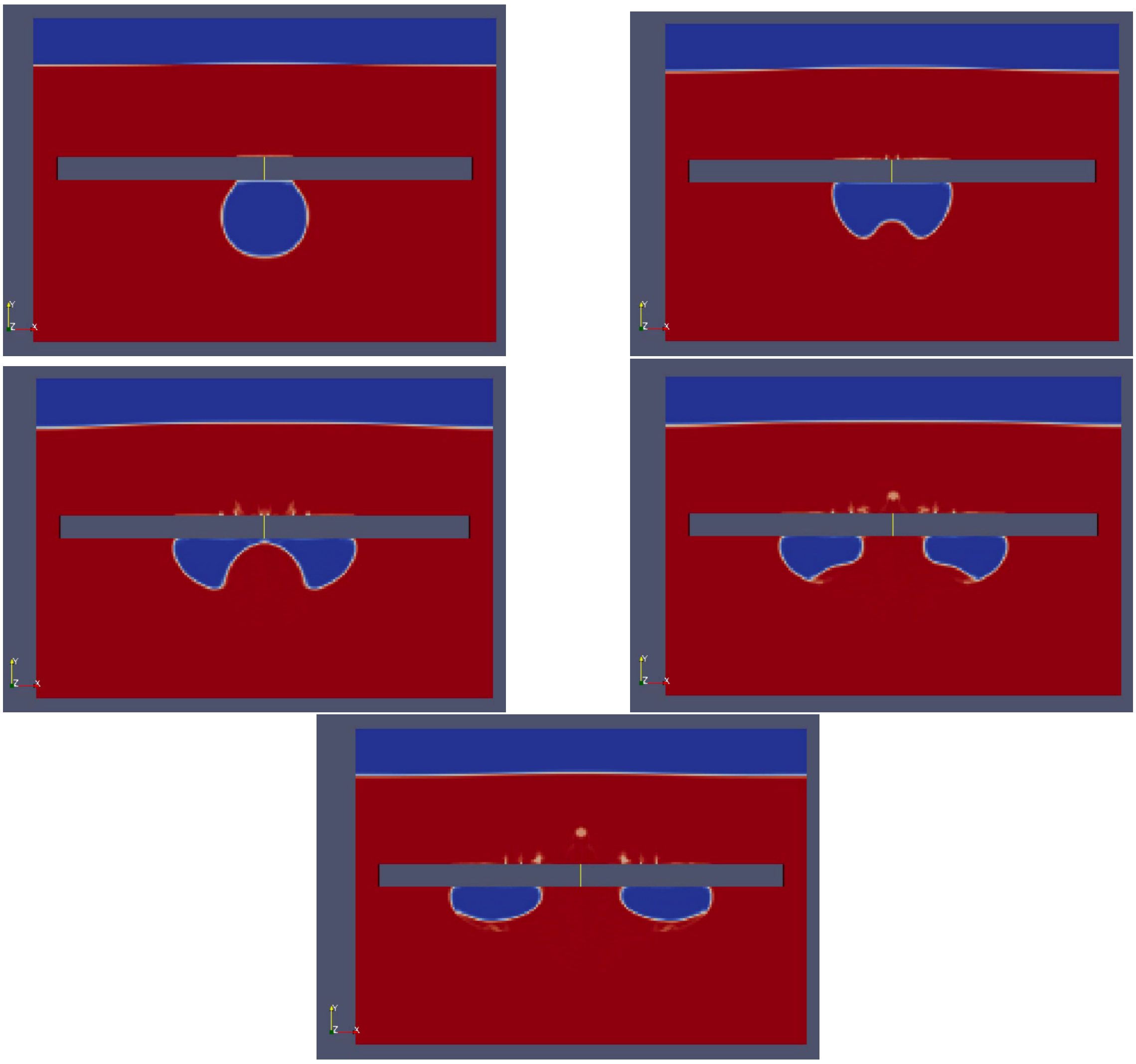

Figure 3.5: 3D gas bubble dynamics in case of a 200 Pa bubble point and a 60 ° contact angle. The order is from left to right and from the top.

From the pictures in Fig.3.5, it is possible to see the bubble rising inside the liquid water and sticking to the screen, which behaves like a wall, and bounces staying attached to it, until viscosity damps this oscillation down.

3.2 CFD Validation for Hybrid Rockets Internal Ballistics

In this section, the rocket configurations used for the validation of the CFD simulations are described. They come from two different experimental set up, built in 2009 and 2011 respectively.
The corresponding CFD geometries created for the numerical study are described as well, and finally the results comparison between experiments and CFD are presented.

The difference between the CFD results and the corresponding experimental findings has been calculated using the average values obtained from the tests conducted and the parameters extracted from the software.
The uncertainty of the software has not been estimated, because this would have required a dedicated study about uncertainty management in CFD and was not the purpose of this preliminary analysis. This kind of an investigation requires many simulations conducted to verify the results sensibility to the input variations or the implementation of an ad hoc modification to the CFD software applied.

3.2.1 Hybrid Rocket Configurations Analyzed

Two different rocket scales have been taken into consideration, to evaluate the reliability of the results obtained from the CFD simulations. Tests have been conducted on different configurations of laboratory-scale and increased-scale hybrid rockets, designed and tested by Grosse in 2009 [18] and by the CISAS hybrid rocket team [7] in 2011.

In particular, the configurations analyzed are the following:

- No-diaphragm lab-scale - Grosse's tests;
- 1-hole diaphragm lab-scale - Grosse's tests;
- 4-hole diaphragm lab-scale - Grosse's tests;
- 1-hole diaphragm lab-scale - CISAS tests;
- No-diaphragm increased-scale - CISAS tests;
- 1-hole diaphragm increased-scale - CISAS tests.

The experiments of both the lab-scale configurations have been conducted in pressure-regulated conditions, whereas the increased-scale tests have been performed in self-pressurized conditions.
The lab-scale and increased-scale geometries are presented in the following subsections.

3.2.1.1 Lab-scale Hybrid Rockets

Some of the lab-scale geometries analyzed by means of the CFD refer to Grosses's hybrid rocket motor, tested in 2009.

It consists of a robust aluminum injection head, an aluminum combustion chamber and a non-cooled nozzle section (these components are visible in Fig.3.6).

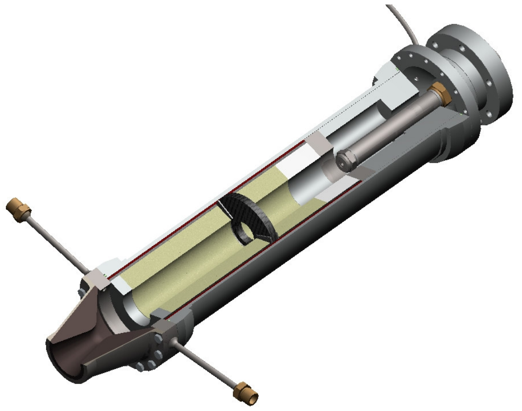

Figure 3.6: Section of Grosse's hybrid rocket laboratory motor.

A single full-cone swirl injector is used to atomize and distribute the nitrous oxide inside the port cross section.
A polyethylene end ring is added to support the grain against the nozzle and to protect its face against regression. A small ring, where pressure sensors are placed, is located between the combustion chamber and the nozzle section.
Another sensor is screwed into the injection head. The additional ring and the converging part of the nozzle form a small post-combustion chamber. More details about the experimental set up of this motor can be found in the paper written by Grosse[18].

Two pressure measurement locations have been used in the experimental set up (see Fig.3.6): the first, near the injection section is called Pc3 and the second, near the nozzle, is Pc1.

The other lab-scale configurations simulated are meant to reproduce and study the hybrid rocket tested at CISAS in 2011. The rocket geometry is presented in Fig.3.7.

Three types of 1-hole diaphragms were tested in this case: the ratio of the center-hole area and nozzle throat area was 1.5, 1 and 0.5. In all the experiments, oxidizer mass flow rate, grain dimensions, diaphragm position, burn time and nozzle dimensions were fixed and a stable combustion was achieved.

The first and second grain segments are 30 mm and 90 mm long, respectively. The port diameter is 30 mm and the diaphragm introduced is 6 mm thick. Injection is performed by a shower-head injection plate (see Fig.1.8).

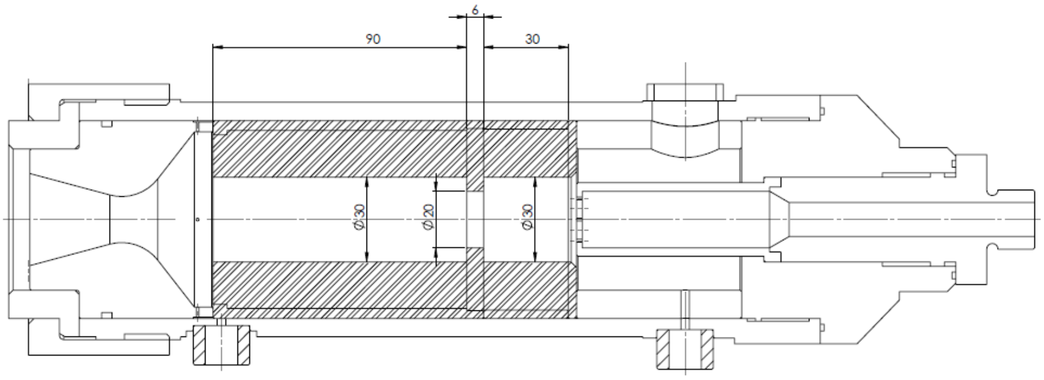

Figure 3.7: CISAS lab-scale rocket with a 1-hole diaphragm.

3.2.1.2 Increased-scale Hybrid Rocket

The increased-scale CISAS hybrid rocket has been tested in two configurations: using a 1-hole diaphragm and without any mixing device introduced into the combustion chamber.
A shower head injector has been used to atomize and distribute the nitrous oxide inside the port (Fig.1.8).
The first section of the fuel grain is 58 mm long and the second one has a length of 172 mm. They both have an average diameter of 57 mm, whereas the 1-hole diaphragm has a diameter of 29.9 mm.
The diameter of the hybrid rocket throat section measures 29.9 mm.

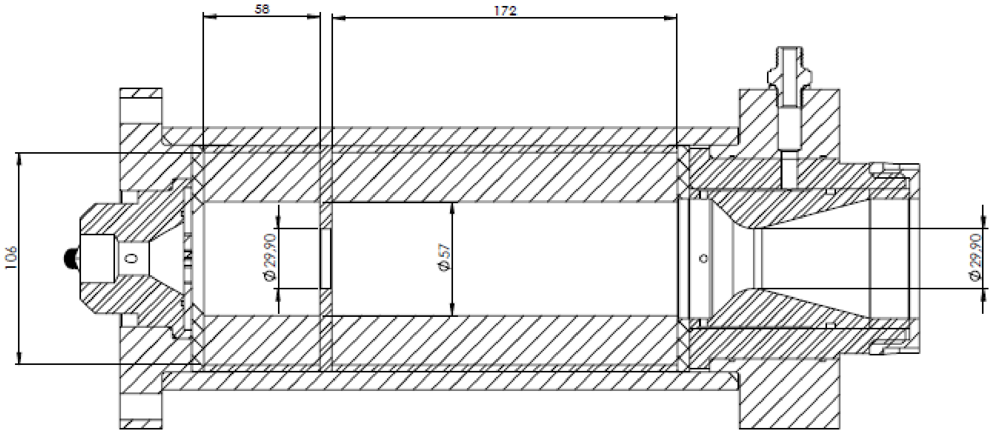

Figure 3.8: Section of the increased-scale hybrid rocket tested at CISAS.

3.2.2 Hybrid Rocket CFD Geometries Created for the Simulations

This section presents the geometries prepared to reproduce the hybrid rockets tested.
They represent the flow field inside the rockets and therefore are created to simulate the

internal volumes.

3.2.2.1 Geometries for CFD Analyses of the Lab-scale Rockets

The geometries used for CFD analyses have been created considering the shape of the flow field inside rocket motors. In Fig.3.9, an example of the geometries created is illustrated: there is a 35 mm splash ring (1–premixing chamber), having a diameter of 29.3 mm. The grain length (2, 3) is 166 mm, and its diameter is 36.6 mm.

The 4-hole diaphragm is 6 mm thick, with two slices of protective material which are 1 mm thick.

After the grain, an end protection (6) is placed, with the same diameter as the splash ring and a thickness of 10 mm.

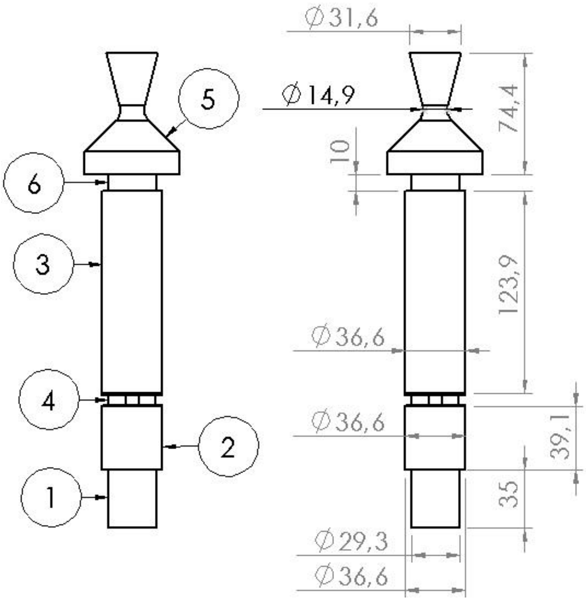

Figure 3.9: CFD geometry, lab-scale configuration analyzed [mm] in Grosse's campaign.

The nozzle (5) starts from a diameter of 58 mm, the throat is 14.9 mm wide and the exit diameter is 31.6 mm, with a cone having a semi-angle of 14 °.

The 4-hole diaphragm modeled for the CFD analyses has the same geometry tested by Grosse[18] (see Fig.3.10).

The CFD geometries have all been created using average diameters for the fuel grain segments. These averages have been determined using the grain thickness before and after the firings, as measured during the tests.

The fuel grain bore diameter has been averaged using the data of more than one test, to run the corresponding numerical simulation.

The same technique has been applied to create the CFD geometries for the analysis of the lab-scale rocket, tested in 2011 by CISAS hybrid rocket team[7]. In Fig.3.11, one of the geometries used for the study of this configuration is illustrated.

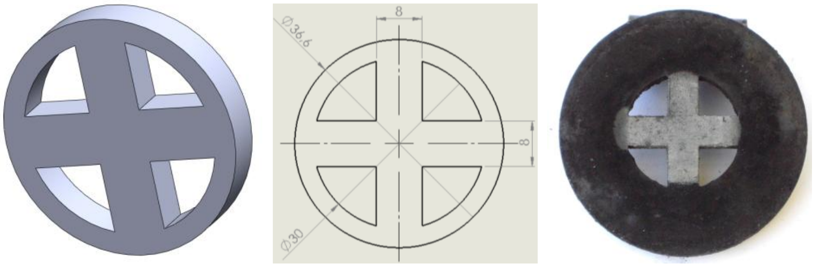

Figure 3.10: 4-hole diaphragm (mm).

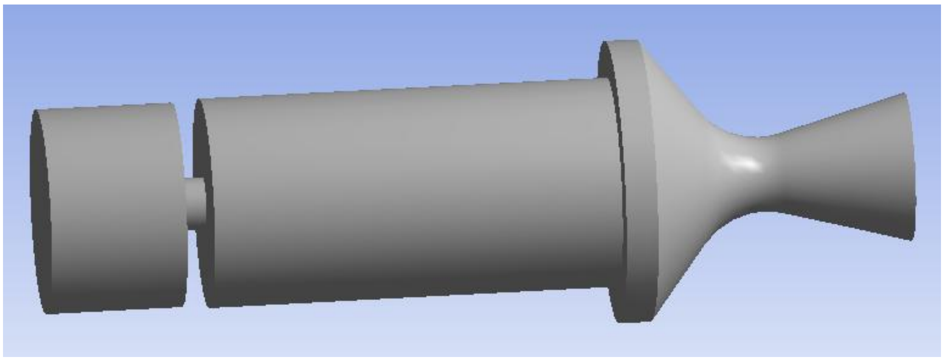

Figure 3.11: CFD geometry for the CISAS lab-scale rocket having a 1-hole diaphragm.

3.2.2.2 Geometry for CFD Analyses of the Increased-scale Rocket

The geometries used for this CFD study are derived from the internal volume of the hybrid rocket and one of them is showed in Fig.3.12. Liquid N_2O is injected from the green surface highlighted, whereas the outlet surface is highlighted by the black arrows.

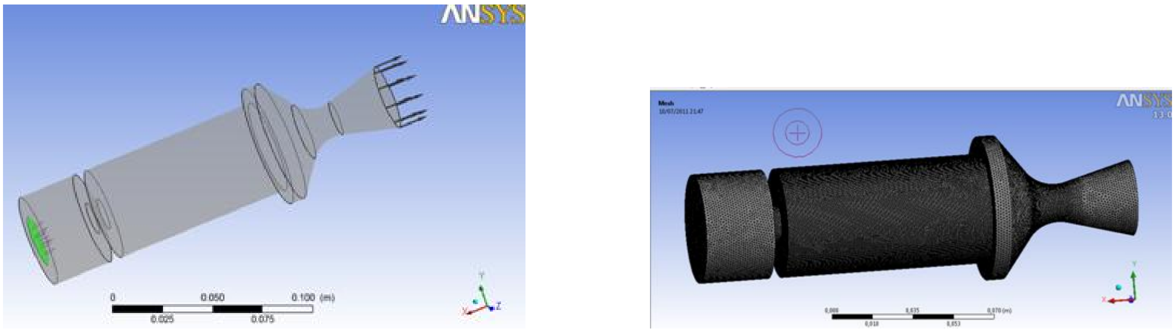

Figure 3.12: Geometry used for the CFD analyses.

These geometries have been created using the average port diameter before and after the motor burn and the grain segments lengths are equal to those of the real motor. The diameters characterizing the various nozzle sections are the same as the corresponding internal diameters of the hybrid rocket tested.

Concerning the meshing technique, it is possible to see in Fig.3.12 that the first grain segment has a characteristic average cell size greater than the second one. This has been necessary to avoid the instabilities created by the flow recirculation caused by liquid injection, when using the steady state solver.

The other geometry tested (Fig.3.13) presents the same characteristics as the one just described, but without any diaphragm.

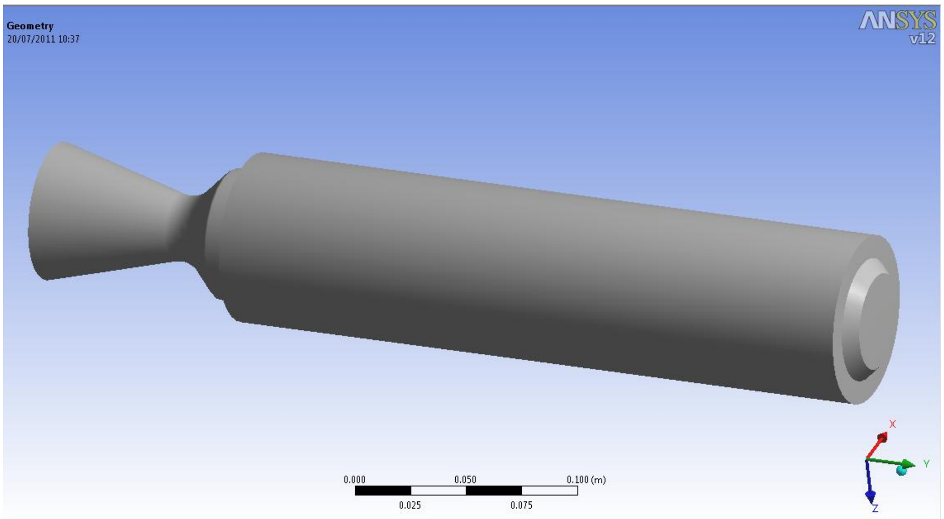

Figure 3.13: Increased-scale rocket without the diaphragm.

3.2.3 Gas Injection Test Cases

In this paragraph, the first studies about hybrid rockets internal ballistics are presented. Injection is simulated using gaseous N_2O and many turbulent models are applied, in order to discuss the differences among them and to verify which is the one giving the best solution compared to experiments.
This study is inherent to the tests conducted by Grosse, with a rocket geometry reproduced for the first analyses verifying CFD capabilities.
The main interest was to prove that CFD is able to predict experimental results and can be used as an efficient tool to analyze different geometries and design performing solutions.
This analysis also wanted to verify if it is possible to define a specific turbulence model as the most suitable to describe those physical problems where turbulent flames are present.

3.2.3.1 Test Matrix for Gaseous Injection Simulations

The analyses conducted on Grosse's geometries are of two types:

- Data related to the single tests is used to obtain the required boundary conditions, to validate the CFD code by examining the differences between a specific experiment and the corresponding simulation;

- Data related to more tests analyzing the same rocket configuration (same diaphragm position and injector type) is used to obtain the average flow field physical parameters, which have been used to assess different turbulence models and to investigate the diaphragm influence on the flow field.

In Tab.3.1 the test matrix is presented:

- 4 simulations (1-4) with the same geometry (no diaphragm, average data) and different turbulence models (k-ω, k-ω SST, k-ϵ RNG, k-ϵ standard);
- 4 simulations (5-8) with the *no-diaphragm* configuration, using single test results from Grosse's campaign, obtained for the configuration without the diaphragm;
- 4 simulations (9-12) with the same turbulence model (k-ϵ standard) and different geometries and positions of the diaphragm (1 and 4 holes, at the 33 % and 24% of the fuel grain length), to study the diaphragm effect on the flow field.

Sim.	**Reference**	$\dot{m_{N_2O}}$ [kg/s]	$\dot{m_{fuel}}$ [kg/s]	**OF ratio**
1	k-ω	0.2916	0.0516	5.65
2	SST	0.2916	0.0514	5.67
3	RNG	0.2916	0.0507	5.75
4	k-ϵ	0.2916	0.0517	5.64
5	test 45	0.2982	0.0485	6.15
6	test 19	0.2837	0.0524	5.41
7	test 13	0.3046	0.0559	5.45
8	test 14	0.2798	0.0487	5.75
9	test 1 hole 33%	0.2967	0.0626	4.74
10	test 1 hole 24%	0.2716	0.074	3.67
11	test 4 hole 33%	0.2412	0.0729	3.31
12	test 4 hole 24%	0.2829	0.0772	3.66

Table 3.1: Test matrix of the first gas injection tests, prepared starting from Grosse's campaign.

To retrieve the averages from the measurements, in order to make a comparison with CFD results, the following experimental data has been used (test numbers are related to Grosse's classification):

- No-diaphragm: tests 13 - 14 - 19 - 45;
- 1 hole, 24 %: tests 52 - 53;
- 1 hole, 33 %: tests 49 - 51;
- 4 holes, 24 %: tests 54 - 55;
- 4 holes, 33 %: test 56.

3.2.3.2 Turbulence Models Comparison

This paragraph resumes the results obtained applying different turbulence models. No specific new model has been implemented, the most famous and used ones have been analyzed and compared.
The difference between the CFD results and the tests has been calculated using the average values presented in the tables and measured during the experiments.

The k-ϵ model and the k-ϵ RNG give the same results. The k-ω model gives different outputs with respect to the k-ϵ, while the k-ω and k-ω SST models give the same results. With the k-ω model, flame temperature is 400 K lower than with the k-ϵ. This lower temperature is due to a lower predicted turbulent mixing (and consequently a slower reaction rate) in the flame zone. Experimental investigation confirms that flame temperature is lower than the maximum adiabatic temperature [24],[10].

Pressure depends on the square of temperature, so that it is lower and this in turn reduces efficiency. The efficiency obtained with k-ω corresponds with a very small error (lower than 1%) to the average efficiency extracted from experimental results.
However, it is not possible to say that all the approximations used in the different models have a negligible effect; in the author's opinion, they probably tend to compensate each other.

Sim.	**Reference**	T_{max} [K]	P_{c1} [bar]	P_{c1} **Exper.**[bar]
1	k-ω	3052	24.8	26.4
2	SST	2993	24.7	26.4
3	RNG	3387	26.5	26.4
4	k-ϵ	3407	25.9	26.4

Table 3.2: CFD gas injection results, compared to the corresponding average parameters measured during Grosse's campaign (I).

Sim.	P_c **Error**	P_{c3} [bar]	Δp [bar]	Δp **Exper.**[bar]
1	-6.2 %	25.2	0.41	0.13
2	-6.5 %	25.2	0.48	0.13
3	0.4 %	27.0	0.49	0.13
4	-2 %	26.3	0.47	0.13

Table 3.3: CFD gas injection results, compared to the corresponding average parameters measured during Grosse's campaign (II).

The theoretical C^* in Tab.3.4 and 3.5 is the characteristic velocity calculated by Grosse[18] for the combination of nitrous oxide and solid paraffin with the ICT thermochemical code[1]. C^* CEA is the characteristic velocity for the adiabatic combustion of gaseous ethylene and hydrogen with gaseous nitrous oxide, the same reactants as in the CFD simulations, calculated

---

[1] see http://www.ict.fraunhofer.de/EN/coreco/EM/Ex/ICTcode/index.jsp

Sim.	C^*[m/s]	C^* **Exper.** [m/s]	C^* **theor.**[m/s]	C^* **CEA**[m/s]
1	1308.8	1313.4	1549.2	1621
2	1305.5	1313.4	1549.2	1621
3	1399.8	1313.4	1549.2	1621
4	1364.8	1313.4	1549.2	1621

Table 3.4: CFD gas injection results, compared to the corresponding average parameters measured during Grosse's campaign (III).

Sim.	**Efficiency**	**Exper. efficiency**	**Efficiency error**
1	0.84	0.85	-0.36 %
2	0.84	0.85	-0.61 %
3	0.90	0.85	6.58 %
4	0.88	0.85	3.91 %

Table 3.5: CFD gas injection results, compared to the corresponding average parameters measured during Grosse's campaign (IV).

with the CEA thermochemical software.
If the wall heat flux is correctly predicted, it is equal to paraffin vaporization energy. For this reason, efficiency has been calculated with the theoretical C^*, in order to have a direct comparison with Grosse's calculation. If the wall heat flux is not correct, this efficiency can exceed one.

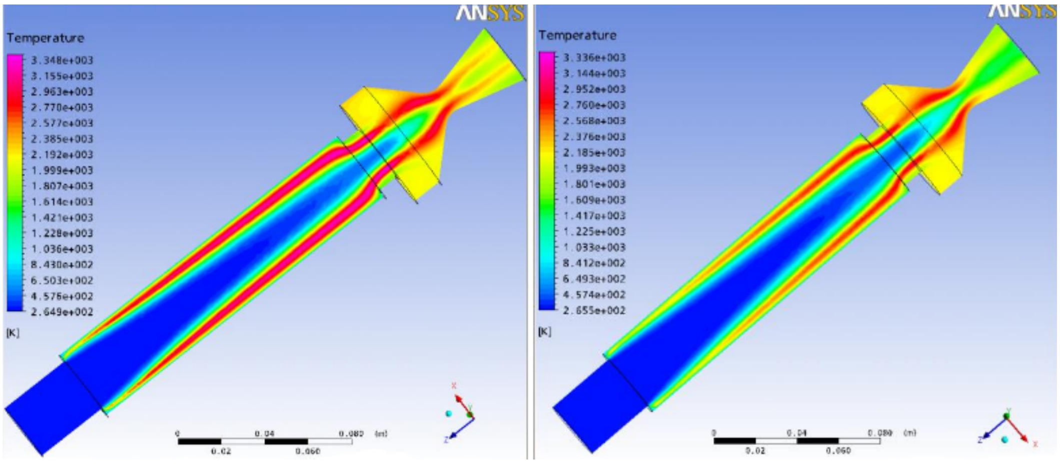

Figure 3.14: Temperature profile for different turbulence models: k-ϵ (left) and k-ω (right).

Apart from the RNG case, the predicted pressure is lower than the average value measured, probably because mass flows due to fuels other than paraffin have been neglected. Considering the uncertainty in the pressure measurement of ±1%, the pressure value determined by the RNG model is within the range of possible values, which is 26.14 bar - 26.67 bar. The other models give pressures that differ more from the average value measured, but they can still be considered as compatible.

Concerning C^*, the uncertainty on this parameter can be determined propagating the uncertainties of the other measured flow parameters. This way, the resulting C^* uncertainty is around ±4% and consequently the values obtained through CFD are in accord with experiments.

3.2.3.3 Analysis of the Basic Rocket Configuration

In this case, the data presented compare some specific experiments to the corresponding CFD simulations. The tests are numbered and the average parameters extracted from experiments are reported in the tables. CFD physical parameters are showed as well.

The CFD-predicted combustion chamber pressure agrees with experiments, considering an uncertainty of ±1% on the measurement. The errors presented in the tables refer to the difference from the CFD value and the average value derived from the tests.

The predicted CFD efficiency has been compared to the average value resulting from experiments, with the aim to verify if the software predicts correctly the most performing geometry solution in terms of diaphragm type (1 or 4 holes) and position (24% or 33% of the fuel grain length).
Considering an uncertainty of ±4% on the estimated C^* deriving from experiments, it can be concluded that the CFD predicts correctly the most promising rocket design.

Sim.	**Reference**	T_{max} **[K]**	P_{c1} [bar]	P_{c1} **Exper.**[bar]
5	test 13	3404	27.5	27.6
6	test 14	3415	24.9	25.2
7	test 19	3429	25.5	26.1
8	test 45	3431	26.2	26.7

Table 3.6: Single tests CFD results: pressure and temperature compared to the average measurements (I).

Sim.	**Error** [%]	P_{c3}[bar]	ΔP [bar]	ΔP **Exper.** [bar]
5	-0.6	28.0	0.51	0.01
6	-1.2	25.3	0.44	0.11
7	-2.1	26.0	0.48	0.49
8	-1.7	26.7	0.47	-0.11

Table 3.7: Single tests CFD results: pressure and temperature compared to the average measurements (II).

In the flame zone there are a temperature and a velocity peak (Fig.3.15), while density is at a minimum (Fig.3.16). The temperature peak is reached slightly above the velocity peak. This is probably due to the higher molecular weight of the carbon dioxide compared to the fuel.
Velocity inside the boundary layer is higher than in the central oxidizer core. This means that

Sim.	C^*[m/s]	C^* **Exper.** [m/s]	C^* **Theor.**[m/s]	C^* **CEA**[m/s]
5	1376.5	1307.5	1539.0	1623
6	1373.2	1309.2	1552.5	1621
7	1375.8	1324.0	1536.8	1622
8	1369.5	1313.0	1568.3	1618

Table 3.8: Single tests CFD results: C^* and efficiency compared to the average measurements (III).

Sim.	**Efficiency**	**Exper. efficiency**	**Efficiency error** [%]
5	0.89	0.85	5.23%
6	0.88	0.84	4.92%
7	0.90	0.86	3.86%
8	0.87	0.84	4.33%

Table 3.9: Single tests CFD results: C^* and efficiency compared to the average measurements (IV).

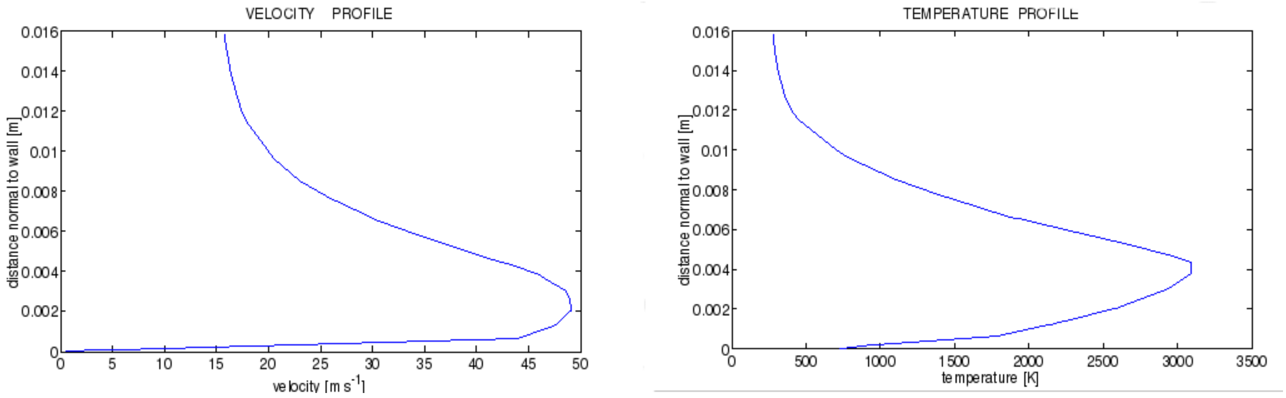

Figure 3.15: Velocity and temperature boundary layer profiles at half the grain length, no-diaphragm case.

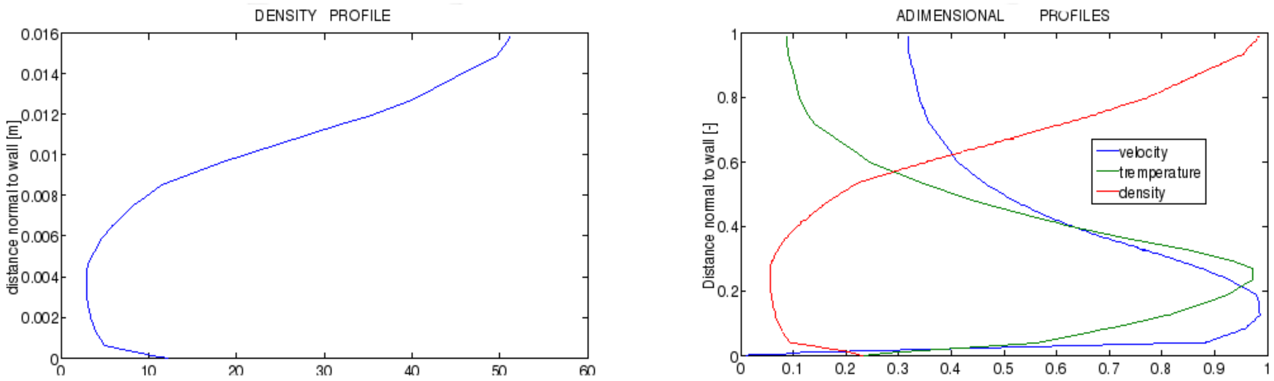

Figure 3.16: Density boundary layer profile at half the grain length, no-diaphragm case (on the left) and summary of all the profiles investigated.

the classical regression rate theory has to be modified to take this into account[13].

The average temperature and velocity increase also in the axis direction, while density decreases (Rayleigh motion).
The flame cone does not close inside the nozzle, so that combustion is incomplete. The flame does not form where reactants join in stoichiometric conditions (higher minimum reactant mass fraction) because reaction rate depends on the turbulent eddy frequency as well.

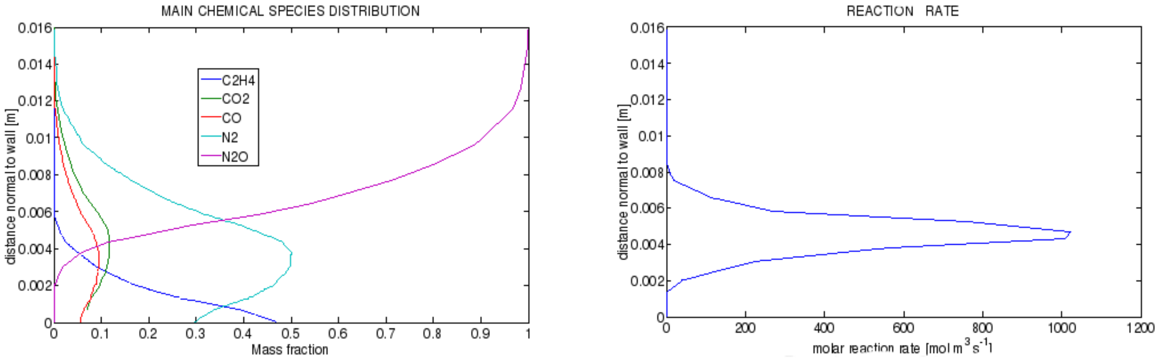

Figure 3.17: Main distribution of the chemical species and reaction rate at half the grain length, no-diaphragm case.

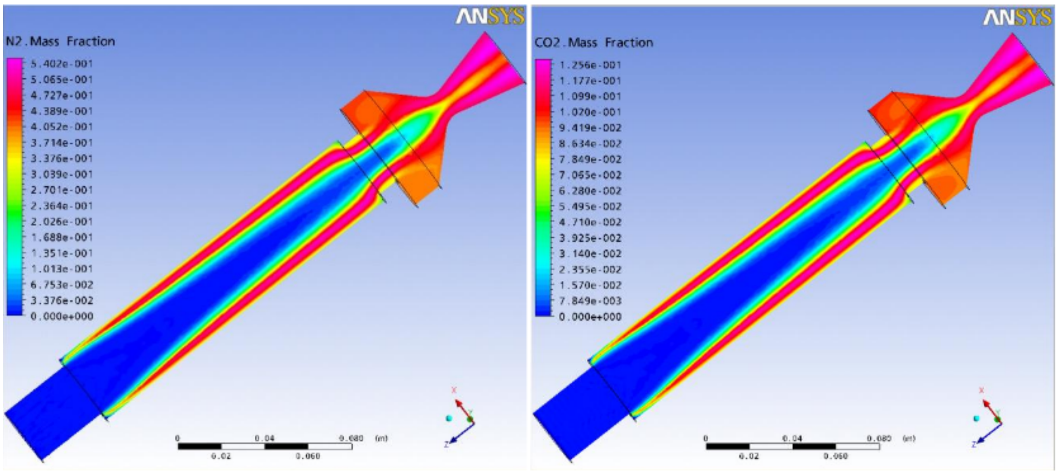

Figure 3.18: N_2 mass fraction (left) and CO_2 mass fraction (right) resulting from CFD for the no-diaphragm configuration.

The turbulent eddy frequency is higher near the walls, this accounts for a fuel-rich flame (sometimes the eddy dissipation model may predict unphysical behaviors, e.g., flames creeping across the walls).
This is confirmed by experimental results and is in contrast with the laminar flame, where the Burke-Schumann model applies [10],[16].

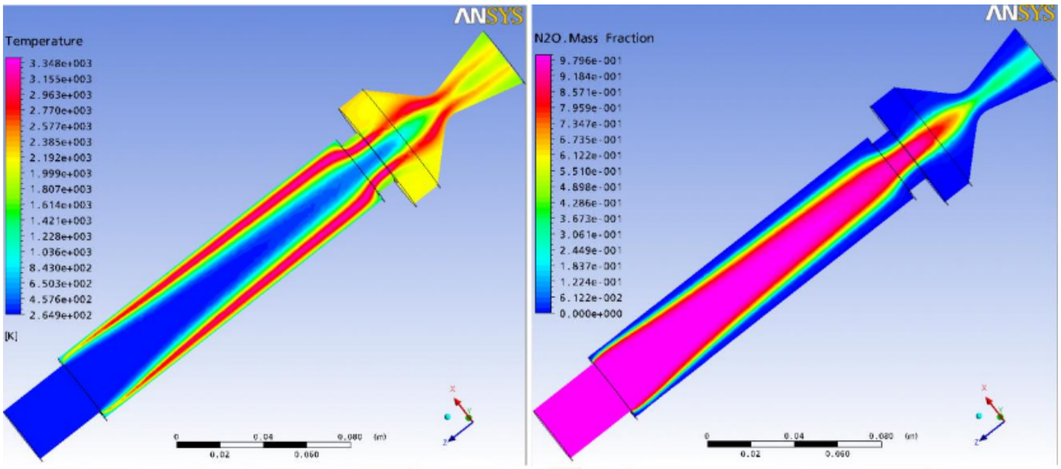

Figure 3.19: Temperature (left) and the N_2O mass fraction (right) resulting from CFD for the no-diaphragm configuration.

In the turbulent case, the flame is thicker. Here it appears to be thick due to time averaging (Fig3.19). In reality, the flame is thin and moves rapidly up and down due to the eddies (wrinkled laminar flame regime).
Probably, the flame is smeared also because of numerical diffusion. To estimate numerical diffusion more quantitatively, a detailed study about mesh convergence is necessary (this work only considers global convergence).

3.2.3.4 Diaphragm Effect on the Flow Field

In this section, a comparison is proposed between the experiments and CFD simulations concerning the effect of the diaphragm introduction on the flow field.
First of all, experimental results are presented and then tables are used to resume the corresponding CFD parameters.

The relationship between the average N_2O mass flow and the resulting average chamber pressure, as derived from experiments, is in Fig.3.20. The reference case is the configuration without the diaphragm, which can be compared with the test results of the positions 24% and 33%.
In general, hybrid rocket chamber pressure variation is not proportional to the oxidizer flow, because the fuel flow response is not linear to the oxidizer mass flow.

The large effect of a diaphragm positioned in the middle of the grain on chamber pressure and OF ratio, is proved in Fig.3.20 and 3.21. For 24% and 33% positions, pressure is about 15% higher compared to the no-diaphragm configuration and for the same oxidizer flow, almost alike for both mixing devices. This effect comes from a large efficiency increase and added fuel flow due to higher regression rates.
The 4-hole diaphragm performs similarly when positioned at the 24% and 33%.

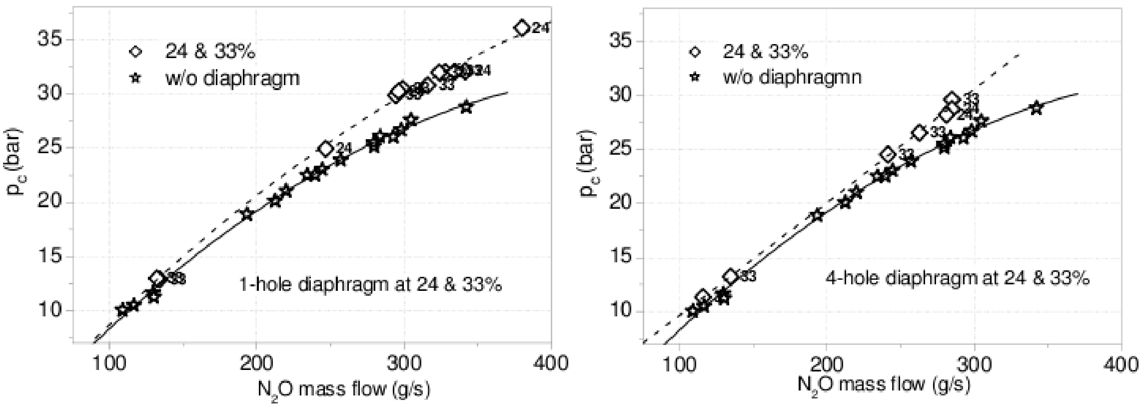

Figure 3.20: Average chamber pressure relative to atmosphere versus average N_2O mass flow.

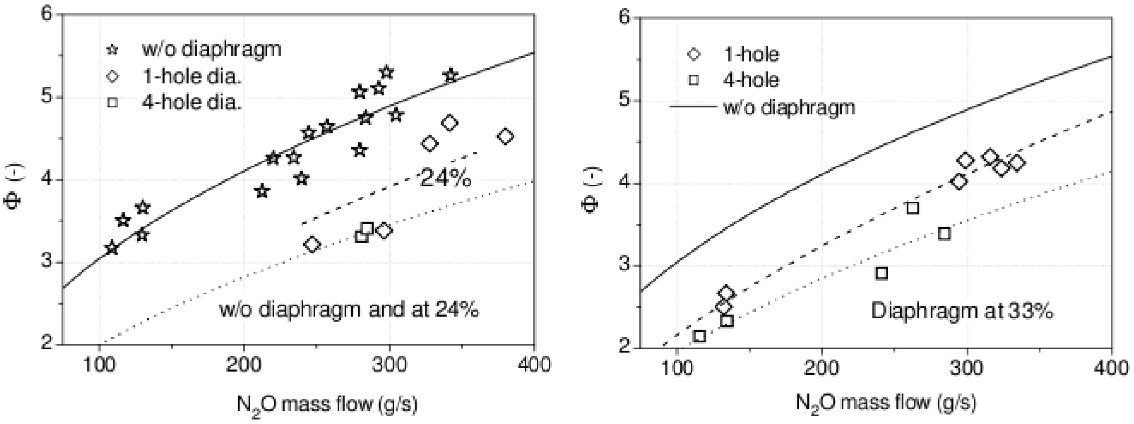

Figure 3.21: Total OF ratio versus average N_2O mass flow.

The fuel proportion in the propellant flow rises together with an increase of the average fuel regression rate as the diaphragm is moved in the injector direction. This can be seen in Fig.3.21 (total OF ratio versus oxidizer mass flow), where the results without the diaphragm are shown together with the diaphragm test results.

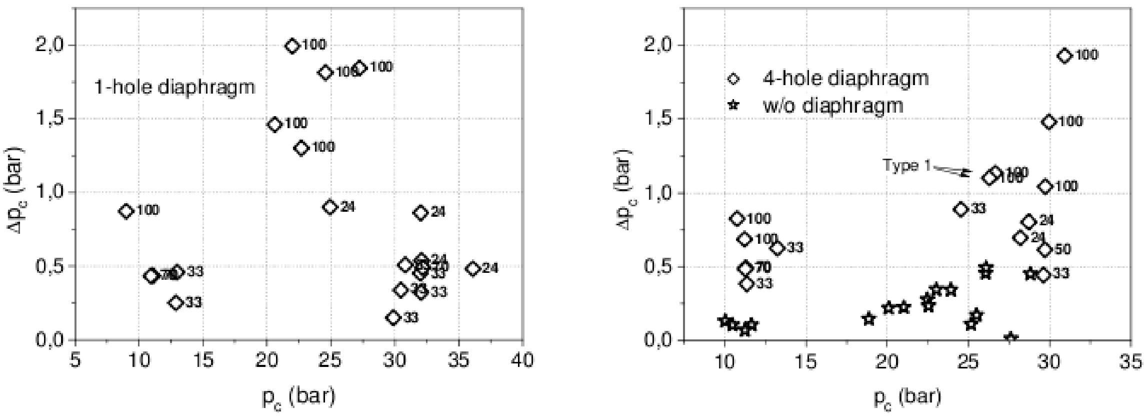

Figure 3.22: Average pressure drop caused by the diaphragms (1 and 4-holes) versus average chamber pressure relative to atmosphere.

The flow through the diaphragm causes a relatively large pressure drop, as in Fig.3.22. It is the price of the flow mixing, which reduces the pressure available to expand the flow in the nozzle. The pressure drop is calculated as the difference between chamber pressure near the injector and near nozzle inlet.

Without any diaphragm, the pressure drop is only ~0.15 bar at 10 bar and has a maximum value of 0.5 bar at 30 bar. At the 24% and 33% of the grain, the pressure loss remains lower than 1 bar for the 1-hole tests, when chamber pressure is 30 bar, and lower than 0.5 bar in most cases. Placing the 4-hole device at these positions results in pressure losses between 0.5 and 1 bar at 30 bar.

Sim.	**Reference**	T_{max} **[K]**	P_{c1} [bar]	P_{c1} **Exper.**[bar]
9	1-33%	3374	28.4	30.2
10	1-24%	3351	26.8	27.6
11	4-33%	3403	23.9	24.5
12	4-24%	3399	27.8	28.4
4	no-diaph.	3407	25.9	26.4

Table 3.10: Diaphragm effect: pressure and temperature compared to the average measurements (I).

Concerning CFD results, the predicted efficiency for the diaphragm configurations is higher than for the basic motor and this is consistent with experimental results. The errors presented in the tables are calculated using the average values derived from experiments, but the real aim of this section is to present some qualitative results that can be inferred from the simu-

Sim.	P_{c1} **Error** [%]	P_{c3}[bar]	ΔP [bar]	ΔP **Exper.** [bar]
9	-5.9	29.6	1.24	0.24
10	-3.0	27.9	1.13	0.24
11	-2.7	25.0	1.11	0.89
12	-2.1	29.1	1.28	0.75
4	-2.0	26.3	0.47	0.13

Table 3.11: Diaphragm effect: pressure and temperature compared to the average measurements (II).

Sim.	C^*[m/s]	C^* **Exper.** [m/s]	C^* **Theor.**[m/s]	C^* **CEA**[m/s]
9	1426	1429.0	1495.8	1524.0
10	1400	1358.3	1395.8	1601.0
11	1379	1319.0	1349.2	1539.0
12	1396	1326.7	1410.0	1569.0
4	1365	1313.4	1549.2	1621.0

Table 3.12: Diaphragm effect: C^* and efficiency compared to the average measurements (III).

Sim.	**Efficiency**	**Exper. efficiency**	**Efficiency error** [%]
9	1.0	0.96	-0.22
10	1.0	0.97	3.08
11	1.0	0.98	4.59
12	1.0	0.94	5.26
4	0.9	0.85	3.91

Table 3.13: Diaphragm effect: C^* and efficiency compared to the average measurements (IV).

lations, showing how the flow can be altered by the diaphragm.

The predicted pressure drop in the combustion chamber is more than two times that of the basic configuration. The experimental pressure drop suffers from a significant scattering. This can be due to an incorrect pressure measurement next to the injector (position called Pc3), due to a local acceleration of the fluid flow.

The diaphragm induces gases recirculation and consequently the mixing of the different chemical species (Fig.3.26). This way, a local reaction rate increase near the diaphragm is obtained.
The diaphragm causes not only local effects, but also a change in the flame structure. Without the diaphragm, there is a clear separation between fuel and oxidizer.

Most of the combustion products are concentrated into the flame. The oxidizer mass fraction in the central core has a value near one, until N_2O is depleted. With the diaphragm, the situation is very different. The fuel still remains under the flame, while there is a mixing between the oxidizer and products.
This way, a higher oxidizer mass flux reaches the flame. The N_2O mass fraction in the central core lowers suddenly beyond the diaphragm due to the products. Flame is thicker and grain consumption higher.

The increased efficiency due to the diaphragm, derives from an increased mixing of the chemical species until all the oxidizer is depleted (see Fig.3.24 and 3.25), while without the diaphragm, combustion is less complete.
The presence of recirculation zones produces a considerable increase of the heat flux slightly above the diaphragm position, and this in turn increases regression rate.
This means that a small shift to higher OF ratios results as well, and that the rocket motor wall is locally reached by the hot combustion gases, so that insulation has to be strengthened to withstand for a longer period of time. Another possibility is to use a higher melting paraffin for the small fuel portion upstream and downstream of the diaphragm.

CFD simulations use a spatially uniform regression rate. In the real motor, regression rate is higher where thermal flux is larger so that, thanks to the blocking effect, the heat flux spatial variations are lower than predicted.
There is a loss of symmetry in the solution where the diaphragm is present: in fact the fluid field changes circumferentially. This is also true for the 1-hole diaphragm even if it is symmetric. Without the diaphragm, it is possible to verify Reynold's analogy and heat flux is proportional to wall shear stress.

This is not true for the configurations using the diaphragm, since it produces a complicated three-dimensional fluid field and the boundary layer approximation is no longer valid.
In the present simulations, wall heat flux can be used only for a qualitative interpretation (Fig.3.27 and 3.28). This is because the predicted blocking effect is much higher than in the real hybrid rocket, which uses a liquefying propellant (paraffin wax).

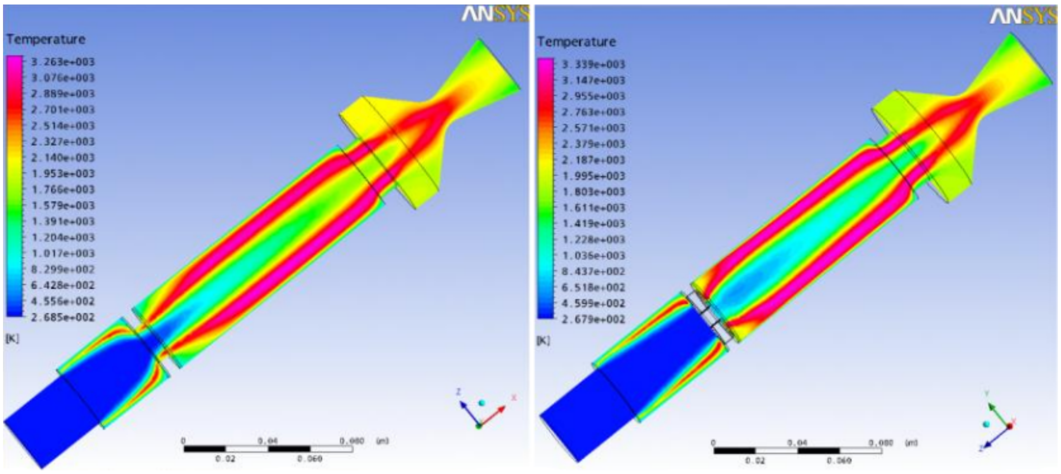

Figure 3.23: Temperature distribution for the 1-hole 24% configuration (left) and 4-Hole 33% configuration (right).

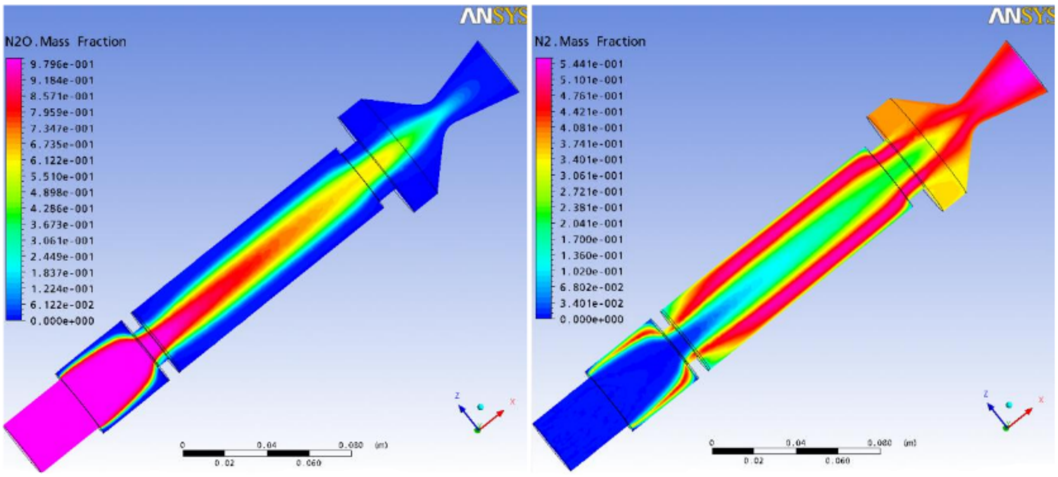

Figure 3.24: N_2O mass fraction (left) and N_2 mass fraction (right) for the 1-hole 24% configuration.

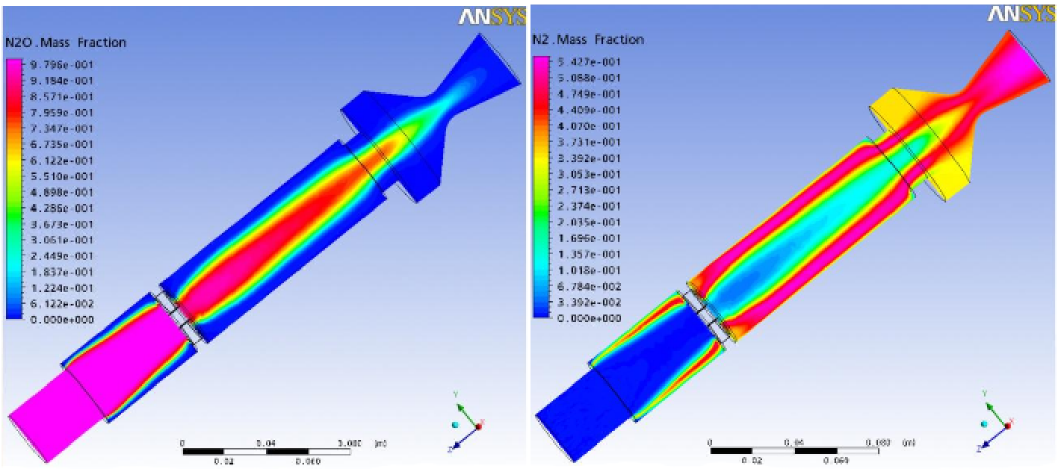

Figure 3.25: N_2O mass fraction (left) and N_2 mass fraction (right) for the 4-Hole 33% configuration.

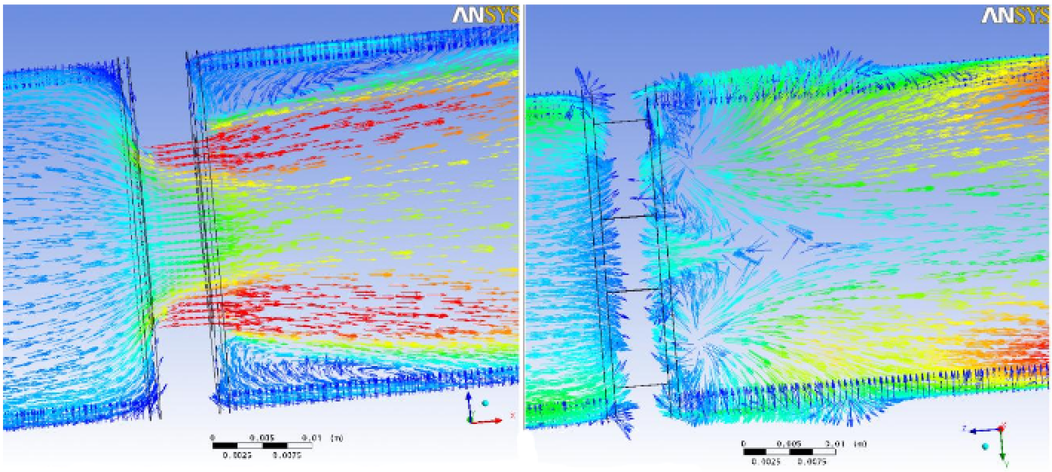

Figure 3.26: Recirculation after the 1-hole 24% diaphragm (left) and the 4-hole 33% diaphragm (right).

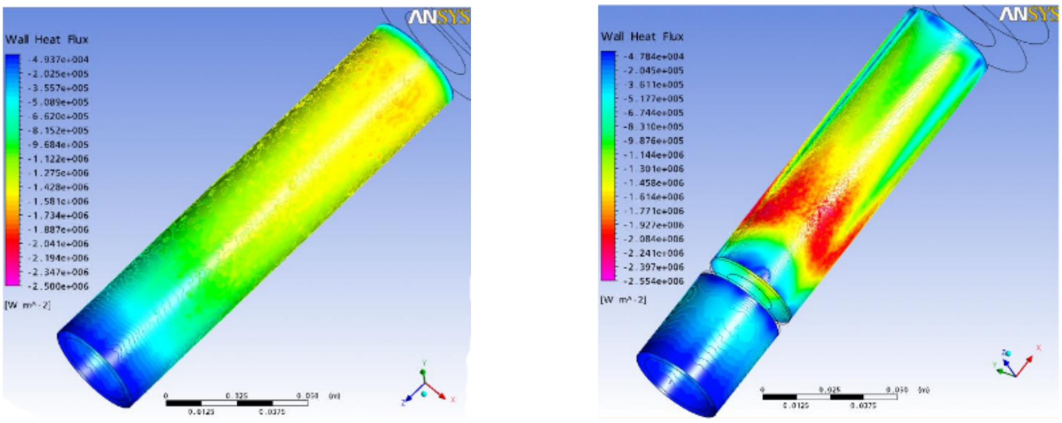

Figure 3.27: Wall heat flux at the grain for the no-diaphragm (left) and the 1-hole 24% configuration (right).

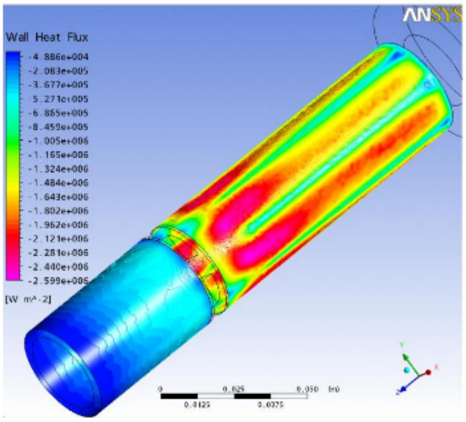

Figure 3.28: Wall heat flux for the 4-hole 33% configuration.

In the numerical simulation, all the fuel enters the domain in the gaseous phase, while in the experiments there is liquid droplets entrainment in the gas stream. In the real case, gaseous mass flux is lower and blowing is reduced; consequently the flame is closer to the wall and heat transfer is higher.

3.2.4 Liquid Injection Test Cases

The test cases created to validate the CFD simulations applying liquid injection are presented here.
CFD results are compared to the measured average physical parameters, and the motor efficiency calculated by the CFD is compared to that deriving from experiments.

3.2.4.1 Test Matrix for Liquid Injection Simulations

Tab.3.14, 3.15 and 3.16 resume the most important inputs for the various CFD test cases prepared.

In particular, Tab.3.14 illustrates the parameters applied to the simulations related to Grosse's lab-scale tests:

- The lab-scale motor with no diaphragm;
- The same lab-scale motor, but with a 4-hole diaphragm at the 24% of the fuel grain length.

Configuration I-Grosse	Rocket with No Diaphragm	4-Hole Diaphragm Rocket
Liquid oxidizer mass flow rate	0.2916 [kg/s]	0.2829 [kg/s]
Fuel mass flow rate	0.0517 [kg/s]	0.0772 [kg/s]
OF ratio	5.64	3.66
Oxidizer injection temperature	260 [K]	260 [K]
Oxidizer injection velocity	51.95 [m/s]	51.95 [m/s]
Initial particle size	1.2e-4 [m]	1.2e-4 [m]
Injection angle	45 [deg]	45 [deg]
Injector diameter	3.3 [mm]	3.3 [mm]
Turbulence model	$k-\epsilon$ std	$k-\epsilon$ std

Table 3.14: Input parameters for the simulations referred to Grosse's tests.

Tab.3.15 and 3.16 illustrate the parameters used for the boundary conditions of the two simulations related to the tests conducted at CISAS on the lab-scale and increased-scale rocket:

- Lab-scale hybrid motor having a 1-hole diaphragm;
- Increased-scale hybrid rocket with no diaphragm and with a 1-hole diaphragm.

Configuration II–CISAS Tests	**Lab-scale 1-Hole Diaphragm Rocket**
Liquid oxidizer mass flow rate	0.25 [kg/s]
Fuel mass flow rate	0.0622 [kg/s]
OF ratio	5.1
Oxidizer injection temperature	260 [K]
Initial particle size	1e-3 [m]
Injection angle	5 [deg]
Injector diameter	1e-3 [mm]
Turbulence model	$k-\epsilon$ std

Table 3.15: Input parameters for the simulations referred to CISAS tests.

Configuration II–CISAS Tests	**Increased-scale 1-Hole/No-Diaphragm Rocket**
Liquid oxidizer mass flow rate	0.937-0.936 [kg/s]
Fuel mass flow rate	0.1943-0.1954 [kg/s]
OF ratio	4.9
Oxidizer injection temperature	260 [K]
Initial particle size	1e-3 [m]
Injection angle	5 [deg]
Injector diameter	1e-3 [mm]
Turbulence model	$k-\epsilon$ std

Table 3.16: Input parameters for the simulations referred to CISAS tests.

Each of the configurations described has been analyzed with both gaseous and liquid injection. The test matrices resuming the simulations organization have the objective to permit the achievement of the main goals of this study, which are:

1. To compare the gas injection simulation results to those obtained for liquid injection;
2. To verify the accuracy of these simulations in reproducing experiments;
3. To assess that the injection model applied to the different injection plates is appropriate.

3.2.4.2 Validation Results for Liquid Injection Simulations

This paragraph presents the results of the study conducted on liquid injection. They have been divided, for clarity, into two different sections. Each of them refers to a specific hybrid rocket configuration or scale.
In particular, first of all the results obtained from the numerical reproduction of Grosse's lab-scale experiments are exposed, then the comparison between CFD results and CISAS lab-scale tests is discussed and finally the comparison between CFD simulations and CISAS increased-scale experiments is presented.

The experimental values in the tables are averages over all the tests run in the same configuration, while the CFD values are averaged on a reference section placed in the post-combustion chamber.

C^* uncertainty is calculated by propagating the uncertainties of the measured variables of interest, whereas the uncertainty on CFD results has not been estimated.

Comparison of the CFD Results with Grosse's Lab-scale Experiments

The results discussed here focus on the main differences between liquid and gas injection applied to the same rocket configuration.
Results are analyzed first of all qualitatively, and then tables are presented to resume the comparison more precisely, using experimental data as well.

CFD simulations for the configuration with the diaphragm predicted an efficiency higher than for the basic motor, and this is consistent with experimental results, both for liquid and gas injection.
The measured pressure drop in the combustion chamber is greater when a diaphragm is used, with respect to the no-diaphragm motor, and CFD predicts this condition correctly.
The diaphragm induces a large turbulence increase in the combustion chamber, enhancing at the same time the propellants mixing and the heat transfer to the wall, thus increasing combustion efficiency.

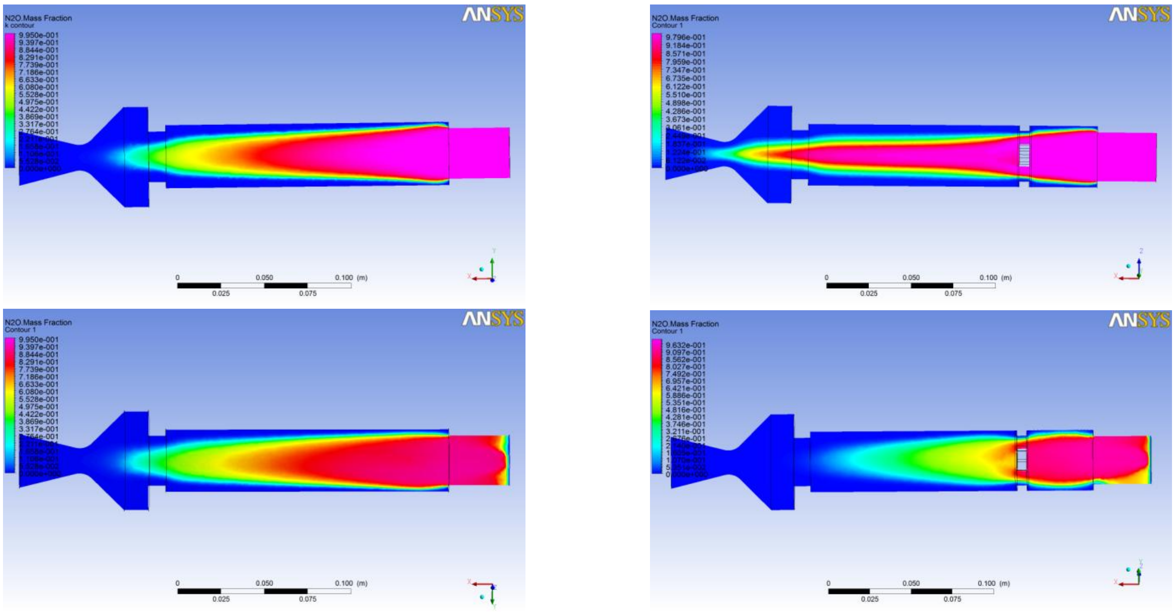

Figure 3.29: N_2O mass fraction of the no-diaphragm configuration (left) and 4-hole diaphragm rocket (right). Above the results of the gas injection test cases are illustrated, below liquid injection results are presented.

As found in a previous study[9] about gas injection, when liquid N_2O is injected, the 4-hole diaphragm configuration allows a faster N_2O consumption and therefore a more efficient combustion with respect to the no-diaphragm rocket.
In Fig.3.29 and 3.30, the two pictures above refer to the gas injection simulation, and the

two images below are related to liquid injection. From Fig.3.29 and 3.30, it can be seen that the gas and liquid injection cases referring to the no-diaphragm configuration are very similar, whereas there is a more diffuse flame in the liquid injection case for the 4-hole diaphragm.

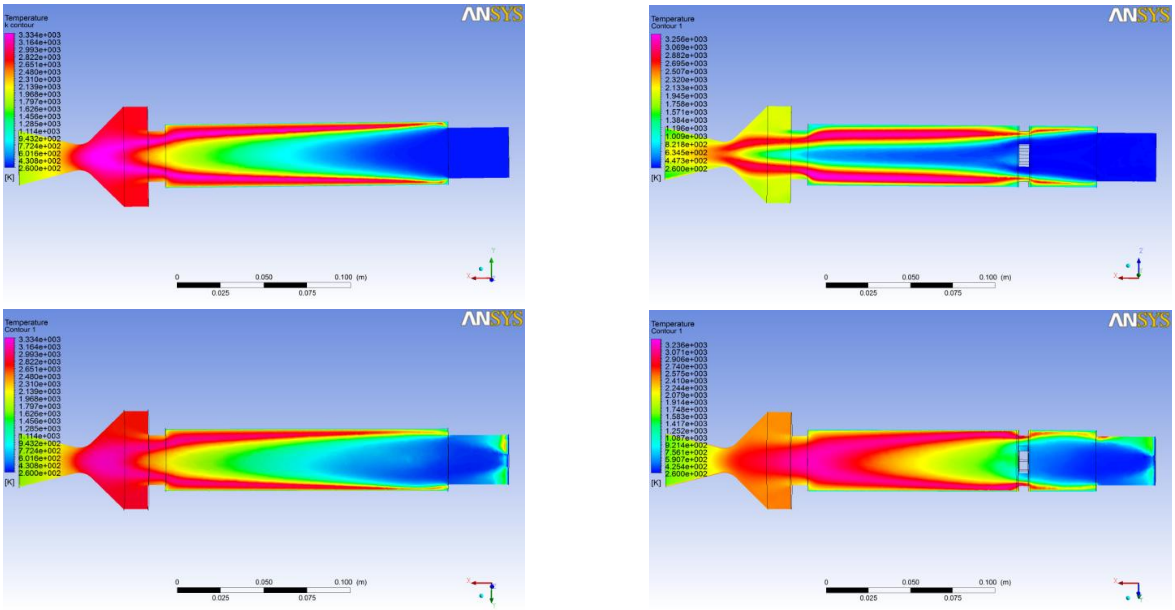

Figure 3.30: Flame structure and temperature for the two hybrid rocket configurations analyzed. Above gas injection results, below liquid injection results.

Between the liquid and gaseous case, the fluid field differs mainly in the motor portion where particles are not yet evaporated, while moving down the combustion chamber it tends to have the same characteristics. Placing a diaphragm in an axial position where the fluid field is still heavily influenced by the presence of liquid particles determines a significant change in the combustion behavior.

The diaphragm causes not only local effects, but also a change in the flame morphology in the rest of the combustion chamber, as already showed by Lazzarin[20]; this is clearly visible by both gas and liquid injection test cases (Fig.3.30).

With a mixing device, temperature remains higher in the combustion chamber core than if no diaphragm is used (Fig.3.30), and this causes a faster evaporation of the droplets in the diaphragm case.

This is also proved by Fig.3.31, where the droplet evaporation time is showed for these two configurations. When a diaphragm is used, particles evaporate faster and travel a shorter path.

A phenomenon appearing in these simulations with liquid injection is pre-chamber flow recirculation.

In Fig.3.30 it can be seen that temperature increases locally, near the injection section. This is due to flow recirculation, which causes a better mixing of the chemical species and a temperature homogenization.

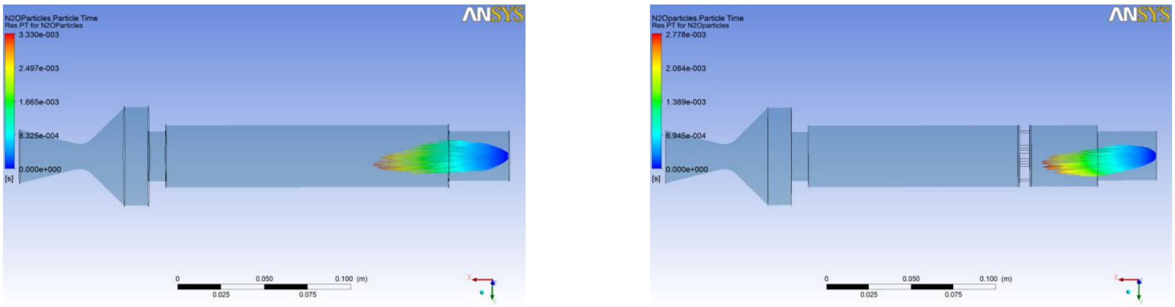

Figure 3.31: Droplet evaporation time for the no-diaphragm (left) and the 4-hole diaphragm (right) configurations.

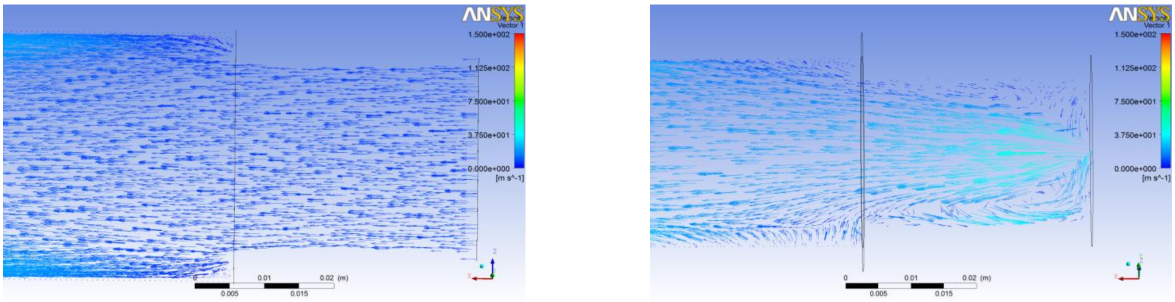

Figure 3.32: 4-Hole diaphragm rocket with gas injection (left) and with liquid injection (right), where a consistent flow recirculation is visible.

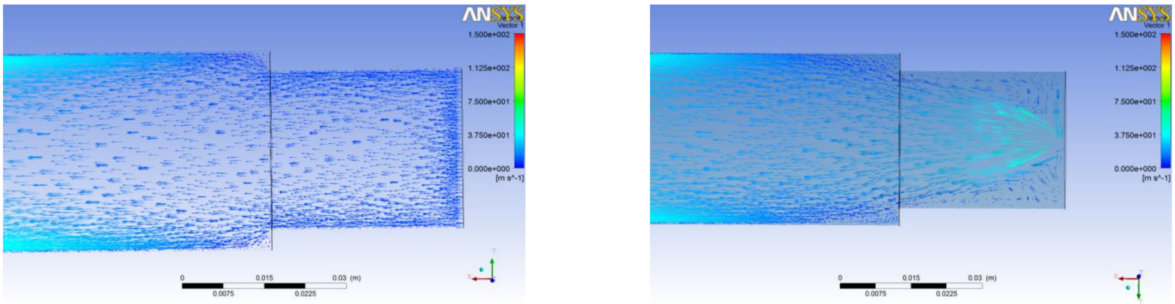

Figure 3.33: No-diaphragm configuration, with gas injection (left) and liquid injection (right), with a strong recirculation.

Tab.3.17 and the following, present the simulations results compared to Grosse's experiments.
Errors have been calculated between the CFD parameters extracted and the corresponding average parameters deriving from the tests.

In general, the simulations conducted with liquid N_2O allow the same conclusions discussed by Lazzarin[20].
The same trends for the global characteristics of one rocket configuration with respect to the other have been found simulating liquid as well as gaseous injection.

Sim. Type	T_{max}**[K]**	P_{postcc}**[bar]**	P_{postcc} **Exper. [bar]**
No-Hole Liquid	3130	27.64	26.39
4-Hole 24% Liquid	3308	26.88	28.45
No-Hole Gas	3341	27.70	26.39
4-Hole 24% Gas	3406	27.59	28.45

Table 3.17: CFD results compared to Grosse's average measurements (I).

Sim. Type	**Error P [%]**	$P_{inlet_{Ox}}$ **[bar]**	ΔP **[bar]**	**Exper.** ΔP **[bar]**
No-Hole Liquid	4.76	28.18	0.54	0.13
4-Hole 24% Liquid	-5.50	28.39	1.51	0.75
No-Hole Gas	4.98	28.45	0.75	0.13
4-Hole 24% Gas	-3.01	28.63	1.04	0.75

Table 3.18: CFD results compared to Grosse's average measurements (II).

Sim. Type	C^***[m/s]**	$C^*Exper.$**[m/s]**	$C^*Theor.$ **[m/s]**	C^*CEA **[m/s]**
No-Hole Liquid	1386.5	1313.4	1549.2	1621
4-Hole 24% Liquid	1303.0	1326.7	1410.0	1569
No-Hole Gas	1405.3	1313.4	1549.2	1621
4-Hole 24% Gas	1333.4	1326.7	1410.0	1569

Table 3.19: CFD results compared to Grosse's average measurements (III).

Sim. Type	**Efficiency**	**Exper. efficiency**	**Efficiency Error [%]**
No-Hole Liquid	0.89	0.85	5.56
4-Hole 24% Liquid	0.92	0.94	-1.78
No-Hole Gas	0.91	0.85	6.99
4-Hole 24% Gas	0.95	0.94	0.51

Table 3.20: CFD results compared to Grosse's average measurements (IV).

Considering the uncertainty of ±1% affecting pressure measurements and that of ±4% obtained using uncertainty propagation for C^*, CFD results can be considered as accurate enough for the purpose of this study.

Comparison of the CFD Results with CISAS Lab-scale Experiments

The results presented here refer to the hybrid rocket tested at CISAS and having a 20 mm diaphragm inside the combustion chamber. Simulations with both gas and liquid injection are discussed and analyzed.

First of all the experimental findings are presented, to allow a better comparison with the software.

During the tests, three types of diaphragms were tested: the ratio of the center-hole area and nozzle throat area was 1.5, 1 and 0.5. In all the experiments, oxidizer mass flow rate, grain dimensions, diaphragm position, burn time and nozzle dimensions were fixed and a stable combustion was achieved.

Tab.3.22 shows the average results for combustion chamber pressure, C^*, regression rate, OF ratio and pressure drop across the diaphragms. Test type 4 was without any diaphragm and with a longer fuel grain.
For all the tests, the average oxidizer mass flow rate was 250 g/s. C^* uncertainty is ±3%, it has been calculated using the average experimental data and their uncertainties. The uncertainty on the measured pressure value is ±1%.

Test	**Ad/At**	P_{cc} **[bar]**	$C*$ **[m/s]**	Δp **[bar]**
3	1.5	21.4	1407	0
6	1	31	1388	1.26
2	0.5	21.3	1339	10.59
4	No diaphragm	15.6	1155	0

Table 3.21: Results of experiments on lab-scale motor: averages for each diaphragm configuration (Ad/At = 1.5, 1 and 0.5).

Test	$\dot{r}$ **pre [mm/s]**	$\dot{r}$ **post [mm/s]**	**OF**
3	3.51	4.50	5.1
6	3.91	3.59	4.70
2	4.04	3.48	3.8
4	0	2.41	4.9

Table 3.22: Experiments results for the lab-scale motor: averages for each diaphragm configuration (Ad/At = 1.5, 1 and 0.5).

Fig.3.34 shows a typical paraffin fuel grain after burn. Most of the left section of the fuel grain was burned. This was seen for all diaphragm types, and the effect increases with decreasing center-hole diameter.

Fig.3.35 shows the regression rate measured upstream and downstream of the diaphragm, for all configurations.
The maximum value of 4.5 mm/s was measured at the grain section downstream of the smaller

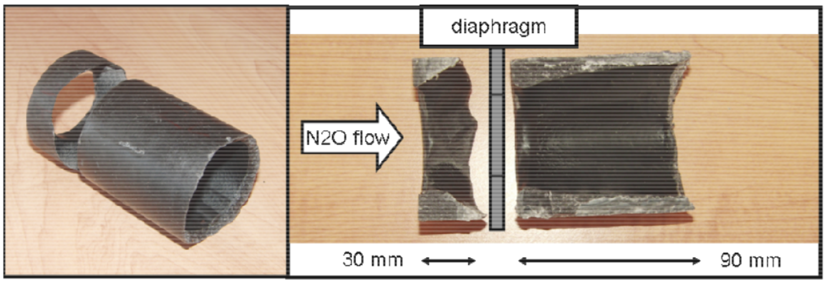

Figure 3.34: Sasol 0907 fuel grain recovered after testing (Ad/At = 1 diaphragm). Non-uniform fuel regression was experienced, especially at the grain section upstream of the diaphragm.

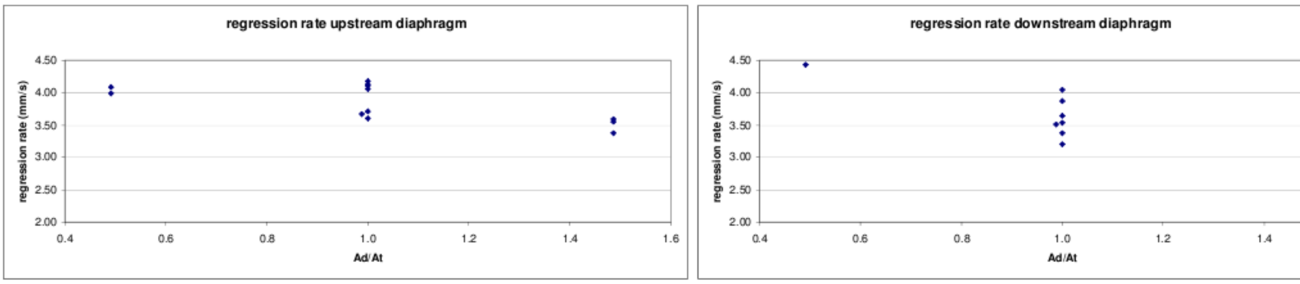

Figure 3.35: Regression rate for lab-scale tests measured upstream and downstream of the diaphragm.

diaphragm. In both grain sections, regression rate increased towards nozzle entrance.
On the other hand, to explain the unforeseen high regression rate measured upstream, it was assumed that a strong recirculation was triggered at this grain section by the liquid oxidizer impinging on the diaphragm (this assumption has then been proved by the CFD analysis of the flow field).
To further understand this behavior, a cold test was prepared to assess the oxidizer jet divergence and to compare it to the diaphragm diameter.

Fig.3.36 shows the larger diaphragm superimposed to the oxidizer jet. For all the tested configurations, liquid oxidizer is expected to hit the disk surface and the diaphragms recovered after burn tests showed marks from injected oxidizer impingement.

Injector holes pattern is clearly visible in Fig.3.37: on the left, a steel diaphragm plate is shown and on the right, there is another CFC diaphragm, that suffered high erosion due to the missing SiC impregnation.

To obtain an increased oxidizer flow rate, more orifices are typically added to the injector plate (same orifice diameter), and this was the case with the increased-scale experiments.
Injection velocity and liquid N_2O vaporization lag are approximately fixed, so at a grater scale less oxidizer is expected to reach the diaphragm and to be deflected back, being the distance between the injector plate and the diaphragm increased. This was assessed with increased

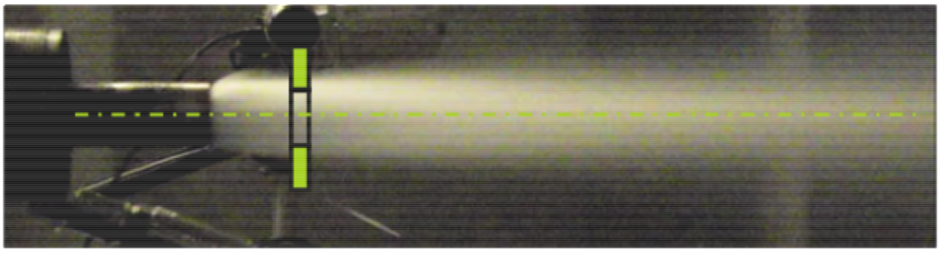

Figure 3.36: N_2O oxidizer flow at ambient pressure with an Ad/At = 1.5 diaphragm. The jet assumes a cylindrical shape with a small divergence angle.

Figure 3.37: Diaphragms recovered after testing. On the left, carbon steel with Ad/At = 0.5. Clear marks from oxidizer impingement are visible. The injector had 6 orifices drilled on a circular pattern. In the middle and on the right a non-impregnated CFC diaphragm (originally Ad/At = 0.5) is presented: high erosion and marks from impinging oxidizer are visible.

scale experiments.

The drawback of the smaller diaphragm configuration having Ad/At=0.5 is shown in Fig.3.38: the pressure drop across the diaphragm was 10 bar, because pressure upstream was increased by the small hole diameter. The measured pressure drop of 2 bar is instead considered acceptable for Ad/At=1.
On the other hand, the diaphragm having Ad/At=0.5 requires an injection pressure increase of at least 10 bar, which would affect the whole feed system mass and size. However, thrusters having stringent requirements related to very high regression rates, can operate in the Ad/At=0.5 configuration as well.

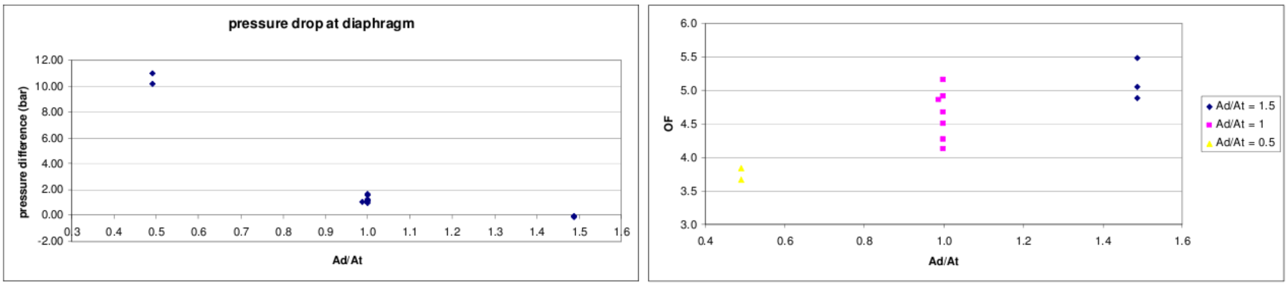

Figure 3.38: Pressure drop across the diaphragm (left) and average OF versus Ad/At (right).

The total fuel mass flow rate increased with smaller Ad/At. Fig.3.38 shows the average OF for these three configurations. The measurement uncertainty was within 6%-8%. The oxidizer mass flow rate was 250 g/s.

Fig.3.39 shows the dependency of C^* efficiency on the diaphragm Ad/At ratio. Efficiency was above 90% for all the tests.

Decreasing the diaphragm center-hole diameter resulted in an increased efficiency.
The ideal C^* used to calculate efficiencies was computed at shifting equilibrium, assuming the same propellant mass flow rate, OF ratio and nozzle throat area of the experiments.
The calculation has been done with the average data for propellant flow rate and OF.

For the liquid injection simulations prepared to reproduce these experimental results, the Blob numerical model has been applied to describe the real injection plate.
A comparison (Fig.3.41) between the real N_2O liquid jet observed during experiments and that simulated by the CFD shows that the model and parameters used (Tab.3.16) are acceptable.

In Fig.3.42 the N_2O mass fractions obtained injecting a gas and a liquid phase are presented. When gas enters the combustion chamber, N_2O is consumed less rapidly and there still is a certain amount of N_2O at the nozzle exit. Whereas, if liquid is injected, N_2O is completely consumed and its profile inside the rocket looks very different.
The N_2O mass fraction in the liquid injection case (Fig.3.42-right) is zero upstream of the

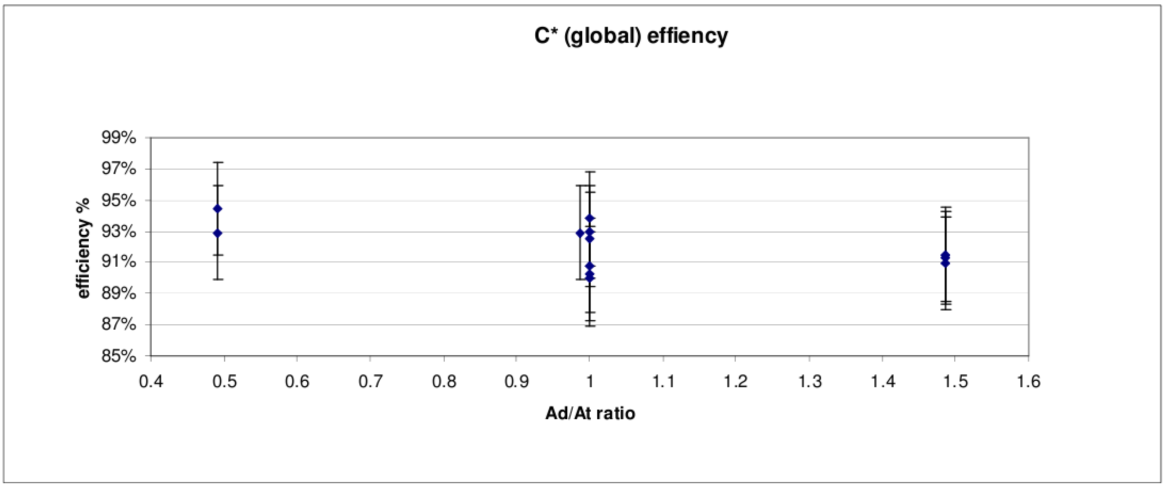

Figure 3.39: Combustion efficiency versus diaphragm area. Uncertainty was 3% for all the tests. The ideal C^* was computed with shifting equilibrium.

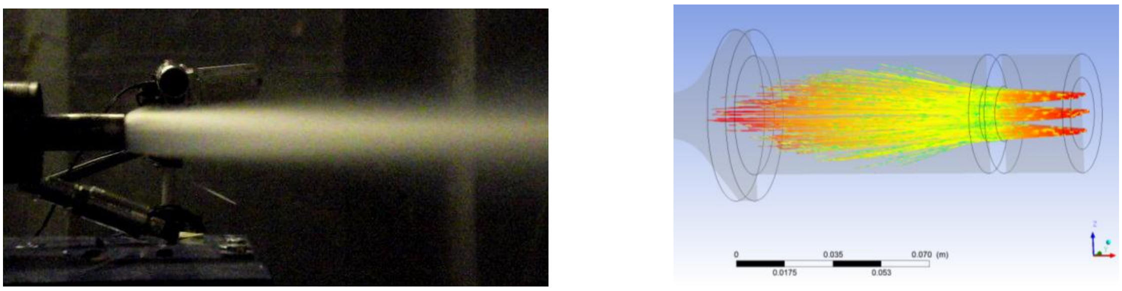

Figure 3.40: Liquid N_2O jet during experiments and according to the CFD simulations for CISAS lab-scale rocket.

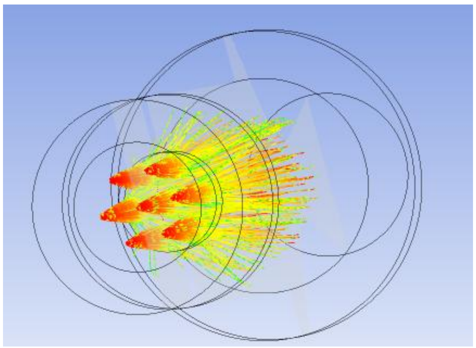

Figure 3.41: Liquid N_2O jet according to the CFD simulations for CISAS lab-scale rocket.

diaphragm because this parameter is calculated for the gas phase and liquid N_2O has not yet vaporized in the first part of the fuel grain.

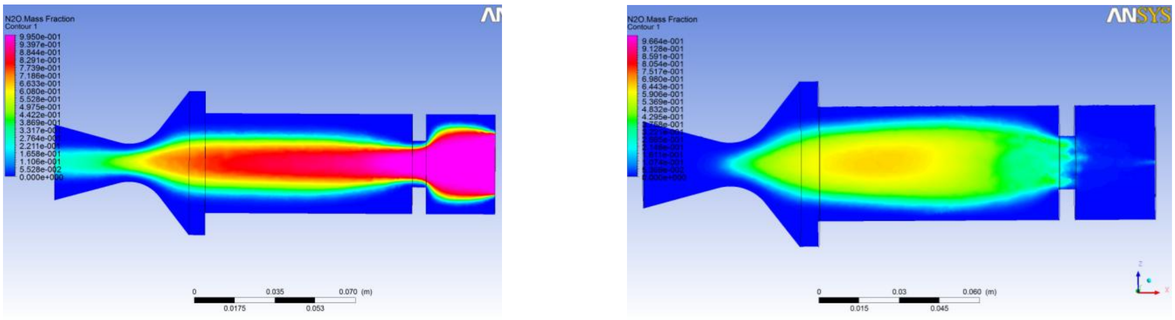

Figure 3.42: N_2O mass fraction in the combustion chamber of the 1-hole diaphragm lab-scale rocket for gaseous injection (left) and liquid injection (right).

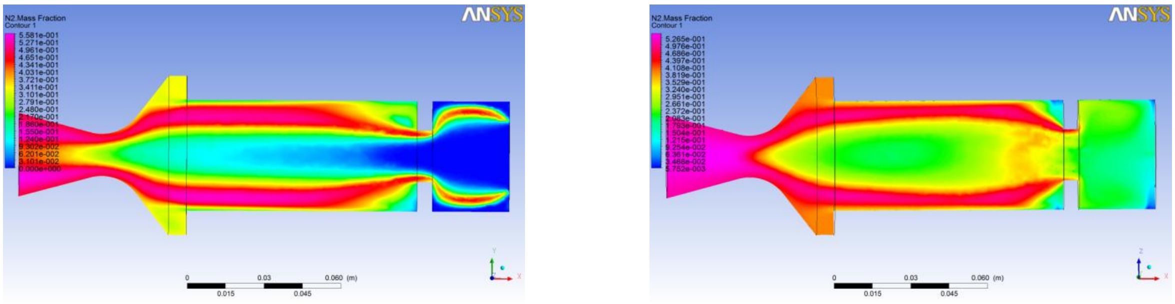

Figure 3.43: N_2 mass fraction in the combustion chamber of the 1-hole diaphragm lab-scale rocket for gaseous injection (left) and liquid injection (right).

Fig.3.43 illustrates N_2 mass fraction inside the rocket. This is important to understand if combustion products are confined in some specific locations inside the combustion chamber. The main difference is that in the gas case, products are formed only close to the flame and they are less diffuse than for liquid injection, where they are more uniformly distributed inside all the combustion chamber.

The flame morphology resulting from these two injection types is completely different. In the liquid case in fact, temperature is more uniform inside the whole combustion chamber and flame is more diffuse. A higher temperature can be found in the combustion chamber core (downstream of the 1-hole diaphragm) for the gas injection case.

The reasons for these different behaviors are well showed by Fig.3.45, where an evident flow recirculation can be observed.
Liquid injection causes strong vortices in the first grain segment, which extend until the diaphragm.
Inside the diaphragm, the flow forms other too smaller eddies, which act as a flame holder

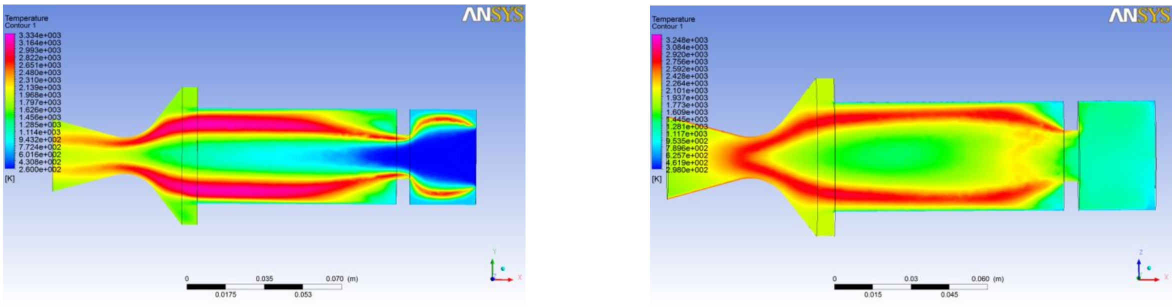

Figure 3.44: Temperature in the combustion chamber of the 1-hole diaphragm lab-scale rocket for gas (left) and liquid injection (right).

and cause the core flow temperature to be higher than in the corresponding simulation with gaseous injection.
The only common flow characteristic is the recirculation at the beginning of the second grain segment, downstream of the diaphragm, which is present when gas is injected as well as in the case of a liquid injection.
These vortices are responsible for the flame stabilization in the second segment of the fuel grain.

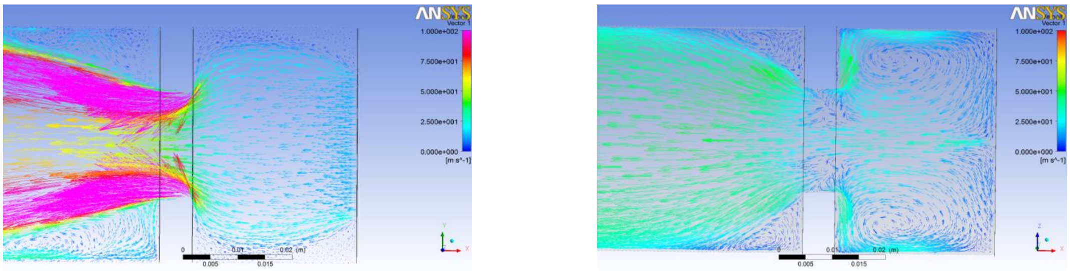

Figure 3.45: Flow recirculation for gas (left) and liquid injection (right).

Tab.3.23 and the following, resume the results obtained from the comparison of the experiments with CFD simulations for the lab-scale rocket with a 1-hole diaphragm.
The simulation where liquid is injected allows a better representation of the experimental condition with respect to gas injection.

Errors are calculated using CFD results and the corresponding average parameters measured during the tests.
In the liquid injection case, the efficiency difference between the software and the average experimental value is lower than 2%.
This is considered as a very good result, because the CFD characteristic velocity is within the experimentally determined range of C^*, which is 1407.00±42.21 m/s.

Sim. Type	T_{max}**[K]**	P_{postcc}**[bar]**	P_{postcc} **Exper.[bar]**	**Error P [%]**
Diaph 200 mm, lab-scale Gas	3271	19.30	21.40	-9.81
Diaph 200 mm, lab-scale Liquid	2922	20.23	21.40	-5.47

Table 3.23: CFD results compared to the average measurements for the CISAS lab-scale 200 mm diaphragm rocket (I).

Sim. Type	$P_{inlet_{Ox}}$**[bar]**	ΔP**[bar]**	**Exper.**ΔP**[bar]**
Diaph 200 mm, lab-scale Gas	19.84	0.54	-0.10
Diaph 200 mm, lab-scale Liquid	20.34	0.11	-0.10

Table 3.24: CFD results compared to the average measurements for the CISAS lab-scale 200 mm diaphragm rocket (II).

Sim. Type	C^* **[m/s]**	C^***Exper.[m/s]**	C^***Theor.[m/s]**
Diaph 200 mm, lab-scale Gas	1362.16	1407.00	1552.00
Diaph 200 mm, lab-scale Liquid	1432.10	1407.00	1552.00

Table 3.25: CFD results compared to the average measurements for the CISAS lab-scale 200 mm diaphragm rocket (III).

Sim. Type	**Efficiency**	**Exper.efficiency**	**Effic. error [%]**
Diaph 200 mm, lab-scale Gas	0.88	0.91	-3.19
Diaph 200 mm, lab-scale Liquid	0.92	0.91	1.78

Table 3.26: CFD results compared to the average measurements for the CISAS lab-scale 200 mm diaphragm rocket (IV).

Comparison of the CFD Results with CISAS Increased-scale Experiments

Two different increased-scale geometries have been analyzed: the no-diaphragm and the same rocket with a 1-hole diaphragm and a diameter of 29.9 mm.
First of all, the experimental findings about the diaphragm configuration are presented, and then a comparison is proposed between the results obtained for gas and liquid injection simulations.

Experiments were run for a diaphragm having Ad/At=1; Tab.3.27 and 3.28 summarize the average experimental results.
Four tests were performed with the diaphragm and two without.

Test	**Ad/At**	P_{cc} **[bar]**	C^* **[m/s]**	C_f
2	No diaphragm	19.1	1187	1.422
5	1	22	1375	1.452

Table 3.27: Increased-scale performance: average measured combustion chamber pressure, C_f and C^*.

Test	$\dot{r}$ **pre [mm/s]**	$\dot{r}$ **post [mm/s]**	**OF**
2	—	3.2	4.9
5	2.9	4.2	4.9

Table 3.28: Increased-scale performance: average regression rates and OF ratio.

The motor configuration did not allow to measure pressure before the diaphragm, thus the pressure loss is only estimated by CFD.
The motor provided with a diaphragm had a more stable combustion and the use of a diaphragm affected motor stability, because it acted as a flame-holder, inducing a better mixing.

Test	**Ad/At**	$\dot{m}_{fuel}$ **[kg/s]**	$\dot{m_{ox}}$ **[kg/s]**	**OF**	$\bar{P_{cc}}$
1	0	1.115	0.923	4.8	18.9
2	0	1.143	0.950	4.9	19.3
3	1	1.226	1.031	5.3	22.4
4	1	1.157	0.959	4.8	22.6
5	1	1.059	0.877	4.8	21.8
6	1	1.071	0.881	4.6	21.4

Table 3.29: Summary of increased-scale motor performance (I).

Tab.3.29 and 3.30 summarize the measured motor parameters for the tests and the corresponding theoretical values. The latter have been computed assuming shifting equilibrium and using the experimental nozzle dimensions and average OF as input.
C^* efficiency average value was 94% in the diaphragm case and 81% without, thus the net

Test	$\dot{r}$ **pre [mm/s]**	$\dot{r}$ **post [mm/s]**	C^* **[m/s]**	C_f
1	0	3.2	1238	1.3654
2	0	3.2	1232	1.3674
3	3	4.3	1333	1.3920
4	2.9	4.4	1425	1.3916
5	3	4.0	1506	1.3799
6	2.9	4.2	1460	1.4182

Table 3.30: Summary of increased-scale motor performance (II).

increase using a diaphragm was +13%.
The uncertainty on C^* calculation was ±4% and for C_f it was ±2%. The high uncertainty on C^* was due to the low accuracy of the burnt oxidizer mass measurement.

Test	ϵC^*	ϵC_f
1	0.830	0.958
2	0.805	0.956
3	0.859	0.962
4	0.934	0.972
5	0.988	0.974
6	0.965	0.978

Table 3.31: Summary of increased-scale motor performance (III). ϵ indicates efficiency.

Experiments 1 and 2 were without diaphragm and had an 80% C^* efficiency, but efficiency was higher with the insertion of the diaphragm (from test 3 to 6).

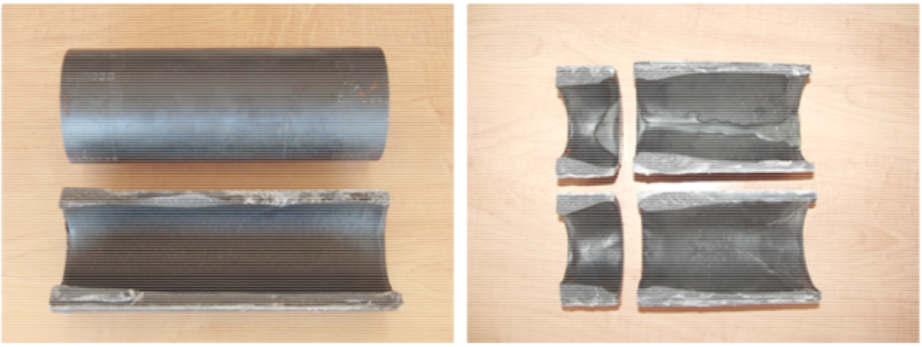

Figure 3.46: Sasol 0907 grain without any diaphragm after firing (left) and with the diaphragm (right). External and initial diameter were the same for both; the total length were 300 mm and 58+172 mm respectively.

Fig.3.46 shows the fuel grain of both configurations after firing: on the left without the diaphragm and on the right with it.

The grain consumption is smooth and uniform without the diaphragm and a lower regression rate is visible in the grain section near the injector. The grain with the diaphragm shows a greater uniformity of the burnt area along grain axis and fuel consumption is much more uniform compared to lab scale. In general, a lower regression rate is experienced near the injector and just downstream of the diaphragm.

The regression rate upstream of the diaphragm had a similar trend compared to experiments without. However, fuel grain consumption was relatively smooth in the no-diaphragm case, while with the diaphragm it was rather non-uniform and resulted in a strong conical shape.
Moreover, the upstream regression rate was lower compared to downstream (35% of the downstream average value); this suggests that the recirculation observed for the lab-scale, is less important at larger scales.

The results coming from the increased-scale tests conducted on the same rocket configuration have been averaged, to be compared with CFD.
In the following, the tests have been simulated using both gas and liquid injection, obtaining some differences in the flow field.
The first difference discussed concerns flame morphology, as in Fig.3.47 and 3.50.

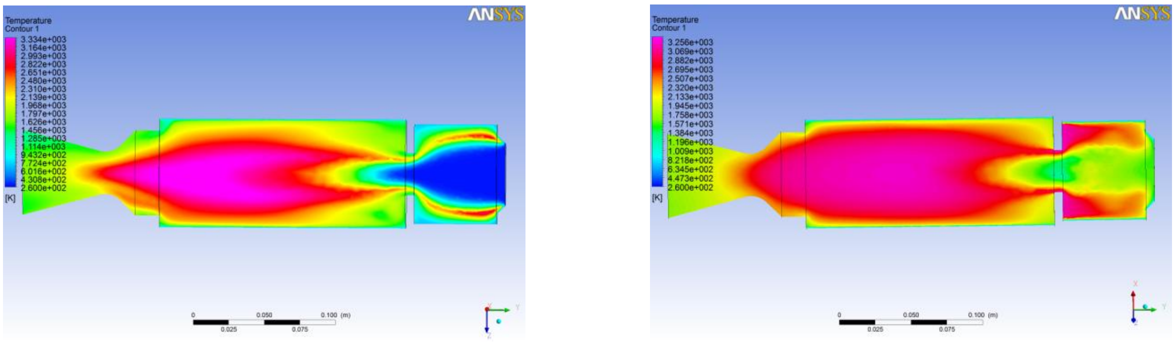

Figure 3.47: Flame morphology for gaseous (left) and liquid injection (right) in the 1-hole diaphragm case.

In fact, the flame has a different shape when liquid N_2O is injected; the average temperature in the first part of the grain is higher than in the gas injection case and the flame appears to be more diffuse.
This is due to the flow recirculation (Fig.3.48) developing inside the first grain segment, upstream of the diaphragm, which helps the chemical species mixing and induces a temperature homogenization. Temperature is also higher in the combustion chamber core, for the liquid case.

N_2O is consumed completely in both cases; the main difference is that, in the liquid case, it is not present at the oxidizer inlet section, because it is still a liquid and this accounts for its mass fraction to be zero (Fig.3.49).

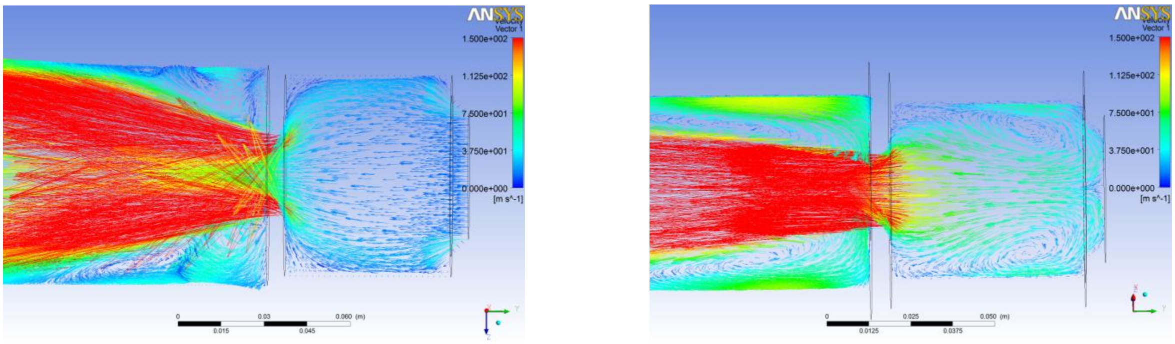

Figure 3.48: Recirculation in the flow field for gas (left) and liquid injection (right).

Its mass fraction is a balance between evaporation and reaction rates: N_2O evaporation and reaction occur simultaneously and this is the reason why its mass fraction cannot reach unity. Moreover, in the liquid case, a faster extinction of this species can be observed with respect to the gas phase.

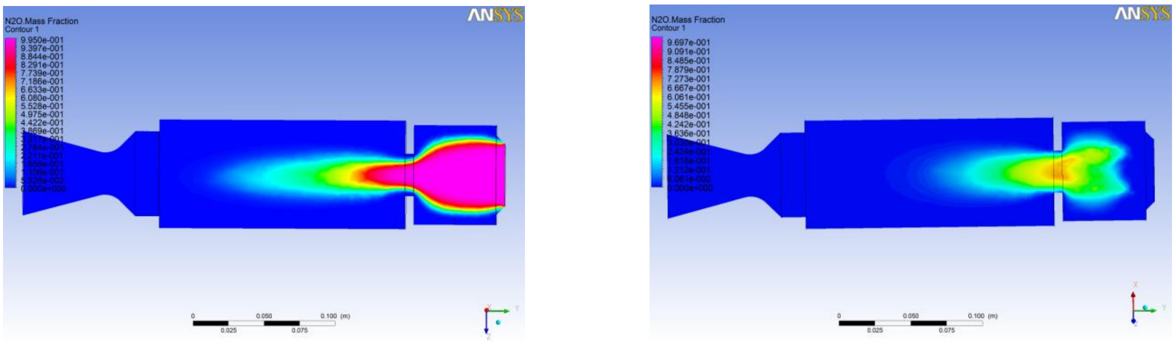

Figure 3.49: N_2O mass fraction in the combustion chamber of the 1-hole diaphragm increased-scale rocket for gaseous (left) and liquid injection (right).

The same simulations have been conducted for the geometry without the diaphragm. Even in this case, the flame appears to be more diffuse and the temperature in the combustion chamber core is more uniform (see Fig.3.50).

Tab.3.32 and the following, resume the main results for the increased-scale hybrid rocket configurations. The symbol NM means not measured, because in the increased-scale test, it has not been possible to retrieve pressure at the oxidizer inlet, due to the sensor size.
The uncertainty on C^* determination is $\pm 4\%$ and pressure is measured with an uncertainty of $\pm 1\%$, but the experimental values presented in the tables are the averages, which have been compared to CFD to obtain the corresponding errors.

Considering the uncertainty on the average experimental results presented in the tables, the CFD proves again to provide results which are acceptable for the purpose of this analysis.

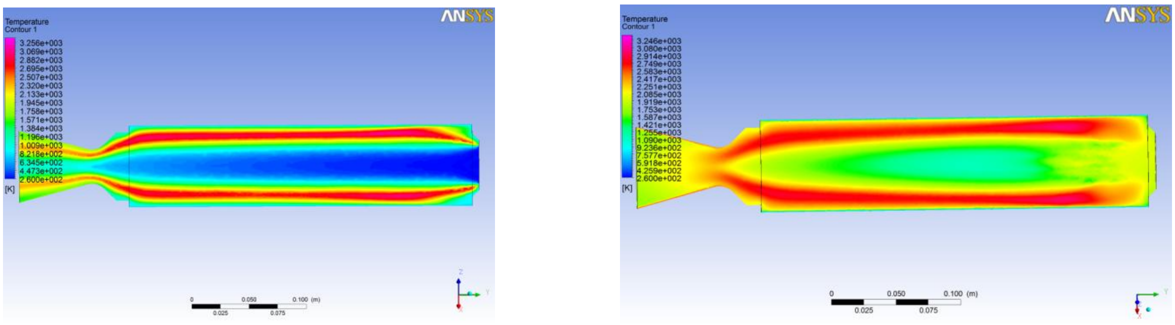

Figure 3.50: Temperature and flame morphology for gaseous (left) and liquid injection (right) for the no-diaphragm case.

Sim. Type	T_{max} **[K]**	P_{postcc} **[bar]**	P_{postcc} **Exper.[bar]**	**Error P [%]**
No diaph-Full scale Gas	3186	19.10	19.10	0.00
No diaph-Full Scale Liquid	3002	20.30	19.10	6.28
1-hole diaph-Full scale Gas	3340	23.21	22.00	5.50
1-hole-Full Scale Liquid	3324	23.18	22.00	5.36

Table 3.32: CFD results compared to CISAS average measurements on the increased-scale rocket (I).

Sim. Type	$P_{inlet_{Ox}}$ **[bar]**	ΔP **[bar]**	ΔP **Exper.[bar]**
No diaph-Full scale Gas	19.40	0.30	NM
No diaph-Full Scale Liquid	20.80	0.50	NM
1-hole diaph-Full scale Gas	25.30	2.09	NM
1-hole-Full Scale Liquid	25.82	2.64	NM

Table 3.33: CFD results compared to CISAS average measurements on the increased-scale rocket (II). NM stands for *not measured.*

Sim. Type	C^* **[m/s]**	C^* **Exper. [m/s]**	C^* **Theor.[m/s]**
No diaph-Full scale Gas	1233.68	1234.70	1526.00
No diaph-Full Scale Liquid	1307.72	1234.70	1526.00
1-hole diaph-Full scale Gas	1499.15	1431.00	1529.00
1-hole-Full Scale Liquid	1418.21	1431.00	1529.00

Table 3.34: CFD results compared to CISAS average measurements on the increased-scale rocket (III).

Sim. Type	**Efficiency**	**Exper. efficiency**	**Efficiency error [%]**
No diaph-Full scale Gas	0.81	0.81	-0.08
No diaph-Full Scale Liquid	0.86	0.81	5.91
1-hole diaph-Full scale Gas	0.98	0.94	4.76
1-hole-Full Scale Liquid	0.93	0.94	-0.89

Table 3.35: CFD results compared to CISAS average measurements on the increased-scale rocket (IV).

This is true for both combustion chamber pressure and C^*.

The uncertainty on CFD parameters has not been determined, because this would have required a dedicated analysis and was not the aim of this work.
Uncertainty management and determination in CFD is currently a subject of advanced research.

Results for Liquid Particles

It has been possible, from the CFD results, to estimate the evaporation rate constant, using the droplet diameter after the secondary breakup process and the evaporation time given by the CFD. The expression used to calculate this parameter is as follows [24]:

$$K = \frac{d_0^2}{T_{evap_{CFD}}} \tag{3.2.1}$$

where K is the evaporation rate constant, d_0 is the particle diameter after secondary breakup and $T_{evap_{CFD}}$ is the estimated time for particle evaporation.

In Tab.3.36, the most important CFD results concerning particles evaporation time and evaporation rate are resumed.

Sim.	**Particle t [s]**	d_0 **[m]**	**Evap.Rate Const.** $[m^2/s]$
No-hole Grosse lab	3.30e-3	2.00e-5	3.71e-7
4-hole 24 Grosse lab	2.78e-3	2.00e-5	3.24e-7
1-hole CISAS lab	3.30e-3	4.00e-5	4.85e-7
No-hole CISAS increased	2.37e-3	2.75e-5	3.19e-7
1-hole CISAS increased	1.50e-3	2.75e-5	5.04e-7

Table 3.36: Evaporation rate constant estimated through CFD.

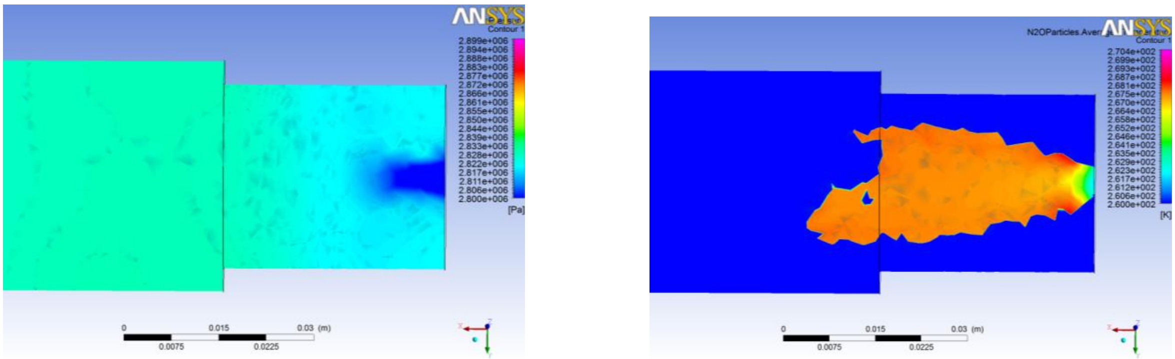

Figure 3.51: Swirl injector simulation: local pressure near the injection section and particles temperature.

The values found for the evaporation rate constant in the different cases simulated agree with theory [24].
A comparison can be made between the characteristics of the liquid particles injected by the shower head injector of the increased-scale CISAS rocket and the swirl injector of the lab-scale configuration tested by Grosse [18].

In Fig.3.51, local pressure is illustrated. The picture refers to the swirl injector of the lab-scale motor tested by Grosse without the diaphragm.
Particles temperature is also shown: liquid N_2O saturation pressure at 28 bar is approximately 269 K, therefore it is proved that CFD results are in good accord with physics.

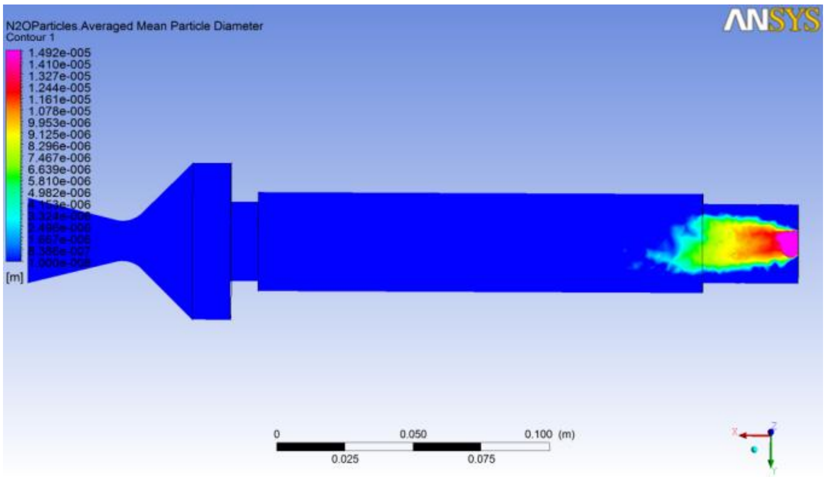

Figure 3.52: Swirl injector simulation: particles average diameter.

From Fig.3.52, it is possible to see that the secondary breakup produces a reduction of the average particles diameter in a section quite close to the injection area. Then, the evaporation process is responsible for a further diameter reduction.

In Fig.3.53, particles velocity is plotted. Velocity is approximately 52 m/s when droplets enter the fluid domain, but it reduces to one half the initial value, due to the aerodynamic forces, as soon as particles leave the pre-combustion chamber.

The same discussion can be extended to the increased-scale hybrid rocket without the diaphragm. For this simulation, the same pictures are presented, in order to make a comparison between the liquid jet morphology for the swirl and the shower head injector.

Compared to Fig.3.52, the shower head injector is characterized by a weaker primary breakup, so that particles show a bigger average diameter, compared to the first lab-scale motor analyzed, as proved by Fig.3.54.
The fact that the aerodynamic action induced by the breakup is stronger for the swirl injector is also proved by Fig.3.55, where particles velocity is shown.

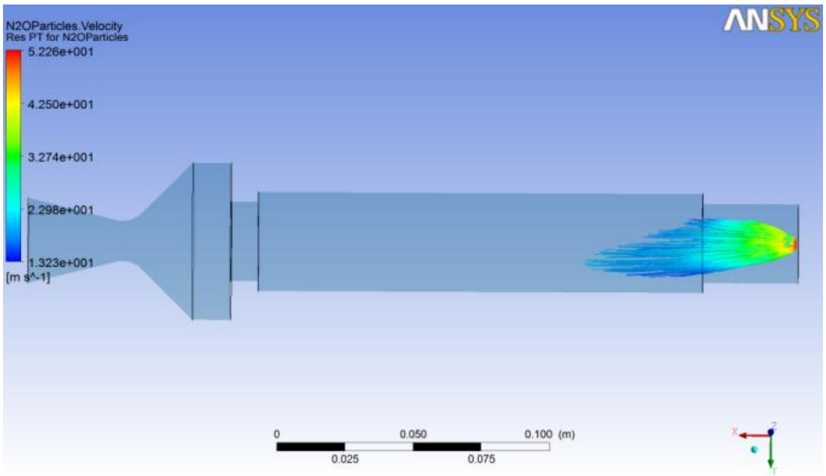

Figure 3.53: Swirl injector simulation: particles velocity.

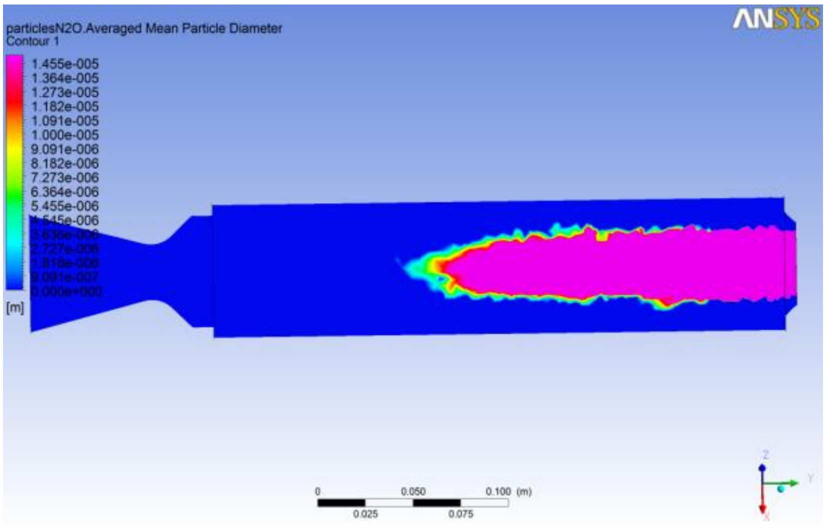

Figure 3.54: Shower head injector simulation: particles average diameter.

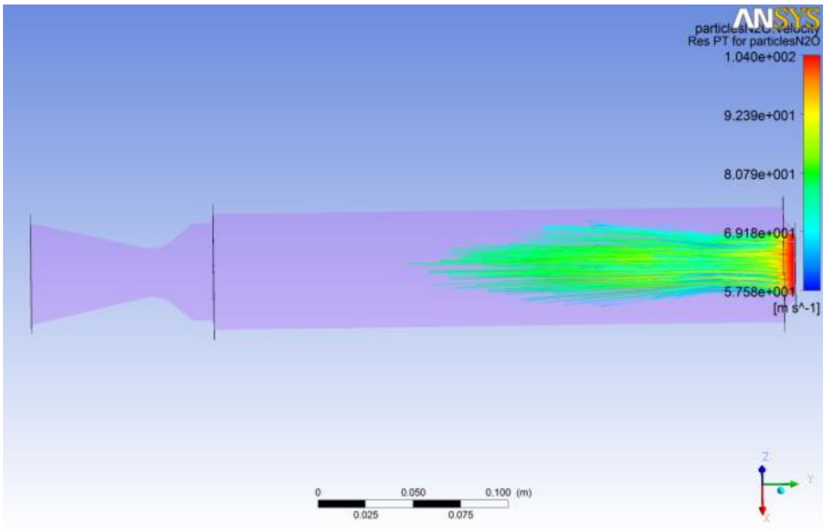

Figure 3.55: Shower head injector simulation: particles velocity.

In fact, velocity does not decrease as in Fig.3.53 for the swirl injector; even when particles have traveled an axial distance corresponding to the combustion chamber center, droplets velocity is still higher than one half its initial value.

The geometries without the diaphragm show a greater similarity between gas and liquid injection test cases.
Considering the CFD analyses conducted on these geometries, the main differences in the flow field and in the fluid parameters between liquid and gaseous injection simulations are present in those areas where particles are not evaporated.

From Fig.3.56, the main difference between the temperature contours obtained for gas and liquid injection is visible at the inlet section of the liquid and in the combustion chamber core until the liquid has completely evaporated.

When a diaphragm is introduced in the combustion chamber at a distance where particles are not completely evaporated, the characteristics of the flow field are very different from those of the gaseous injection case.
Fig.3.58 shows that, as the diaphragm is moved towards the injection section, the difference between gas and the liquid injection test cases, in terms of combustion, increases.
In fact, Grosse's 4-hole diaphragm rocket has a pre-chamber helping liquid evaporation, whereas CISAS lab-scale rocket does not. Consequently, in the latter case, a greater difference can be seen between the liquid and gaseous injection simulations.

Another peculiar effect of liquid injection is the strong recirculation of the flow field, which was not observed in the previous simulations (Fig.3.59).

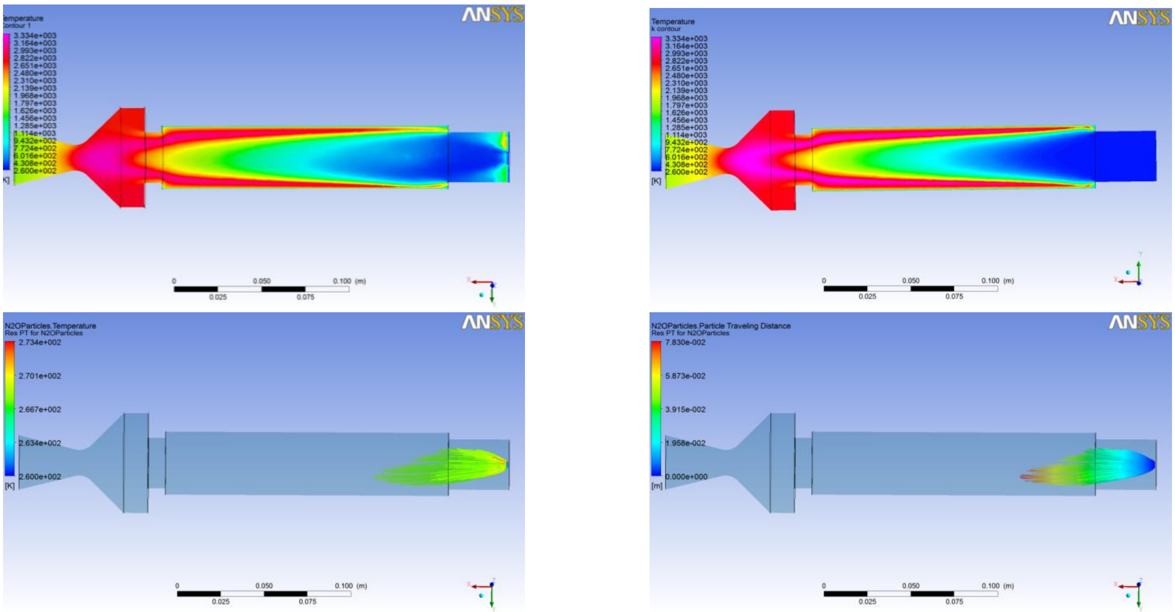

Figure 3.56: No-diaphragm lab-scale rocket used in Grosse's tests. The flow fields and flame morphology are similar after particles have evaporated; liquid injection is on the left, gaseous injection on the right.

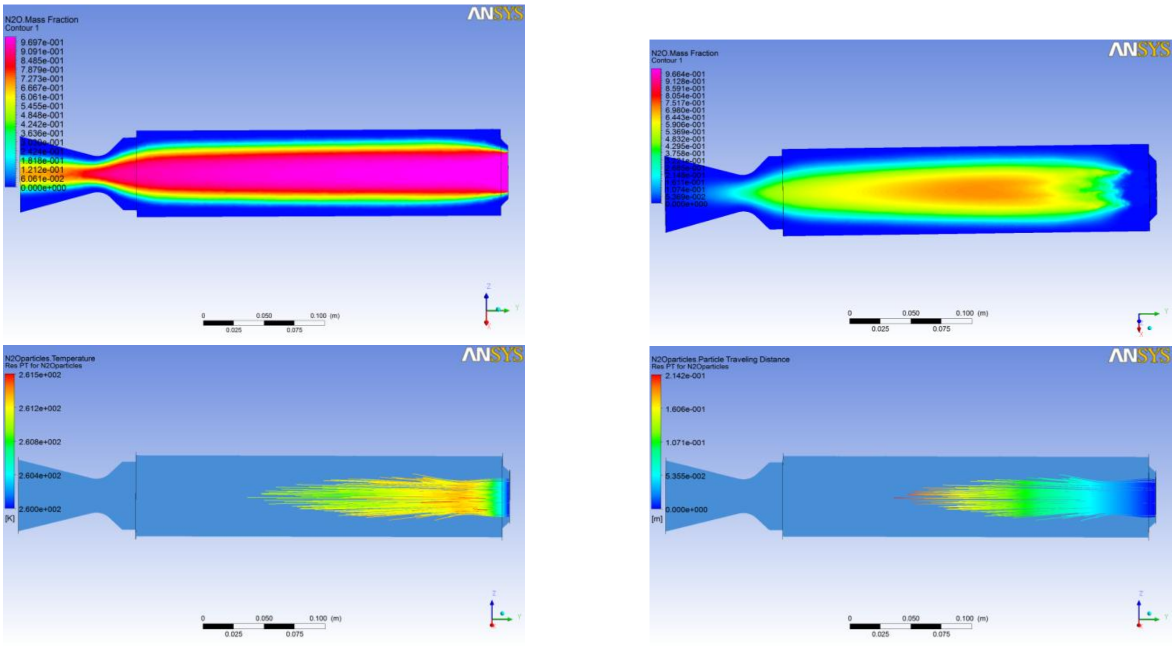

Figure 3.57: No-diaphragm increased-scale rocket used by CISAS. The flow fields and N_2O mass fraction are very different at the inlet section; liquid injection is on the left, gaseous injection on the right.

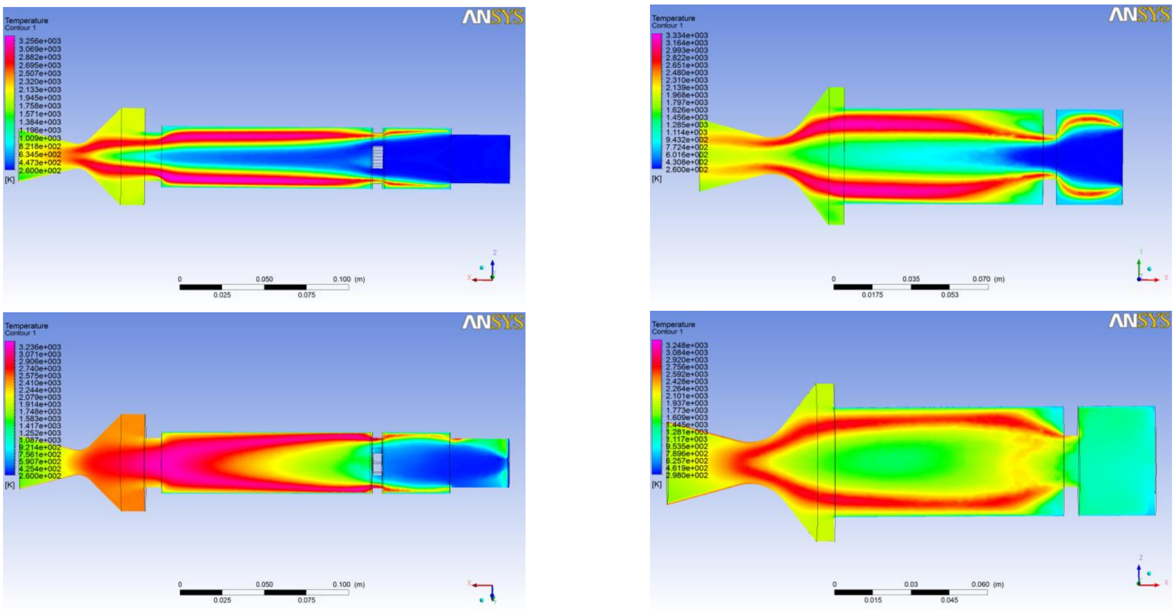

Figure 3.58: Above, gas injection test cases are shown for Grosse (left) and CISAS (right) lab-scale rockets. Below, the corresponding results are shown for liquid injection.

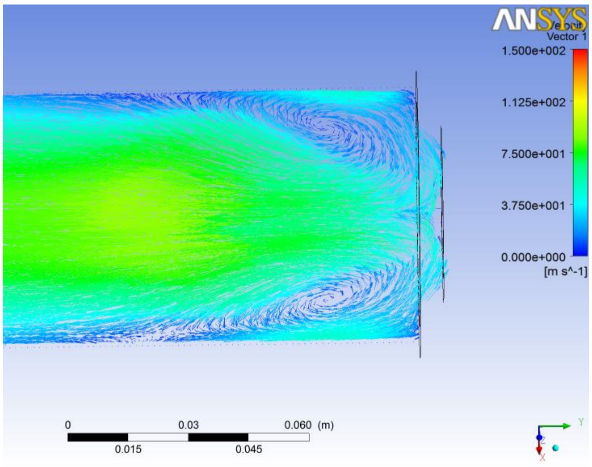

Figure 3.59: Flow recirculation close to the injection plane, extending inside the pre-chamber for a liquid injection test case.

This is the cause of a more uniform temperature and of a flame-holding effect downstream of the diaphragm, which can be seen from Fig.3.58.

3.2.5 CISAS Lab-scale: Results Discussion

This section discusses the different performance of the three diaphragm configurations used for the lab-scale CISAS rocket.

Preliminary simulations were run to assess the flow field and combustion efficiency for these three configurations of the lab-scale rocket. The CFD model requires as input the regression rate value for paraffin wax.
As a first attempt, the reference regression rate constants a and n were taken from [17]: a = 0.1618, n = 0.489 for the grain section upstream of the diaphragm, and a = 0.5387, n=0.360 for the other section. Regression rate is expressed as:

$$\dot{r} = aG_{ox}^{n} \tag{3.2.2}$$

the result is in mm/s and G_{ox} must be expressed with SI units: kg/sm^2. All the simulations were set with the same OF ratio of 5.8.

After having performed the experimental tests, new CFD simulations have been set, using the measured average oxidizer and fuel mass flow rates as inputs. A specific simulation was run for each diaphragm tested. Oxidizer mass flow rate was computed as the average value among all the tests run for the same configuration.
The measured instantaneous fuel mass flow rate was not available, thus its value has been computed fitting the above regression rate formula to the measured burnt fuel mass, assuming the same n coefficient of the preliminary simulations.
The input OF ratio is the average OF calculated from experiments. This same procedure was applied to compute the grain port diameter at a burn time of 1.5 seconds (average).

Sim. Type	**Inj. Type**	$\dot{m}_{ox}$ **[g/s]**	**Ad/At**	**Diaph. center hole diam.**[m]
Preliminary	gaseous	280	1.5, 1, 0.5, no diaphragm	20,16.3,11.5
Post fire	gaseous	250	1.5, 1, 0.5, no diaphragm	20,16.3,11.5
Post fire	liquid	250	1.5	20

Table 3.37: CFD simulations set up for the lab and increased-scale configurations. Additional data is provided in the following sections.

Tab.3.37 summarizes input data of preliminary and post-fire simulations.

Fig.3.60 shows the comparison between the C^* efficiency resulting from the simulations and the average experimental values, for the lab-scale rocket.
CFD predicts an efficiency increase when the hole-diameter decreases, as expected.
The use of a diaphragm produces an increase in combustion efficiency (+20%) and this is confirmed by the CFD. Efficiency is overestimated at Ad/At = 0.5 (+5%). In general, both

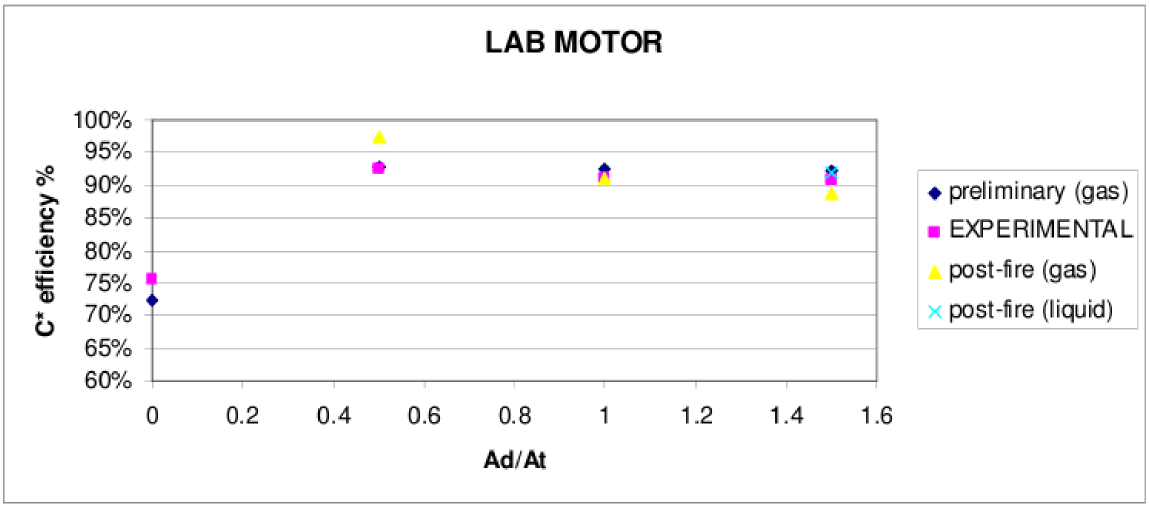

Figure 3.60: Combustion comparison between CFD and experiments.

preliminary and post-fire simulations gave the same results.

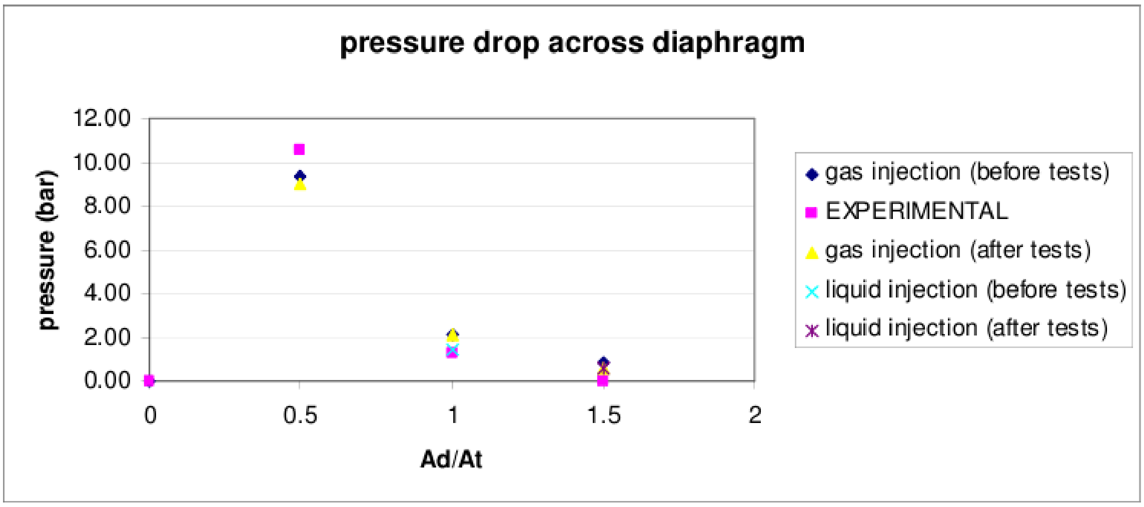

Figure 3.61: Comparison of the pressure drop across the diaphragm as computed by CFD and measured with experiments.

Fig.3.61 shows the pressure drop, measured and simulated. The diaphragm with Ad/At=0.5 results in a too high pressure drop, even if the average combustion efficiency is the highest.

Fig.3.62 shows the comparison between N_2O mass fraction for the three diaphragm area ratios and for the no-diaphragm motor: the more unreacted N_2O reaches the nozzle, the lower the combustion efficiency.

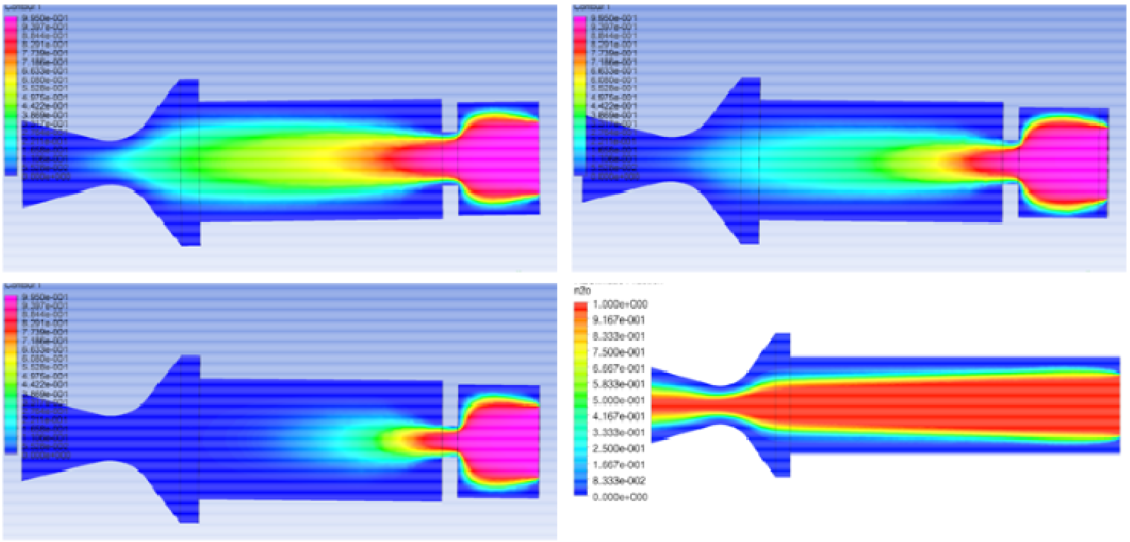

Figure 3.62: N_2O mass fraction for the three diaphragms: on top and from left to right Ad/At= 1.5, and 1. In the second row and from left to right Ad/At=0.5 and the no-diaphragm configuration. Gaseous oxidizer.

With Ad/At = 1.5 a small N_2O fraction reaches nozzle throat, while for Ad/At = 1 and 0.5 almost all the oxidizer flow is burnt. Without the diaphragm, a large N_2O fraction is wasted resulting in a low measured average combustion efficiency (75%).

Fig.3.63 shows the temperature field inside the combustion chamber. The effect of the diaphragm is to shift the flame position towards the motor center-axis, so that the oxidizer can readily diffuse into it. The temperature reaches its maximum values when diaphragms are used. The larger diaphragm is enough to achieve a good mixing and high gas temperature just upstream of the nozzle entrance.
Flame appears to attach at the diaphragm, since gasified fuel and oxidizer are forced to pass across the center-hole at that position.
For this reason, the diaphragm could also affect combustion stability. In fact, it will be shown with increased-scale experiments, that the motor with the diaphragm is more stable compared to the motor without.

CFD simulations with liquid N_2O have been run to confirm the presence of a recirculation in the flow field upstream of the diaphragm, which was hypothesized from experimental results.
In Fig.3.64 a flow recirculation can be observed: liquid injection causes a great vortex in the first grain segment, which extends until the diaphragm.

Just upstream of the diaphragm, a very high regression rate was observed, and according to this, CFD predicts high velocity and gas temperature (Fig.3.65) in its second half section.

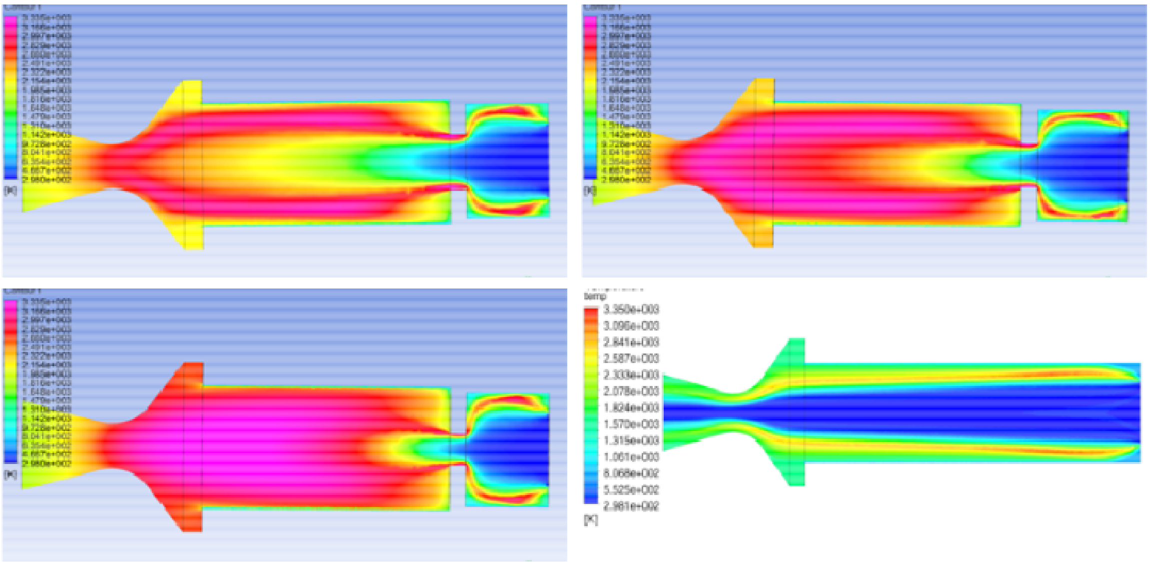

Figure 3.63: Combustion chamber temperature for the three diaphragms: on the top and from left to right Ad/At= 1.5, and 1. In the second row and from left to right Ad/At=0.5 and the no-diaphragm configuration.

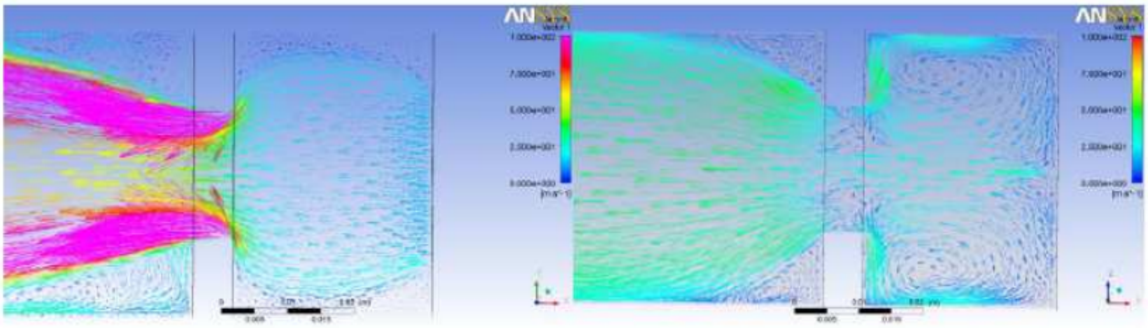

Figure 3.64: Flow recirculation for gaseous (left) and liquid injection (right).

A high local flow velocity probably enhances heat transfer and fuel droplets detachment from the fuel surface. In conclusion, the high regression rate measured could by explained by such a recirculation.

Downstream and in the close proximity of the diaphragm, gas velocity is low compared to its value towards the nozzle, therefore less heat is exchanged with the fuel surface.
Temperature is lower near the diaphragm as well, and this result is in line with experiments, where a conical grain consumption was observed just downstream of it.
In Fig.3.65 blue circles highlight the zones where a lower grain consumption develops due to a lower net heat in close proximity of the fuel grain and to a lower heat transfer caused by a slower gas velocity.

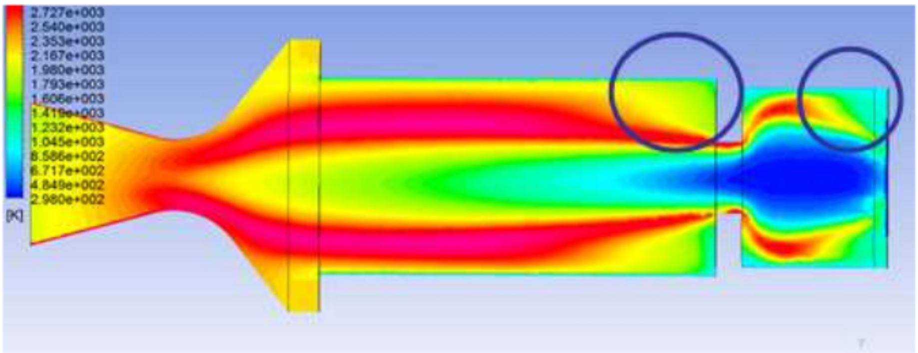

Figure 3.65: Gas temperature inside the combustion chamber with liquid injection.

As reported here, lab-scale experiments showed that combustion efficiency increases with a smaller diaphragm center-hole and this trend is found by the CFD as well. This is due to the flame shifting toward the motor center-axis, which triggers enhanced N_2O diffusion/mixing with gasified fuel.
Downstream of the diaphragm, regression rate was higher with smaller center-hole diameters.

3.2.6 CISAS Increased-scale: Results Discussion

As already discussed for the lab-scale, preliminary simulations were run to assess the flow field and combustion efficiency for the selected diaphragm with Ad/At = 1.
Regression rate was not believed to be influenced by the motor scale or the injector type, especially at the grain section upstream of the diaphragm.
For this reason, regression rate constants a and n were taken from [18]: a = 0.162, n = 0.489 for the grain section upstream of the diaphragm and a = 0.539, n = 0.360 for the section downstream.

The simulation of the diaphragm rocket was run in steady state, with a burn time of 2 s. A similar simulation was run without the diaphragm: the ballistic coefficients were assumed

to be a = 0.132 and n = 0.555[25].
The grain length was increased to obtain the same OF ratio of the motor with the diaphragm.

Post-fire simulations were set using as inputs: the average oxidizer mass flow rate, the grain diameter and regression rate measured from experiments.
Calculations were made both for gaseous and liquid N_2O injection. The experimental OF ratio was 4.8 with the diaphragm and 4.9 without. Tab.3.38 summarizes the input data for the simulations.

Sim. type	**Inj. type**	**Average** $\dot{m}_{ox}$ [g/s]	**Ad/At**	**Diaph. hole diam.** [mm]
preliminary	gas	812	1, no diaph.	29.9
preliminary	liquid	812	1, no diaph.	29.9
post-fire	gas	939	1, no diaph.	29.9
post-fire	liquid	939	1, no diaph.	29.9

Table 3.38: Preliminary and post-fire simulations set up for the increased-scale motor.

Good agreement was found between CFD simulations and experimental averaged results (Fig.3.66). Post-fire simulations agree better with experimental results and the difference between gas and liquid injection is negligible.

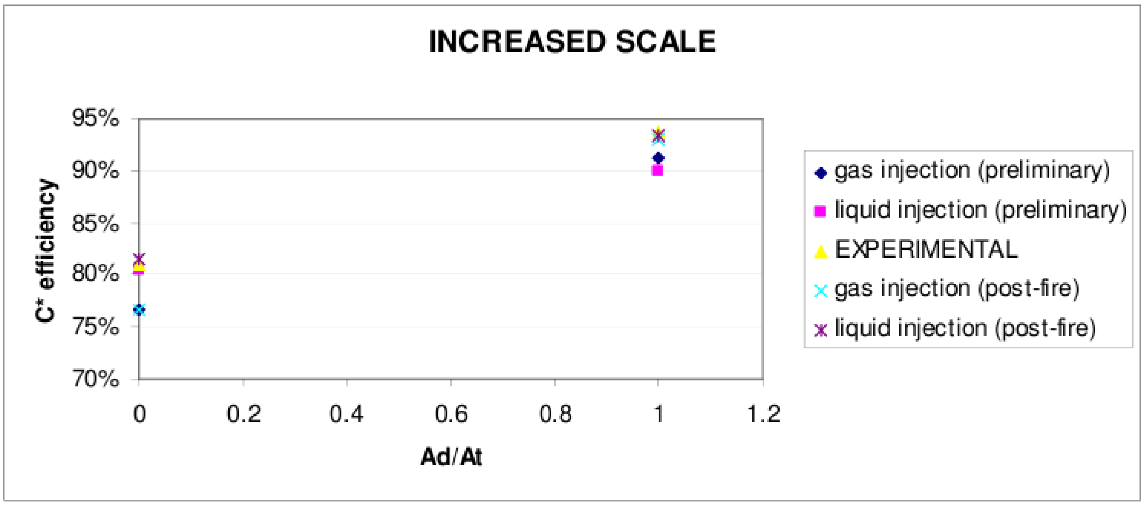

Figure 3.66: C^* efficiency measured with experiments and resulting from CFD, both preliminary and post-fire (liquid and gaseous).

Simulations agree with experiments also in the no-diaphragm case. The differences between the flow field with and without the diaphragm are shown in Fig.3.67.
As for the lab-scale, if the diaphragm is not used, N_2O consumption is incomplete, and it partially exits the nozzle without burning. This justifies the higher combustion efficiency mea-

sured with the diaphragm, where N_2O consumption is almost complete.

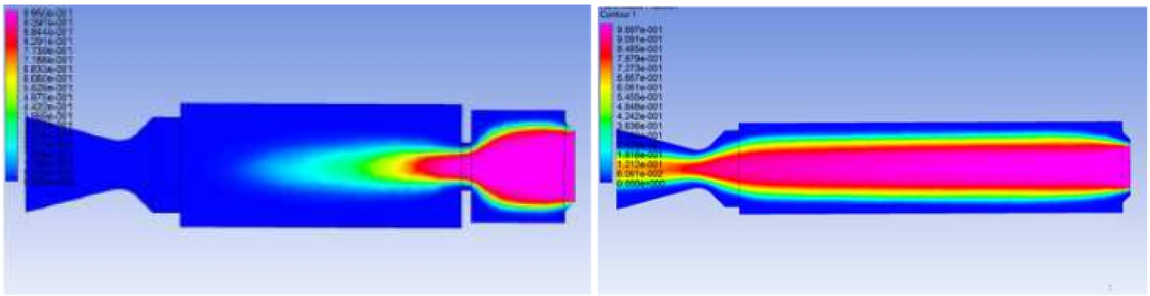

Figure 3.67: N_2O mass fraction simulated for the increased scale: on the left, the diaphragm Ad/At = 1, on the right, the rocket without the diaphragm.

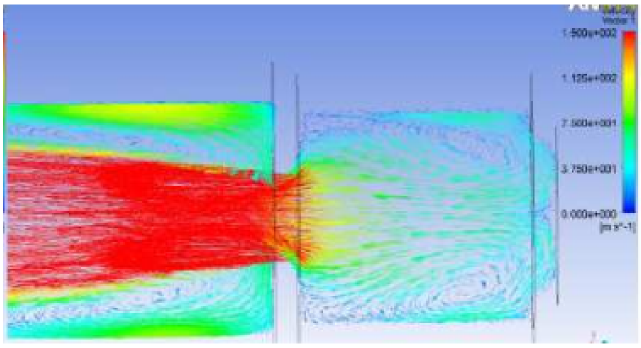

Figure 3.68: Recirculation in the flow field.

In the increased-scale configuration with diaphragms, CFD predicts recirculation.
Fig.3.68 shows the liquid oxidizer triggering two large recirculation vortices.
Two more eddies are established downstream of the diaphragm. In the close vicinity of the mixing device, gas velocity is high and CFD predicts high heat transfer with the fuel surface. This result is not in line with experiments, where conical grain consumption is observed just downstream of the diaphragm.

However, there is another concurring parameter: gas temperature.
As shown in Fig.3.69, temperature is higher (doubled) upstream, near the diaphragm, and downstream in the second half of the grain. This temperature distribution is in line with the grain consumption observed (right picture of Fig.3.69).
Red circles highlight grain sections where both regression rate and gas temperature were high.
Blue circles show sections at low regression rate and gas temperature.
Thus, the hypothesis is that heat transfer is higher in close proximity of the recirculation eddies, but regression rate is more influenced by the net gas heat distribution along the fuel grain.

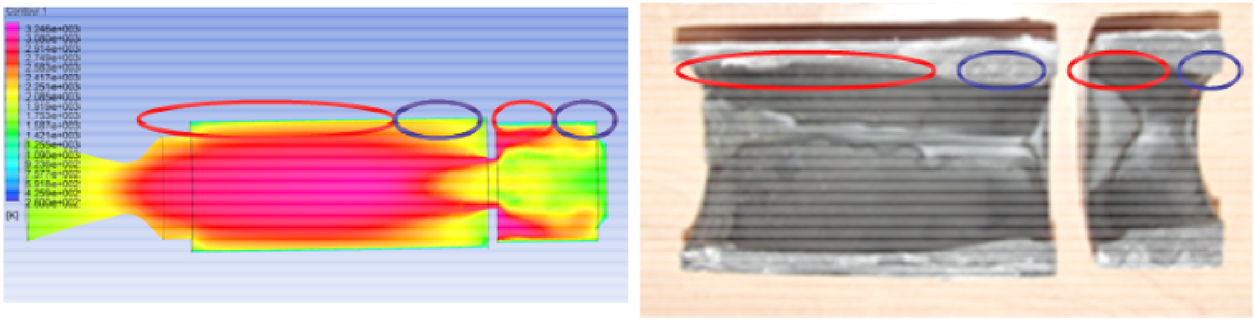

Figure 3.69: Comparison between gas temperature and the observed fuel grain consumption.

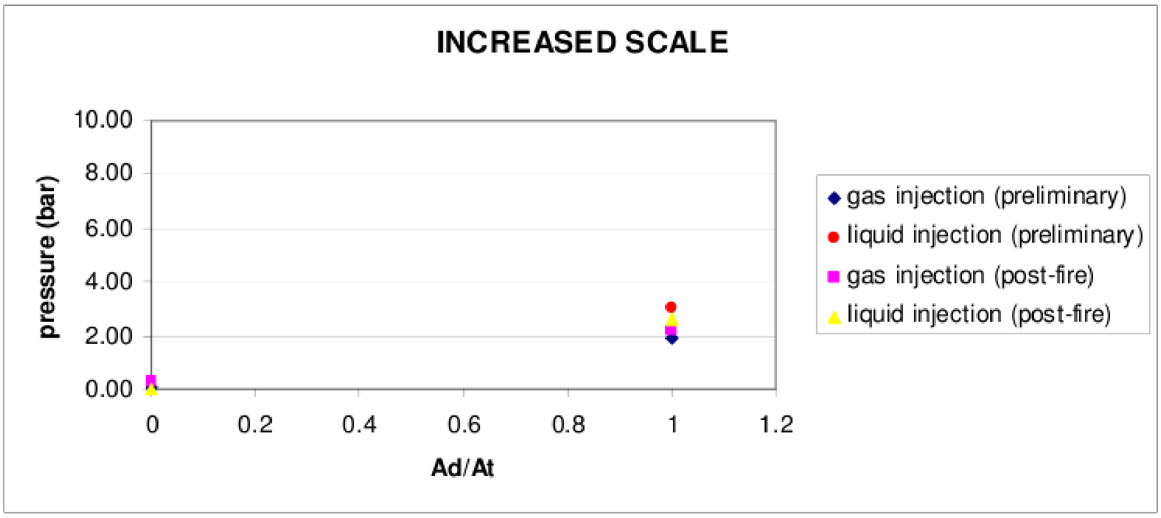

Figure 3.70: Pressure drop across the diaphragm as evaluated by the CFD.

The pressure drop across the diaphragm was evaluated with CFD, because the direct measurement was not feasible due to the combustion chamber shape, refurbished from past activities and is presented in Fig.3.70.
The average pressure drop is 2.5 bar, in line with the values measured for the lab-scale motor and an increase of 0.5 bar was observed with liquid injection, due to the higher vorticity established in the grain section upstream of the diaphragm.

Chapter 4

Conclusions

Conclusions are presented separately in two different sections: the first concerns the PMD software and the experiment created to validate it, whereas the second is about the validation of a software reproducing the fluid dynamic behavior of a hybrid rocket.

4.1 PMD Code Validation and SPONGE Experiment

To study the fluid dynamics of a liquid inside a tank provided with a PMD, an experiment has been designed and flown on board a sounding rocket. Data coming from the sensors (gyro, accelerometers, RTD, cameras) have been down-linked to the ground station and recorded on board.
The frames recorded by the two cameras monitoring two views of the liquid surface (up and side-view) have been collected and analyzed, in order to synchronize them with external loads. This way it has been possible to correlate the liquid behavior to the external loads acting on the system.

4.1.1 Experiment Results and Data

4.1.1.1 Data Recorded on Board

During the preliminary analysis of the frames acquired, a video was mounted and some aspects of the liquid dynamics were discovered. Not enough liquid had entered the sponge device, but it was possible to see:

1. The stable position of the liquid due to the centrifugal force, deriving from the rocket spinning;

2. A great liquid displacement on the tank wall, due to a quite great impulse or external force;

3. A minor movement;

4. A displacement of a certain amount of liquid finally trapped inside the sponge. Unfortunately, the quantity absorbed was insufficient to consider the scientific goal completely achieved.

After the launch campaign, the video has been synchronized with sensors data and the flight time line. In particular, it has been necessary to find which flight events in the time line had caused a specific result on the liquid.

Concerning accelerometers, a problem was found related to an exchange of the signals coming from the different channels. Accelerometers have been synchronized with both the video and gyro data, following a non-automatic procedure, also due to the difficult interpretation of how the signals exchange happened. What is believed to have caused channels inversion is a bug in the Helios boards software.
Gyro signals revealed that probably SPONGE platforms started to rotate, but then stopped. An investigation was performed to clarify this behavior and what was found is that SPONGE plates rotated an angle of about 70 °. After that, a detached cable prevented the experiment from concluding its velocity profile or something else caused its stop.

4.1.1.2 Signals and Time Line Correlation

Fig.4.1 shows the signals after their synchronization with the flight events time line.

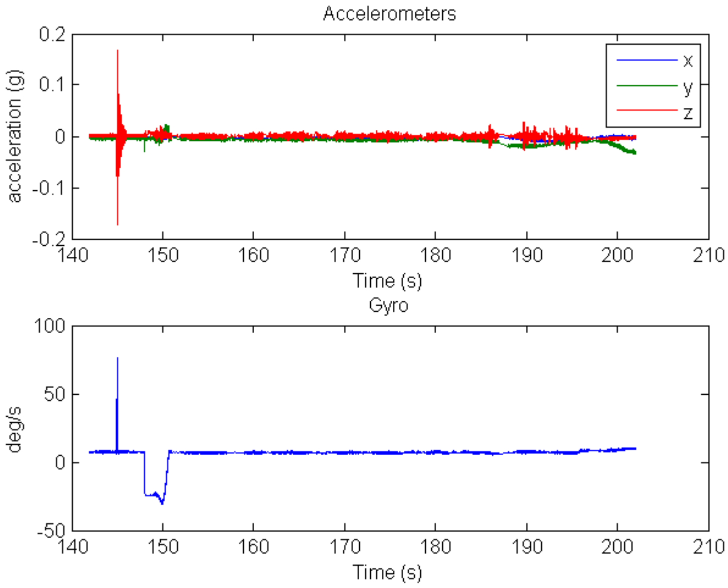

Figure 4.1: Image showing that SPONGE rotated an angle of 70 ° after its activation.

The number of frames acquired is not always constant in equal time intervals. This depends on the Helios board acquisition and in particular is due to the lower data acquisition speed compared to the frame grabber transmission velocity.
A video has been created (Fig.4.2) after the synchronization of the various signals. The liquid

dynamics is therefore related to some specific events during the flight and it is possible to identify them.

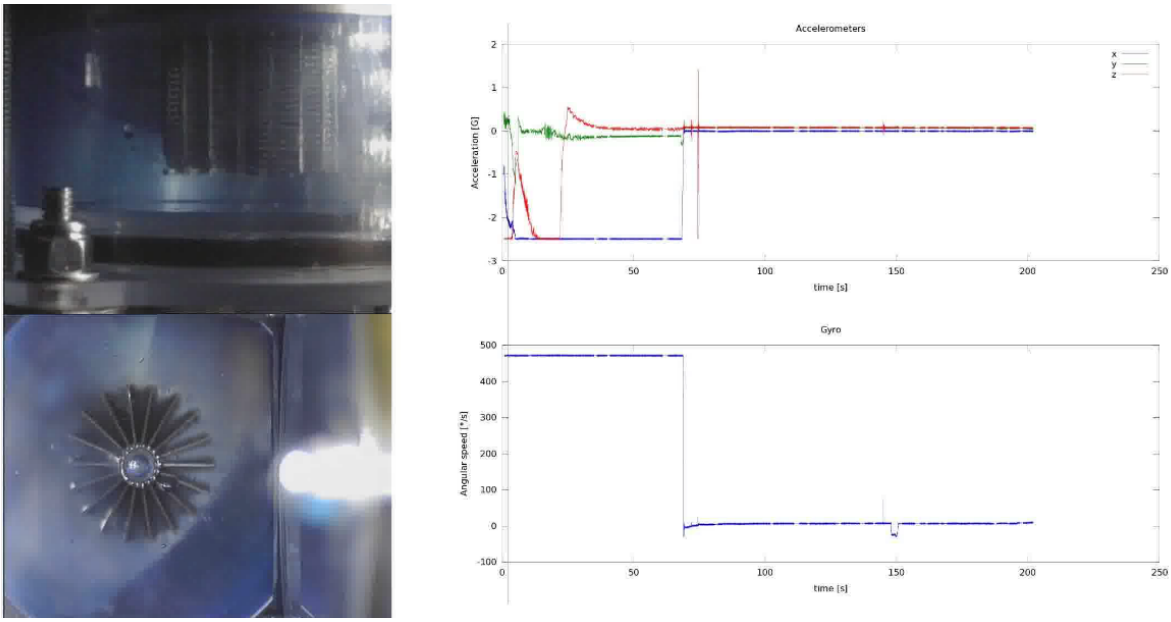

Figure 4.2: Screen shot of the video mounted to show a correlation between signals and frames acquired during the launch phase.

The following list resumes the main aspects of liquid motion inside the tank during the initial spinning phase and until the end of the experiment, when it was switched off.

- At the beginning, the liquid is attached to the tank wall due to the rocket spin;
- The first important movement of the liquid is due to REXUS yo-yo despin. After this event, it spreads remaining attached to the wall and occupies a more extended region.
- When the nosecone detaches, a movement is slightly visible through the liquid bulk, but it does not cause its absorption into the sponge.
- When the motor detaches, this causes an excitation on the liquid, which is pushed towards the sponge device and partially absorbed.

4.1.2 PMD Code Results

A complete validation of the 3D numerical code implemented to describe PMD behavior has been impossible, due to the lack of data coming from bubble point experiments and contact angles. These tests are foreseen in the near future and TAS-I is in charge of organizing them and collecting related results.
The full list of the tested configurations is reported in 3.1.1. Anyway, the code has been verified and proved to work correctly in different possible bubble point conditions. Capillary behavior was reproduced and simulated as well, giving the expected results.

4.2 Hybrid Rocket CFD Results

In the first studies about how to simulate the internal fluid dynamics of hybrid rockets by means of CFD, gas injection was simulated.
Simulations have been important first of all to assess the effects of different diaphragm types on the performance of a laboratory hybrid rocket built and tested by Grosse.
Several approximations of the reacting fluid dynamics have been made and simulations have been run as steady state.
The CFD geometries used derived from some configurations tested by Grosse during his experimental campaign[18]. In particular, the test cases considered for this study are:

- 1-hole Diaphragm at 24% grain length;
- 4-holes Diaphragm at 24% grain length;
- 1-hole Diaphragm at 33% grain length;
- 4-holes Diaphragm at 33% grain length;
- No-diaphragm hybrid rocket motor (cylindrical grain).

First of all, the no-diaphragm configuration global convergence was verified, to determine the mesh characteristics suitable for a reliable result.
Due to this analysis and to reach global convergence, approximately 1.5 million elements have been used to create the meshes. The elements have a side size of 1 mm, with a minimum on the grain surface of 0.75 mm.
Then, for the same motor configuration without any diaphragm, some simulations have showed the effect of different turbulence models on the flow field.
The k-ϵ and k-ϵ RNG models give the same results as well as the k-ω and k-ω SST models, whereas the k-ω model gives different outputs with respect to the k-ϵ.
With the k-ω model, the resulting flame temperature is lower. The efficiency obtained with k-ω corresponds with an error lower than 1% to the average experimental value.

Finally, the hybrid rocket motor configurations with 1 and 4 holes located at the 24% or 33% of the fuel grain length have been studied.
The numerical results of the no-diaphragm basic configuration agree with experiments, in fact the error on efficiency is lower than 6% (calculated using the average experimental C^*) for each of the test cases analyzed and the error on pressure prediction is lower than 3%.
The simulations reproducing the diaphragm configurations, have all showed an error on the average maximum pressure value lower than 6%, whereas the maximum error on the average measured efficiency is 5.3%.

These results validate the approach described to CFD simulations for the numerical investigation of the effect of mixers in hybrid rockets. This also means that CFD is a useful tool for pre-design purposes, because of the good agreement between numerical simulations and experiments, despite the several approximations applied.

To assess the quality of these CFD simulations into greater detail and with a higher accuracy, the mesh process shall be analyzed more thoroughly.
The characteristic size of the cells shall be reduced in those areas corresponding to section variations, or in the zones characterized by a high gradient of the physical quantities, such as near the diaphragm and the grain walls, in order to be able to treat physics more accurately. Moreover, the wall thermal flux and regression rate should be studied better to run a simulation closer to real physics. A further step could be to extend the simulations to the unsteady case, to analyze the the hybrid rocket transient behavior.

The suitable numerical models have been presented and discussed for the simulations reproducing liquid injection, in particular for liquid particles evaporation and combustion. Results from experiments have been used for this study as well:

- A lab-scale no-diaphragm geometry from Grosse's tests (2009);
- A lab-scale 4-hole diaphragm geometry from Grosse's tests (2009);
- A lab-scale 1-hole diaphragm geometry from CISAS tests (2011);
- An increased-scale no-diaphragm geometry from CISAS tests (2011);
- An increased-scale 1-hole diaphragm geometry from CISAS tests (2011).

It has been proved, by means of comparisons with experiments, that liquid injection simulations give reliable predictions of the flow field. In fact, the differences between the CFD-calculated C^* and the average experimental characteristic velocity for the different configurations analyzed are:

- Grosse lab-scale no-diaphragm: 5.56 %;
- Grosse lab-scale 4-hole diaphragm: -1.78 %;
- CISAS lab-scale 1-hole diaphragm: 1.78 %;
- CISAS increased-scale no-diaphragm: 5.91 %
- CISAS increased-scale 1- hole diaphragm: -0.89 %.

Errors are lower than 6% and liquid simulations show a good agreement with experiments, especially considering that the uncertainty on the measured C^* is $\pm 4\%$.
CFD results predict correctly a higher efficiency for those geometries provided with a diaphragm, compared to the same configurations without it.
Compared to the corresponding gas injection test cases, liquid injection causes a remarkable difference in the flow field, as long as particles are not evaporated. Results start to be similar from those regions in which both the simulations are characterized by the gas phase alone.
As the diaphragm is moved towards the section from which liquid particles are injected, the flow field starts to differ more from the corresponding gaseous simulation, because particles do not have the necessary time to evaporate upstream of the mixing device.

Different ways of simulating liquid injection have been described as well, each suitable to represent a different injector type or to model a specific injector plate geometry. If the channels number is high, it is acceptable to simulate the injection plate as an injection plane having a diameter corresponding to that of the plate, but this approximation cannot be used when channels are few, because the liquid jets interaction resulting from the model would be very different from reality.
Liquid injection simulations also show a peculiar phenomenon: a recirculation near the injection section. It helps species mixing, particles evaporation (because it increases the average residence time of the particle in a specific combustion chamber area) and can induce a flame holding effect, if the recirculation forms downstream or inside of a diaphragm.

The future objective is to further complete the CFD analyses introducing:

1. A new boundary condition able to avoid imposing a constant mass flux and allowing the simulation of a regression rate depending on the wall heat flux;
2. Liquid droplets entrainment, in order to properly simulate paraffin-based fuels.

Chapter 5

Conclusioni

Le conclusioni sono presentate in due diverse sezioni: la prima riguarda il software che descrive il comportamento dei PMD e l'esperimento per validarlo, mentre il secondo riguarda la validazione di un software per riprodurre la fluidodinamica di un razzo ibrido.

5.1 Validazione del Codice per PMD e SPONGE

Per studiare la dinamica di un liquido all'interno di un serbatoio dotato di PMD, è stato progettato un esperimento che ha volato a bordo di un sounding rocket, grazie ad un programma ESA. Dati provenienti dai sensori di bordo (giroscopio, accelerometri, RTD, fotocamere) sono stati trasmessi alla stazione di terra e registrati su flash disk. I fotogrammi registrati dalle due fotocamere puntate sul liquido sono stati raccolti e analizzati, per sincronizzarli con la time line degli eventi e la dinamica del razzo. Si è quindi correlato il comportamento del liquido con i carichi esterni agenti sul sistema.

5.1.1 Risultati dell'Esperimento e Dati

5.1.1.1 Dati Registrati a Bordo

Durante l'analisi preliminare dei fotogrammi acquisiti, è stato montato un video che ha permesso di indagare la dinamica del liquido. Una quantità troppo ridotta di liquido è entrata nella sponge per poter ottenere dati precisi, ma si è visto con chiarezza quanto segue:

1. La posizione stabile del liquido a causa della forza centrifuga dovuta allo spin del razzo;
2. Un grande spostamento del liquido, che si schiaccia sulla parete del serbatoio a causa di un impulso sufficientemente intenso;
3. Un movimento di ridotta entità;
4. Uno spostamento di una certa quantità di liquido, che è infine entrato nella sponge. La quantità assorbita non è stata sufficiente a considerare l'obiettivo scientifico completamente raggiunto.

Dopo la campagna di lancio, i dati video sono stati sincronizzati con quelli dei sensori e con la time line. In particolare, è stato necessario trovare quali eventi di volo hanno provocato uno specifico comportamento del liquido.

Per quanto riguarda gli accelerometri, si è notato un problema relativo ad uno scambio di segnali provenienti da diversi canali. Questi scambi sono stati trovati con un procedimento non automatico. I dati degli accelerometri sono stati sincronizzati sia con il video che con i segnali del giroscopio senza seguire una procedura automatica, anche per la difficile interpretazione dello scambio di segnali tra i canali.
Ciò che si crede abbia causato l'inversione dei canali, è un bug nel software della scheda Helios. I segnali del giroscopio hanno rivelato che probabilmente la piattaforma dell'esperimento ha iniziato a ruotare, ma poi si è bloccata. Si è condotto uno studio per chiarire questo comportamento e si è visto che la piattaforma ha ruotato di un angolo di circa 70 °. Successivamente, un cavo staccatosi ha impedito la conclusione del profilo di velocità dell'esperimento o una qualche altra causa ne ha provocato l'arresto.

5.1.1.2 Segnali e Correlazione Temporale

Fig.5.1 mostra i segnali dopo la loro sincronizzazione con la time line di volo.

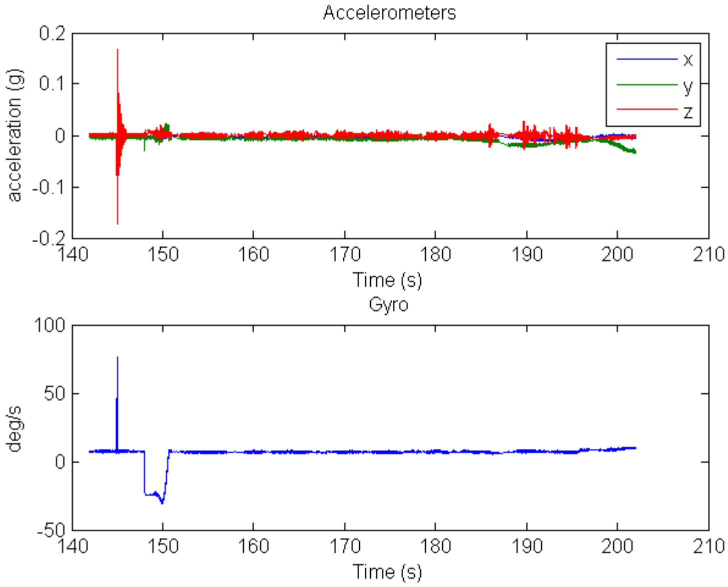

Figure 5.1: SPONGE ha effettivamente ruotato per alcuni secondi (angolo di 70 °) dopo l'attivazione.

Il numero di fotogrammi acquisiti non è sempre costante per intervalli di tempo uguali. Questo dipende dalle caratteristiche della scheda di acquisizione Helios ed in particolare è dovuto alla velocità di acquisizione dei dati ridotta rispetto alla velocità di trasmissione del frame grabber.
Dopo la sincronizzazione dei vari segnali è stato creato un video (Fig.5.2). La dinamica del liquido è quindi relativa ad alcuni eventi specifici e identificabili del volo.

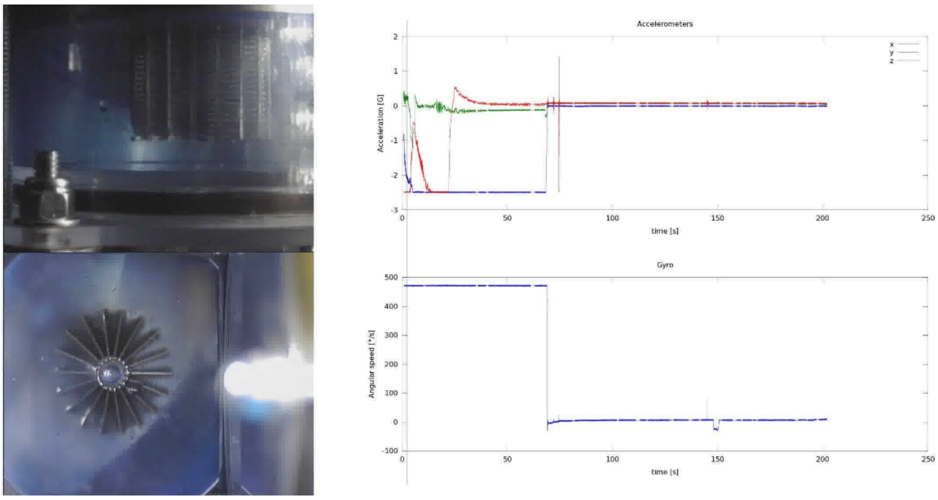

Figure 5.2: Screen shot del video realizzato per correlare i segnali e i frame acquisiti durante il volo.

L'elenco che segue riprende i principali aspetti del movimento del liquido all'interno del serbatoio durante la fase iniziale e fino alla fine dell'esperimento.

- All'inizio, il liquido è attaccato alla parete del serbatoio a causa dello spin del razzo;
- Il primo movimento importante del liquido è dovuto al despin yo-yo. Successivamente, il liquido si diffonde rimanendo attaccato alla parete del serbatoio e occupa una regione più estesa.
- Quando si stacca il nosecone, un movimento è leggermente visibile attraverso la massa liquida, ma non è tale da provocare il suo assorbimento completo nella sponge.
- Quando il motore si stacca, questo provoca una sollecitazione sul liquido, che è spinto verso la sponge e viene parzialmente assorbito.

5.1.2 Risultati della Validazione del Codice per PMD

Una validazione completa del codice 3D implementato per i PMD non è stata possibile, a causa della mancanza di dati provenienti da esperimenti di bubble point. Questi test sono previsti nel prossimo futuro e TAS-I ha il compito di organizzarli e raccogliere i relativi risultati.
In ogni caso, il codice è stato verificato e ha dimostrato di funzionare correttamente per diversi possibili bubble point. Il comportamento capillare è stato anche riprodotto e simulato dando i risultati attesi.

5.2 Risultati della Validazione del Codice per Razzi Ibridi

Nei primi studi su come simulare la fluidodinamica interna di un razzo ibrido per mezzo di software CFD, si è simulata l'iniezione gassosa.
Le simulazioni effettuate sono servite prima di tutto per valutare gli effetti di vari diaframmi,

agenti come dispositivi di miscelazione, sulle prestazioni di un motore a razzo ibrido costruito e testato dal Dr.Grosse.
Si sono fatte approssimazioni diverse della reale fluidodinamica reattiva all'interno del motore e tutte le simulazioni sono state eseguite allo stato stazionario.
I risultati numerici sono stati confrontati con alcune delle configurazioni testate da Grosse durante la sua campagna sperimentale[18]. In particolare, i test case considerati sono:

- Diaframma a 1 foro al 24% della lunghezza del grano;
- Diaframma a 4 fori al 24% della lunghezza del grano;
- Diaframma a 1 foro al 33% della lunghezza del grano;
- Diaframma a 4 fori al 33% della lunghezza del grano;
- Configurazione base del motore ibrido (grano cilindrico) senza diaframma.

Prima di tutto è stata verificata la convergenza globale della configurazione senza diaframma, per determinare le caratteristiche della mesh adeguata ad ottenere un risultato affidabile. A causa di questa analisi e per raggiungere la convergenza globale, circa 1.5 milioni di elementi sono stati usati per creare le mesh CFD. Gli elementi hanno una dimensione di lato pari a 1 mm, con un minimo sulla superficie del grano pari a 0.75 mm.
Per lo stesso motore senza diaframma, alcune simulazioni hanno mostrato l'effetto di diversi modelli di turbolenza. I modelli k-ϵ e k-ϵ RNG danno gli stessi risultati del k-ω e k-ω SST, mentre il k-ω ha output diversi rispetto al k-ϵ.
Con il modello k-ω, la temperatura della fiamma è inferiore. L'efficienza ottenuta con il k-ω corrisponde con un errore inferiore all'1% a quella media ottenuta dagli esperimenti.

Infine si è studiato il motore a razzo ibrido delle configurazioni con diaframma a 1 e 4 fori, posizionato al 24% o 33% della lunghezza del grano. I risultati numerici della configurazione base senza diaframma sono in accordo con gli esperimenti, infatti l'errore sull'efficienza è inferiore al 6% (calcolato usando il C^* sperimentale medio) per ciascuno dei casi analizzati, e l'errore sulla pressione è inferiore al 3%.
Le simulazioni riproducenti le configurazioni con diaframma, hanno tutte un errore sulla pressione media misurata inferiore al 6%, mentre l'errore massimo sull'efficienza media misurata è del 5.3%.

Questi risultati confermano la validità dell'approccio descritto alle simulazioni CFD per l'indagine numerica degli effetti dei diaframmi nei motori ibridi. Questo significa anche che il CFD è uno strumento utile per la pre-progettazione, dato il buon accordo tra le simulazioni numeriche e gli esperimenti, nonostante le varie approssimazioni applicate.

Per valutare la qualità di queste simulazioni CFD con maggior precisione, occorre analizzare il processo di realizzazione della mesh. La dimensione caratteristica delle celle va ridotta ulteriormente nelle aree corrispondenti alle variazioni di sezione, o nelle zone caratterizzate da un alto gradiente delle grandezze fisiche di interesse, come ad esempio vicino al diaframma e alle pareti del grano, in modo da trattare la fisica con più accuratezza.

Inoltre, il flusso termico a parete e la velocità di regressione dovrebbero essere studiati meglio, al fine di eseguire una simulazione più vicina alla realtà. Un ulteriore passo potrebbe essere quello di analizzare il comportamento transitorio del motore ibrido.

I modelli numerici per descrivere opportunamente l'evaporazione delle particelle e la combustione sono stati descritti anche nel caso di iniezione liquida. Per questo studio si sono utilizzati i risultati di alcuni esperimenti:

- Geometria lab-scale senza diaframma testata da Grosse nel 2009;
- Geometria lab-scale con diaframma a 4 fori testata da Grosse nel 2009;
- Geometria lab-scale con diaframma a 1 foro testata al CISAS nel 2011;
- Geometria increased-scale senza diaframma testata al CISAS nel 2011;
- Geometria increased-scale con diaframma a 1 foro testata al CISAS nel 2011.

E' stato dimostrato, attraverso un confronto con i risultati sperimentali, che le simulazioni con iniezione liquida forniscono previsioni attendibili del campo di moto. Infatti, gli errori del CFD calcolati sull'efficienza delle diverse configurazioni sono:

- Configurazione lab-scale senza diaframma di Grosse: 5.56%;
- Configurazione lab-scale con diaframma a 4 fori di Grosse: -1.78%;
- Configurazione lab-scale del CISAS con diaframma a 1 foro: 1.78%;
- Configurazione increased-scale del CISAS senza diaframma: 5.91%
- Configurazione increased-scale del CISAS con diaframma a 1 foro: -0.89%.

Tutti gli errori sono inferiori al 6% e le simulazioni con iniezione liquida sono in accordo con gli esperimenti, specialmente se si considera che l'incertezza sulla velocità caratteristica C^* misurata è ±4%.
Il software CFD prevede correttamente una maggior efficienza per le geometrie dotate di diaframma, rispetto allo stesse configurazioni che ne sono prive.
Per quanto riguarda i corrispondenti casi con iniezione di gas, l'iniezione di liquido provoca una notevole differenza nel campo di moto, fino a quando le particelle non sono evaporate. I risultati cominciano a essere simili a partire dalle regioni in cui entrambe le simulazioni sono caratterizzate dalla sola fase liquida.
Quando si sposta il diaframma verso la sezione da cui vengono iniettate le particelle liquide, il campo di flusso comincia a variare di più rispetto alla corrispondente simulazione gassosa, perché le particelle non hanno il tempo di evaporare a monte del diaframma stesso.

Ci sono diversi modi per simulare l'iniezione liquida, ciascuno adatto a rappresentare un diverso tipo di iniettori o uno specifico modello di piastra di iniezione. Se il numero di canali è alto, è accettabile simulare la piastra di iniezione con un piano di iniezione avente un diametro corrispondente a quello della piastra d'iniezione, ma questa approssimazione non può

essere utilizzata quando i canali sono pochi, perché l'interazione dei getti liquidi che ne deriva sarebbe molto diversa dalla realtà.
L'iniezione di liquido mostra anche un particolare fenomeno: un ricircolo presso la sezione di iniezione. Esso aiuta la miscelazione delle specie chimiche, così come l'evaporazione delle particelle (perché aumenta il tempo medio di residenza della particella in una data area della camera di combustione) e può indurre un effetto di flame holding, se il ricircolo si forma a valle o all'interno del diaframma.

L'obiettivo per il futuro è completare ulteriormente l'analisi CFD introducendo:

1. Una condizione al contorno nuova, in modo da evitare d'imporre un flusso costante di massa; in tal modo si potrebbe simulare una regression rate dipendente dal flusso di calore a parete;

2. Il trascinamento delle goccioline di liquido (entrainment), in modo da simulare correttamente i combustibili paraffinici.

Chapter 6

Summary

The aim of this thesis is to implement and use CFD codes and solvers describing some vital aspects of hybrid rockets, such as propellant dynamics inside tanks containing PMD devices and internal ballistics.

A 3D CFD tool has been implemented to simulate PMDs, and other commercial codes have been tested to analyze their capabilities in terms of simulating rockets fluid dynamics. Test beds and experiments have been used to retrieve the data for codes validation.

A brief description follows of the two main parts in which the work can be divided.

PMD Study

Hybrid rockets often use a propellant pressurization system ensuring a higher combustion chamber pressure and therefore the desired performance. This system is generally composed of a certain number of tanks, containing liquid propellant.

PMDs are used to control liquid behavior inside tanks, especially in micro-gravity conditions. They allow liquid propellant flow without gas ingestion and can be used not only in hybrid, but also in liquid rockets.

PMDs are static metal structures using surface tension and capillary phenomena, and are often made of titanium, which allows their use in corrosive propellants. With no moving nor deforming parts, they are inherently reliable.

They can be used in water, thermal and cryogenic systems, which makes the field of their possible applications even wider.

In fluid dynamics, the behavior of these devices cannot be simulated with standard tools because a very specific physics needs to be reproduced concerning capillarity, contact angle, sloshing, bubble point and multiphase fluid dynamics: it is necessary to develop a tool on purpose. The CFD software developed is 3D, can work in transient conditions and is based on OpenFOAM. It can handle bubble point phenomena, sloshing in various gravity conditions, interface transport between two fluid phases and the pressure drop due to the presence of a screen in the fluid domain.

An experiment has been designed and manufactured in order to validate the CFD code implemented; it was called SPONGE and was created in the framework of the REXUS program, a hands-on experience started by Lazzarin in 2009.

REXUS9, where SPONGE was installed, has been launched in February 2011 from Esrange Space Center in northern Sweden.

The data acquired during the flight have been transmitted to the ground station and recorded for successive analysis and for the sponge behavior assessment. The code has been validated comparing the frames deriving from the CFD simulations to the images saved during the real experiment.

Internal Ballistics Study

The other part of this thesis, describes the CFD study performed on hybrid rockets internal ballistics.

In this case, the aim was first of all to verify the capabilities of commercial CFDs in reproducing the physics of hybrid rockets and to assess their performance. The objective was to prove that CFD can be used as a powerful design tool, able to reduce the costs connected with experiments and manufacturing.

Different test cases have been created to validate these simulations reproducing the hybrid rocket geometries analyzed during the experimental tests conducted. Parameters such as pressure, characteristic velocity and efficiency are compared between CFD and experiments, to verify that the software can predict the most performing geometry configurations.

These studies are fundamental in the framework of theSPARTAN European research program, aiming at developing a throttable propulsion technology, which is needed for any planetary soft and precision landing. It relies on the hybrid engine technology, exploiting its capability of being throttled and its performance.

This program is supported by an advanced coding, and this is the reason why CFD becomes so important.

Chapter 7

Riassunto

Lo scopo di questa tesi è di implementare e utilizzare i codici e solutori CFD in grado di descrivere alcuni aspetti di vitale importanza per i razzi ibridi, come la dinamica del propellente all'interno dei serbatoi contenenti PMD e la balistica interna.
Uno strumento CFD 3D è stato implementato per simulare i PMD e altri codici commerciali sono stati testati rispetto alla possibilità di simulare la fluidodinamica interna dei razzi.
Banchi di prova ed esperimenti sono stati preparati per raccogliere dati da utilizzare per la validazione dei codici.
Le due parti principali in cui si è organizzato questo lavoro sono brevemente descritte in seguito.

Studio dei PMD

I razzi ibridi spesso utilizzano un sistema di pressurizzazione del propellente, che garantisce una più alta pressione in camera di combustione e di conseguenza le prestazioni desiderate. Questo sistema è generalmente composto da serbatoi contenenti propellente liquido.
I PMD sono utilizzati per controllare il comportamento del liquido nei serbatoi, soprattutto in condizioni di microgravità; essi consentono il deflusso senza ingestione di gas e possono essere utilizzati anche in razzi a propellente liquido.
Si tratta di strutture metalliche statiche, che usano la tensione superficiale e fenomeni capillari, e spesso sono in titanio, che ne consente l'utilizzo in propellenti corrosivi. Senza parti in movimento né deformanti, sono molto affidabili e possono essere utilizzati in acqua, in sistemi termici e criogenici, il che rende il campo delle loro possibili applicazioni ancora più vasto.
In fluidodinamica, il comportamento di questi dispositivi non può essere simulato con strumenti standard, perché dev'essere rappresentata una fisica molto specifica riguardante sia la capillarità che l'angolo di contatto, fenomeni di sloshing, il bubble point e la fluidodinamica multifase.
Il software CFD implementato è in grado di lavorare in condizioni transitorie e si basa su OpenFOAM. Esso gestisce lo sloshing in varie condizioni di gravità, il trasporto di interfaccia tra due fasi fluide e la perdita di carico dovuta alla presenza di una lastra sottile perforata (screen) nel dominio fluido.
Un esperimento è stato progettato e realizzato al fine di validare i risultati del software creato; si tratta di SPONGE, facente parte del programma REXUS, a cui Lazzarin ha partecipato dal 2009.
REXUS è il sounding rocket a bordo del quale è stato installato e lanciato l'esperimento,

nel febbraio 2011, dal Centro Spaziale Esrange nel nord della Svezia. I dati acquisiti durante il volo sono stati trasmessi alla stazione di terra e registrati per analisi successive e per la valutazione del comportamento del PMD. L'obiettivo era validare il codice confrontando i fotogrammi derivanti dalle simulazioni CFD con le immagini salvate durante l'esperimento vero e proprio.

Studio della Balistica Interna

L'altra parte di questa tesi descrive lo studio CFD della balistica interna dei razzi ibridi.
In questo caso, lo scopo è prima di tutto quello di verificare le capacità dei CFD commerciali nel riprodurre la fisica dei razzi ibridi. L'obiettivo è dimostrare che il CFD può essere utilizzato come strumento di progettazione potente, in grado di ridurre i costi connessi ad esperimenti e produzione di componenti.
Diversi test case sono stati creati per validare alcune simulazioni riproducenti le geometrie dei razzi ibridi testate durante le prove sperimentali. Parametri quali pressione, velocità ed efficienza vengono confrontati tra CFD ed esperimenti, per verificare che il software sia in grado di prevedere quali siano le configurazioni geometriche più performanti.
Questi studi sono fondamentali nell'ambito del progetto SPARTAN, un programma di ricerca europeo volto a sviluppare una tecnologia di propulsione throttable, necessaria per qualsiasi atterraggio di precisione in missioni planetarie. Esso si basa sulla tecnologia del motore ibrido e sfrutta la sua capacità di essere regolato in spinta e le sue prestazioni.

Acknowledgment

I was able to conclude this work thanks to the support of my family, all of my friends and colleagues. They always helped me and made this possible.

First of all, I would like to thank Marco Manente and Davide Rondini for helping me with everything belonging to the computational and numerical field, and for their support.
Then I would like to thank all of my friends who worked with me during the REXUS/BEXUS campaign: it's been hard guys, but finally we made it!

Many thanks also to Daniele Pavarin, always helping me even from a human point of view.

A special thank to Marco, who always supported me, even during the five years of University and to my Family, who made everything easier for me.

I will remember these three years as one of the most beautiful periods of my life! It's been great working with all of you guys!

Bibliography

[1] *Fluent User Manual*, 6.2 edition, July 2005.

[2] *OpenFOAM Programmer's Guide*, 1.6 edition, July 2009.

[3] *CFX User Manual*, 13.0 edition, July 2011.

[4] A.H.Lefebvre. *Atomization and Sprays.* Hemisphere Publishing Corporation, 1989.

[5] Akyuzlu K.M Antoniou.A. A Physics Based Comprehensive Mathematical Model to Predict Motor Performance in Hybrid Rocket Propulsion System. *JPC Paper*, 2005.

[6] Guobiao C. and Hui T. Numerical Simulation of the Operation Process of a Hybrid Rocket Motor. *JPC Paper*, 2006.

[7] A.Bettella M.Lazzarin N.Bellomo F.Barato D.Pavarin and M.Grosse. Testing and CFD Simulation of Diaphragm Hybrid Rocket Motors. *JPC Paper*, 2011.

[8] H. Norman Abramson et al. *The New Dynamic Behaviour Of Liquids in Moving Containers.* NASA, 1966.

[9] N.Bellomo M.Lazzarin F.Barato and M.Grosse. Numerical Investigation of the Effect of a Diaphragm on the Performance of a Hybrid Rocket Motor. *JPC Paper*, 2010.

[10] Marxman G.A. Combustion in the Turbulent Boundary Layer in a Vaporizing Surface. *10th International Symposium on Combustion*, 10(1):1337–1349, 1965.

[11] D.Etling U.Muller K.R.S.Sreenivasan U.Riedel H.Oertel, M.Bohle and J.Warnatz. *Prandtl's Essentials of Fluid Mechanics.* Springer-Verlag, 2nd edition.

[12] D.E.Jaekle Jr. Propellant Management Device Conceptual Design and Analysis: Sponges. *JPC Paper*, 1993.

[13] Johnson D.K. Serin N. Risha G.A. Merkle C.L. Kuo K.K.Lu.Y., Chiaverini M.J. and Venkateswaran S. Fundamental Phenomena on Fuel Decomposition and Boundary-Layer Combustion Process with Applications to Hybrid Rocket Motors. *Final Report for Contract no. NAS8-39945.*

[14] V.G. Levich. *Physicohemical Hydrodynamics.* Prentice Hall, 1962.

[15] L.P.Hsiang and G.M.Faeth. Near-Limit Drop Deformation and Secondary Breakup. *International Journal of Multiphase Flow*, 18(5):635–652, 1992.

[16] Gilbert M. Marxman G.A. Turbulent Boundary Layer Combustion in the Hybrid Rocket. *10th International Symposium on Combustion*, 9(1):371–383, 1963.

[17] Wooldridge C.E. Marxman G.A. and Muzzy R.J. Fundamentals of Hybrid Boundary Layer Combustion. *Heteregeneous Combustion, Progress in Astrounautics and Aeronautics*, 15(1):495–521, 1964.

[18] M.Grosse. Effect of a Diaphragm on Performance and Fuel Regression of a Laboratory Scale Hybrid Rocket Motor Using Nitrous Oxide and Paraffin. *JPC Paper*, 2009.

[19] M.Plich and C.A.Erdman. Use of Breakup Time Data and Velocity History Data to Predict the Maximum Size of Stable Fragments for Acceleration-Induced Breakup of a Liquid Drop. *International Journal of Multiphase Flow*, 13(6):741–757, 1987.

[20] M.Lazzarin M.Faenza F.Barato N.Bellomo and M.Grosse. CFD Simulation of a Hybrid Rocket Motor with Liquid Injection. *JPC Paper*, 2011.

[21] D.Quéré P.G. de Gennes, F.Brochard-Wyart. *Capillarity and Wetting Phenomena-Drops, Bubbles, Pearls, Waves.* Springer, 2004.

[22] G.Maier R.Schmehl and S.Wittig. CFD Analysis of Fuel Atomization. Secondary Breakup and Spray Dispersion in the Premix Duct of a LPP Combustor. *Bth Int. Conf. on Liquid Atomization and Spray Systems*, 2000.

[23] S.C.Kong S.C.Kuensberg and R.D.Reitz. Modeling the Effects of Injector Nozzle Geometry on Diesel Sprays. *SAE Paper*, 1999.

[24] S.R.Turns. *An Introduction to Combustion: Concepts and Applications.* Mc Graw-Hill.

[25] Skinner M. Buchanan A. Gulman R. Chan H. Karabeyoglu M. A. Cantwell B. Van Pelt D., Hopkins J. Overview of a 4-Inch OD Paraffin-based Hybrid Sounding Rocket Program. *JPC Paper*, 2004.

[26] P.V.Farrell Z.Han, S.Perrish and D.Reitz. Modeling Atomization Processes of Pressure-Swirl Hollow-Cone Fuel Sprays. *Atomization and Sprays*, 7(6):663–684, Nov-Dec 1997.